UNIVERSITY OF LEEDS

Tuning Synthetic Antiferromagnetic and Ferromagnetic Multilayers for Hosting Skyrmions

Emily Rachel Darwin
University of Leeds
School of Physics and Astronomy

Submitted in accordance with the requirements for the degree of
Doctor of Philosophy

June, 2023

I dedicate this thesis to John and Marian Darwin,
to Marie, Howard and Eva Darwin,
and to Riccardo.

Intellectual Property Statement

The candidate confirms that the work submitted is his own and that appropriate credit has been given where reference has been made to the work of others.

Work from the following jointly authored paper is in Chapter 6 of this thesis:

"Key points in the determination of the interfacial Dzyaloshinskii-Moriya interaction from asymmetric bubble domain expansion" A. Magni, G. Carlotti, A. Casiraghi, E. Darwin, G. Durin, L. Herrera Diez, B. J. Hickey, A. Huxtable, C. Y. Hwang, G. Jakob, C. Kim, M. Kläui, J.Langer, C. H. Marrows, H. T. Nembach, D. Ravelosona, G. A. Riley, J. M. Shaw, V. Sokalski, S. Tacchi, M. Kuepferling, *IEEE Transactions on Magnetics*, DOI:10.1109/TMAG.2022.3217891, (2022).

- **Work attributed to the candidate:** Preparation of samples a1 to a10, measurements of samples a1 to a10 at the University of Leeds, and some preparation of manuscript.
- **Work attributed to others:** A. Magni: experimental work, theoretical modelling, data analysis, simulations and main preparation of manuscript. G. Carlotti: experimental work and manuscript preparation. A. Casiraghi, A. Huxtable, C. Y. Hwang, C. Kim, S. Tacchi: experimental work. G. Durin, B. J. Hickey, C. H. Marrows: Discussions. L. Herrera Diez, G. Jakob, M. Kläui, J.Langer, D. Ravelosona: sample deposition. H. T. Nembach, G. A. Riley, J. M. Shaw: theoretical modelling and discussions. V. Sokalski: theoretical modelling, discussions and manuscript preparations. M. Kuepferling: discussions, management and manuscript preparation.

Acknowledgements

My appreciation goes foremost to my supervisor Prof. Bryan Hickey for his guidance and encouragement in this PhD during these turbulent years and for sharing his passion in research with me, and to Prof. John Cunningham, who was always available to help and guide me through the part of my project in electrical engineering. I would like to thank Dr. Mannan Ali for endless discussions, help and training with all aspects of my PhD, especially when they came with an espresso hit. I would like to thank Dr. Gavin Burnell for the huge amount of work that he put into creating codes which run half of the equipment in the physics labs, and for useful insights into results and help with coding. I would like to thank Prof. Chris Marrows for his discussions and guidance in the TOPS project, and Dr. Joe Barker for writing the code for the thin film approximation of Bloch's law. I would like to thank Dr. SaeJune Park for all of his kindness, training and guidance from the cleanroom to the THz bench. I would like to thank Dr. Joshua Freeman for creating the code to run the THz bench and Dr Said Ergoktas for performing a last minute measurement for me on the THz bench. I would like to thank Dr. Mark Rosamond and Dr. Li Chen for their training, help and guidance for everything cleanroom related. I would like to thank Dr. Ben Johnson for performing the XPS measurements for me, and Dr. Simon Connell and Dr. Lekshmi Kailas for training me in MFM. I would like to thank the electrical and mechanical workshop staff, particularly for fixing the power supply that was pouring out smoke and to Leigh for helping me carry power supplies, magnets and watercoolers back and forth between physics and engineering. Plus, Dave and Adam, for constantly supplying the helium and nitrogen to keep the experiments going. I would like to thank Prof. Thomas Hase for passing on his knowledge of complicated GenX fitting. I would like to thank Prof. Hans Hug, Dr. Andrada-Oana Mandru and Dr. Yaoxuan Feng for their willingness to measure my samples and for the guidance and discussions that followed. I would like to thank Prof. Pedram Khalili-Amiri for the opportunity to spend a fantastic month and a half in his group at Northwestern University in the USA and Dr. Victor Lopez Dominguez for all his help with measurements there and his interesting sense of humour. I would like to thank the EMPIR TOPS project and partners, Dr. Mark Bieler for organising the project and Dr. Michaela Kuepferling and Dr. Alessandro Magni for their discussions. I would like to thank the members of the condensed matter the group at Leeds, specifically Dr. Philippa Shepley for all the discussions and guidance with Victor, and Dr. Nathan Satchell and Dr. Matt Rogers for training me on equipment and helpful discussions, it was a pleasure to work with them all. Dr. Alex Stacey for her companionship in the TOPS project and her unwavering friendship. I'd like to also thank Chris Barker, Abiral Tamang and Sean Stansill for their friendship, helpful chats and keeping me sane with little adventures and early morning climbing sessions.

Plus, Dr. Mohammed Alyami, Dr. Satam Alswage and Dr. Khulaif Alshammari for their friendship and positivity. I would like to thank Prof. Giovanni Finocchio for the opportunities he has brought to me and all of his kind guidance. I would like to thank my friends, Aimee, Holly, Beth, Sophie, Becca, Daisy and Rach for providing me with doses of laughter throughout. I'd like to thank Stella and Nuccio for taking care of me as I was writing at their home. I'd like to thank my sister, Eva, and my mum, Marie, for their kindness, belief in me and loving support, especially when I was working long hours. I'd like to thank my dad, Howard, for his advice, support, and first inspiring me with physics, and my grandparents, John and Marian, for their constant encouragement, interest and warmth. Finally, I would like to thank Riccardo, for the advice, love and happiness he has always given me.

Abstract

We present ways to characterise and optimise multilayers for skyrmion-based devices using Co and CoB with Pt, Ir and Ta. Magnetic proximity effects at the interface of a ferromagnet and a non-magnet were studied to find agreements between literature - a topic which is often disputed. It was confirmed that Pt and Ir experience induced moments at a magnetic interface, particularly Pt, and Ta causes a magnetic dead layer. More moment was measured for CoB/Pt interfaces than Co/Pt, and an inhomogeneity in the layer was seen below 8 Å of ferromagnet. The Pt spin polarisation depth was shown to be ∼10 Å, and the top interface to contribute more moment than the bottom. These effects must be considered in the saturation magnetisation of a multilayer thin film. Attention was also given to the Dzyaloshinskii-Moriya interaction and its strength, a key parameter of a skyrmion. It was shown, via collaborative work, that this value could vary, even when the same sample was measured in different laboratories using both different and the same method. Proximity effects, and using an approximation of Bloch's law specific for thin films could also change the strength of the Dzyaloshinskii-Moriya interaction. Synthetic antiferromagnets consisting of CoB, Ir and Pt were also designed to produce a device with capabilities more suited for skyrmion racetrack memories. Multiple parameters were characterised and trends were established as a function of repetitions, material thicknesses and temperature. An understanding of the hysteresis mechanisms was established via electrical measurements. A synthetic antiferromagnet was built with the ability to host magnetic field-nucleated skyrmions, however, the skyrmions were not coupled together antiferromagnetically across the two ferromagnetic layers. These samples were also probed with THz waves by depositing the material on a nanofabricated coplanar waveguide. Adaptations of the waveguide and the measurement set-up were successful, however, further work is necessary to confirm the observed trends.

Contents

Abbreviations

AFM-IEC	Antiferromagnetic interlayer exchange coupling
AHE	Anomalous Hall effect
AMR	Anisotropic magnetoresistance
BCC	Body centered cubic
BCT	Body centered tetragonal
BLS	Brillouin light scattering
CPW	Coplanar waveguide
DC	Direct current
DL	Dead layer
DMI	Dzyaloshinskii-Moriya interaction
emf	Electromotive force
FCC	Face centered cubic
FCT	Face centered tetragonal
FFT	Fast Fourier transform
FM	Ferromagnet/ic
FMR	Ferromagnetic resonance
FWHM	Full width half maximum
IP	In-plane
LHS	Left-hand side
LT-GaAs	Low temperature gallium arsenide
MBE	Molecular beam epitaxy
MFM	Magnetic force microscopy
ML	Monolayer
MOKE	Magneto-optic Kerr effect
MPE	Magnetic proximity effect
NM	Non-magnetic
OP	Out-of-plane
PC	Photoconductive
PMA	Perpendicular magnetic anisotropy
RHS	Right-hand side
RKKY	Ruderman, Kittel, Kasuya and Yosida
SAF	Synthetic antiferromagnet
SkHE	Skyrmion Hall effect
SQUID	Superconducting quantum interference device
STM	Scanning tunneling microscope
TAFF	Thermally assisted flux flow
THz-TDS	Terahertz time domain spectroscopy
VSM	Vibrating sample magnetometry
XMCD	X-ray magnetic circular dichroism
XRD	X-ray diffraction
XRMR	X-ray resonant magnetic reflectivity
XRR	X-ray reflectivity

CHAPTER 1

Introduction

1.1 Introduction

Our planet has eight billion people, people whose lives become more and more dependent on technology. Our planet faces a climate disaster, a disaster fueled by the increasing demand for technology. The topic of this thesis is a magnetic particle called a ‘skyrmion’. This particle presents a promising gateway to a planet that benefits from spintronics technology, and therefore less power consumption.

An environment for skyrmions suitable for spintronic application is a magnetic multilayer. We present ways to characterise and optimise multilayers for skyrmion-based devices using Co and CoB with Pt, Ir and Ta. The intention of this thesis is to both establish conformity in the methods used to carry out research into skyrmions, and to contribute knowledge, understanding and progress into the field of research. In particular, involving synthetic antiferromagnets (SAFs), with the hope that this work can promote further research and contribute to the battle against climate change. Skyrmions have a unique set of topological properties, which lead them to be highly stable in their environment. They can have diameters in the nanometer range, can now be stabilized at room temperature without a magnetic field and can also be manipulated using an electric current - all of which makes them suited for applications such as data storage and logic devices.[1–3] SAFs have become a favoured choice for hosting skyrmions as they help counteract problems which arise in ferromagnetic skyrmion hosting materials. Terahertz technology provides ultrafast speeds and is becoming more common, such as in communication devices. Combining the field of skyrmions and THz means potential ultrafast, ultra-stable devices could be designed for data storage and transfer.

This thesis focuses on the characterisation and investigation of skyrmion hosting ferromagnetic (FM) materials and SAFs, using typical characterisation techniques, such as x-ray reflectivity, Kerr imaging and magnetometry. Other more complex techniques which required nanofabrication of devices were also performed, such as Hall resistance measurements and terahertz time domain spectroscopy (THz-TDS).

1.2 Thesis Overview

Chapter 2 describes theoretical concepts relevant to the thesis. Chapter 3 provides a review of relevant literature and progress in the research field. Chapter 4 details the experimental methods which are used though out this thesis. Chapter 5 summarises literature from multiple decades into the research of magnetic proximity effects (MPE) at a FM/Non-magnetic (NM) interface. It compares these results with measurements taken on sputtered Co and CoB samples, interfaced with Pt, Ir and Ta layers - sample structures commonly present in skyrmion literature.

Chapter 6 is part of a multi-partner research investigation into discrepancies when calculating the Dzyaloshinski-Moriya interaction (DMI) in Co multilayers. Various approaches are considered to work out different parameters that contributed to the DMI constant. Also explored, is how proximity effects affect the DMI, and the difference between using Bloch's law for bulk or thin films. The work from this chapter was published in Reference [4].

Chapter 7 investigates the antiferromagnetic interlayer exchange coupling (AFM-IEC) of CoB/Ir /Pt multilayers as a function of temperature, number of repeats and thickness of the different material components. It also proposes a sample design to host skyrmions in SAFs, which is also studied as a function of temperature and thickness of the layers.

Chapter 8 describes the characterisation of coplanar waveguides, adapted from Reference [5], to perform on-chip THz-TDS measurements. The waveguides include a Hall bar in which it is possible to deposit the FM multilayers or SAFs which are studied throughout the thesis, and therefore investigate high frequency behaviours. Results from field dependent measurements are also reported.

The results from all the chapters are summarised in Chapter 9, including an outlook on future work which could be performed to further the studies and consolidate the conclusions.

CHAPTER 2

Theoretical Background

2.1 Magnetisation

Magnetisation (**M**) is defined as the dipole moment per unit volume. When a material is placed into a magnetic field (**H**), **M** is usually proportional to **H**, with a factor of magnetic susceptibility (χ) - which describes by how much a material will become magnetised when subjected to an applied magnetic field.

$$\mathbf{M} = \chi\mathbf{H} \tag{2.1}$$

Magnetic flux density (**B**) describes the amount of flux in an area perpendicular to the direction of the flux, it considers both the applied field and the magnetisation, with a factor of μ_0, the vacuum permeability.

$$\mathbf{B} = \mu_0(\mathbf{H} + \mathbf{M}) \tag{2.2}$$

One way to represent the magnetisation of electrons is the Bohr magneton (μ_B), it is derived from the angular momentum of orbiting electrons and is quantised in units of $\hbar$. e is the charge and m_e is the electron rest mass.

$$\mu_B = \frac{e\hbar}{2m_e} \tag{2.3}$$

In addition to the susceptibility, another magnetic property of a material is the permeability (μ), which represents the magnitude of resistance a material has against aligning with an applied magnetic field. As $\mu = \mu_0(1 + \chi)$, using Equation 2.1 and 2.2, **B** can be defined in terms of the permeability and **H**.

$$\mathbf{B} = \mu\mathbf{H} \tag{2.4}$$

There are five main categories of materials in magnetism: diamagnetic, paramagnetic, ferromagnetic, ferrimagnetic and antiferromagnetic. All materials behave diamagnetically, however, if a material is solely diamagnetic, it means there are no unpaired electrons in the system. The orbiting electrons in the atoms have a magnetic field associated with them as they are in circular motion and therefore accelerating. An external field can cause the electrons to change their orbital motion which causes their magnetic field to oppose the direction of the external field, so diamagnets have a magnetic susceptibility less than zero ($\chi<0$).

A paramagnetic material has some unpaired electrons and therefore it is possible for a net alignment of the dipoles to occur. This can be induced when a magnetic field is applied to the paramagnetic material in a certain direction (for example ↑), the electrons with spins parallel (↑) to the field will have less energy and the electrons with spins opposing (↓) the field will have more energy - determined by $\mu_B\mathbf{B}$. This causes some ↓ electrons to rotate and align to the direction of the field, reducing energy of the system to the Fermi energy (E_F, which is the energy difference between the highest and lowest states), as can be seen in Figure 2.1. As the moments of the unpaired electrons align with the applied field, they produce a magnetic field parallel to the applied magnetic field - in this state, the band diagram for the system would look like that of a ferromagnet. If the temperature was raised above 0 K, the Fermi energy would not have a flat distribution as the density of states follows the Fermi Dirac distribution.

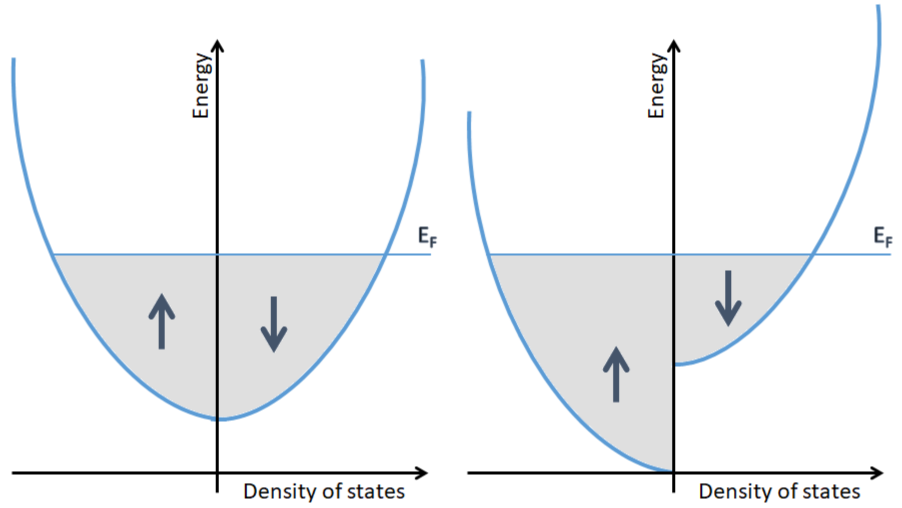

Figure 2.1: These are the band diagrams for a paramagnet at zero Kelvin, with the density of states split into spin up (↑) and spin down (↓) electrons. In the first instance there is no magnetic field. In the second instance, there is a magnetic field applied parallel to the electrons with up spins. The unit of energy is arbitrary and E_F represents the Fermi energy.

For a ferromagnetic material the proportionality of **M** and **H** is not applicable, when the applied field is zero, the magnetisation may be non-zero. The relationship between **M** and **H** is characterised by a hysteresis loop, from which various material dependent parameters can be determined. The saturation magnetisation, M_S, occurs at the point when increasing the applied field can no longer increase the magnetisation of the sample. The remanence, M_r, is the magnetisation that is still measured when the applied field is removed. The coercivity, H_c, is the field required to cause the demagnetisation of a sample, this also signifies the resistance of the sample to magnetic changes. Also, the energy lost within the system throughout the hysteresis can be calculated as: work density $= \mu_0 \int \mathbf{M}.d\mathbf{H}$. It should be noted that these parameters have temperature dependence, except M_S which is independent of the temperature until a certain temperature defined as the Curie temperature (T_c), above this point the material exhibits paramagnetism.[6]

There also exists incipient ferromagnets, otherwise known as exchange enhanced metals. In these metals, there is some magnetic ordering, though not strong enough to declare it ferromagnetic. The ordering only has an effect at, for example, low temperatures, or at interfaces with ferromagnetic materials. Materials such as platinum and palladium fulfil this criteria.[7]

Antiferromagnetism describes a state when spins are ordered antiparallel (↑↓↑↓), and ferrimagnetism describes antiparallel spins, however, the opposing spins are unequal ($\uparrow_\downarrow\uparrow_\downarrow$).

2.2 Hund's Rules and Spin-Orbit Coupling

Electrons experience two types of angular momentum. Orbital angular momentum causes a magnetic moment to occur as the electron orbits its nucleus; this orbital moment can be modelled as a current loop. Spin angular momentum is intrinsic to the electron, causing a magnetic moment which can possess one of two directions relative to a magnetic field. Despite these magnetic moments, atoms do not necessarily possess natural, non-negligible magnetism due to pairs of oppositely orientated spins cancelling out. To determine whether an atom is magnetic or not, Hund's rules must be primarily considered. They give a guide to determining how the electrons are maximised within the atomic shells in order to achieve a state with the lowest possible energy. Hund's rules are as follows: first, the spin angular momentum (**S**) are configured, i.e. spins will align parallel before they align antiparallel, therefore occupying different orbitals when possible due to the Coulomb interaction. Secondly, the sub-orbitals fill up in a way to maximise the orbital angular momentum (**L**). Finally, the total angular momentum (**J**) is determined depending on the fullness of the shell. If the shell is less than half full, $\mathbf{J} = \mathbf{L}$ - $\mathbf{S}$, if the shell is more than half full, $\mathbf{J} = \mathbf{L} + \mathbf{S}$, and in the condition when the shell is exactly half full, $\mathbf{L} = 0$ and $\mathbf{J} = \mathbf{S}$. These rule stem from spin-orbit coupling, which is the coupling of the spin and orbital angular momenta. It can be understood by viewing the system from the electron's point of view. To the electron, it appears as if the atomic nucleus is revolving around it - this can be modelled as a current loop, meaning a magnetic field magnitude ($\mathrm{B}_{so} = \mu_0\mathrm{Zev}/4\pi\mathrm{r}^2$, Z is the atomic number, e is the charge and v is the speed of the nucleus) is created which acts on the electron's moment and causes the spin-orbit interaction. The interaction energy ε_{so} = -$\mu_B\mathrm{B}_{so}$ can be worked out using the Bohr model for an inner electron, r $\simeq \mathrm{a}_0/\mathrm{Z}$ and $\mathrm{m}_e\mathrm{vr} \approx \hbar$, so that ε_{so} is proportional to Z^4 meaning that elements which are heavier have a stronger spin-orbit interaction. This becomes important in numerous phenomena such as magnetocrystalline anisotropy, and the spin Hall effect.

2.3 Exchange

Between two electrons there is the Coulomb interaction (U) and the magnetic dipole interaction. The energy from the magnetic dipole interaction is very weak in comparison to that of the Coulomb interaction. However, the Coulomb interaction cannot perfectly describe the energy of electrons (E). It must be considered that indistinguishable electrons are constantly exchanging and the energy difference that comes from swapping two electrons is called the exchange energy ($\mathcal{J}$). This can be used to correct the Coulomb interaction (E = U ± $\mathcal{J}$). The wave function used to describe the energy consists of two parts; the spatial part and the spin part. The wave function as a whole must be antisymmetric (i.e. doesn't vanish if particles are exchanged) due to the Pauli exclusion principle as electrons are fermions, $\Psi(1,2) = -\Psi(2,1)$. For two electrons (1,2) in two orbitals (m, n), it can consist of a symmetric spatial part, Equation 2.5, meaning the two electrons are in the same place, and an antisymmetric spin part, Equation 2.8, meaning the electrons are of opposite spins, a singlet state. Alternatively, it can consist of an antisymmetric spatial part, Equation 2.6, meaning the electrons are in different energy levels, and a symmetric spin part, Equation 2.7, meaning the electrons have the same spin, a triplet state. The antisymmetric wavefunction will consist of a symmetric spatial function and an antisymmetric spin function, or vice versa. It is more likely for the spatial function to be antisymmetric due to the nature of the wavefunction, in this scenario, U is lower as the electrons are further away meaning the energy is lower and the Equation E = U - $\mathcal{J}$ is used, this is the theory behind Hund's rules. For the alternative scenario, E = U + $\mathcal{J}$ is used.

$$\psi_s = (1/\sqrt{2})[\psi_m(1)\psi_n(2) + \psi_m(2)\psi_n(1)] \tag{2.5}$$

$$\psi_a = (1/\sqrt{2})[\psi_m(1)\psi_n(2) - \psi_m(2)\psi_n(1)] \tag{2.6}$$

$$\chi_s = |\uparrow_1, \uparrow_2\rangle, \text{ or } (1/\sqrt{2})[|\uparrow_1, \downarrow_2\rangle + |\downarrow_1, \uparrow_2\rangle], \text{ or } |\downarrow_1, \downarrow_2\rangle \tag{2.7}$$

$$\chi_a = (1/\sqrt{2})[|\uparrow_1, \downarrow_2\rangle - |\downarrow_1, \uparrow_2\rangle] \tag{2.8}$$

Exchange is often described by the Heisenberg Hamiltonian, $\mathcal{H}$, (Equation 2.9), with the dot product giving the difference in energy between parallel and antiparallel spins. Within an atom, $\mathcal{J}$ is usually positive and a positive $\mathcal{J}$ causes ferromagnetic exchange. In neighbouring atoms, molecular orbits must be considered. $\mathcal{J}$ can be positive, bonding, again implying a ferromagnetic interaction. However, $\mathcal{J}$ can also be negative, antibonding, as there is greater curvature, so a larger kinetic energy is required and it becomes more energetically costly for the electrons to be further apart. This leads to antiferromagnetism, meaning the energy will be lower when the spins align antiparallel.[6; 8]

$$\mathcal{H} = -2\mathcal{J}\mathbf{S_1} \cdot \mathbf{S_2} \tag{2.9}$$

2.4 Stoner Criterion

Returning to the magnetic susceptibility in a paramagnetic material (χ_p, Pauli susceptibility), for most paramagnets, only a small fraction of electrons with a comparable energy to the Fermi energy will be affected by a magnetic field. An electron gas obeys Fermi-Dirac statistics and can be described in terms of the density of states, $\mathcal{D}(\mathcal{E}_F)$, as shown in Equation 2.10.

$$\chi_p = \mu_0 \mu_B^2 \mathcal{D}(\mathcal{E}_F) \tag{2.10}$$

The susceptibility of a material increases when the bandwidth is narrower and therefore the density of states is larger, this means that in a system with a high density of states, it's more likely (energetically favourable) for the ↑ and ↓ bands to split - this is one factor that will cause a material to be spontaneously ferromagnetic. Furthermore, an internal field ($\mathbf{H_m}$) arises due to the exchange interaction which is a product of the magnetisation and an exchange coefficient ($\mathbf{H_m}$=$\lambda\mathbf{M}$), so the magnetisation of a material includes both $\mathbf{H_m}$ and any applied field (Equation 2.11).

$$\mathbf{M} = \chi_p(\mathbf{H} + \mathbf{H_m}) \tag{2.11}$$

Using Equation 2.1, an expression for χ can be made in terms of χ_p and λ (Equation 2.12). This equation indicates that if $\lambda\chi_p$<1, the susceptibility becomes enhanced and if $\lambda\chi_p$=1, $\chi \rightarrow \infty$, therefore spontaneous magnetism can occur.

$$\chi = \frac{\chi_p}{1 - \lambda\chi_p} \tag{2.12}$$

This is called the 'Stoner criterion', commonly seen as I$\mathfrak{D}(\mathcal{E}_F)$>1, where I=$\lambda\mu_0\mu_B^2$ (the Stoner exchange parameter). Therefore, to achieve a natural ferromagnetic order, a material must have specific attributes: a large density of states (usually from a narrow band which has a peak near E_F) and a large exchange parameter (comparable to the bandwidth). The density of states changes depending on lattice types and length scales. In the 3d band, shown in Figure 2.2, only Fe, Co and Ni fulfil the Stoner criterion and experience spontaneous splitting of the 3d band. If enough spins rotate to allow the band to be fully below the Fermi energy, the ferromagnet is strong (Co and Ni), and otherwise it is weaker (Fe). Despite this, Fe has the largest magnetisation.[6; 9]

Additionally, if each unpaired electron in Fe, Co and Ni had a magnetic moment of 1 μ_B, it is expected that the saturation magnetisation of each would have an integer value. However, this is not the case, supporting the theory for itinerant ferromagnetism.[6; 8]

2.5 Exchange Interactions

There are different types of exchange interaction, direct exchange (when usually only electrons on neighbouring atoms are relevant) depends mostly on the occupancy of the bands. One example of this is in the 3d band, a ferromagnetic exchange tends to arise if the band is nearly full or nearly empty, this is because the electrons on neighbouring sites can move into empty states without changing their spin. Whereas, if the band is approximately half full, the exchange will only occur if the neighbouring spins are antiparallel, so antiferromagnetic exchange is more likely, see Figure 2.3. After band occupancy, interatomic spacing is also considered, if the spacing is larger, ferromagnetism is more likely. However, as bandwidth becomes larger, electrons become delocalised irrelevant of their spin, nullifying this direct exchange.[6; 8]

Another type of direct exchange is the s-d model, which refers to an exchange via the conduction electrons, these electrons get polarised by the unpaired electrons, therefore, allowing both coupling between neighbouring atoms and longer range coupling.

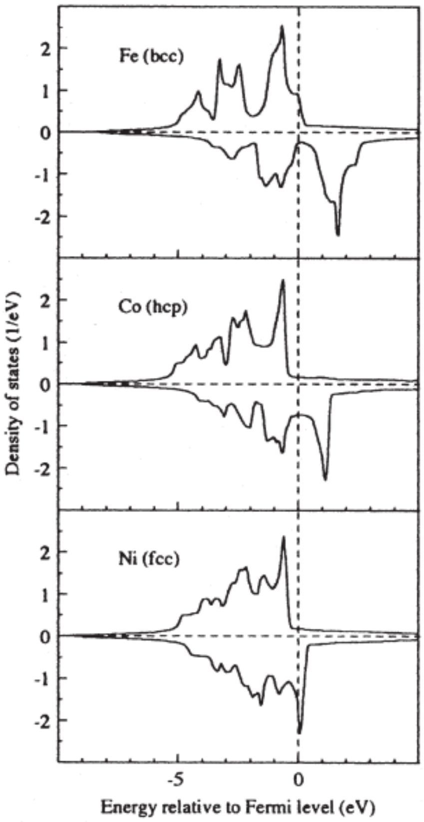

Figure 2.2: Fe, Co, and Ni fulfil the Stoner criterion, as is evident from their spin split density of state diagrams at 0 K. The upper part of each plot represents spin up and the bottom half, spin down. Both Co and Fe are strong ferromagnets, whereas Ni is weaker.[6; 9]

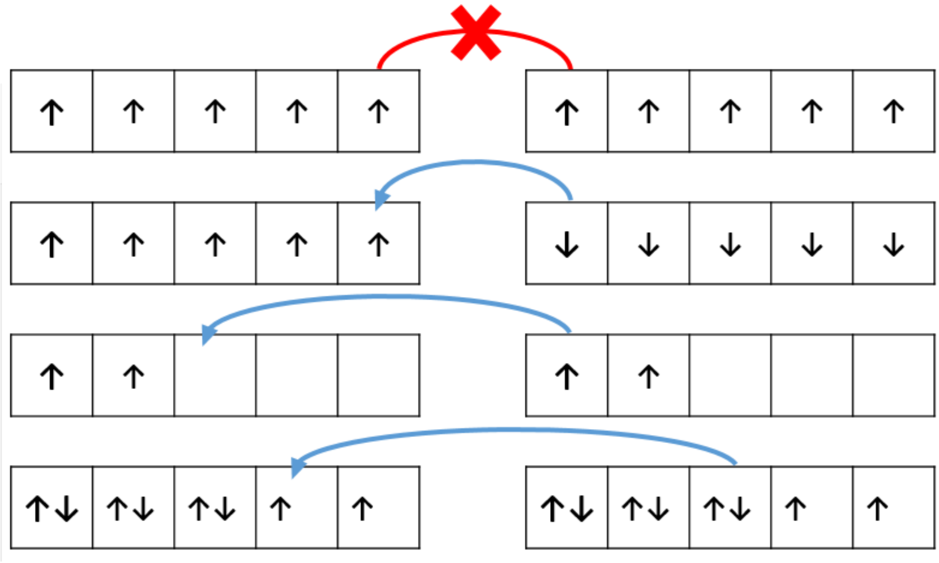

Figure 2.3: These diagrams show the permitted exchange interactions between half full bands, nearly empty bands, and nearly full bands. This diagram was reproduced from Reference [6].

There are also types of indirect exchange, which describes the exchange between non-neighbouring atoms. An extension to the s-d model was explored by Ruderman, Kittel, Kasuya and Yosida (RKKY model), to explain the indirect exchange in metals which have localised unpaired electrons with wave functions that do not overlap.[10–12] They demonstrated that the polarisation of the conduction electron spins exhibit a damped oscillatory pattern, meaning the coupling switches between ferromagnetic and antiferromagnetic depending on the distance between the magnetic ions. When the effect occurs in layers of FM material separated by a NM spacer layer, it is referred to as interlayer exchange coupling. When this occurs antiferromagnetically, the stack is referred to as a synthetic antiferromagnet or a SAF. In Reference [13], Parkin et al. showed that the dampened oscillatory pattern occurred in several elements - see Figure 2.4. The antiferromagnetic exchange in a SAF is weak in comparison to antiferromagnetism resulting from direct exchange or superexchange.[14]

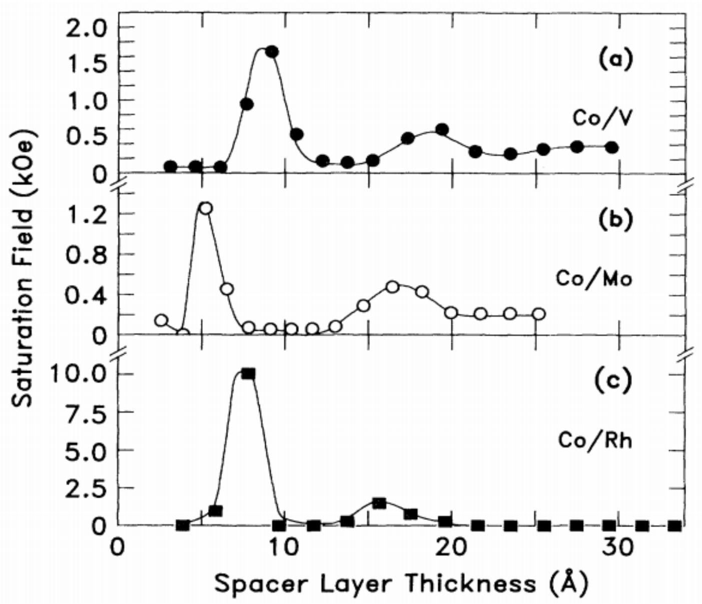

Figure 2.4: These graphs show how the saturation field depends on the thickness of the spacer layer (in this case Mo, Rh and V). The damped oscillation is visible in all three elements, with antiferromagnetic coupling peaks occurring at different thicknesses.[13]

Superexchange is an indirect exchange that occurs when there is not sufficient 3d-3d orbital overlap between two magnetic ions, but the exchange effect can be induced by placing another non-magnetic ion between them (this usually occurs in oxides and tends to be antiferromagnetic). Other forms of indirect exchange include double exchange, a ferromagnetic exchange when magnetic ions have mixed valency and can exist in more than one oxidation state. Anisotropic exchange (or DMI) stemming from the spin-orbit interaction, forces spins perpendicular to each other.[8; 15]

2.6 Magnons

As stated, ferromagnetism does not occur after the temperature of a material goes above its Curie temperature due to critical thermal fluctuations, but also at low temperatures, the ferromagnetism of a material can be affected by spinwave excitations. At low temperatures, it is not energetically favourable to flip individual spins, so all the atoms experience periodic oscillations of deviation in spin orientation. Within a lattice, this is called a spin wave, and when quantised in a solid, they are referred to as magnons, with energy related to the spinwave dispersion; $\varepsilon_{\mathbf{k}} = \hbar\omega_{\mathbf{k}}$ ($\omega_{\mathbf{k}}$ being the spin wave frequency). The relationship between the energy and the wavevector, $\mathbf{k}$, for a chain of one dimensional isotropic spins, i.e. the spinwave dispersion relation, is shown in Equation 2.13, where D_{sw} is the spinwave stiffness: $D_{sw}=2\mathfrak{J}Sa^2$ ($\mathfrak{J}$ is the exchange constant, S is the spin at each lattice site, and a is the lattice constant).[6]

$$\varepsilon_k = D_{sw}\mathbf{k}^2 \tag{2.13}$$

When in a thermal equilibrium, the average number of magnons excited in the mode $\mathbf{k}$, $\langle n_{\mathbf{k}} \rangle$, can be written in the Planck distribution, shown in Equation 2.14,

$$\langle n_{\mathbf{k}} \rangle = \frac{1}{e^{\frac{\hbar\omega_{\mathbf{k}}}{k_B T}} - 1} \tag{2.14}$$

where $\langle n_{\mathbf{k}} \rangle$ is the magnon distribution with wave vector $\mathbf{k}$ within the first Brillouin zone, k_B is the Boltzmann constant and T is the temperature.[16] The saturation magnetisation of a sample at zero Kelvin, $M_S(0)$, can be written as in Equation 2.15, where V is volume of a unit cell, g is the g-factor (which for FCC Co is 2.1)[17], and N is 1, 2, 4 for an simple cubic (SC), BCC, FCC lattice respectively.

$$M_S(0) = \frac{g\mu_B NS}{V} \tag{2.15}$$

Combining Equation 2.14 and 2.15, an equation for the magnetisation at temperature T, $M_S(T)$, can be achieved, shown in Equation 2.16 where a is the lattice parameter (3.54 Å for FCC Co)[16], which comes from the volume term.

$$\frac{M_S(T)}{M_S(0)} = 1 - \frac{a^3}{NS}\sum_{\mathbf{k}} \langle n_{\mathbf{k}} \rangle_T \tag{2.16}$$

For a bulk sample, $\sum_{\mathbf{k}} \langle n_{\mathbf{k}} \rangle_T$ - the total number of magnons excited at temperature T, can be written as three integrals in the x, y and z directions. As the thermal occupation is not dependent on the Brillouin zone, this can then be transformed into cylindrical co-ordinates, allowing the angular parts to be solved trivially, the result of which is shown in Equation 2.17.[16; 18]

$$\sum_k \langle n_k \rangle_T = n_m(T) = \frac{4\pi}{(2\pi)^3} \int_{k=0}^{\sqrt{k_{max}}} \frac{1}{e^{\frac{\hbar\omega_{\mathbf{k}}}{k_B T}} - 1} k^2 dk \tag{2.17}$$

$$n_m(T) = \frac{1}{4\pi^2} \left(\frac{k_B T}{D_{sw}} \right)^{\frac{3}{2}} \int_0^\infty dx \frac{x^{\frac{1}{2}}}{e^x - 1} \tag{2.18}$$

Following this, a substitution can be made with Equation 2.13 and $x = D_{sw}k^2/k_BT$, the result of which is shown in Equation 2.18. Then, by replacing the standard integral ($\int_0^\infty \frac{x^{1/2}}{e^x-1}dx$) for the Gamma function and Riemann's Zeta function ($\Gamma(\frac{3}{2})\xi(\frac{3}{2})$), Bloch's law is established - Equation 2.19 and 2.20.[16]

$$\frac{M_S(T)}{M_S(0)} = 1 - \frac{a^3\eta}{NS} \left(\frac{k_B T}{D_{sw}} \right)^{\frac{3}{2}} \tag{2.19}$$

$$\eta = \frac{\Gamma(\frac{3}{2})\xi(\frac{3}{2})}{4\pi^2} = 0.0587 \tag{2.20}$$

In a thin film however, η is less simple as it cannot be assumed to integrate in all directions, in one direction there will be far fewer k-points. In the thin film scenario, the reduced volume accounts for fewer thermally excited magnons, as the spinwave modes along the reduced axis will be lost, so the effect on n_m(T) is negligible. The ferromagnetic resonance (FMR) mode is the lowest order of excitation in a solid and the reduction in sample volume does not have a large impact on it, the FMR modes continue to be highly occupied. This means that n_m(T) increases as the sample thickness decreases. If z is chosen to be perpendicular to the film, and the axis of much less thickness, Equation 2.16 can be evaluated similarly to bulk films, though the sum in the z-axis remains and the transformation is done into cylindrical co-ordinates. The result of this is shown in Equation 2.21, where n_z is the number of atomic layers in the z direction and a_z is the distance between atomic layers in the z direction.[19; 20]

$$n_m(T) = \frac{1}{4\pi} \frac{1}{n_z a_z} \sum_{k_z=0}^{\pi/a} \int_{k_\rho=0}^{\sqrt{k_{\rho,max}}} \frac{1}{e^{\frac{\hbar\omega_k}{k_B T}} - 1} k_\rho dk_\rho \tag{2.21}$$

Again, a substitution is made from Equation 2.13 and $x = \frac{D_{sw}k_\rho^2}{k_BT}$, and $y = \frac{D_{sw}k_z^2}{k_BT}$, assuming an isotropic ferromagnet, to get Equation 2.22.

$$n_m(T) = \frac{1}{4\pi} \frac{1}{n_z a_z} \frac{k_B T}{2D_{sw}} \sum_{k_z=0}^{\pi/a} \int_0^{x_{max}} \frac{1}{e^{x+y} - 1} dx \tag{2.22}$$

Then a substitution is made for the definite integral, $\int_0^{x_{max}} \frac{1}{e^{x+y}-1}dx = -\ln(1-e^{-y})$, and $k_z = \frac{n\pi}{n_z a_z}$. Also, in a thin film, an applied field or anisotropy is needed for ferromagnetism, so an additional energy term $\hbar\omega_0$ is added into the exponential, as shown in Equation 2.23. It is of the form hf_{FMR} if FMR measurements are made, or of the form $\hbar\omega_0 = g\mu_B\mu_0(H_{sat} - H_{demag})$, if the measurements were taken without an external field, note that H$_{sat}$ is the saturation field, and H$_{demag}$ the demagnetising field in A/m. The latter equation comes from the Kittel equation, Equation 2.24, where H' is an external field.[16]

$$n_m(T) = -\frac{1}{4\pi}\frac{1}{n_z a_z}\frac{k_B T}{2D_{sw}}\sum_{n=0}^{n_z}\ln\left(1 - e^{-(D_{sw}(\frac{n\pi}{n_z a_z})^2+\hbar\omega_0)/k_B T}\right) \tag{2.23}$$

$$\omega_0 = \frac{g\mu_B}{\hbar}\mu_0(H' - H_{demag} + H_{sat}) \tag{2.24}$$

The equation $\eta = n_m(T)/\left(\frac{k_B T}{D_{sw}}\right)^{\frac{3}{2}}$ - where η is proportional to the magnon density in thermal equilibrium and Equation 2.23 can be substituted into Equation 2.19 to describe Bloch's law in a thin film: Equation 2.25.[19; 20]

$$\frac{M_S(T)}{M_S(0)} = 1 + \frac{a^3}{NS}\frac{1}{4\pi}\frac{1}{n_z a_z}\frac{k_B T}{D_{sw}}\sum_{n=0}^{n_z}\ln\left(1 - e^{-(D_{sw}(\frac{n\pi}{n_z a_z})^2+\hbar\omega_0)/k_B T}\right) \tag{2.25}$$

Additionally, Equation 2.25 can be fitted to magnetisation vs. temperature data to output a value for the zero temperature spinwave stiffness. As $D_{sw} = 2\mathscr{J}Sa^2$, a characteristic of a ferromagnet called the exchange stiffness, A, can be calculated using Equation 2.26 by substituting in for $\mathscr{J}$. The exchange stiffness describes how much energy is required to rotate the magnetisation away from the main magnetisation direction, unlike the anisotropy energy, it is based solely on the strength of the direct exchange interactions between neighbouring spins.[20]

$$A = \frac{N\mathscr{J}S^2}{a} \tag{2.26}$$

The value for the exchange stiffness is the zero temperature value. To work out the value at a temperature T, the value would need to be renormalised. The bulk value for the exchange stiffness of cobalt is 31 pJm^{-1}.[6; 19] Mohammadi et al. showed that a decrease in thickness of the magnetic material, caused an increase in η, and a decrease in D$_{sw}$ and therefore A.[20] Nembach et al. also showed a similar trend with permalloy samples, as the magnetic material thickness increased, η decreased until it plateaued to the bulk value of 0.0587 after 10 nm, as shown in Figure 2.5.[19]

2.7 Anisotropy

In a solid, the atoms can form in an amorphous structure (no long range order), a crystal structure (e.g. cubic, hexagonal or tetragonal with high order), or a polycrystalline structure (somewhere in between with short range order). One form of anisotropy is magnetocrystalline anisotropy. It is the difference in energy of a sample that is magnetised along its easy axis and its hard axis. It can be thought of as the energy required to overcome the spin-orbit coupling of a sample. To change the direction of the spin means also to change the direction of the orbit, which usually

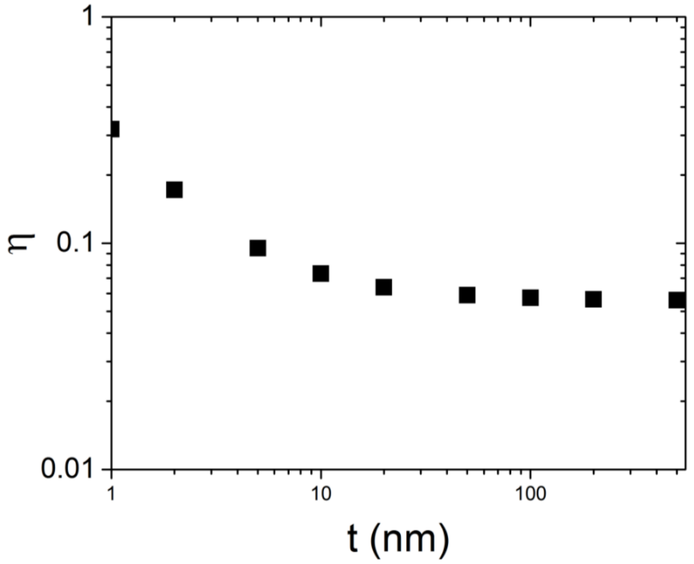

Figure 2.5: This figure shows η as a function of thickness for permalloy with a lattice constant of 0.354 nm.[19]

has a strong coupling to the lattice. For magnetocrystalline anisotropy, the preferred magnetic orientation is based on its crystallographic direction and properties.[6] The magnetocrystalline anisotropy originates from the crystal field interaction. When an atom is part of a crystal lattice, its Coulomb interaction with the other atoms in the lattice should be taken into account - this is referred to as the crystal field interaction. The crystal field can stabilise specific orbitals which, due to the spin-orbit interaction, means the electron moments will align in a certain direction within the crystal.[6] Magnetic anisotropy can also arise from a lack of symmetry, for example, anisotropic exchange.[6]

Another factor which affects the anisotropy is sample shape. Shape anisotropy (K_{sh}) is sample dependent as it is based on the demagnetising field in a sample. If a magnetic volume is considered as a whole, when magnetised in a certain direction, it can be thought of like a bar magnet with a north and south pole and therefore having a magnetic field originating from the north pole and terminating at the south. As shown in Figure 2.6, inside the magnet, the **H**-field does not resemble the **B**-field as it is in the opposing direction, as well as to the direction of the magnetisation (**M**); it is called the demagnetising field ($\mathbf{H_{demag}}$). It is defined by Equation 2.27 to be proportional to the magnetisation with N_d as the demagnetising tensor, assumed to be diagonal and dependent on the sample shape. The stray field (also called magnetostatic or dipolar field) is the field outside the sample which can be measured and interacts with other dipoles. The internal field ($\mathbf{H}_i$) is equal to the external applied field ($\mathbf{H}'$) minus the demagnetising field, see Equation 2.28.[6; 21]

$$\mathbf{H_{demag}} = -N_d\mathbf{M} \tag{2.27}$$

$$\mathbf{H}_i = \mathbf{H}' - N_d\mathbf{M} \tag{2.28}$$

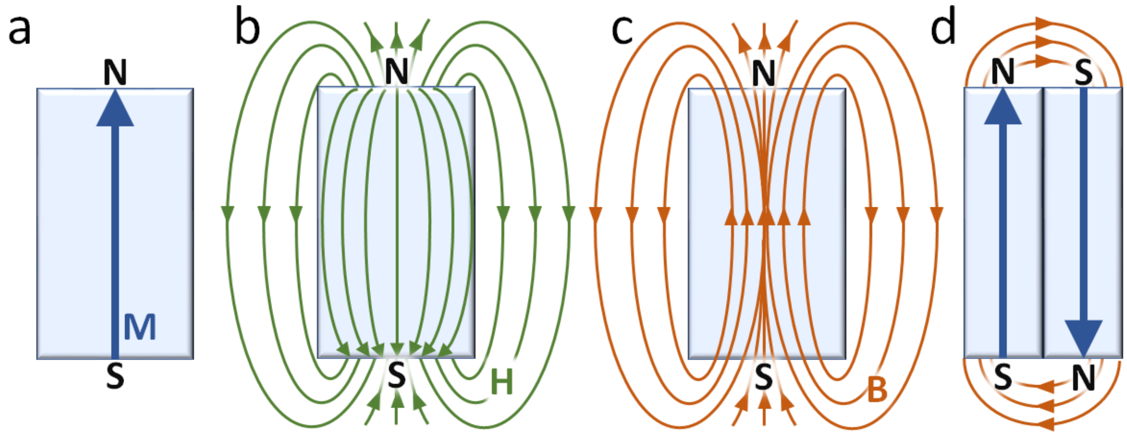

Figure 2.6: a) shows the magnetisation within a sample, going from the south to the north pole. b) shows the demagnetising field within the sample, going from north to south and the stray field outside the sample. c) shows the B field of the sample, $\mathbf{B}=\mu_0(\mathbf{H}+\mathbf{M})$. Outside the sample $\mathbf{B}=\mu_0\mathbf{H}$, as M=0, and is therefore the same as b), the inside however, it is very different to b). d) shows a sample with two domains which reduces the demagnetising field and therefore the magnetostatic energy. The sketch shows the stray field also reduced compared to c). These diagrams were adapted from Reference [16].

As the magnetostatic energy relies on the demagnetising field and therefore the sample's shape; it can be reduced by introducing domains within the sample in such a way to reduce the demagnetising field. An example of a domain configuration is shown in Figure 2.6d in which the demagnetising field would be reduced. There is still a stray field outside the sample, however, it is also reduced.

A different way in which anisotropy of a sample can be controlled is by inducing it, primarily to achieve uniaxial anisotropy. This can be done in ways such as annealing or atomic deposition of thin films in a magnetic field.[6]

In magnetic materials, several types of magnetic anisotropy exist (uniaxial, easy plane, biaxial, cubic, etc.). In particular, magnetic uniaxial anisotropy means that there is one preferred axis for the direction of the aligned spins, this preferred direction is called an easy axis (as opposed to a hard axis). Therefore, the magnetic properties of a material will be different depending on the axis of measurement, excluding M_S which is independent of the measurement direction, although different field strengths are required to saturate different materials. A uniaxial anisotropic energy density, E_a (in J/m^3), can be defined by Equation 2.29, where K_1 is the anisotropy constant and θ is the angle between the magnetisation direction and the anisotropy axis.

$$E_a = K_1 \sin^2 \theta \tag{2.29}$$

2.8 Thin Film Anisotropy

Magnetic thin films, i.e. materials with 1 or more dimension shorter than a critical length scale, have numerous differences with bulk films. Some of their properties are intrinsically different, such as magnetisation, Curie point and anisotropy. There are three common origins of the anisotropy in a thin film: shape, surface and strain.

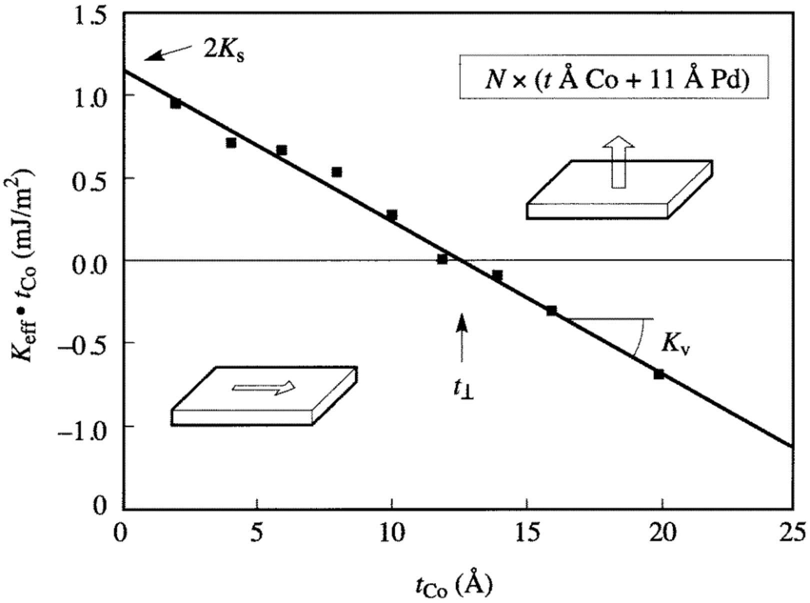

Figure 2.7: A graph showing effective anisotropy multiplied by the thicknesses of different cobalt samples plotted against each thickness of cobalt, in Co/Pd samples. $K_{eff}t_{FM}$ against t_{FM} (thickness of the ferromagnet), gives the intercept as twice of K_s and the gradient of the line as K_V.[22]

Additionally, when the magnetisation of a thin film is perpendicular to the plane, the system can be described as having perpendicular magnetic anisotropy (PMA). This can occur due to a surface effect caused by spin-orbit coupling in systems with a thin magnetic film interfaced with a heavy metal. A uniaxial shape anisotropy, in other words the demagnetising anisotropy (K_{demag}), is defined in Equation 2.30. The demagnetising factor in the easy axis for a thin film is equal to 0 when the easy axis is parallel to the plane, and 1 when perpendicular to the plane.

$$K_{demag} = -\frac{\mu_0 M_S^2}{2} \tag{2.30}$$

In thin films, there is an additional surface anisotropy. Surface anisotropy comes from coupling between the crystal field and atoms at the surface of the film. The effective anisotropy can be considered as in Figure 2.7, K_{eff} is written as a combination of the surface anisotropy, K_s, and the volume anisotropy, K_V (Equation 2.31).

$$K_{eff} = \frac{2K_s}{t_{FM}} + K_V \tag{2.31}$$

The volume term contains the shape and magnetocrystalline anisotropy which usually tends the easy axis to point in the plane. The surface anisotropy can direct the anisotropy out of the plane. These contributions will compete to determine whether the easy axis of a thin film will point in or out of the plane. The orientation of the easy axis will be evident in the hysteresis loop of the thin film - see Figure 2.8.

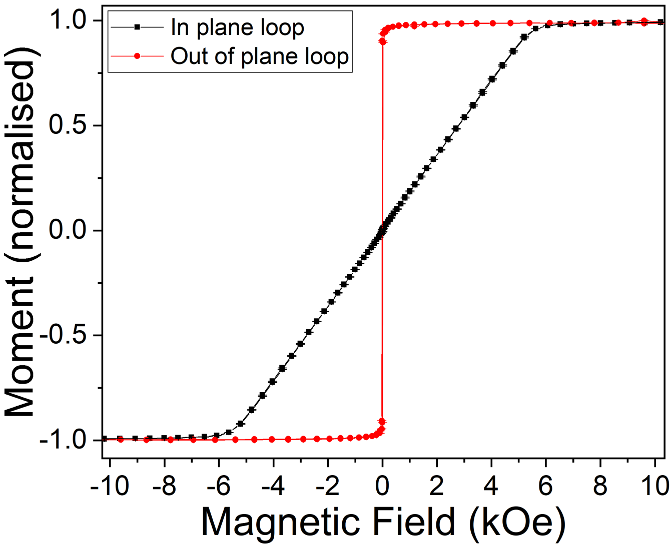

Figure 2.8: For a PMA sample, when you measure the hysteresis loop out of the plane, i.e. in the easy axis, the loop is square. When measuring it in-plane, i.e. in the hard axis, the loop is slanted as there is no domain wall motion, only rotation of the spins.

As previously mentioned, the anisotropy can usually be made to favour the out-of-plane orientation by interfacing the magnet with certain heavy transition metals which have strong spin-orbit coupling.[22–26] This is because magnetic material and the heavy metal hybridise, which combined with spin-orbit coupling effects, causes a perpendicular anisotropy component. For example, in a Co/Pt system, the 3d Co electrons hybridise with Pt 5d electrons, this hybridisation also invokes an orbital moment in the interfacial platinum atoms with a magnetisation aligned with the Co.[27–29] Strain anisotropy can also affect a thin film, and can overcome the surface anisotropy if the film is thin enough.[6]

The effective anisotropy in a uniaxial sample can be described with Equation 2.32, where H_{sat}

is the field at which it is saturates in the hard axis, i.e. the saturation field or anisotropy field. This can then be combined with the demagnetising anisotropy (Equation 2.30) in Equation 2.33 to extract the uniaxial anisotropy.

$$H_{sat} = \frac{2K_{eff}}{\mu_0 M_S} \tag{2.32}$$

$$K_u = K_{eff} + K_{demag} \tag{2.33}$$

Another interfacial effect occurs between a ferromagnet and an incipient ferromagnet (e.g. Pt and Pd which are heavy metals, close to the Stoner criterion), this effect is often labelled the proximity effect, or proximity induced magnetism. At a Co/Pt interface, the Pt becomes polarised and exhibits a magnetic moment which adds to the total moment of the sample. The cause behind this induced magnetism stems from the hybridisation between the 3d electrons in the Co and the 5d Pt electron. Measurements of this effect started in the 1990s when properties of Fe or Co interfaces with Pt or Pd or Ir were probed due to larger Kerr rotations being observed in systems with these interfaces. [30–35]

2.9 Magnetic Domains

A domain is an area within a sample in which the magnetisation is in a uniform direction, see Figure 2.9. The cause behind the formation of domain structures is to minimise the total free energy (ε_{tot}), this energy term can be formulated with four main components: exchange energy (ε_{ex}), anisotropy energy (ε_a, which is usually magnetocrystalline), demagnetising energy (ε_d), and energy from an applied field (ε_z). Additionally, there are energy terms due to applied stress (ε_{stress}) and magnetorestriction (ε_{ms}), however, their contributions are relatively small. An expression can be written for the free energy as in Equation 2.34; it can also be written as a volume integral over a sample (Equation 2.35, not including ε_{stress} and ε_{ms}), when A is the exchange stiffness, **M** is the magnetisation at distance r and z is taken in the anisotropy axis.[6]

$$\varepsilon_{tot} = \varepsilon_{ex} + \varepsilon_a + \varepsilon_d + \varepsilon_z + \varepsilon_{stress} + \varepsilon_{ms} \tag{2.34}$$

$$\varepsilon_{tot} = \int [A(\nabla \mathbf{M}/M_S)^2 - K_1 sin^2\theta - ... - \frac{1}{2}\mu_0 \mathbf{M} \cdot \mathbf{H}_d - \mu_0 \mathbf{M} \cdot \mathbf{H}] d^3r \tag{2.35}$$

With the existence of domains comes the existence of domain walls, the area that separates different domains in which the magnetisation will usually rotate from one direction in the easy axis to the opposite direction. When a magnetic field applied to a sample with domains is swept from positive to negative, the total magnetisation of the sample can change either by the magnetisation in the domains rotating with the applied field, or the movement of domain walls. Rotation of the

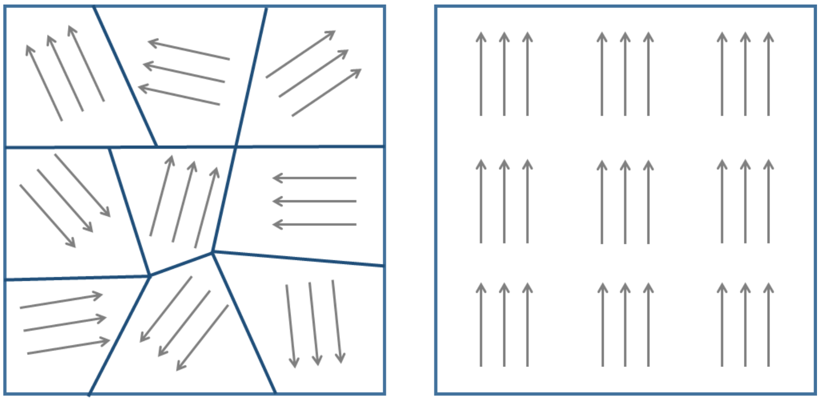

Figure 2.9: The left diagram shows multiple domains (areas in which the magnetic moments are aligned) within a sample which are randomly aligned, or demagnetised. The right diagram shows how the domains align when magnetised - spontaneously or with an external field.

magnetisation happens when the applied field is perpendicular to the samples easy axis. Whereas, if the applied field is parallel to the easy axis, the domain walls move to create larger domains with magnetisation in the same direction as the applied field, and fewer domains of the opposite direction. The magnetostatic energy is dictated by how domains are orientated and their sizes. Micromagnetics is a method used to simulate magnetism on a sub-micrometer scale, it discards the atomic structure and focuses on magnetic structures, such as domain walls and vortices. It is used to predict the equilibrium states of systems with known exchange stiffness and anisotropy. Inside a domain wall, the rotation of the magnetisation can either be in the plane (Néel wall), or out of the plane (Bloch wall), as seen in Figure 2.10. The wall will have a width (δ_w), relating to the anisotropy and exchange stiffness - Equation 2.36. Essentially, the exchange makes inhomogeneities unfavourable causing the wall to widen in order to reduce the angle between adjacent spins, whereas the anisotropy prefers the spins to point in as few different directions as possible, favouring a narrower domain wall. Néel walls will only become stable within a thin film, i.e. when the film is thinner than the width of the wall. Néel walls can be categorised as having either left or right handed chirality, Bloch walls usually consist of both, see Figure 2.10.[6]

$$\delta_w = \sqrt{\frac{A}{K_{eff}}} \tag{2.36}$$

Within a real sample, there will be surface defects, grain boundaries and other inhomogeneities, which invoke strong local demagnetising fields. This means that they can become nucleation points - a small volume from which domain can form and expand. As well as becoming nucleation points, they can also have an opposing effect and behave as a pinning site - a point at which the domain wall motion can get ‘stuck’ or ‘pinned’.[6]

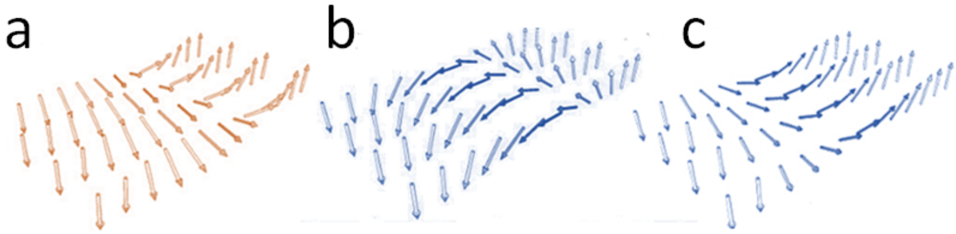

Figure 2.10: a) shows the spin orientations in a Bloch wall. b) shows the spin orientations in a right handed Néel wall. c) shows the spin orientations in a left handed Néel wall. This figure is adapted from Reference [36].

$$\sigma = 4\sqrt{AK_{eff}} - \pi|D| \tag{2.37}$$

The energy of a domain wall when considering the DMI is described by Equation 2.37. The DMI constant is D, K_{eff} is the effective anisotropy constant and A is the exchange constant. This signifies that there is a critical DMI energy constant ($D_{crit}=4\sqrt{AK}/\pi$), above which the domain wall energy becomes negative and skyrmions become energetically favourable.[37] In an infinite 2D system, if $D < D_{crit}$, single skyrmions are in a metastable state, and as $D \rightarrow D_{crit}$, the skyrmion radius increases. If $D \geq D_{crit}$, a skyrmion lattice becomes favourable over a single skyrmion with an infinite radius.

The previously mentioned domain wall motion is usually instigated with the application of a magnetic field or electric current, however, there are different regimes that cause the domain walls to exhibit different behaviours due to different driving strengths. Below a critical field the domain wall can get pinned. In this scenario, referred to as the creep regime, the domain wall is analogous to an elastic string, it can become unpinned due to thermal fluctuations. In the creep regime, which was first shown experimentally by Lemerle et al., the driving force is low enough that the walls will travel a few μm/s.[38] The velocity is represented by the creep law, Equation 2.38, where U_c is the pinning energy barrier, H_{dep} is the depinning field and v_0 is a prefactor proportional to the pinned domain wall length.

$$v = v_0 e^{-\frac{U_c}{k_B T}\left(\frac{H_{dep}}{H}\right)^{1/4}} \tag{2.38}$$

Following the creep regime is the thermally assisted flux flow (TAFF) regime, although both occur at temperatures above zero Kelvin as they are dependent on thermal energy. When the driving strength becomes greater, the domain wall velocity increases into the depinning regime, followed by the flow regime, which no longer has a strong dependency on the thermal energy and pinning. It holds a linear relationship between wall velocity and driving force - it has wall velocities up to m/s. A regime of precession can also occur above the Walker breakdown field.[38; 40–42]

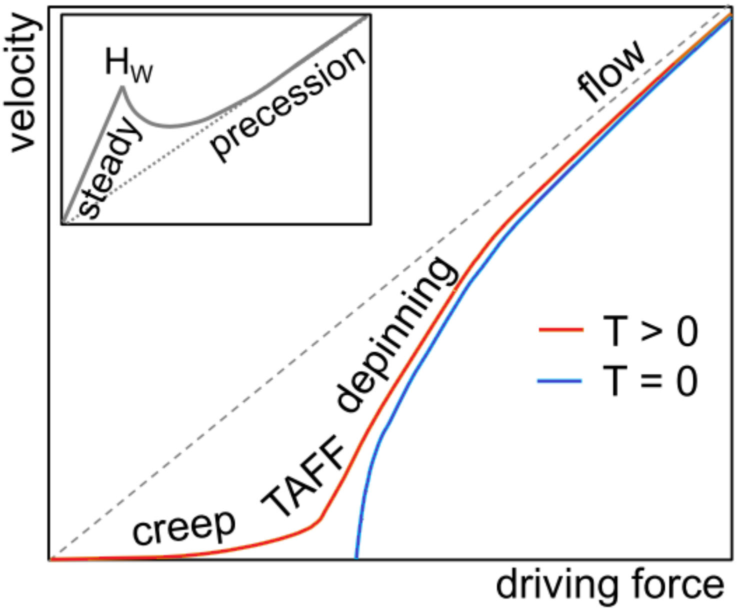

Figure 2.11: The driving force, i.e. magnetic field strength, is plotted against velocity of the domain wall. When the temperature (T) is above 0 K, the thermal regimes (creep and TAFF) are present at low driving forces. At higher driving forces, or when T=0, only depinning and flow mechanisms occur. The Walker breakdown is shown in the inset, above a certain field (H_W), the velocity decreases due to a precession of the domain wall. This figure was adapted from References [39; 40].

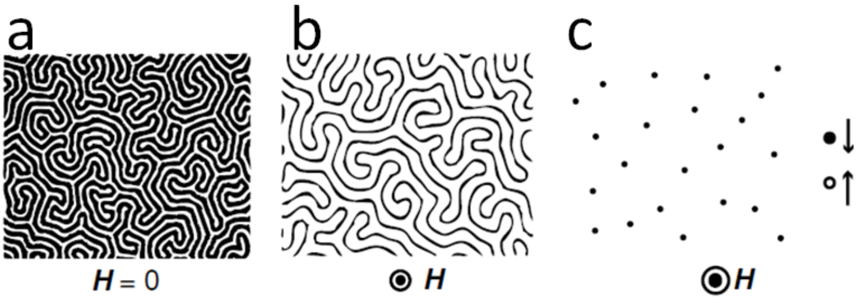

Figure 2.12: a) shows maze domains. b) shows maze domains which favour one magnetisation direction when an out-of-plane magnetic field is applied. c) shows the domains after a further increased field strength, so bubble domains remain which are of micrometer diameters. This figure is from Reference [6].

In thin magnetic films, a PMA sample can exhibit maze domains, see Figure 2.12. In their demagnetised state, they consist of equal areas of spin up and spin down magnetisation in a maze-like pattern, with no applied field. When an external magnetic field is applied, the domains magnetised against the field reduce and the domains with the field widen. The field strength can be increased until only small circular domains remain against the field, known as bubbles or skyrmions depending on factors such as size, DMI and domain wall structures. These are annihilated when sample becomes saturated at a certain field.

2.10 The Dzyaloshinski-Moriya Interaction

A type of antisymmetric exchange is called the Dzyaloshinski-Moriya interaction (DMI), it occurs in materials that lack inversion symmetry and leads to weak antisymmetric coupling. It is represented in Equation 2.39, where $\mathbf{D}_{12}$ is a vector which is directed along the axis with high symmetry, and $\mathbf{S}_1$ and $\mathbf{S}_2$ are the vectors of two neighbouring spins.

$$\mathcal{H} = -\mathbf{D}_{12} \cdot (\mathbf{S}_1 \times \mathbf{S}_2) \tag{2.39}$$

The equation indicates that the two spins prefer to couple perpendicular to each other, and to $\mathbf{D}$, therefore causing spin canting to occur, Figure 2.13. Its occurrence is often present at an interface between a FM and NM layer, where there is a broken inversion symmetry and when the NM layer has strong spin-orbit coupling. The DMI is a factor required when studying phenomena such as magnetic skyrmions.[6; 43] The strength of the DMI (D) can be measured using Equation 2.40 where M_S is the saturation magnetisation, δ_w is the domain wall width and H_{DMI} is the DMI field as explained in Chapter 4.

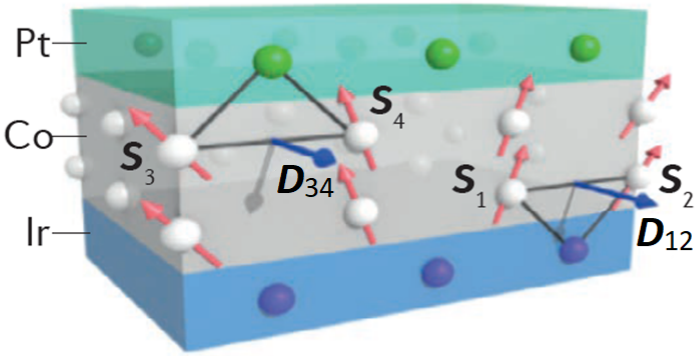

Figure 2.13: DMI schematic where S_1, S_2, S_3 and S_4 are the spins of the magnetic atoms, and D_{12} and D_{34} are the corresponding DMI vectors. This figure was taken from Reference [1].

$$D = \mu_0 M_S \delta_w H_{DMI} \tag{2.40}$$

2.11 Skyrmions

There are various types of topological spin textures in magnetic materials. Skyrmions are chiral, topologically non-trivial, spin textures with a magnetisation vector which rotates continuously around a 2π angle.[44–46] There are Bloch skyrmions, which have a circular chirality and Néel skyrmions, which have a radial chirality as can be seen in Figure 2.14. Both of these skyrmions are topologically stable and characterised by the skyrmion winding number (N, as shown in Equation 2.41) which has integer values,

$$N = \frac{1}{4\pi}\int \mathbf{m} \cdot (d_x\mathbf{m} \times d_y\mathbf{m})dxdy \tag{2.41}$$

where $\mathbf{m}$ is a unit vector that points along the local magnetisation direction, and $d_x\mathbf{m}$ means $\frac{\partial \mathbf{m}}{\partial x}$. The winding number is ±1 for a single cylindrical skyrmion.[3] This is depicted in Figure 2.14, for 2.14a and b, N=-1 with a core magnetisation of -m$_z$. Other types of skyrmions have also been identified, for example, the antiskyrmion (2.14c) has N=+1, for the biskyrmion (2.14d) N=+2, the bimeron (2.14g) has N=-1, and the skyrmionium (2.14h) has N=0. Figure 2.14 also shows a vortex (2.14e) which has N=-0.5, and a meron with N=-0.5 (2.14f).[43; 47]

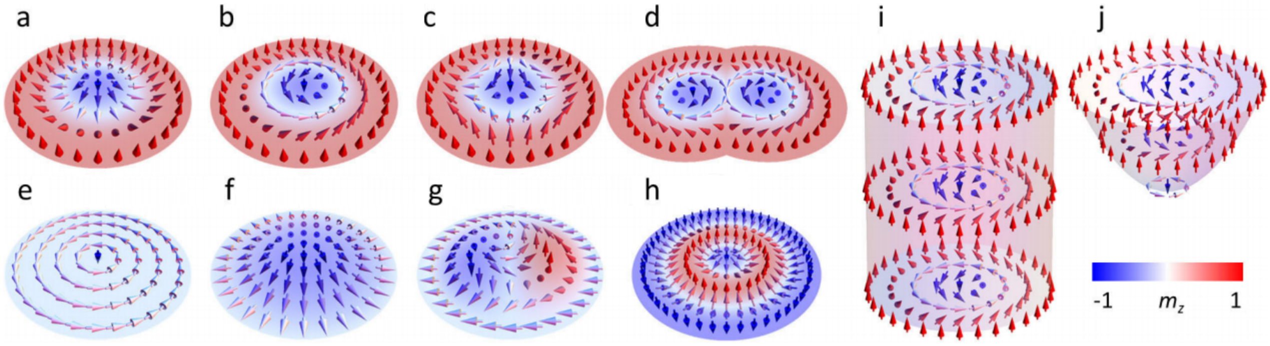

Figure 2.14: (a) is a Néel-type skyrmion, (b) is a Bloch-type skyrmion, (c) is an antiskyrmion, (d) is a biskyrmion, (e) is a vortex, (f) is a meron, (g) is a bimeron, (h) is a skyrmionium, (i) is a skyrmion tube, and (j) is a magnetic bobber. The arrow direction indicates the orientation of the spin (m$_z$). Red areas and blue areas represent the out-of-plane and in-plane components respectively. This figure was taken from Reference [47].

Néel skyrmions in magnetic multilayers (e.g. heavy metal/magnet/heavy metal) can form as a result of a large DMI at the interface due to inversion symmetry breaking and a strong spin-orbit coupling of the neighbouring heavy metals. In Figure 2.13, Pt and Ir are substituted as the heavy metals due to their large spin-orbit coupling. In order to understand why two different heavy metals are used, Equation 2.39 should be referred to. Due to the cross product, the direction of the DMI vector is determined by the right hand rule. For the platinum layer, the vector points out of the page (see Figure 2.13). If platinum was also used for the bottom layer its DMI vector would act to oppose the top layer due to the inversion of the interaction. Iridium, which has an oppositely signed spin-orbit term to platinum, causes the DMI vector to point out of the page instead; this causes the DMI interactions to add together constructively resulting in a stronger interaction.[1]

In contrast, for a Bloch skyrmion, the DMI vector points in the direction of the plane (i.e. along the line connecting the two spins).

2.12 The Hall Effect

In non-magnetic metals a potential difference (Hall voltage) is measured in the direction transverse to an electric current in a conductor with an applied magnetic field perpendicular to the current.[8] This is known as the ordinary Hall effect (OHE) and was discovered in 1879 by Edwin Hall.[48] The key aspect of this effect is the Lorentz force, **F**, on the charge carriers, q, which are moving in a magnetic field, Equation 2.42. The electric field acting on the charge carriers is given as **E**, and their drift velocity ν, with a magnetic induction, **B**.

$$\mathbf{F} = q(\mathbf{E} + \nu \times \mathbf{B}) \tag{2.42}$$

In materials which already have an intrinsic magnetic field, e.g. ferromagnets, antiferromagnets and paramagnets, the effect has additional components which depend on the materials magnetisation. This is termed the anomalous Hall effect (AHE), and has a high dependence on temperature.[8] The contributions to this effect can be of an intrinsic nature, based on the material band structures, and extrinsic nature, due to the scattering of the charge carriers. These effects can be measured by performing electrical transport measurements using a Hall bar, whilst applying an out-of-plane field (see Chapter 4).

2.13 Magnetoresistance

Another aspect of electrical transport measurements is magnetoresistance, which describes how the resistance of a metal changes under an external magnetic field. One type of magnetoresistance is called anisotropic (AMR), which describes how the resistance of a ferromagnet is dependent on the angle between the current and the magnetisation. It was first investigated by Lord Kelvin (William Thomson) in 1857.[49] Generally, if the magnetisation is perpendicular to the current, there is a reduction in the resistance, however, if the current and magnetisation are parallel, there is an increase in resistance. This is related to spin-orbit coupling and due to s-d scattering being dependent on the angle between the magnetisation and the moment of the electron.[50] Samples which consist of two FM layers separated by a NM spacer show a different type of magnetoresistance, termed giant magnetoresistance (GMR) due to it showing a larger effect than AMR. For electrons passing through a FM material, the scattering rate depends on the orientation of the magnetisation. Therefore, if there is negative interlayer exchange coupling between the two FM layers and the two layers are magnetised antiparallel, the up and down spin electrons will undergo a low or high scattering rate depending on the layer.

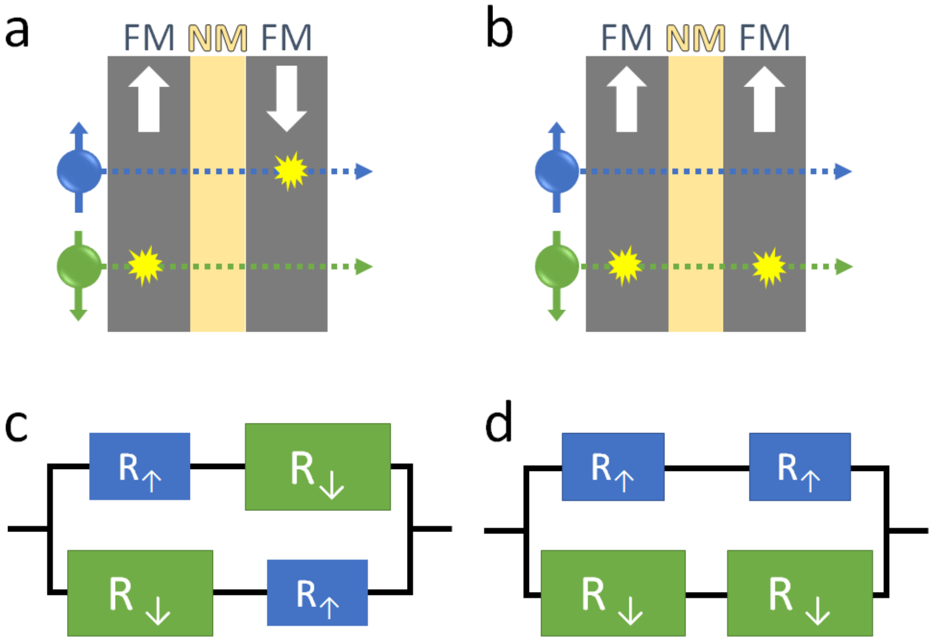

Figure 2.15: a) and b) show two FM layers separated by a non-magnetic spacer with up and down spin electrons passing through the layers. a) shows the two FM layers aligned antiparallel, therefore both electrons experience scattering. b) shows the two FM layers aligned parallel due to an applied magnetic field. The spin up electrons experience less scattering in both layers than the spin down electrons. c) and d) show the two-resistor model of a) and b), respectively. This figure was adapted from Reference [51].

A method to understand this is by considering the two layers as two resistors in parallel (see Figure 2.15). In 2.15a, the two FM layers are magnetised antiparallel, therefore the up spin electrons have a higher resistance with the second layer, and a lower resistance with the first layer - vice versa for down spin electrons. 2.15c shows the effect in a two-resistor model, there is no scatter free path for the electrons. In 2.15b, the two ferromagnetic layers are aligned parallel with a high magnetic field, therefore the spin up electrons experience less scattering and there is a low resistance path. This is the reason why SAF samples experience a higher resistance at zero field and a lower resistance at higher fields.[5]

CHAPTER 3

Literature Review

3.1 Skyrmions

Magnetic skyrmions have been receiving a huge amount of attention since they combine unique topological properties together with promising technological applications. A magnetic skyrmion is a localized spin texture where the magnetization vector rotates continuously within a 2π angle.[44–46] This feature leads to an integer winding number which provides the skyrmion with a so-called topological protection, and hence, an additional energetic stability in physical systems.[52] In the past, the main focus of investigations into skyrmions has revolved around Bloch skyrmions in bulk, B-20 type materials (such as MnSi and FeGe) below room temperature (250 K).[53; 54] Following this, Néel skyrmions were found in epitaxially grown monolayers and bilayers; Fe and PdFe on Ir, as shown in Figure 3.1a.[55] This fueled research into these skyrmions, though the materials were still not optimised since the skyrmions were only found at low temperatures (around 30 K) and magnetic fields of 0.1 T.[43]

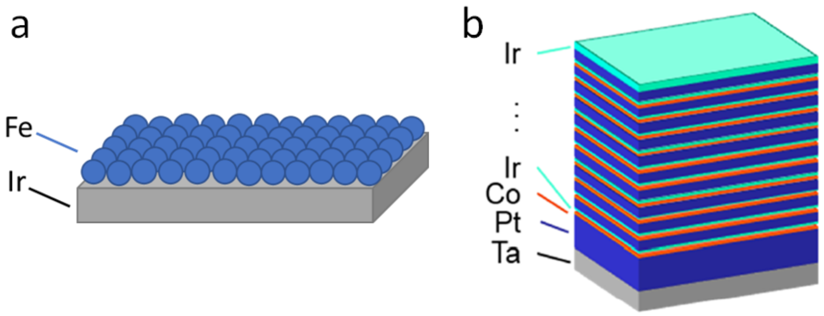

Figure 3.1: a) is a monolayer of iron on an iridium substrate. b) is magnetic multilayers of Co/Ir/Pt on a tantalum and platinum base taken from Reference [56].

3.1.1 Skyrmions in Magnetic Multilayers

Focused research over the past few decades has allowed Néel skyrmions to be observed in heavy metal/ferromagnet/heavy metal multilayers.[43; 57–61] Materials were used such as cobalt for the ferromagnet, and iridium and platinum for the heavy metals, as in Figure 3.1b.[56] These observations have been made at room temperature and required either little or no magnetic field, which is favourable for a skyrmion-based device. In addition, these multilayers were grown via sputtering, which is a more mainstream industrial technique as it provides more uniform films grown over shorter timescales than other growth techniques.

In magnetic multilayers, skyrmions arise due to competition between magnetostatic interactions and an interfacial DMI which is an antisymmetric exchange interaction at interfaces with broken inversion symmetry, for example, Co/Pt or Co/Ir.[62; 63]

Skyrmions in these multilayers are envisaged to be suitable for applications such as data storage, skyrmion based frequency devices, unconventional computing, logic devices, and skyrmion racetrack memories.[1; 64–67] Racetrack memories can encode information with a sequence of individual skyrmions on a magnetic track.[1; 68] The overall aim of current skyrmion investigations worldwide are four-fold: controlled nucleation and annihilation must be possible for individual skyrmions, they must be able to be displaced in a controlled manner, controlled excitation of skyrmion modes should be possible (such as breathing modes and gyration modes) and skyrmions must be detected individually. All of these processes should be possible electrically and at room temperature.[1] Research has shown that skyrmions are highly stable and can be nanometers in size.[69] Both theoretical and experimental studies have been done into skyrmion dynamics[70], they can be manipulated by currents, and require a low current density to produce movement.[71; 72] Electrical detection[3; 73; 74] and systematic skyrmion nucleation and deletion has been achieved[58; 71; 75; 76], plus, skyrmion resonant modes have been probed.

3.1.2 Skyrmion Nucleation

Investigations have been done into many different procedures to nucleate skyrmions.[1] Jiang et al. used a method which involved the conversion of domain walls driven by the spin Hall effect in a wire which was designed to be symmetric and restrictive.[57] This method was used with layers of Ta/CoFeB/MgO at room temperature with fields of 0.5 T.

Another method was found by Romming et al. at temperatures of 8 K and magnetic fields of 1 T or more, using spin-polarised electrons generated by a scanning tunneling microscope (STM) in PdFe.[77] A more recent method was adopted by Zeissler et al. in Co/Ir/Pt multilayers, in which skyrmions were nucleated at room temperature using a current pulse and magnetic field protocol, this is shown in Figure 3.2.[3; 56] Other procedures are also being considered, such as a skyrmion injector[2] or magnetic force microscopy (MFM).[78]

3.1.3 Skyrmion Motion and Detection

Current induced motion of skyrmions has been observed to exceed 100 ms^{-1} by Woo et al. on a magnetic racetrack.[58] Although, a current problem affecting skyrmion motion is pinning, which increases the current density needed for skyrmion motion and therefore reduces the performance of devices.[79] An option to reduce this pinning effect in the Co/Ir/Pt multilayers could be to replace the crystalline cobalt with an amorphous magnetic material, e.g. cobalt boron (CoB). Finizio et al. observed reliable nucleation of skyrmions in CoB multilayers using a current injector - see Figure 3.3.[2] Electrical detection of skyrmions has been observed by Zeissler et al. via the Hall signal which was related to the presence and size of a single skyrmion.[79]

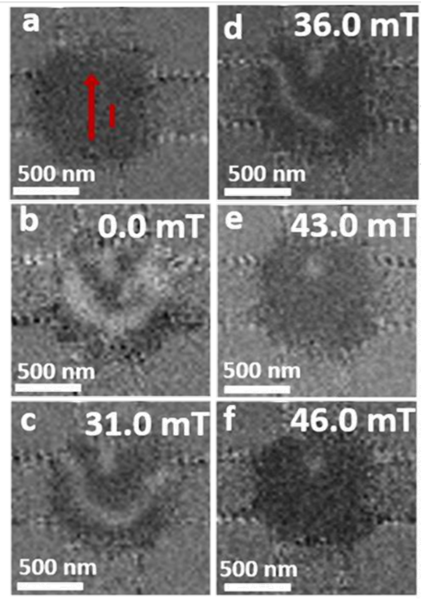

Figure 3.2: This figure was taken from Reference [3]. a) shows a nanodisc which has been fully saturated. A current pulse was applied across it in the direction of the red arrow and this caused a domain pattern to form, shown in b) where the dark and light regions show antiparallel magnetised domains. In c) the magnetic field was applied antiparallel to the nucleated domain magnetisation and the domain sizes decreased. At high fields, only a stable skyrmion remained (e and f).

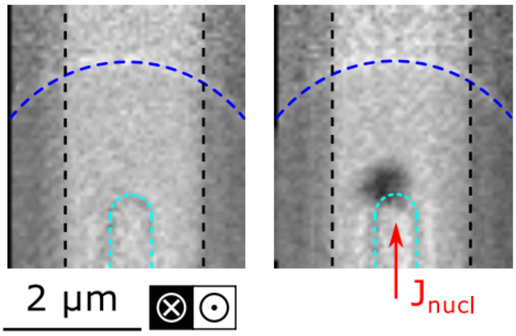

Figure 3.3: This figure, taken from Reference [2], shows a skyrmion being nucleated in a CoB sample using a 5 ns current pulse from a nanoengineered injector.

3.1.4 Skyrmion Dynamics

Skyrmions have been both predicted and observed to exhibit breathing and rotational modes.[80; 81] The core of the skyrmion can rotate clockwise or counter clockwise in the rotational modes and in the breathing mode, the skyrmions core gets bigger and smaller - as shown in Figure 3.4. These dynamical modes can have frequencies in the microwave range and are well understood for bulk-like systems.[81; 82] When considering thin films with less measurement sensitivity and a lower quantity of skyrmions, measurements become more difficult, though there are theoretical and experimental results.[83–87]

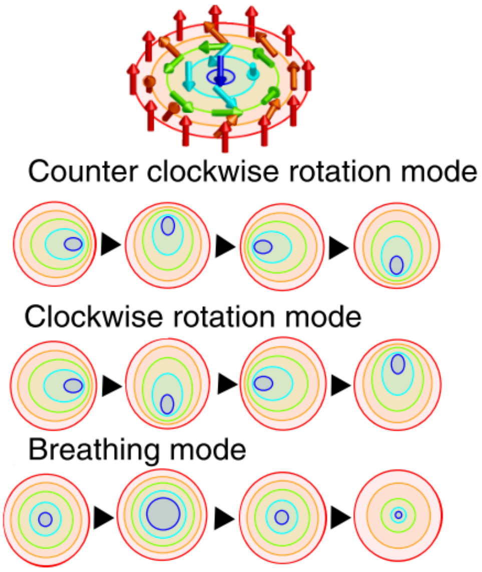

Figure 3.4: This figure shows the rotation and breathing modes of a skyrmion, taken from Reference [82].

Shen et al. proposed skyrmion based spin torque nano-oscillators as next generation microwave signal generators, however, due to ferromagnetic materials being unable to achieve high enough frequencies of oscillation, they utilize the circular motion of an antiferromagnetic skyrmion with frequencies in the tens of GHz.[88] A similar proposal was presented by Jiang et al. using SAFs to make a terahertz spin Hall nano-oscillator, simulating frequencies up to THz.[89] Zhong et al. showed frequencies up to the THz range in a SAF spin-transfer torque oscillator without an applied field, assuming the AFM-IEC is sufficiently strong and the thickness of the top SAF layer is sufficiently thick to allow for a wide current density and frequency window.[90]

Onose et al. observed the breathing and rotational modes of skyrmions in Cu_2OSeO_3 with different frequency resonant peaks: a counter clockwise circulating mode at 1 GHz with a parallel magnetic field on the skyrmion and a breathing mode at 1.5 GHz with a perpendicular magnetic field.[82] Other theoretical work has been done involving skyrmions in the same material predicting resonances in the GHz range.[91–94]

A magnetic resonance study was performed by Satywali et al. on [Ir/Fe/Co/Pt] multilayers with Néel skyrmions at room temperature. They discovered two separate resonances, with frequencies between 6-12 GHz of the skyrmion phase upon an in-plane ac excitation.[83]

3.2 Research into Synthetic Antiferromagnets

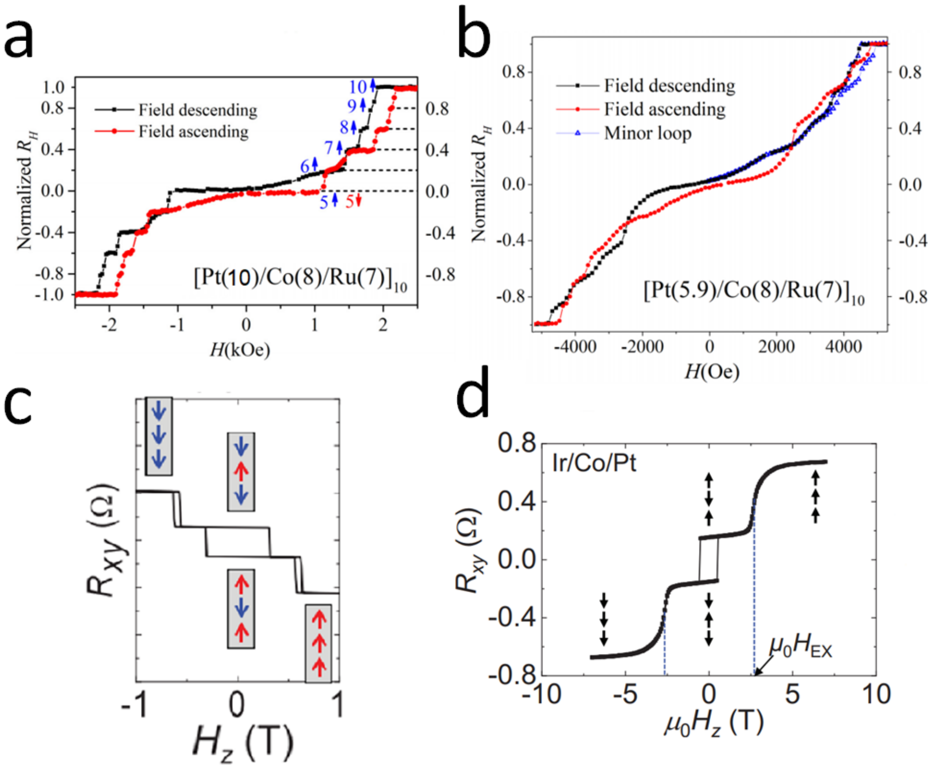

Figure 3.5: a) shows how the ascending and descending field sweeps have 10 individual switches for the stack written in the inset. b) is the same stack with a lower platinum thickness, showing crossing during the hysteresis loop.[95] c) shows the hysteresis loop of a [Pt(0.6 nm)/Co(0.9 nm)/Ir(0.5 nm)]$_{\times 3}$ sample which is antiferromagnetically coupled. The arrows represent the spin orientations of each cobalt layer after each switch.[96] d) similarly shows a [Ir(0.6 nm)/Co(0.9 nm)/Pt(1.3 nm)]$_{\times 3}$ sample, which is in agreement with the spin orientations of c).[97]

Karayev et al. showed antiferromagnetic interlayer exchange coupling (AFM-IEC) in Pt/Co/Ir and Pt/Co/Ru PMA samples which are of interest due to their large interfacial DMI. They investigate multilayer repeats of 1, 2, 3, 5 and 10, and in the 10 repeat sample they saw a switch for each layer (Figure 3.5a) due to the AFM-IEC from the Ru and Ir. They also saw hysteresis loops crossing between ascending and descending fields, as shown in Figure 3.5b.[95] Other examples of antiferromagnetic coupling in Co, Ir, Pt systems came from Lau et al. and Ishikuro et al. - see Figure 3.5c and d.[96; 97] Lau et al. studied a direct dependence of the anisotropy and exchange coupling fields with iridium layer thickness. Ishikuro et al. also performed a study with variance in the thickness of the iridium layer and compared the difference in spin-orbit torque between ferromagnetically and antiferromagnetically coupled cobalt layers. The graphs of three repetition samples in Figure 3.5c and d are fundamentally similar, however, Lau et al. show outer switches which are less sharp and their saturation field values are unusually high. This difference could be due to 3.5c showing Pt/Co/Ir and 3.5d showing Ir/Co/Pt. Lau et al. ascribed this to different growth related intermixing and therefore different electronic structures.[97]

3.2.1 Skyrmions in Synthetic Antiferromagnets

There are still many challenges to overcome and ferromagnetic skyrmions have drawbacks for real-world applications. Skyrmion diameters are limited to 10s of nanometers or more due to the non-local stray fields within ferromagnets.[52] Though stable at room temperature, they usually require an external field to stabilize them[57; 59; 60], and their velocities are limited as they are inhibited by topological damping[52; 76; 98]. Skyrmion motion in ferromagnetic materials is restricted by the skyrmion Hall effect (SkHE), a Magnus-like force that causes skyrmions to drift towards the edge of a sample when a current is applied, instead of following the direction of the current.[99; 100] As previously mentioned, further complications with most skyrmion hosting materials (e.g. cobalt) comes from pinning properties of the materials, the skyrmions can often become 'pinned' at the lattice boundaries or at defects, removing their potential for applications such as racetrack memory.[56] Efforts have been made to host skyrmions in antiferromagnets[52; 101–104] or ferrimagnets[76; 105; 106], however, drawbacks still arise. Synthetic antiferromagnetic materials hosting skyrmions provide a way to counteract these problems as the opposite spin orientation of different magnetic layers can suppress the SkHE, as shown theoretically by Zhou et al. in Figure 3.6b[104], and SAF skyrmions have much higher velocities.[101; 107–110] When placing a NM spacer between two FM materials, the ferromagnetic layers can undergo interlayer exchange coupling (IEC). Particular spacers, such as Ir and Ru, cause coupling which switches between ferromagnetic and antiferromagnetic depending on the distance between the magnetic layers. Therefore with a specific thickness, the two magnetic layers will experience AFM-IEC due to the RKKY interaction, which is how a SAF is designed.[10–14]

Recently, skyrmion bubbles have been shown in a SAF in an applied field being driven with smaller current densities than their ferromagnetic counterparts and with a negligible SkHE.[112] The stack used was designed to be slightly uncompensated to allow the skyrmion bubbles to be imaged using the magneto-optic Kerr effect (MOKE). Nanometer sized skyrmions were also recently shown in a SAF, stabilized at zero field using a bias layer. This is because it is difficult to bias a SAF using an external magnetic field as their magnetization is compensated. They measured them

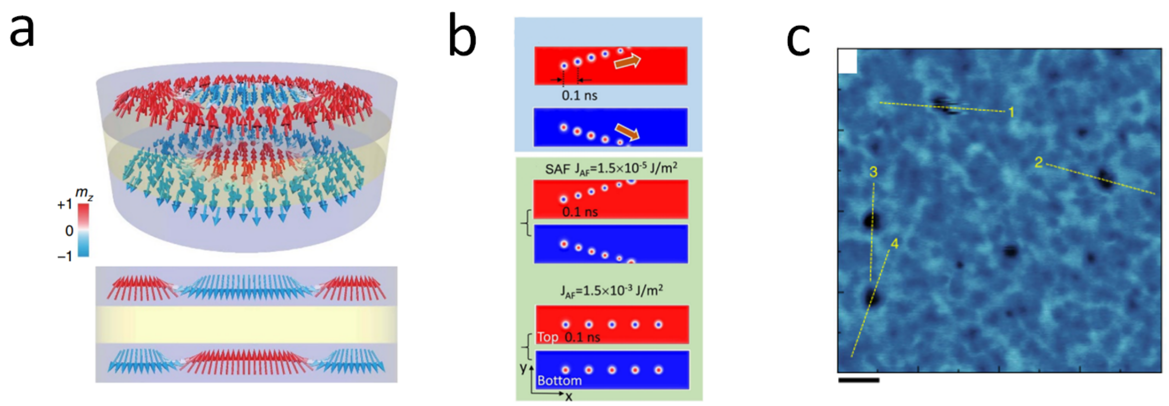

Figure 3.6: a) shows two skyrmions in an antiferromagnetically coupled bilayer, and underneath is the side view of the spins. It is evident that the spin orientations in each layer are opposite.[107] b) shows skyrmion motion trajectory when applying an in-plane current. In a monolayer, the skyrmion tends towards the sample edges. In a SAF and using a high enough current density, the skyrmion stays central.[104] c) shows antiferromagnetic skyrmions observed in a SAF via MFM with an applied magnetic field perpendicular to the sample of $\mu_0 H_{ext}$=100 mT, scale bar 500 nm.[111]

using MFM, shown in Figure 3.6c.[111] Juge et al. reported fully compensated SAF skyrmions both at room temperature and in zero field, in a sample consisting of two different ferromagnetic materials (Co/$Ni_{80}Fe_{20}$/Co and Co) separated by Ru, which they could nucleate and observe using x-ray microscopy techniques.[113]

3.3 Terahertz

3.3.1 Sources and Detection

When using any type of radiation in a useful way, there are always two components to consider: the source of the radiation and the detection of the radiation. Most types of radiation can be put to good use in everyday life; for example, microwave satellite signals, police infrared thermal imaging cameras and x-ray imaging of broken bones. However, electromagnetic radiation in the far infrared or THz region with frequencies between 0.1 THz to 10 THz was more difficult to harness into useful applications. This region especially started to get attention in the 1980s and became known as the ‘terahertz gap’.[114] THz radiation is non-ionising, can penetrate materials such as wood, plastic and fabric, gets absorbed by water and is reflected by metals. All of these properties could be harnessed to create advances in various industries, but first, an efficient source and detector was needed.[115]

For a potential THz source, narrow band frequencies in the infrared spectrum were initially found by Rubens and Nichols in 1897 using reflections from different ionic crystals; they produced

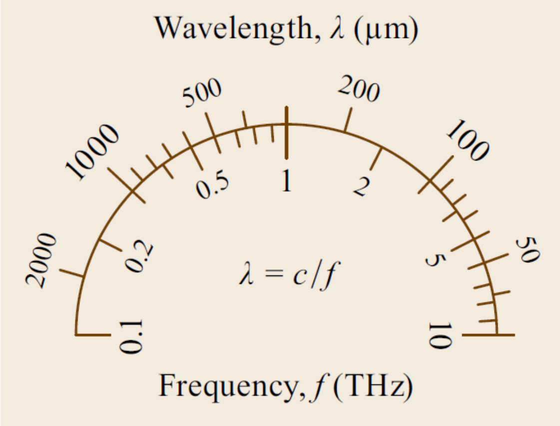

Figure 3.7: This shows the range of wavelengths of light that THz frequencies correspond to (taken from Reference [115]).

near monochromatic light using Restrahlen plates.[116] The next development was the production of the backward wave oscillator in the 1950s, followed by the first high power far infrared laser which was manufactured in 1964. Subsequently, a surge of new lasers ensued: the optically pumped far infrared laser in 1970, the free electron laser in 1977, femtosecond (fs) lasers in the 80s - specifically the Ti-sapphire laser in 1991 and quantum cascade lasers in 2002.[115] The advancement of fs lasers brought techniques such as terahertz time-domain spectroscopy, which could incorporate photoconductive antennas. In these antennas made with photoconductive materials, carriers generated by a laser with sufficient energy to exceed the bandgap are accelerated by an applied voltage, causing a THz pulse.[117]

The first detector for THz radiation was called a bolometer, it was invented by Langley in 1880 and worked when IR radiation was incident on a material (e.g. platinum). The radiation would cause the material to increase in temperature resulting in a change in resistance. If a controlled current was passed through the material, the change in resistance could be determined by a voltage measurement.[118] In 1947, there was another significant discovery - a pneumatic detector called the 'Golay Cell' which worked at room temperature. Like the bolometer, it had plates which would absorb IR radiation, however, the plates enclosed a cylinder of xenon gas and when they increased in temperature, the xenon gas expanded causing the deformation of a diaphragm. The amount of deformation could be calibrated for detection of THz radiation.[119; 120] In the 1950s, Fourier transform spectroscopy was developed, which allowed analysis of more than one wavelength of light in a complex interferogram. By 1959 many types of bolometers had been invented, as well as the first photoconductive detector, which was based on the concept that an increase in the number of free electrons occurred when light of a specific energy struck the material. When THz radiation was incident on the photoconductive material, the THz electric field accelerated these charges leading to a current that could be detected.[116; 119] More recently, the photoconductive material is made from low temperature grown gallium arsenide (LT-GaAs) and used in combination with fs laser pulses as a source and detector in THz-TDS.

The terahertz gap has begun to close and applications in both sensing and communications are arising at a significant pace. Technology using TDS and frequency domain spectroscopy provides insights into numerous fields such as biological, astronomical, environmental, industrial and security applications. Terahertz frequencies are now being used in wireless and satellite communications and have potential for high speed data processing.

3.3.2 Ultrafast Manipulation of Magnetism

A similar area of research involves manipulating the magnetisation of a material at high frequencies, i.e. short timescales, a variety of techniques are used; optical pulses, magnetic field pulses, and spin torque transfer. A more recent interest has been into THz frequencies. Antiferromagnetic materials have magnon precessions up to THz frequencies and Kampfrath et al. showed that THz pulses could be used to manipulate antiferromagnetic magnons on a fs timescale and therefore in the THz range - as ferromagnets do in the GHz range. The ultrafast spin control is possible due to the Zeeman interaction, as the magnetic component of the THz wave couples to the antiferromagnet's electron spins and the Zeeman torque forces the spins away from the easy axis so the anisotropy field causes the resonant motion.[121]

Research has also been done into ferromagnetic thin films as a source of THz radiation. This was first discovered by Beaurepaire et al. who showed that when a fs laser is incident on a nickel thin film, it caused ultrafast demagnetisation, which gave rise to THz radiation. Beaurepaire explained that the optical pulse excites the film's electrons into an electron bath in thermal equilibrium over a timescale of around 500 fs. As the Curie temperature is approached, the film becomes demagnetised. Then, the energy transfers to the lattice via electron-phonon interactions on a 1-10 ps timescale. This gives rise to a photon with THz energies and as the magnetisation varies (from Maxwell's equations) an electric field in the far infrared (i.e. THz range) is propagated.[122–125] There have been other hypotheses for the demagnetisation mechanism/s such as super spin diffusive spin transport[126], and Elliot-Yafet scattering[127].

Vicario et al. observed off-resonant femtosecond magnetisation dynamics in 10 nm cobalt films. The cobalt undergoes a coupling with the THz pulse which is phase-locked and the magnetisation dynamics are coherent with the THz field oscillations. The dynamics are two orders of magnitude faster than the Larmor precessional response as they are off-resonant excitations. They explain this ultra-fast dynamical response using a Landau–Lifshift–Gilbert semi-empirical model. As the timescale is so fast, the energy does not have time to dissipate, therefore the damping term in the Landau–Lifshift–Gilbert equation can be ignored (Equation 3.1),

$$\frac{d\mathbf{M}}{dt} = -\gamma(\mathbf{M} \times \mathbf{H}) \tag{3.1}$$

where γ is the gyromagnetic ratio, M is the magnetisation along the direction responding to the THz magnetic field and H is the effective magnetic field (anisotropy field, applied field, THz field). When the THz pulse hits the sample, it causes the magnetisation to precess by invoking a torque.[128; 129]

Kampfrath et al. also experimented using FM/NM metallic heterostructures as spintronic THz emitters. When a femtosecond laser pulse is incident upon an iron film, it drives the spins into the non-magnetic cap layer (Au or Ru) where the inverse spin Hall effect was exploited to convert the spin flow into a THz pulse.[130] Furthermore, Choi et al. investigated the ultrafast spin dynamics in permalloy, using a Fe/Au THz emitter and the time-resolved magneto-optic Kerr effect. They showed that the THz pulse coupled to the permalloy's magnetisation in phase-locked precessional responses, with high efficiency due to the geometry of their devices. They also indicated that the spin dynamics were driven by Zeeman coupling between the magnetic field of the THz pulse and the permalloy's magnetisation.[131]

3.4 Motivations

This work participates in a meticulous study around understanding areas of dispute and areas of agreement when calculating standard parameters of magnetic thin films. Specifically, in magnetic multilayers with Co or CoB, which are known as reliable skyrmion hosts. All experimental methods are described in Chapter 4. Chapter 5 focuses on interfacial effects between FM and NM materials, which are often ignored but can have significant effects on basic parameters, such as saturation magnetisation. When performing experiments with an aim towards understanding skyrmion properties and designing skyrmion devices, a key parameter is the DMI strength, of which values can often disagree in literature. Methods of calculating the DMI strength were analysed in Chapter 6, including comparing the reliability of different approaches of data modelling, analysis, and different experimental methods. The aim was to provide informed options for how to conduct the experiments and analysis for measuring these crucial parameters. Furthermore, Chapter 7 methodically investigates SAF behaviour of CoB/Ir/Pt multilayers to understand the intricate competitions between different internal effects, with the aim to create a suitable SAF host for skyrmions. This work then goes on in Chapter 8 to use nanofabrication to design a coplanar waveguide (CPW), developed from Reference [5], with the ability to host magnetic multilayers. The magnetic multilayers fabricated into the waveguides have been shown to host skyrmions, in order to probe any possible responses from magnetic skyrmions within the Hall bars, and synthetic antiferromagnets which have been shown to have resonances in the THz frequency range, not dissimilar to ferrimagnets.[87; 89; 90; 132–134]

Chapter 4

Experimental Methods

4.1 Thin Film Deposition

One of the main deposition techniques used is sputtering. Sputtering uses argon gas to eject target material onto a substrate. A vacuum is made inside a main chamber using a rotary pump, a cryo pump and a Meissner trap - reducing the pressure to around 10^{-8} Torr. A rotary pump is an oil based pump which forces air out of the main chamber by making the area that the air from the main chamber flows into smaller. This increases its pressure and forces it out of a second exit. A cryo pump uses very low temperatures (around 15 K) to condense gases from the main chamber onto a charcoal array with a temperature gradient. Charcoal is used as it is very porous and has a large surface area, so it can hold a lot of molecules such as H_2O, carbon, N_2 which freeze onto it at their different condensation points. The Meissner trap uses liquid nitrogen and works in a similar way to the cryo pump but at higher temperatures. Also, a residual gas analyser uses a quadrupole mass spectrometer to measure specific gases in the main chamber.

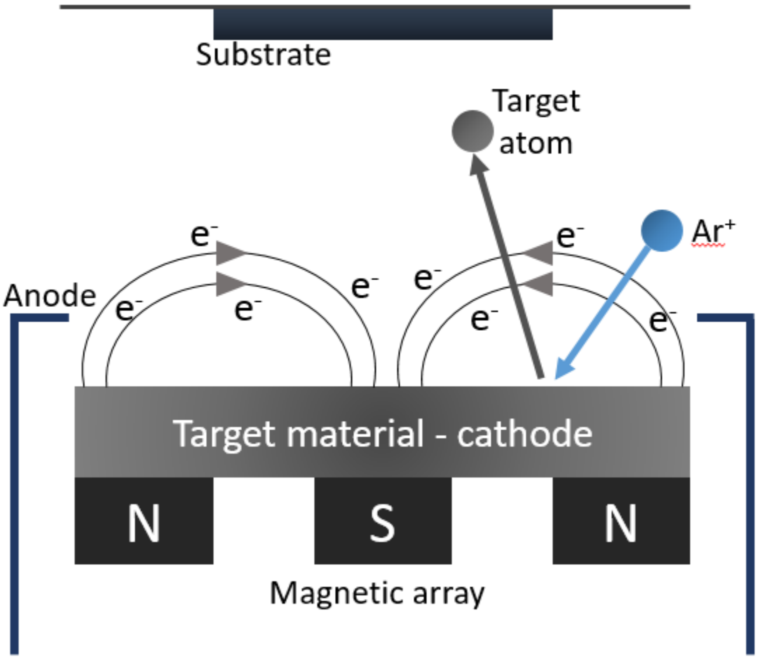

Figure 4.1: This shows the set up for typical DC magnetron sputtering. A target material is sputtered onto a substrate via argon ions.

Argon gas is used as it is unreactive; it is pumped into the vacuum (increasing the pressure to approximately 3 mTorr) and then ionized by a high voltage applied between the target material and an anode. The ionised particles are then accelerated into the target, consequently creating more ions as they collide with neutral atoms while travelling to the target, and a plasma is created around the target. Upon hitting the target material, the argon ion ejects the target material via secondary momentum scattering onto the substrate in layers. Electrons also get ejected which contributes to maintaining the plasma. A magnet assembly can also be used to confine the plasma in order to stop electrons hitting the substrate, it also increases the probability of electrons colliding with the argon as the field causes the electrons the follow helical trajectories (Figure 4.1). Sputtering can require fine tuning as a low pressure could lead to roughness (the particles don't have enough energy to move on the substrate) and a high pressure to lower growth rates (if particles have too much energy they could re-sputter from the substrate). Furthermore, the product of the target-to-substrate distance and the pressure must be considered.[6]

E-beam evaporation was also necessary for fabrication of a coplanar waveguide. It is a deposition technique which also uses a high vacuum to create conditions for a large mean free path, ensuring directional deposition. Thermionic emission from a filament causes high energy electrons to be accelerated into a metal target in a water-cooled crucible. The electrons heat the metal until it melts, then begins to evaporate onto a substrate which is face down above the crucible.[5]

4.2 X-ray Characterisation

X-ray radiation can be used to probe information about the atomic crystal structure of a material. Specifically, x-ray diffraction (XRD) or x-ray reflectivity (XRR) measurements are used to get information about the lattice, the thicknesses, roughness and densities of a sample or the layers within the sample. When an x-ray (with wavelength comparable to interatomic spacing) scatters off atomic electrons or nuclei, it gets scattered at a specific angle relative to the crystal lattice, and Bragg's law, Equation 4.1, and Equation 4.2, can be applied to determine lattice parameters.

$$n\lambda = 2dsin\theta \tag{4.1}$$

$$d = \frac{a}{\sqrt{h^2 + k^2 + l^2}} \tag{4.2}$$

The x-ray wavelength is represented by λ, d is the spacing of the atomic planes, n is an integer corresponding to the order of reflection, θ is the angle of diffraction, a is the lattice constant and h, k and l are the Miller indices.[16; 135] A schematic of the x-ray reflection is shown in Figure 4.2. X-rays were formed from a tungsten filament at one end of a vacuum tube (the cathode), at the other end of the tube is a copper target (the anode). A voltage was applied between the anode and the cathode, causing electrons to be emitted by thermionic emission from the filament and accelerated towards the copper. The electrons cause two types of radiation: Bremsstrahlung, which occurs when the free electron is decelerated by the positive charges of the copper ion, and characteristic x-rays, which occur as the accelerated electrons 'knock out' electrons in the n=1 shell of the copper atoms. Higher energy electrons drop down to fill the gap which releases energy as Kα and Kβ x-rays. A monochromator consisting of an ordered single crystal is used to destructively scatter the Kβ x-rays and Kα2 x-rays, leaving only Kα1 x-rays.

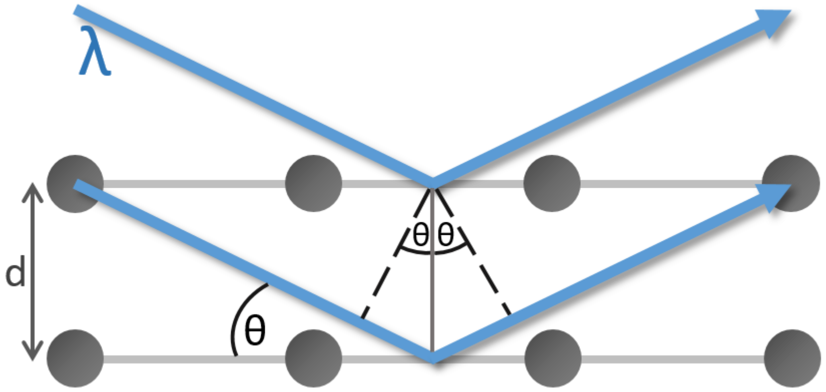

Figure 4.2: This figure shows how x-ray reflectivity works, the incident beam is shown hitting the material (shown at an atomic level) and reflecting off the crystal structure. λ is the x-ray wavelength, d is the spacing of the atomic planes, and θ is the angle of diffraction.

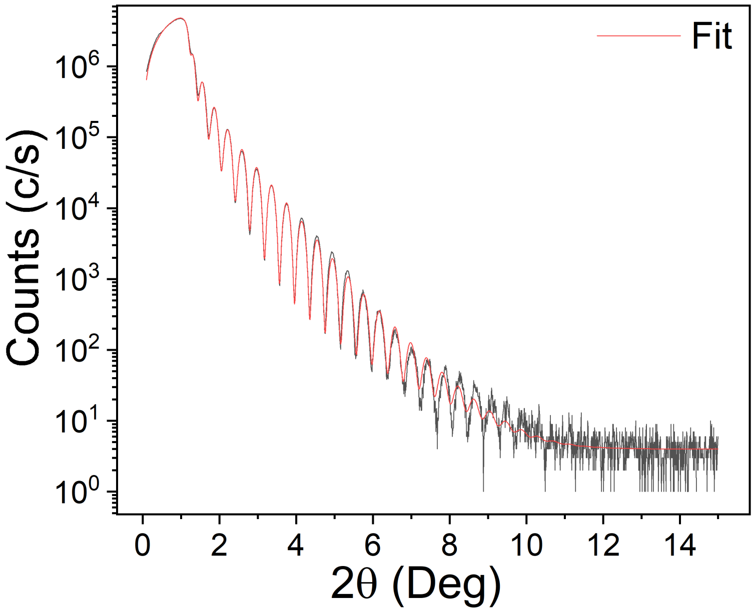

Figure 4.3: In this figure, the black line shows a typical XRR scan of a ∼200 Å platinum sample, the angle is plotted against the number of x-ray counts/second. The red line shows the fit performed by GenX.[136]

During a scan, called a specular scan, the angle of incidence of the x-ray on the sample was swept across a certain range. In a material with different interfaces, e.g. a material on a substrate or multilayers, the reflected x-rays which scatter from the different surfaces interfere constructively and destructively, causing Kiessig fringes as a function of angle. This is performed with the x-ray beam positioned at low angles relative to the plane of the sample (XRR). From the Kiessig fringes, the electron density and the critical edge (which is dependent on the refractive index when the x-rays first penetrate the film) were determined. The spacing of the fringes provided the thickness and the roughness was determined by the angle at which the curve significantly decays. Material compositions were modelled using the program 'GenX',[136] an example of XRR data is shown in Figure 4.3.

4.3 Magnetometry

Measurements to determine the magnetisation as a function of applied field of a sample can be either closed circuit or open circuit (if the sample is part of the magnetic circuit or not). More commonly open circuit measurements are used, however, the demagnetising field has to be taken into account. Open circuit measurements utilise either force on a sample or change of flux in a circuit when the sample is displaced. The basic principle behind flux measurements is to place a sample within a coil in a field, when it is moved (removed or vibrated at a certain frequency), the movement causes a change of flux in the coil, which is proportional to the magnetic moment of the sample. A vibrating sample magnetometer (VSM) is one way to do this: a mounted sample is placed within a set of pick up coils, surrounded by electromagnets and vertically vibrated from 10-100 Hz. The changing magnetic field from the samples causes an electric current due to Faraday's law, i.e. an emf (electromotive force) is induced in the coils. Two coils are wound in opposite orientations which results in their insensitivity to uniform fields or linear field gradients (gradiometer), and the induced emf from only local field disturbance is additive. In a quadrupole set-up, two pairs of coils are used. The sensitivity of a VSM extends to 10^{-8} Am^2, however, for further sensitivity, a superconducting quantum interference device (SQUID) can be used to achieve up to 10^{-12}Am^2 when in AC mode.[6] This method utilises pick up coils which are inductively coupled to a SQUID by a flux transformer. The SQUID is made up of two Josephson junctions on a superconducting ring, it combines flux quantisation and Josephson junctions to convert extremely small currents to voltages.[137; 138]

SQUID measurements were performed to determine various sample defining parameters: M_S, H_{sat}, and H_c. A sample can be positioned with the magnetic field of the SQUID either in-plane (IP) or out-of-plane (OP) to run typical measurements in which the field is swept at a set temperature, or the temperature is swept at a set field. From a SQUID hysteresis loop (sweeping the field), a value for the saturation magnetisation (M_S) of a sample can be derived from the measured magnetic moment (m) and sample volume (V) using $M_S = \frac{m}{V}$. Its only dependence is on the atomic magnetic moments and the number of atoms per unit volume. When measurements are made using the SQUID, a signal due to the diamagnetic substrate can also be present and therefore need subtracting via a linear correction, as shown in Figure 4.4.[16]

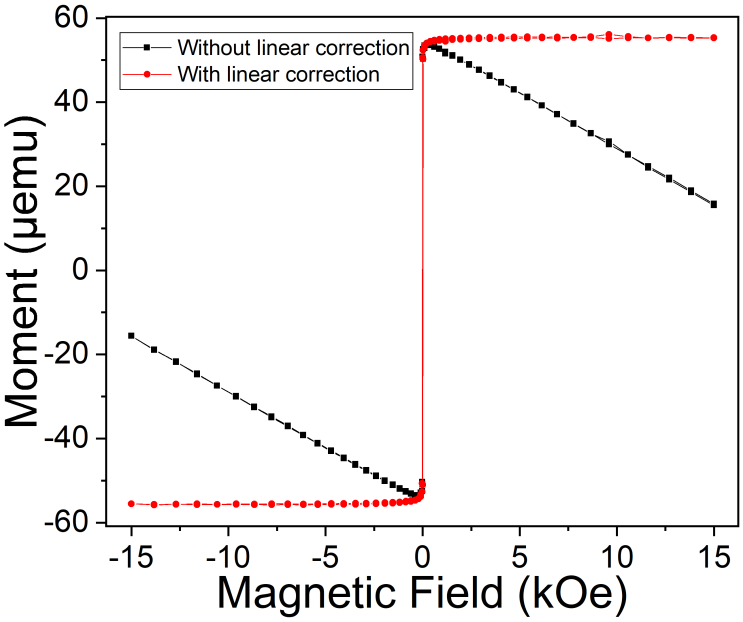

Figure 4.4: A Si or SiOx substrate contributes a linear background signal to the total moment as it is diamagnetic. A negative linear gradient, that is clear above the saturation field, was subtracted from the data.

The sample shape and size can affect the measured parameters, as well as the vibration amplitude. This is because a small sample may have flux lines which close inside the coils and therefore evade detection with no net flux. A larger sample, filling the detection coils may instead have no flux lines which close within the coils, allowing the total moment to be detected. Considering thin films, the measured moment will be heavily reliant on the orientation of the thin film. As a SQUID is calibrated to a cylindrical palladium sample, differences in shape and size from this can also result in different calibration errors from different vibration amplitudes. Due to these influences, a fill factor is required to compensate and correct the magnetic moment. The details of this are found in Reference [139], in which the fill factor for thin films measured in both a horizontal and vertical orientation for different sample areas can be found. Figures 4.5a and b, show a summary of the fill factors when the vibration amplitude is 5 mm. From the linear fit, a fill factor can be assigned for any sample area for both horizontal and vertical (i.e. OP and IP) measurements.

In Figures 4.5c and d, the IP and OP hysteresis loops of a 300 Å Co film are shown with a

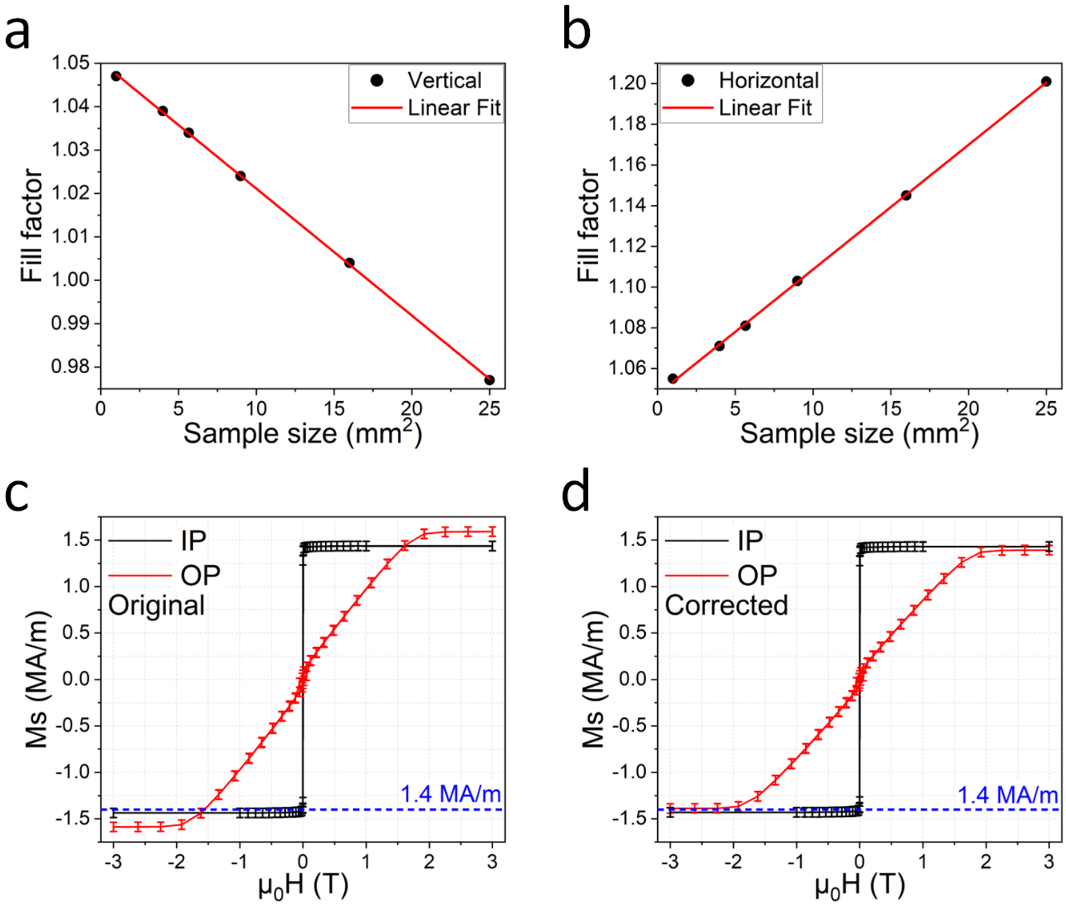

Figure 4.5: a) and b) show the fill factor vs. sample area for thin films measured in a Quantum Design SQUID in both the vertical and horizontal orientation, taken from Reference [139]. The equation of the linear fit can give a guide for the appropriate fill factor. These plots are based on a vibration amplitude of 5 mm. c) and d) show the IP (vertical) and OP (horizontal) SQUID hysteresis loops of a 300 Å Co sample, with linear correction. c) shows the original SQUID measurements, whereas d) shows the measurements when corrected with the corresponding fill factor. The bulk saturation magnetisation for Co is also displayed, at 1.4 MA/m .[16]

linear correction applied. The original measured measurements in 4.5c, show a disagreement of the saturation magnetisation when the sample was measured vertically and horizontally. Once the moments were divided by the corresponding fill factors, the saturation magnetisation of the two measurements were in agreement with each other (within the error) and also with the literature value for the saturation magnetisation of Co.[16]

4.4 Magneto-optic Kerr Effect

A similar characterisation can be performed using the magneto-optic Kerr effect, which can also determine which plane the magnetisation of the sample lies in. There are two different MOKE configurations discussed in this report: longitudinal and polar. In both versions, a laser of linearly p-polarised light hits the sample. As linearly polarised light can be considered as two oppositely polarised circular light components, when the light excites the electrons in the sample, the absorption of one circular direction is different from the other (circular dichroism). This means that when the electrons de-excite, the light released has an out of phase component, perpendicular to the incident light, resulting in the light becoming elliptically polarised (Kerr ellipticity). The reflected light is also rotated in its major axis due to spin-orbit coupling (Kerr rotation). Similar to the Faraday effect, the direction in which the light rotates depends on the magnetisation orientation within the sample - up or down magnetised domains cause light to rotate in opposite directions, see Figure 4.6.

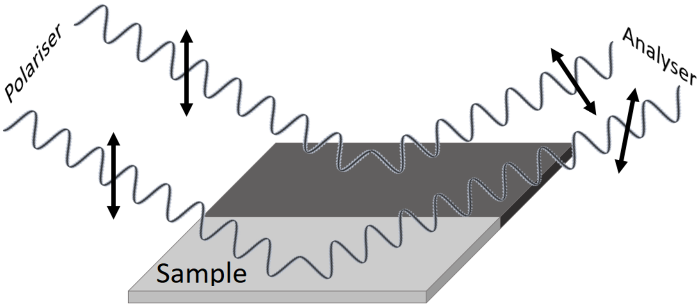

Figure 4.6: This figure represents a sample with two domains of opposite orientation. When the polarised light hits one domain, it gets rotated in one direction which will be fully transmitted by the analyser. When it hits the other domain, it gets rotated in the other direction, unaligned with the analyser, so experiences reduced transmission. This figure is adapted from Reference [21].

The reflected light is directed through a compensator to convert it back to plane polarised light which will be at an angle to the incident light corresponding to the magnetisation within the sample. Then, it is passed through an analyser which is set to near extinction for one magnetised state. This means that a photodiode, which reads small differences in the intensity of the light, will measure an increase in intensity as the magnetisation of the sample goes from one direction to the opposite. The photodiode converts the intensity into a current which is read by a lock-in amplifier as a voltage. This is usually done while a magnetic field is swept in order to see how the domains within the sample change. A schematic of the MOKE set up can be seen in Figure 4.7.[6; 140]

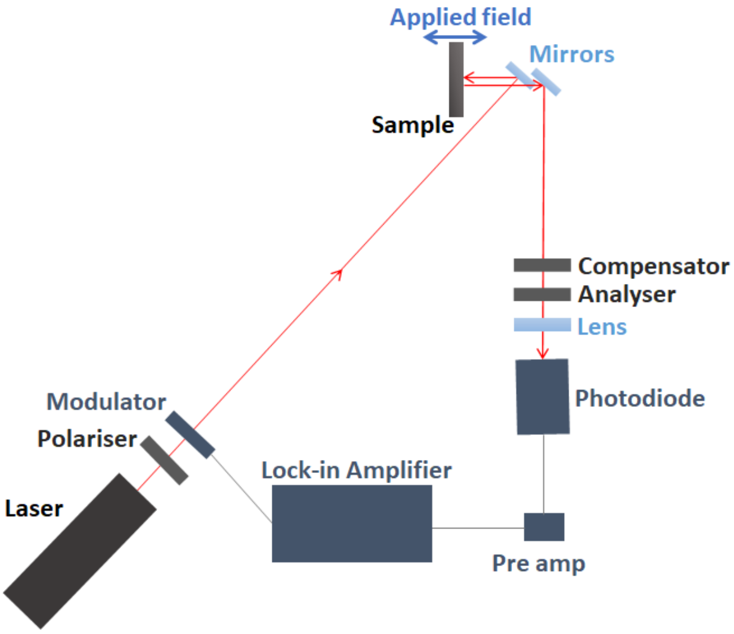

Figure 4.7: The set up for polar MOKE. A sample reflects polarised, modulated light from a HeNe laser. The light is modulated to allow the signal to be read by a lock-in amplifier, in order to reduce the signal to noise ratio. A lens is used to focus the laser onto the photodiode.

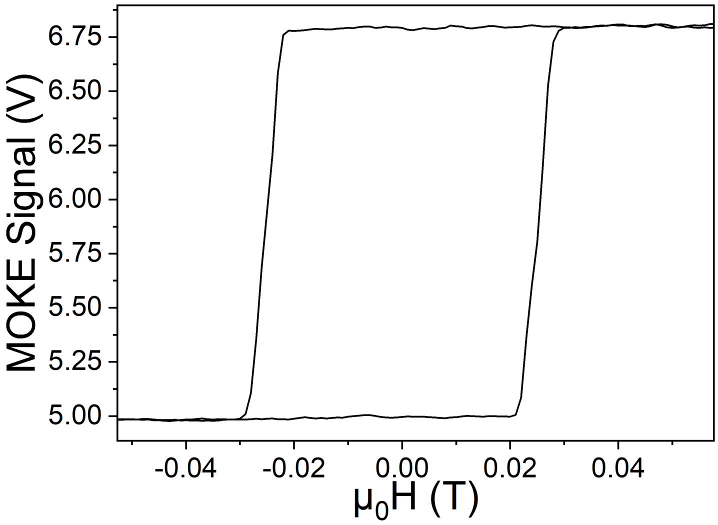

Figure 4.8: This figure shows a typical MOKE hysteresis of a Co multilayer PMA sample. The y-axis is arbitrary.

Longitudinal MOKE has the magnetic field across the plane of the sample, in this case, the laser is incident at a 60° angle from the sample. Polar MOKE, on the other hand, has the magnetic field perpendicular to the plane of the sample, the laser was set up to reflect at a right angle to the sample plane. The laser MOKE set up consisted of a HeNe laser with a power of less than 15 mW, a wavelength of 633 nm and a spatial resolution of up to 5 mm, and the position of incidence of the laser upon the sample could be altered using the mirrors. The applied magnetic field ranged between ±600 mT, from an iron pole piece electromagnet. The laser MOKE was used to measure the hysteresis loops of samples, the exact magnetic moment could not be determined from the measurements as the effect is not independent of factors such as surface angle of incidence, temperature and dielectric constants. It did, however, return information such as the coercivity and remanence, and in general confirm whether a sample exhibited PMA. A typical measurement of a PMA sample is shown in Figure 4.8.

4.5 Bubble Expansion Method

A Kerr microscope was also used, which harnesses MOKE techniques to observe domain orientation and how the domains behave under the influence of a magnetic field. This method focuses polarised light from an LED using an objective lens to observe an area of a sample under a microscope. Again, the light reflected from the sample is directed through an analyser and compensator, however this time, the magnetisation patterns are displayed as an image via a CCD camera. In the image, different domain orientations (spin-up or spin-down) are represented by lighter and darker areas. One method, provided by the Kerr microscope, to work out the DMI constant of a material is called a bubble expansion. This method uses the domain wall velocity of bubble domains experiencing an expansion in accordance to an increase in magnetic field strength to determine the material's DMI field. This DMI term is expresses as an effective IP field within the domain walls of a PMA magnetic multilayer, perpendicular to the wall direction.

The set up used for this method included an IP magnet, surrounding an OP coil magnet on which samples were placed (see Figure 4.9), both powered by Kepco power supplies. It was important that the sample was not tilted as angles from the IP field could cause an OP field component and reduce the symmetry of the measurement. This symmetry was ensured by repeatedly nucleating a bubble in positive and negative IP fields and ensuring the expansion was of the same distance in both. In this method, the domain walls follow the creep regime of motion, which was checked by ensuring the expansion of the bubble follows the creep law with increasing OP field. To do this the bubble was nucleated with OP field pulses of different magnitudes without an IP field, and fit to Equation 2.38. This experiment was performed with the microscope in polar mode and with a 20x magnification lens.

The basic technique of the bubble expansion measurements is as follows: the sample was first

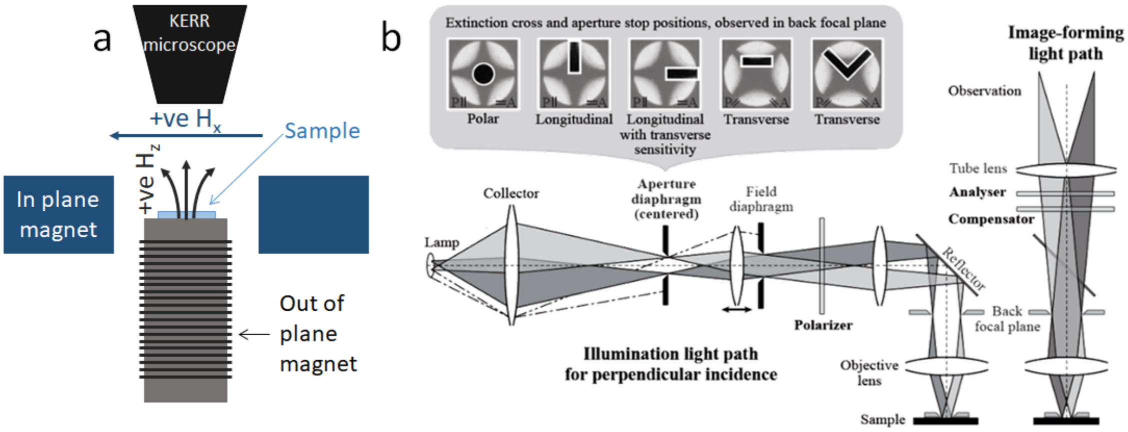

Figure 4.9: a) shows the magnet set up for the Kerr microscope for doing DMI bubble expansions. It includes both an OP magnet and an IP magnet. b) is a figure taken from Reference [141] showing the set up within the microscope itself and the path of the light to the sample. Then from the sample to the detector/observation point. The set up can switch between polar, longitudinal and transverse measurements by adjusting the aperture as shown in the inset.

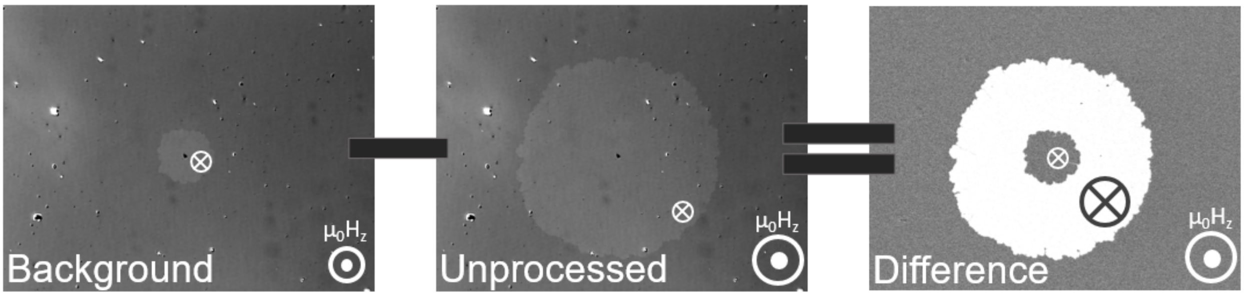

Figure 4.10: This figure first shows a small bubble made with an OP magnetic field pulse after putting the sample in a saturated state. The bubble was made into the sample plane surrounded by a domain pointing out of the plane. Then, it shows the same bubble with a larger OP magnetic field pulse (during a bubble expansion measurement, the larger bubble would be bias towards one side using an IP field - see Figure 4.11). The final image shows the difference between the first two images.

saturated by a negative field from the OP magnet. Then, a small circular-like domain was nucleated with a positive field pulse from the OP magnet. The bubble had to be almost exactly reproducible in diameter and not interact with other bubbles. The image of this initial bubble was stored as the background image. This bubble nucleation was repeated, however, with an IP field set which caused the bubble to expand with the direction of the IP field when the OP magnet was pulsed (unprocessed image). The image of the small circular-like domain was then subtracted from the image of the newly expanded bubble in order to get an accurate measurement of the difference in distance that the bubble expands with the IP field (difference image). Details of this are shown in Figure 4.10, typical bubble growths are by tens of micrometers.

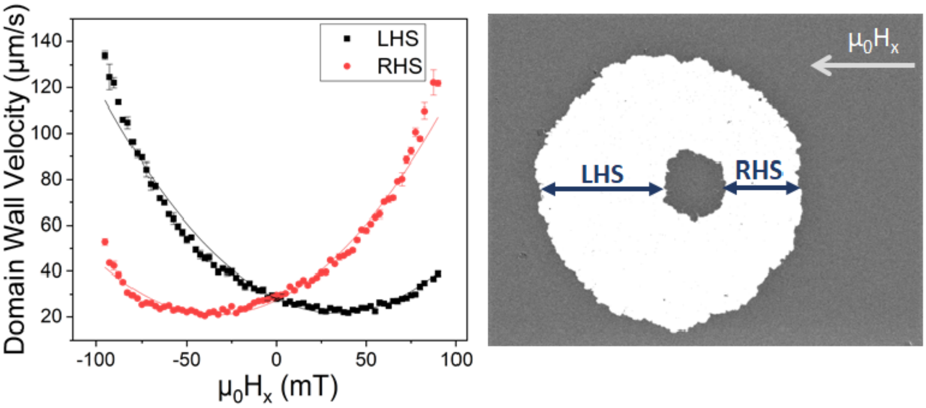

Figure 4.11: This figure shows a graph of the domain wall velocity against the IP magnetic field for a left handed Néel wall. The LHS and RHS curves come from taking the change in distance on the LHS and RHS of the bubble as shown by the example bubble on the right from a measurement. The curve are fitted with a Gaussian fit to determine the minima.

This process was repeated with increasing IP fields in the positive and negative x-directions causing the bubble to increasingly expand. Its progress was tracked using a code which worked out the velocity of the domain wall on the left hand side (LHS) and the right hand side (RHS) of the bubble by doing a simple velocity=distance/time calculation with the distance the bubble travels and the OP pulse length. This sweep of the IP field can be done with various different pulse lengths and OP fields. The DMI field can be evaluated by examining the changes in domain wall velocity with the different strengths of applied IP bias field.

A plot of the IP field vs. bubble velocity was made and fitted with a Gaussian curve, as shown in Figure 4.11. The DMI field is the opposite sign of the IP field at the point in which the velocity of the domain wall is at a minimum, it is the point at which the IP field and the DMI field cancel each other out. As the wall on the LHS of the bubble and the RHS have oppositely faced DMI fields in both Néel chiralities (Figure 4.12), the minimum velocity of each side of the bubble was at the same IP field magnitude, but of opposite sign. Therefore, the sign of the DMI field determines

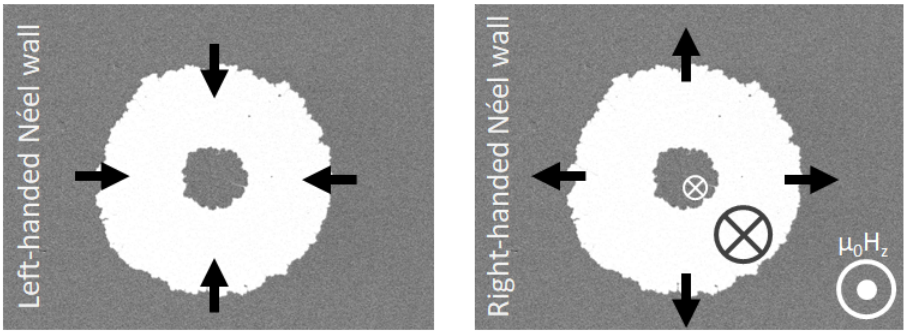

Figure 4.12: This figure shows how the DMI field direction differs in domain walls of left handed and right handed bubbles.

whether the Néel wall has left or right handed chirality.

For example: if the plot of wall velocity vs. IP field had a minimum at a negative IP field for the LHS bubble wall, the DMI field would be in the positive x-direction and the bubble walls will have left handed chirality. This is important as in a stack such as FM/HM, different heavy metals invoke different domain wall chirality, such as Pt and Ir.[142–145] The magnitude of the DMI field in this thesis came from averaging the velocity minima for the LHS and RHS of the bubble, and it was assigned that left handed Néel walls have a negative DMI field and right handed Néel walls have a positive DMI field.[36; 146; 147]

4.6 Magnetic Force Microscopy

Magnetic force microscopy, or MFM is another technique used to image domains. The principle behind it came from atomic force microscopy (AFM), which is a scanning probe microscopy technique used to map out a surface. These scanning probe methods involve a laser being reflected from a cantilever onto a photodiode. As the cantilever changes height due to the sample, the laser is reflected onto a different part of a four quadrant photodiode so that when properly calibrated, a profile of the sample is produced, see Figure 4.13. For MFM, a magnetic tip is attached to the cantilever, this allows the cantilever to be controlled by the magnetic fields from a sample. The cantilever is often placed on a piezoelectric stage in order to move around the sample. The tip is typically placed between 10 and 100 nm from the sample so that the stray field is observed and a resolution of up to 20 nm can be observed. When a magnetic tip probes the flat surface of a ferromagnet, it encounters the magnetic force, but also Van-der-Waals forces, hence both contribute to the returned signal and must be separated. The Van-der-Waals forces are more dominant when the tip is closer to the sample's surface, and the stray field forces dominate when the tip is further away. The tip scans first whilst closer to the surface in order to record the sample topography. Then, the tip is moved further away to the point at which it receives a strong magnetic signal and repeats the scan whilst following the surface topology to observe the phase shift from the magnetic forces - this is called the dual pass technique.[148–152]

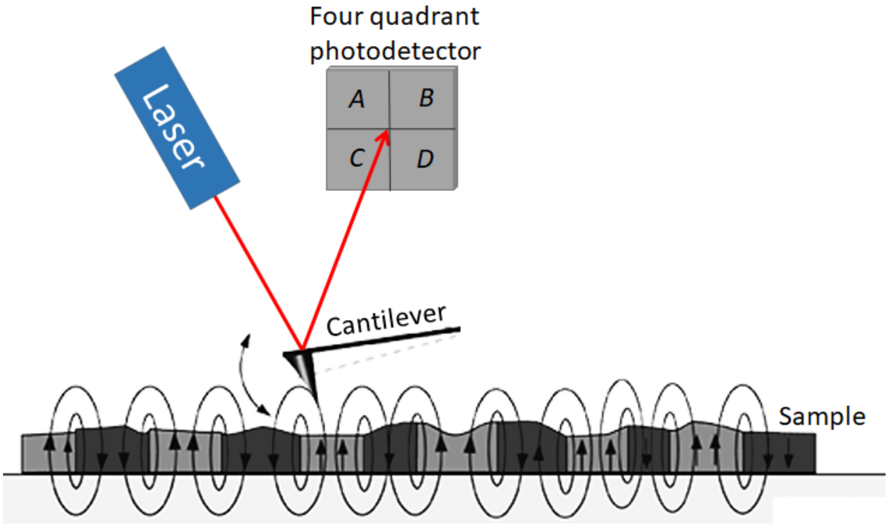

Figure 4.13: A schematic showing a cantilever incident on a sample with magnetic domains represented by the darker and lighter patches in the sample. The tip on the cantilever gets deflected by the stray fields and the deflections are monitored via the reflections of a laser onto a photodetector. This figure is adapted from Reference [153].

MFM has two main modes for scanning: constant height mode and vibration mode. In constant height mode, the tip remains at the same height with respect to the topography throughout the scan, this is restricted to samples with minimal roughness. In vibration mode, the cantilever is set to resonate at a certain frequency using a phase locked loop, so the change in resonant frequency reflects the magnetic force gradient of the sample. This is due to a the spring constant being altered by the magnetic force from the samples surface. Attention is paid to the orientation of magnetisation of the tip, when the tip magnetisation opposes the samples domain magnetisation the resonance frequency decreases which results in a darker area on the image.

4.7 Electrical Transport Measurements

Electrical transport measurements were performed at room temperature to determine magnetoresistive and Hall effects within both FM and SAF, PMA samples. The measurements took place with the configurations shown in Figure 4.14 (and one measurement as 4.14b, but with a rectangular sheet film instead of a Hall bar). In 4.14a and b, electrical connections were made by wirebonding the Hall bar contacts onto a pad on a sample mounting head, which was connected to a breakout box. This set up allowed measurements in configuration 4.14a and b to be done simultaneously as the breakout box could connect different pads to different instruments: a current source and two voltmeters. The NI LabVIEW^{TM} software controlled the measurements and calculated the corresponding longitudinal (R$_{xx}$) and transverse resistance (R$_{xy}$) from the configuration in Figure 4.14a and b, respectively. A magnetic field could also be set up in either the z-axis, allowing OP field sweeps as the resistance was measured, or the x-axis, to perform IP field measurements. These measurements were performed at the University of Leeds.

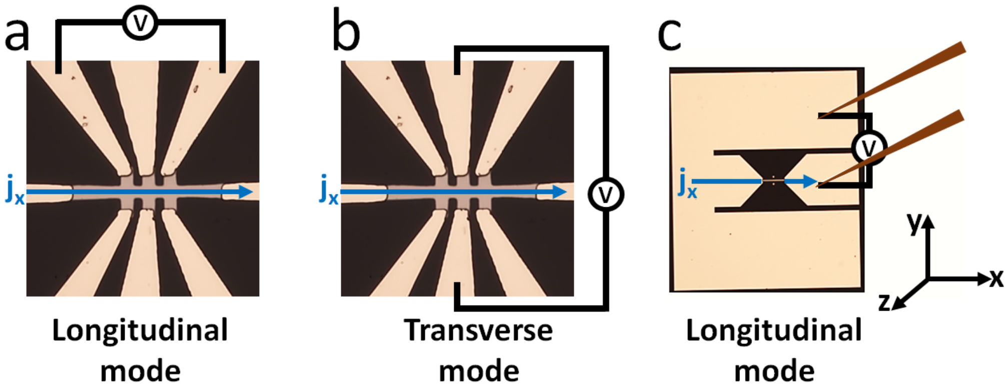

Figure 4.14: a) and b) show a nanofabricated Hall bar made from magnetic material, with gold contacts. a) shows the electrical configuration to perform longitudinal resistance measurements and b) shows the electrical configuration to perform transverse resistance measurements. These devices were used at the University of Leeds. c) shows a different nanofabricated device, with a rectangular area of FM material, which can also measure the longitudinal resistance. This was carried out using probes with two separate electrical components to supply current and measure voltage, j$_x$ shows the current path. This device was used at Northwestern University, Illinois.

Figure 4.14c, shows a different set up to measure the longitudinal resistance, which was used at Northwestern University, Illinois. Instead of wire bonding to a Hall bar, it used a small bar of magnetic material with gold contacts on either side of it. The contacts were connected to the hardware by placing a probe on each contact which contained two separate electrical connections, one for supplying a current, and one for measuring a voltage. This set up was also equipped with an IP or OP magnetic field.

When performing longitudinal measurements as a function of magnetic field, magnetoresistive effects are observed. When performing measurements in transverse mode, the resistance reflects the Hall effects present.

4.8 Terahertz Time Domain Spectroscopy

In this thesis, on-chip waveguides were used to allow for strong confinement of the THz signal. A nanofabrication method to create these devices was already well defined and practised.[5] The

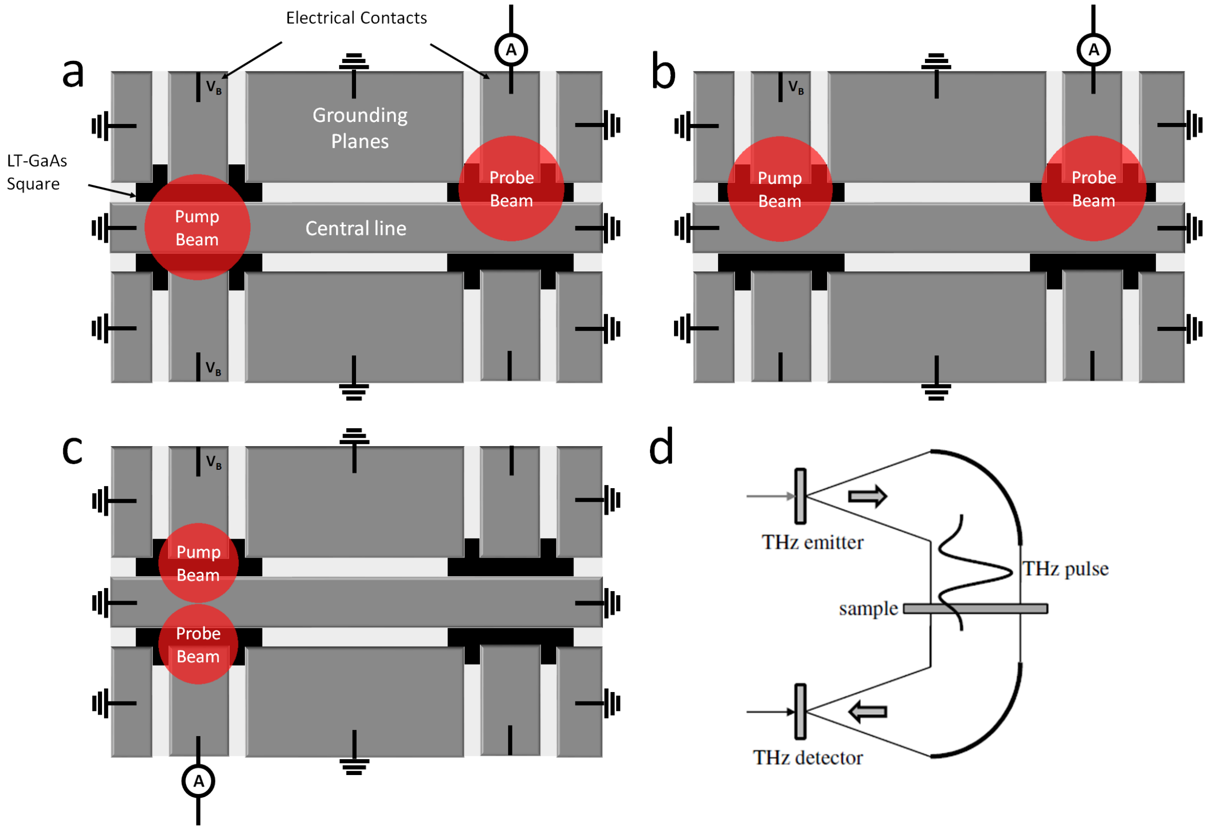

Figure 4.15: a) shows a coplanar waveguide which has a pump beam and probe beam. The THz waves emitted at the pump beam get coupled to the waveguide's central line and driven towards the detector (probe beam). The ammeter represents a lock-in amplifier configured to measure the current and V_B represents the voltage bias. The areas where the lasers cover the gap between the central line and the electrical contacts (dark grey) are referred to as the optical switches. Measurements made in this configuration are called coplanar mode. b) shows the configuration for slotline mode. c) shows the configuration for input mode. d) shows an example of how free space THz measurements are set up with a laser incident upon a THz emitter and detector, with an area where the THz waves are directed through a sample in free space.[119]

basic principle of on-chip THz-TDS measurements is the process of producing, transmitting and then measuring the THz response.[154] For the production of THz radiation, a photoconductive (PC, in this case LT-GaAs) material is placed in a gap between two electrical contacts (in this case one electrical contact is the central line), across which a DC voltage bias is applied. When light of energy sufficient to exceed the bandgap hits the gap (pump beam), electrons in the photoconductor are excited from the valence band into the conduction band resulting in a current, hence it being called a photoconductive switch. If the laser has a femtosecond optical pulse, it causes a picosecond current pulse due to limitations in the carrier generation and recombination lifetimes. The acceleration of carriers by the DC bias behaves like an antenna and produces THz radiation. In normal circumstances, the THz radiation would propagate in all directions, so to guide the THz waves through a sample material and towards a detector, a coplanar waveguide is used (see Figure 4.15a). Another example of TDS measurements is free space THz, which uses a spherical mirror to guide the THz pulse through a sample (see Figure 4.15d).

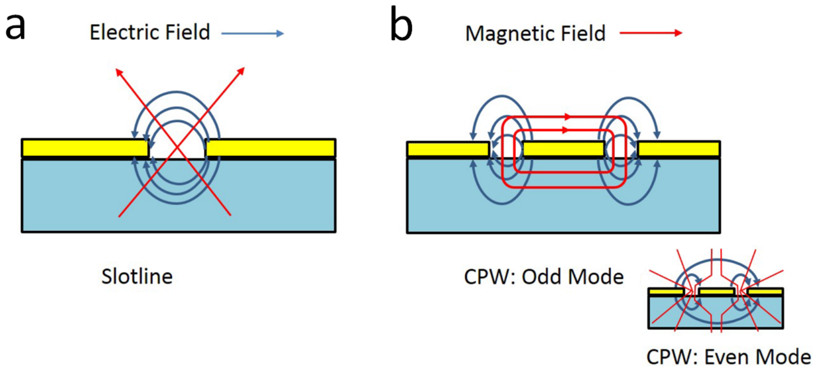

Figure 4.16: a) shows the planar waveguide for THz transmission in slotline mode, indicating the magnetic and electric field lines. b) shows coplanar waveguide in odd mode, even mode in the inset. This figure was adapted from Reference [5].

On the CPW, the detector consists of an identical photoconductor-gap (switch) set up but without a DC bias. If a femtosecond laser pulse hits the detector (probe beam), the electrons are excited, however, without the DC bias they are accelerated by incoming THz radiation. Therefore, when a THz pulse hits the detector at the same time as the optical pulse, a voltage is measured. If the time at which the probe beam hits with respect to the pump beam is gradually changed, it is possible to sweep across the waveform of the THz pulse. This is because the voltage that is measured will be proportional to the amplitude of the THz pulse during the detection. From measurement data obtained in time resolved space, the waveform can be mapped in frequency resolved space using a fast Fourier transform (FFT). This provides information about the bandwidth and any features within it due to the sample. For example, a dip can occur when the THz radiation is absorbed, or a peak can be generated by resonance effects. Three modes of measurements are possible on this waveguide design: coplanar mode, slotline mode and input mode. Coplanar mode (odd) is demonstrated in Figure 4.15a, it places the pump beam and DC bias over two switches on the same LT-GaAs square, and the probe beam on one switch on the other LT-GaAs square. Figure 4.15b shows the laser positions during slotline mode which has the pump beam on only one switch, however, still gathers information about transmitted THz pulse along the central line. Both slotline and CPW had strong surface field confinement, see Figure 4.16, compared to other waveguides/modes, such as microstrip and planar Goubau line. Figure 4.15c shows the laser positioning during input mode, this mode measures the THz pulse at the same point that it is generated, therefore the pump beam and the probe beam are on switches on the same LT-GaAs square. This means THz wave will have propagated hardly at all, resulting in a higher current amplitude due to less energy being lost during propagation and acts as a good reference signal.[5; 119]

4.9 Coplanar Waveguide Fabrication

The fabrication of a CPW starts with a bilayer grown by molecular beam epitaxy (MBE): 350 nm of LT-GaAs on top of 100 nm of aluminium arsenide (AlAs), on a semi-insulating GaAs substrate. LT-GaAs was used as the photoconductive switch since it has a short carrier lifetime and can generate picosecond pulses. It was grown at a relative 'low temperature' of 205°C in an arsenic atmosphere to allow defect sites to form in the GaAs from excess arsenic. These defect sites are trapping regions during carrier recombination and are the cause of the short carrier lifetime.[5] The stack was then annealed at 550°C for 15 minutes in a nitrogen atmosphere in order to increase the LT-GaAs resistivity. The next step was to melt a small piece of mounting wax, called Apiezon wax W (black wax), in an oval-like shape onto the surface of the LT-GaAs without it touching the edges. The black wax was used as it is etch resistant, which is necessary for the next step; to etch the LT-GaAs into the same oval-like shape using sulfuric acid, hydrogen peroxide and deionised (DI) water (H_2SO_4:H_2O_2:H_2O, 1:40:80) for 3-4 minutes. Following this, a slow hydrofluoric acid etch (HF:H_2O, 1:9) over 24 hours at 3°C was done to remove the AlAs and separate the LT-GaAs with the black wax. The HF solution was then diluted and the LT-GaAs/black wax was left floating in a beaker of DI-water, from which it could be picked up using a vacuum probe and placed on a new quartz substrate. The LT-GaAs was left on the quartz for around 7 days to allow for Van-der-Waals bonding between them. Then, the black wax was removed from the LT-GaAs with trichloroethylene. To ensure no water remained and to improve the adhesion, the LT-GaAs on quartz was placed into a vacuum oven for 15 hours at 250°C.

The first lithography step was to remove areas of the LT-GaAs so that only two squares remained on the quartz substrate, to act as the two PC switches. Positive resist, S1805, was spun onto the sample, then it was baked at 115°C for 2 minutes. Mask-less lithography was used for the exposure,

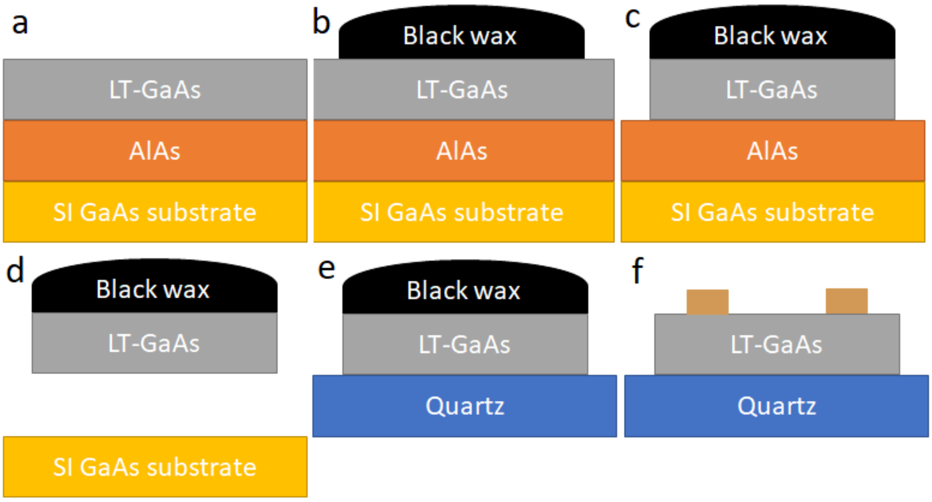

Figure 4.17: a) shows the original bilayer and substrate. b) shows after black wax is melted on the LT-GaAs. c) shows after a sulfuric acid etch removed edges of the LT-GaAs, making it the same ovular shape as the black wax. d) shows after an HF etch removed the layer of AlAs. e) shows the LT-GaAs and black wax placed on a quartz substrate. f) shows after the black wax is removed and two squares of resist are placed on top of the LT-GaAs.

ultra-violet light is exposed to the areas where the resist should be removed and this caused the resist to change chemically and become more soluble in ‘developers’ such as MF-351 (4:1 with water). In this case, it removed the resist from all areas, except for two squares of LT-GaAs, in 30 seconds.[5] Then a ‘slow’ sulfuric acid etch (H_2SO_4:H_2O_2:H_2O, 1:8:950) of 10 minutes was performed to remove all of the LT-GaAs but the two squares - this was confirmed visually via a microscope. Samples were then placed in acetone for 3 minutes to remove the remaining resist. The lithography process was repeated, however, this time with the waveguide design exposed to the UV light to remove the resist for the waveguide material to be deposited. The only difference in this case was prior to using the MF-351 developer, samples were placed in chlorobenzene for 2 minutes in order to harden the resist to invoke undercuts which allow for better metal deposition. The central line, electrical contacts, and grounding plane were all made by depositing Ti(5 nm)/Au(150 nm) by e-beam evaporation. Acetone was used for the ‘lift-off’ of the excess Ti/Au material which was deposited on top of the resist. This was the original design of the CPW, as can be seen in Figure 4.18g, however, for the experiments in this thesis, the central line of the waveguide was tapered down to a small Hall bar in its centre (second design, see Figure 4.18h, i, j). This meant a separate lithography step to deposit multilayers of Co or CoB with Ir and Pt via sputtering. Then, the rest of the waveguide (all but the Hall bar) was made from Ti/Au deposited in a third lithography process. Following this, samples were wire bonded for THz-TDS measurements.

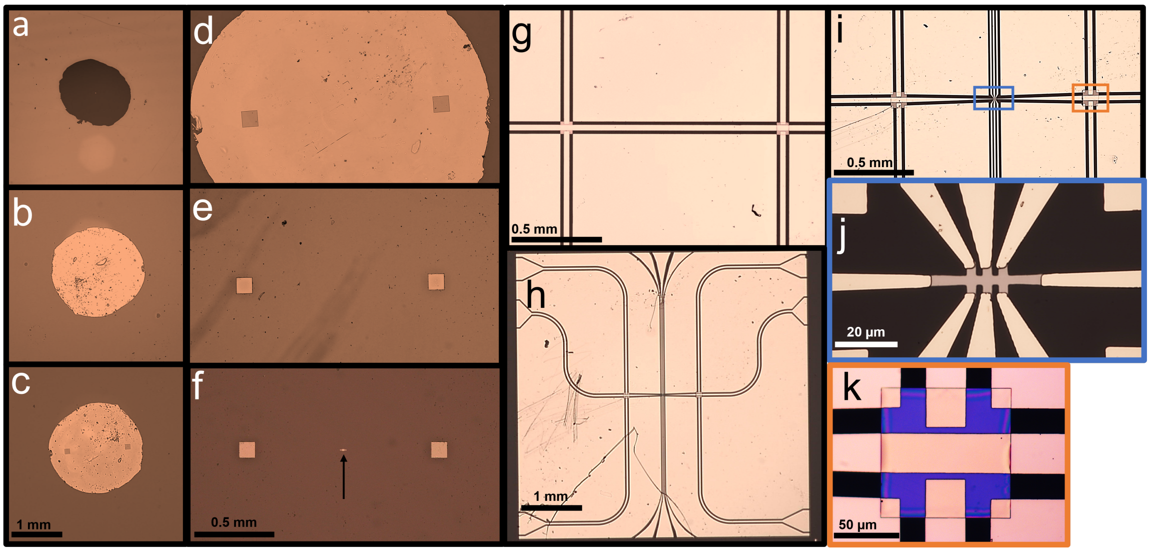

Figure 4.18: a) shows an oval-like shape of black wax on quartz. On the underside of the black wax was a 350 nm layer of LT-GaAs. b) shows the LT-GaAs once the black wax is removed. c) shows two squares of resist on the LT-GaAs. d) shows a zoomed in version of c). e) shows the two squares of LT-GaAs after the sulphuric etch. f) shows the two squares of LT-GaAs with a Hall bar of deposited magnetic multilayer in the centre. g) shows a zoomed in image of the original design, a non-tapered Ti/Au CPW. h) shows an image of whole CPW with the second design, including tapering and magnetic Hall bar in the centre. i) shows a zoomed in version of the centre of h). j) shows a zoomed in image of the Hall bar made from magnetic material in i). k) shows a zoomed in version of an LT-GaAs square with contacts patterned over it.

4.10 THz-TDS on Optical Bench

The principles of THz-TDS measurements have been explained; experimentally, this can be set up in a system as shown in Figure 4.19. The laser source used was a Ti-Sapphire laser since its 80 MHz repetition rate caused 100 femtosecond pulses, and central wavelength of 800 nm meant it was compatible with LT-GaAs (since the laser energy is larger than its band gap of 1.4 eV).[5] After leaving the laser source, the light was passed through a beam splitter, creating what was defined as the 'pump beam' and the 'probe beam'. The pump beam was directed straight towards the sample and caused the generation of the THz radiation. The probe beam path included a delay stage and an optical chopper and was used for the detection of the THz signal. The delay stage consisted of a movable retroreflector in order to alter the time at which the probe beam arrived at the sample with respect to the pump beam, i.e. to control the time resolved aspect of the measurement. The optical chopper was set to a specific frequency (1545 Hz) to allow the lock-in amplifier to focus on the signal with this oscillation, resulting in a signal with less noise. An OP magnet was also placed behind the sample with a controllable field for field dependent measurements.

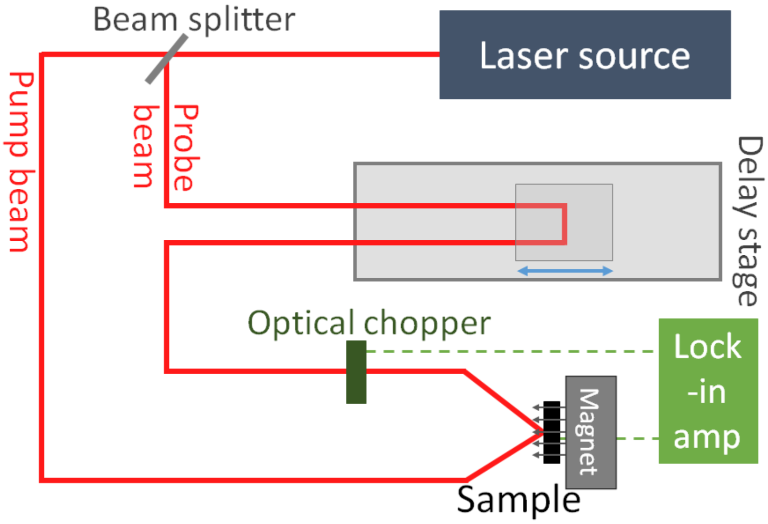

Figure 4.19: This shows a simplified version of the optical bench set up required to make on-chip THz measurements with coplanar waveguides.

CHAPTER 5

Magnetic Proximity Effects at the Ferromagnetic/Non-magnetic Interface

5.1 Introduction

Before experimenting with different types of structures of magnetic multilayers, it was paramount to understand how the interfaces of these structures work. Since magnetic proximity effects (MPE) at ferromagnetic/non-magnetic interfaces were realised there have been various studies using different methods, designed to pin-point how these effects can have an effect on different materials and magnetic structures. The effects refer to when two materials (FM and NM) that share an interface affect each other on an atomic level, leading to induced moments or magnetically dead layers (DL, i.e. a paramagnetic region) at the interface. These studies have one thing in common - they tend to disagree with each other. This is due to these interactions taking place at an atomic level, the magnetic properties are intricately linked to the electronic structure and the effects can have a dependence on numerous factors within a system. This includes the size/thickness of the materials used, the saturation magnetisation of the FM, the orientation of the interface (FM/NM or NM/FM), the lattice structure, and the interfacial roughness. For many experiments with magnetic thin films, it's important to consider these interfacial effects (which isn't always done [40; 155]), particularly as they can have a substantial effect on the value of the measured saturation magnetisation of a system, which in turn could affect the measured anisotropy, or DMI constant. It is also vital for research involving systems used to do spin-orbit torque experiments or spin current detection.[156] In this thesis, three main NM materials were used at the interface with a FM; Ta, Pt and Ir, therefore, the literature with proximity effects for these materials was reviewed and compared to our own results.

5.2 Measurement Techniques

There are three main ways used within literature to make estimations for induced moments or DL thicknesses: measuring the thickness dependence of the magnetic moment of the FM using a SQUID/VSM, x-ray magnetic circular dichroism (XMCD) and x-ray resonant magnetic reflectivity (XRMR).

5.2.1 VSM Method

The method using VSM involves growing a sample set with a range of FM thicknesses, sandwiched by specific non-magnetic materials at a set thickness (e.g. Pt(20 Å)/Co(x)/Pt(20 Å) where x is a range between 5 Å and 200 Å). These samples are measured using a SQUID/VSM, and the FM thickness vs. the measured moment/sample area is plotted and fitted with a straight line. This fit determines three key pieces of information: if the line fit crosses x-axis before zero, it indicates that an area of the FM is magnetically dead, and the value signifies the total thickness of the DL within the whole sample. Alternatively, the line may cross the x-axis at a negative value, and therefore cross the y-axis at a positive value. This value on the y-axis represents the total induced moment/area in the sample. Therefore, the gradient of the line represents the saturation magnetisation of the FM material regardless of the interfacial effects. This method is therefore able to probe DL thicknesses and induced moments at FM/NM interfaces, and does not require a synchrotron radiation facility. However, this method does not take into account that the top and bottom interfaces may have different DL thicknesses or induced moments, nor can it estimate the length scale (decay length) of the induced moments within the NM.

5.2.2 XMCD

XMCD, on the other hand, is a version of X-ray absorption spectroscopy which allows interface specific measurements of induced moments. It uses the difference between left and right circularly polarised light incident upon a sample to obtain the spin and orbital moments of a specific element.[157] The incident light gives enough energy to excite electrons, for example, from the p levels (L edges) into the unoccupied d level. The measured signal intensity (absorption spectra) at the particular photon energies, can be associated to the unoccupied d states. Due to an imbalance in up and down spins, the difference in the signals from the right circularly polarised and the left circularly polarised light can be used with the sum rules [158; 159] to calculate an average orbital and magnetic moment for a specific element. Simply, the transitions from the majority and minority spin states at the Fermi level have probabilities which are related to the difference in density of states between the levels, which is correlated to the magnetic moment of the atoms.[160] Although an induced magnetic moment for a specific material at a specific interface can be determined, it gives an average moment over the volume of material. However, for induced moments in a NM, the magnetisation may not be spread across the whole volume and instead reduce exponentially from the interface. This limits the techniques ability to measure an outright moment and polarisation depth profile without creating a thickness series, varying the thickness of the NM.[161–164] This method, however, is only valid assuming the NM induced moments depend solely on the distance from the FM interface, not on the thickness of the NM.[165] The sum rules used in this method are also based on multiple assumptions which may not be valid in every case.[157; 165; 166]

5.2.3 XRMR

A third technique used is XRMR, which allows for depth specific probing of elements within a sample. It changes the angle at which the circularly polarised light is incident upon the sample, combining XRR and XMCD. As with XRR, the momentum transfer and scattering occur within the sample, plus the XMCD response which is observable in the light reflected from the interfaces, allows both structural and magnetic properties to be extracted. When spins have different magnetisation directions, this causes a slight change in the optical constants of the material; this means that

XRR measurements of the spin polarised interface with circularly polarised light will be slightly different (i.e. asymmetric). Importantly, the results are independent of the layer thicknesses as the main signals arise from the interfaces. [161; 167–171] However, compared to the sum rules used when performing XMCD, additional measurements or calculations are needed to define the spin moment quantitatively. For example, Klewe et al. compared three different models to find the spin polarisation of Pt.[171] The XRMR technique was compared by Graulich et al. to XMCD, for the purpose of detecting the MPE. They found the quantitative results to be in good agreement, proving XRMR to be a reliable method to measure induced magnetic moments.[156]

5.3 Origins of the MPE

When atoms are close to each other, their electronic bands can overlap and this causes hybridisation between the atoms. This can be to various degrees based on the proportions of the band overlap. At an interface where a FM material meets a NM, different types of effects can occur due to the hybridisation between the different elements (e.g. PMA, DMI). One effect of the hybridisation at the interface, for example between the NM 5d band of Ta, Pt or Ir and the 3d band of ferromagnets Co, Fe or Ni, is spin polarisation in the NM, i.e. an induced moment. This polarisation can extend from the interface to several atomic layers, and it tends to occur with heavy metals which are close to the Stoner criterion with a high susceptibility. It has also been demonstrated that there is another effect at FM/NM interfaces; a suppression (dead layers)/reduction of the magnetic moments of the FM at the interface, which also occurs from hybridisation of the FM and NM parts.[30; 31] When these effects occur via two elements meeting at an interface, it is often described as interfacial ‘alloying’ or ‘intermixing’ and can be enhanced by properties such as, higher interfacial roughness, or with different lattice structures.[172] In this chapter, these effects are explored in thin films with PMA.

5.4 Pt Proximity Effects

5.4.1 Nickel

A dead layer/reduction was shown by multiple groups at Ni/Pt interfaces.[164; 173–175] Kim et al. showed a magnetic dead layer in Ni/Pt multilayers found using SQUID magnetometry, which gives a sum of all the combined effects in a sample. They further investigated whether the effect was a consequence of intermixing Ni and Pt at the interface by growing one sample rougher than another, they found no correlation between intermixing and the existence of dead layers.[175] Although, as suggested by Poulopoulos et al., perhaps there isn’t significant intermixing at the Ni/Pt interface.[164] Shin et al. also demonstrated a two atomic layer magnetic dead zone using the VSM method in Ni/Pt samples, suggested to be due to a suppression of Ni moments caused by sp-d hybridisation.[173] On the other hand, only a reduction of Ni moment at the interface measured by XMCD was presented by Wilhelm et al., noting that for thin Ni layers, a thicker Pt layer resulted in a stronger reduction of the Ni magnetic moments.[174] Poulopoulos et al. confirmed this trend with XMCD and the absence of a fully magnetically dead layer at Ni/Pt interfaces. Their samples with only two monolayers (ML), equivalent to ∼ 7 Å, of Ni still showed a magnetic moment which would not be the case if a dead layer were present. They also alleged that the reduction in interface Ni moments was due to alloying between the Ni and Pt.[164] Then, Kim et al. provided proof of a 5.7 Å magnetic dead layer at room temperature at the Ni/Pt interface via magnetic circular dichroism and SQUID measurements, as no moment was found on the Ni atoms for Ni thicknesses less than 6.6 Å, counteracting the measurements of Poulopoulos et al. and Wilhelm et al.. They attributed the dead layers to 3d-5d hybridisation between the Ni and Pt, which caused a reduction in the exchange splitting.[176]

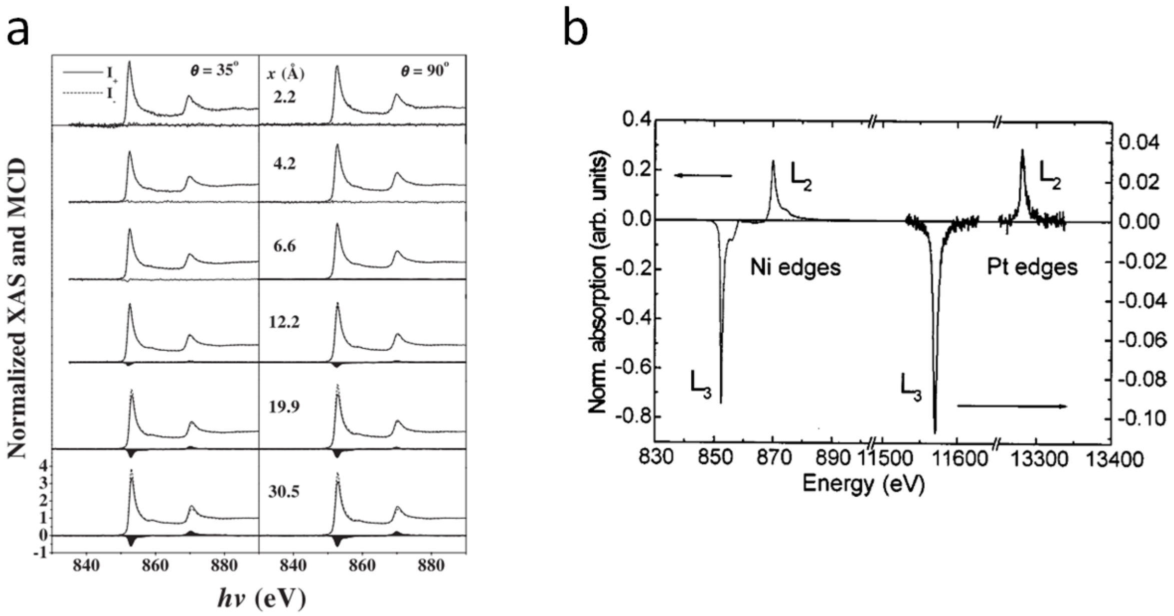

Figure 5.1: a) shows the magnetic circular dichroism results of Kim et al. for [Ni(x)/Pt(4.5 Å)]$_{\times 30}$/Pt(30 Å), showing the Ni absorption spectra for all Ni thicknesses at room temperature, proving no magnetic circular dichroism signal below 6.6 Å.[176] b) shows the XMCD spectra results at 10 K from Poulopoulos et al. for Ni and Pt in a Ni(2 Å)/Pt(2 Å) multilayer, showing a moment in both the Ni and the Pt.[164]

The cause of this could have stemmed from different growth methods, the dead layers were found in sputtered multilayers, which involves higher adatom energetics, as opposed to multilayers deposited by e-beam evaporation.[177] Kim et al., however, stated that it is not guaranteed that there is more interfacial alloying in sputter grown samples compared to e-beam grown, though magnetic dead layers may arise from interfacial alloying in the thinnest Ni films.[176] Furthermore, the samples showing a dead layer had smaller Pt thicknesses than the samples showing a reduced Ni moment and induced Pt moment, as can be seen in Figure 5.2a, which could be a root of the discrepancies seen. The final difference was that the reduced Ni moment samples were measured by XMCD at 10 K, whereas the dead layer samples were measured at room temperature. This could be significant as the Curie temperature of an NiPt alloy is below room temperature, plus, the Ni moment is lower at room temperature.[175]

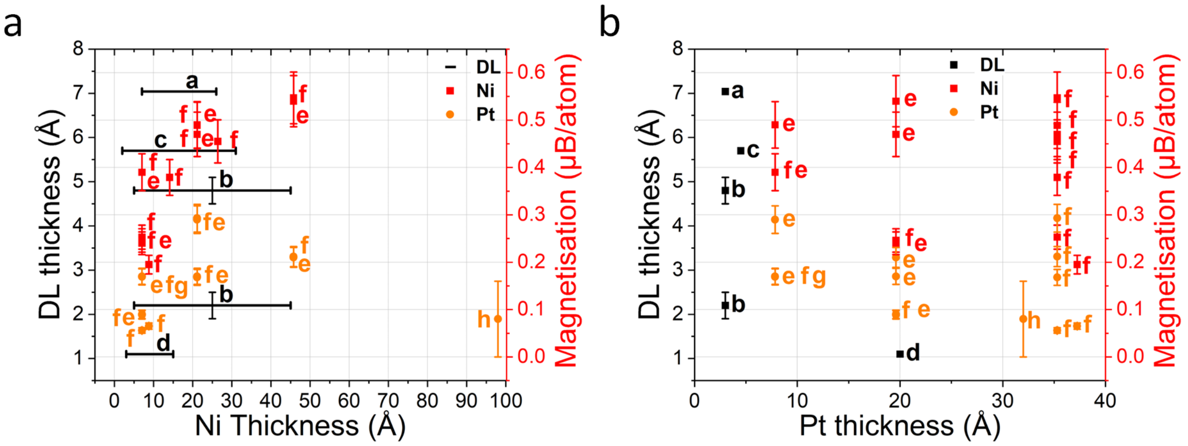

Figure 5.2: a) and b) show both reported induced moments and reported dead layer thicknesses for Ni/Pt interfaces in multilayers, plotted against the Ni thickness (a) and Pt thicknesses (b). The references are as follows: a-[173], b-[175], c-[176], d-[178], e-[174], f-[164], g-[179], h-[171]. The dead layer samples were all grown via sputtering and measured using the VSM method at room temperature, hence the range of Ni thicknesses in (a). For the magnetisation values, they were all grown via e-beam evaporation and measured via XMCD, except Reference h, which was grown via sputtering and measured with XRMR at room temperature. The samples from Reference d contains Co as well as Ni for the FM. For Reference b, the thicker dead layer sample was grown with a lower growth chamber pressure.

As can be seen in Figure 5.2a, the thickness of the Ni tends to decrease with the Ni magnetic moment, and the Pt moment follows a similar trend, this trend holds true for all the considered Pt thicknesses. Klewe et al. also back up this by showing that as the moment in the FM increases (in this case, by increasing the Fe to Ni content in a FM alloy), the Pt moment increases.[171] The outlier in terms of magnetisation magnitude was from h-[171], the only sample measured using XRMR, showed a much lower Pt magnetic moment of (0.08±0.08) μ_B/atom. This was, however, performed at room temperature, as opposed to 10 K, which could partially account for the differences between the results in References [164; 174; 179]. However, XMCD predictions tend to be underestimated compared to XRMR predicted moments.[156] The only other difference is that the Ni thickness is much larger than all other samples considered.[171] The DL thicknesses vary considerably over similar Ni ranges. The smallest DL thickness (d) used only a small thickness range between 0 and 15 Å which could lead to an inaccurate value, however, this sample also included Co with the Ni and a higher Pt thickness than the other samples, which could be the cause of a smaller DL thickness. From Reference b-[175], it was displayed that a change in the sample growth chamber pressure can have an effect on the DL thickness.

Little trend appeared in the Ni moments as a function of Pt thickness, shown in Figure 5.2b. For each Pt thickness, the Ni moments showed a range of values, as do the DL thicknesses for similar Pt thicknesses. From the XMCD experiments, Wilhelm et al. and Poulopoulos et al. also showed that the Pt at the interface had induced magnetic moments, which decreased with increasing Pt thickness, supporting the localisation of the moments at the interface due to XMCD measurements presenting an average moment over the whole Pt layer.[164; 174; 180] All of these Ni moments are less than the bulk moment of 0.61 μ_B/atom, though Ni thicknesses didn't go beyond 50 Å.[164; 174; 181] Poulopoulos et al. claim that the Pt moments in Ni/Pt samples are comparable to the Pt moments within an alloy of NiPt, however, the Ni moments exhibit a larger reduction in alloys than in multilayers.[164] A Co impurity in bulk Pd would have over 200 neighbouring Pd atoms to polarise, resulting in a giant magnetic moment.[182] Despite a lot of different conclusions and methods, a few patterns can be drawn from the data. It is likely that there is an induced moment in the Pt and also that the Ni has an interfacial moment reduction, as these combined effects could result in an overall dead layer via the VSM method, allowing the literature to agree somewhat, especially when one considers the measurement temperature differences.

To summarise the above trends for proximity effects at Ni/Pt interfaces:

- The VSM method always found an interfacial dead layer.
- XMCD always found a reduction of the moments of Ni at the interface and induced Pt moments.
- Room temperature measurements tended to find lower moments/dead layers compared to those at 10 K.
- Both Ni and Pt moments increased with Ni thickness, irrespective of the Pt thickness, suggesting a link between the Ni and Pt moments.
- As an average, the dead layer thickness was (4±2) Å, the induced Pt magnetisation was (0.15±0.07) μ_B/atom, and the Ni magnetisation at the interface was (0.4±0.1) μ_B/atom.

5.4.2 Iron

Studies on the proximity effects at a Fe/Pt interface displayed relatively consistent results for the induced moment in the Pt. Antel et al. investigated the changes when a sputter grown (001)

Fe/Pt multilayer is in a BCT (1-4 Å) or FCT phase (>4 Å), to advocate the importance of Pt contributions to magnetometry data and volume and surface anisotropy. They found from XMCD measurements that the Fe moments were 10% over the bulk value (2.15 μ_B/atom) in the BCT phase, and 10-20% under the bulk value in the FCT phase, see Figure 5.3a. The Pt moments, on the other hand, showed an almost constant moment of 0.5 μ_B/atom between 2-10 Å of Pt, which included both lattice phases, see Figure 5.3b. The sample with 0.9 Å of Pt showed a much lower moment of 0.36 μ_B/atom, comparable to FePt alloys, therefore it was suggested that at this Pt thickness, the sample is considered more as a FePt alloy separated by Fe layers.[183]

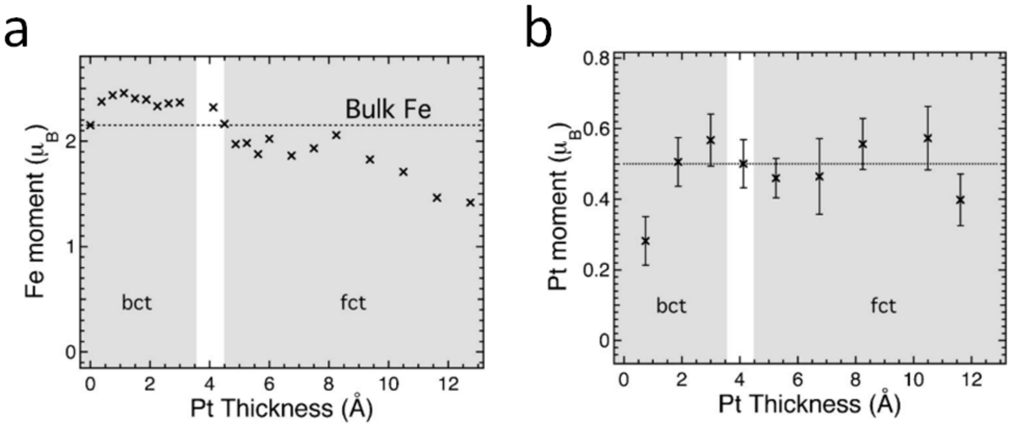

Figure 5.3: a) and b) are taken from Reference [183]. They show the Fe moment (a) and the Pt moment (b) plotted against the thickness of the Pt layer in sputter grown Fe/Pt multilayers. They also show the Pt thickness at which the layer undergoes a phase change, from BCT to FCT.

Kuschel et al. showed, using XRMR, a maximum spin polarisation of (0.6±0.1) μ_B/atom for Pt in sputter grown Fe/Pt bilayers with Pt thickness 59 Å and 200 Å. A Pt thickness of 18 Å, however, gave a moment of (0.2±0.1) μ_B/atom, much lower than other literature values (see Figure 5.4, reference b).[168] A Pt moment of (0.43±0.08) μ_B/atom was found by Klewe et al. using the XRMR technique on sputter grown Fe/Pt bilayers.[171] Finally, Graulich et al. used sputter grown Fe/Pt bilayers in a comparison of the techniques: XMCD and XRMR. The results showed that via XMCD, the Pt spin moment was (0.22±0.05) μ_B, although, once scaled to a more reasonable polarisation length within the Pt, compared to considering an average over the whole Pt layer, the spin moment becomes (0.45±0.14) μ_B. This compared well with their result from the XRMR of (0.47±0.10) μ_B. The orbital moment calculated for the sample was <0.05 μ_B. For the Pt/Fe sample, the full width half maximum of the induced moments depth was found to be 15.6 Å, with an interfacial roughness of 5.5 Å.[156]

Based off Figure 5.4, it can be seen that the Pt magnetisation is more constant with an average of (0.5±0.1) μ_B/atom, higher than the values found from studying Ni/Pt interfaces, though the

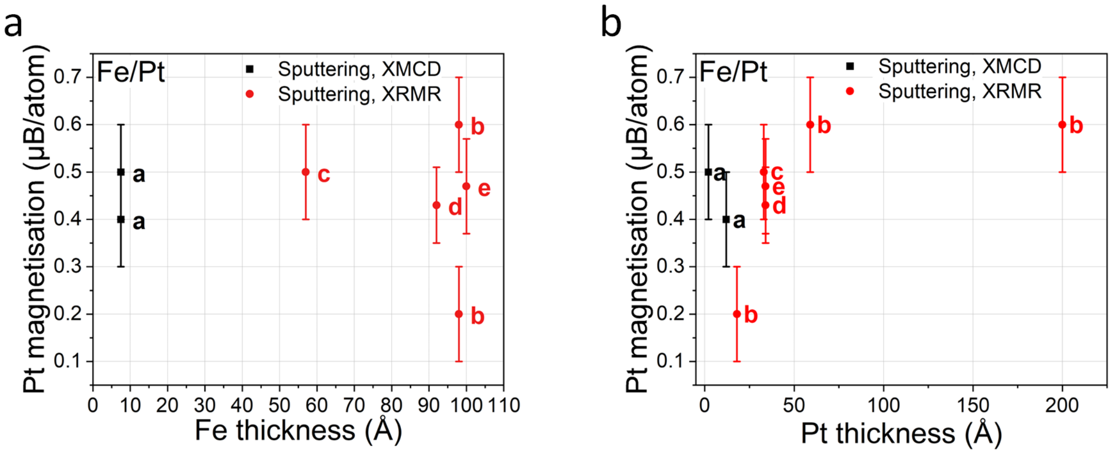

Figure 5.4: a) and b) show literature values for the magnetisation of Pt induced by Fe atoms at an interface, plotted against the thickness of the Fe layer (a) and thickness of the Pt layer (b). The letter label represents the reference: a-[183],b-[168], c-[170], d-[171], e-[156]. All samples were bilayers grown via sputtering and all were measured by XRMR except from reference a, which was a multilayer measured using XMCD.

bulk magnetisation of Fe is 2.22 μ_B (at 0 K), considerably higher than that of Ni.[16] Furthermore, the Pt magnetisation showed a relatively constant trend with increase in Fe thickness (Figure 5.4a), although there were not many low Fe thicknesses considered. An increasing magnetisation with Pt thickness was observed (Figure 5.4b), this contradicts the results in Figure 5.3, though in the Pt thickness range studied was much lower and there are fewer values in Figure 5.4a, taken from different sources, allowing for growth inconsistencies which may be a factor. It is more likely that the Pt magnetisation of 0.2 μ_B/atom was an outlier.

To summarise the results for the proximity effects at an Fe/Pt interface:

- Pt magnetisation at the Fe/Pt interface was on average (0.5±0.1) μ_B/atom.
- Different phases of Fe, due to different Pt thicknesses, caused different Fe magnetisation (consistently above bulk in BCT then gradually decreasing in FCT).
- No significant change in the Pt magnetisation was observed with increasing Fe thickness.
- No significant change in the Pt magnetisation was observed with increasing Pt thickness (except for very thin Pt layers).

5.4.3 Cobalt

XMCD

The Co/Pt interface is possibly the system most investigated in the literature, due to interest in Co/Pt multilayers for magnetic recording devices. Early research into these proximity effects was performed by Schütz et al., in 1991 they used XMCD to probe the Pt moment in multilayer samples and found a maximum of 0.55 μ_B.[184] Schütz et al. also investigated with XMCD the depth of the platinum polarisation, by substituting the innermost three Pt ML, equivalent to $\sim$ 8 Å, for Ir. They concluded that the innermost Pt moments in a 30 Å layer were around 0.03 μ_B and similar to those of Ir. However, this method is valid only if the Ir atoms have the same induced moment as Pt.[185] XMCD was used by Wilhelm et al. who found a high Pt moment of 0.68 μ_B/atom.[186] A trend of lower average Pt moment, decreasing with increasing Pt layer thickness, was shown by Rüegg et al. in electron beam evaporated Co/Pt multilayers via XMCD.[163]

Suzuki et al. also used XMCD to probe Pt induced moments within a sputtered Co/Pt bilayer, and found a Pt moment of 0.61 μ_B/atom at the Pt/Co interface. As they did a Pt thickness dependent study, they were able to estimate the depth profile of the Pt atoms. They found that the Pt moment tended to zero at some point after 10 Å, and therefore 90% of the total Pt magnetisation existed within 10 Å of the interface, see Figure 5.5c. Furthermore, the orbital moments only existed within two atomic layers from the interface. They proposed an exponential function to model the decay,

$$m_{tot}(z) = m_0 e^{-z/\lambda} \tag{5.1}$$

where a decay distance (λ, the effective range of coupling between Co and Pt) of 0.41 nm was used, m(z) was the depth profile of the Pt moments at distance (z) from the interface. m_0 is the Pt moment at the interface, and m_{tot} represents the combined orbital and spin moments. Although, they noted that there may be a systematic error present in the results due to the depth profile potentially having a dependence on the Pt layer thickness. They also noted a nearly constant interfacial roughness for all samples of 10 Å.[162] Angelakeris et al. found with XMCD a Pt moment of 0.485 μ_B/atom in e-beam evaporated Co/Pt multilayers of 50 repetitions, which is an average value for the whole Pt layer of 7 Å. They used a thin Co layer of 2 Å in these measurements, which is barely a monolayer and could be quite inhomogeneous, and the Pt showed polarisation.[34] In 2017, Koyoma et al. successfully observed SOT-induced switching of the induced Pt moments together with the Co moments in a sputtered Pt/Co/Pd system using XMCD and current injections. The total Pt moment reported was low at 0.114 μ_B/atom, this value allegedly is in agreement with Suzuki et al. when considering the difference in Pt thicknesses.[187]

Lau et al. found using XMCD that the moments of a top Pt interface (Co/Pt) were higher than a bottom interface (Pt/Co) with a ratio of around 2.3:1 for the top Pt spin moments to bottom Pt spin moments when using 6 Å of Pt at both interfaces. This is also true for the orbital moments

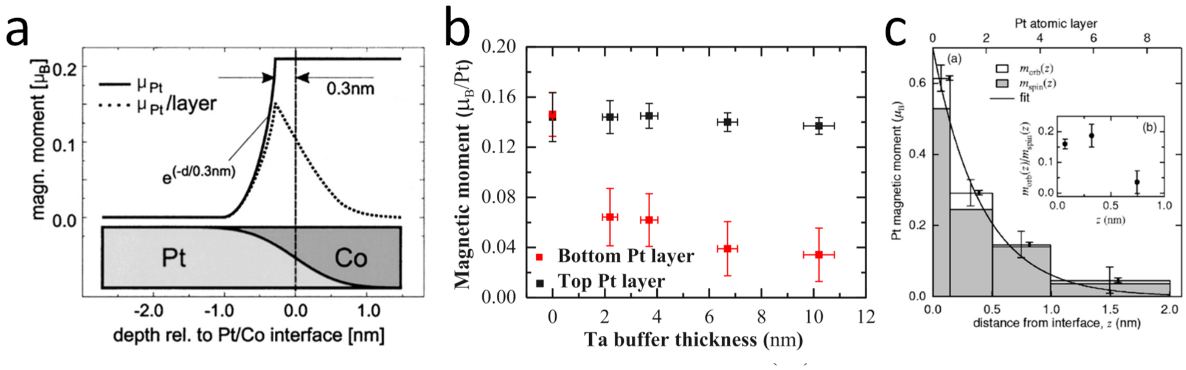

Figure 5.5: a) shows the model used by Geissler et al., showing the Pt moment at the interface with Pt, and its decay until 10 Å after the interface.[188] b) is from Reference [161], showing the dependence of the Pt moment on the Ta buffer thickness for the top and bottom interface in a Pt/Co/Pt system. c) shows the decline in spin and orbital Pt moments from a Co/Pt interface, from Reference [162].

with a ratio of 4:1. These values came from sputter grown Ir/Co/Pt and Pt/Co/Ir multilayers, and furthermore, measurements via the VSM method on these samples concluded there was also a dead layer within the films, as the linear fit to the Co thickness vs. moment/area, cuts the x-axis at a positive value (at 1 and 2 Å). The results showed both a small dead layer thickness and a small amount of induced moments within the Ir, Co, Pt samples, however, as the VSM method shows an average of all the effects, effects from the Ir/Co and Pt/Co interfaces may be cancelling each other out to some respect.[97]

VSM Method

Although it gave no specific values, a plot of the Co thickness vs. MOKE signal for MBE grown Pt(111)/Co samples from McGee et al. showed that the MOKE signal (which is proportional to a magnetic moment) decreased linearly with thickness in the range 0 to 28 Å). Around 2 ML (around 7 Å), it diverted from the linear trend and the moments reduced quicker with decreasing Co thickness, potentially due to inhomogeneity (see Figure 5.13). If the linear part was extrapolated to 0 Å of Co, it still shows a MOKE signal, suggesting induced moments in the Pt.[189] Lv et al. showed a similar Pt moment to Angelakeris et al. of 0.48 μ_B/atom in sputter grown Co/Pt multilayers, measured using the VSM method and Equation 5.1. They claimed the moment remained above 0.1 μ_B/atom until the fourth atomic layer of Pt after the interface.[190] Utilising MOKE, Ece et al. described two models for working out the magnetisation in Co/Pt multilayer thin films. For the model which accounted for induced Pt moments, an equation similar to Equation 5.1 was presented,

$$Q_{Pt} = Q_{Ptmax} e^{(-\beta(d_{Pt}-0.2))} \tag{5.2}$$

where Q_{Pt} is the total Pt moment, Q_{Ptmax} is the maximum Pt moments (within the monolayer at the interface), d_{Pt} is the magnetisation delay length (only Pt thicknesses above 1 monolayer are considered, >2 Å), and β is the exponential decay constant (which they took as 6.36 nm^{-1}).[191] Yu et al. used the VSM method to study Pt/Co/[Co/Ni]$_{\times 4}$/x samples, where x = Ta, Pt, MgO and Cu. They showed a dead layer for all samples, including the one with Pt at both interfaces, which one would expect to show induced moments. However, studying the FM thickness vs. moment/area data for this sample, the whole range is short, between 2.5 Å and 15 Å and there appears to be a change in trend below around 8 Å which is not accounted for, suggesting that below this thickness, the thin film becomes discontinuous.[178]

Bersweiler et al. performed a study via the VSM method into the Co/Pt interface in bilayer repeats after noting that the PMA can be altered by various factors. This includes: deposition methods[192], annealing temperature, sputtering pressure and configuration, which all contribute to changes in the interfacial roughness. They showed that the Pt roughness doesn't change with Pt thickness, however, the Co roughness tends to decrease with increasing Pt thickness. They also showed that the roughness was reduced when using a Pt buffer layer, instead of MgO or AlO$_x$. Furthermore, the values for M$_S$ calculated were much higher than bulk, indicating an induced moment in the Pt. As their Pt thicknesses were less than the approximated Pt polarisation depth of 10 Å, it could be assumed that the whole Pt layer had induced moments, and therefore an estimation could be made for the magnitudes of the Pt polarisation. These moments ranged between around 0.15 to 0.5 μ_B/atom, depending on Pt thickness and the buffer layer material. The results also followed a similar trend to that of the Co roughness, proving a link between Co roughness and induced Pt moments due to more Pt atoms being in direct contact with Co atoms. There was a decrease in the induced moment as the Pt thickness increased, this is because the Pt moment decays as the distance from the interface increases. An estimation could be made by assuming the Pt moment was independent of the distance of the Pt atom from the interface, however, it would be less accurate.[193] Bandiera et al. demonstrated, with SQUID magnetometry, an asymmetry in the interfacial anisotropies in sputtered Pt/Co/Pt films showing a higher anisotropy at the Pt/Co interface. They concluded that this was due to more interdiffusion at the top interface, perhaps due to the sputtered Pt atoms having more energy when they hit the sample surface than Co atoms. They reported that the diffusion caused the formation of magnetic alloys that have lower T$_c$ values than Co, however, this is only significant when studying thin films (<10 Å).[194]

XRMR

Ferrer et al. used the technique of resonant magnetic diffraction along a crystal truncation rod (a less used method [195; 196]) and found the magnetic moment of Pt to be 0.2 μ_B in a layer in contact with Co atoms, and 10 times smaller in the following layer. They claimed that the Pt induced moment increased as the Co thickness increased (and therefore the Co magnetisation), however,

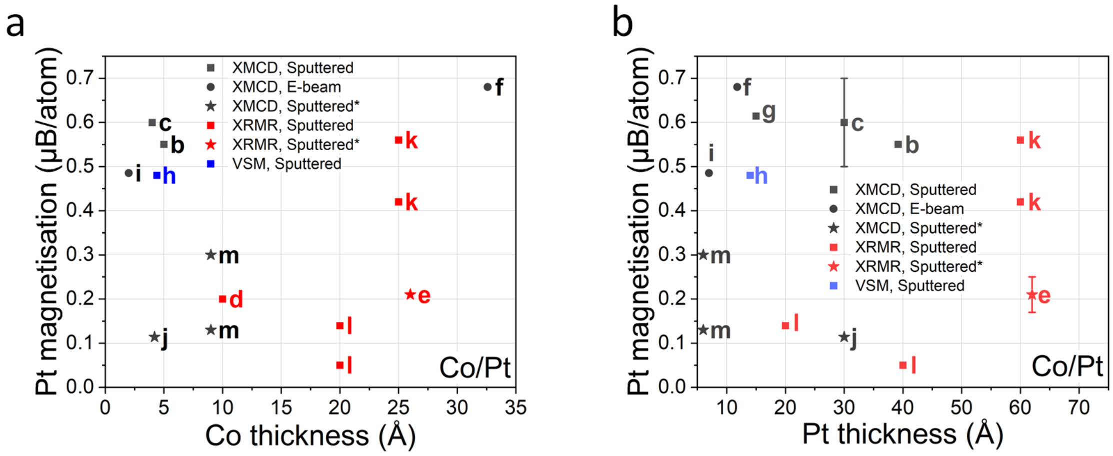

Figure 5.6: a) and b) show the reported Pt magnetisation in Co/Pt samples plotted against Co thickness (a) and Pt thickness (b). The references are as follows: b-[184], c-[185], d-[160], e-[188], f-[186], g-[162], h-[190], i-[34], j-[187], k-[32], l-[161], m-[97]. The stars represent a sample in which the Co has an interface with another material that is not Pt. Samples from references c, f, h, i, j, k, l, m are multilayers, d, e, g are bilayers. Not shown on a), g has a Co thickness of 140 Å. Samples m, l and k have two different values depending on whether the top of bottom Co interface is measured, details of these samples are shown in Figure 5.8a.

this could be due to a relationship between the x-ray intensity and the Co thickness. Furthermore, their results showed that the Pt moment was slightly larger when Co had hcp packing, compared to when it had FCC packing.[160]

In 2001, Geissler et al. compared simulations and XRMR measurements on sputtered Co/Pt interfaces. They found that the induced 5d moment was 0.21 μ_B, similar to Ferrer et al., for 1 ML (∼ 4 Å) after the interface, then, the polarisation decayed over (3 ± 1) Å (Figure 5.5a).[188] Mukhopadhyay et al. also prepared sputtered Pt/Co/Pt samples as a function of different thickness Ta bases (0, 20, 40, 70, 100 Å). Using XRMR, they found that the top Pt layer had a Pt(111) phase, as did the bottom Pt layer when the Ta base layer is very thin. When the Ta base layer thickness was increased, the bottom Pt existed in the Pt(001) phase, which caused a decrease in the induced Pt moment. For the bottom Pt layer, the maximum Pt moment decreased as the Ta thickness increased. The top Pt layer moments followed a more steady trend and were higher than the bottom layer, with a ratio of 2.3:1 top to bottom for Ta thicknesses below 60 Å - see Figure 5.5b. This asymmetry however, was not attributed to the roughness, as a similar roughness of around 4 Å was found for both top and bottom interfaces in all samples. It was shown by density functional theory calculations that Pt(001) has less induced moments due to the proximity of the Co layer.[161] The flaw in this theory comes when looking a very thin magnetic layers which do not support defined crystal structure. Verna et al. proved via XRMR that for thinner FM layers, the interdiffusion during sample deposition played a key role in the asymmetry at Pt/Co vs. Co/Pt interfaces. They predicted a region up to 10 Å of Co-Pt intermixing on the top interface, but only 5 Å on the bottom. They showed that these effects in trilayers are reproducible in multilayers.[197]

Rowan-Robinson et al. showed that the XRMR measured induced Pt moments in the top layer of a Pt/Co/Pt trilayer were at least twice those of the moments induced on the bottom layer. They also commented that despite this, the DMI contributed symmetrically from both interfaces. Though it should be noted that the two Pt layers are of different thicknesses.[33] Further XRMR measurements performed by Moskaltsova et al. confirmed a larger induced moment in the top Pt layer than the bottom in sputter grown Pt/Co/Ta and Ta/Co/Pt trilayers with a top layer to bottom layer ratio of 1.3:1, which is a smaller ratio compared to similar samples.[32] This may be due to the bottom Pt layer being grown onto Si/SiOx instead of Ta or Ta/Ru, as in other studies.[97; 161] The polarisation depth for the Pt was also found to be 8 Å for Pt/Co/Ta and 9 Å for Ta/Co/Pt, in good agreement with the other studies. Inyang et al. also showed that the induced moments are larger at the top interface than at the bottom interface. They did experiments using polarised neutron reflectivity and XRMR on Pt/CoFeTaB/Pt trilayers and defined a new model which attributed the asymmetry to the difference in effective susceptibilities of the Pt interfaces, which could have occurred due to interfacial roughness or intermixing.[31] Another study showing the asymmetry was Reference [198], in which it was ascribed to variations in roughness on the top and bottom interfaces, the larger moment and interfacial mixing on the top Co/Pt interface.

Plots comparing literature values for the Pt magnetisation as a function of Co and Pt thickness is shown in Figure 5.6. The values reported for the Pt magnetisation cover a large range, from 0.05 to 0.68 μ_B/atom, and there is no obvious trend between the magnetisation and the Co or Pt thickness, nor between the measurement type or growth method. There are perhaps too many variables at play that can affect the magnetisation value which drowns out any potential trends with respect to thickness. Alternatively, there is no dependence upon the layer thicknesses and the moment instead depends more on specific growth conditions, which would need to be considered for individual experiments.

Considering, very generally, all the Pt moments reported in all the papers discussed, including Fe, Co and Ni, it could be interpreted that there are two levels of Pt moments. A higher range for Fe samples (generally above 0.4 μ_B/atom) and a lower range for Ni samples (generally below 0.3 μ_B/atom). The Co magnetisation values seem to fit into both of these categories, with the majority in the higher range - see Figure 5.7a. One further aspect not yet summarised, was a dependence of the Pt magnetisation on the interfacial roughness. Values from literature were combined in Figure 5.7b, which show a potential weak trend between the roughness and magnetisation, supporting previously mentioned claims.

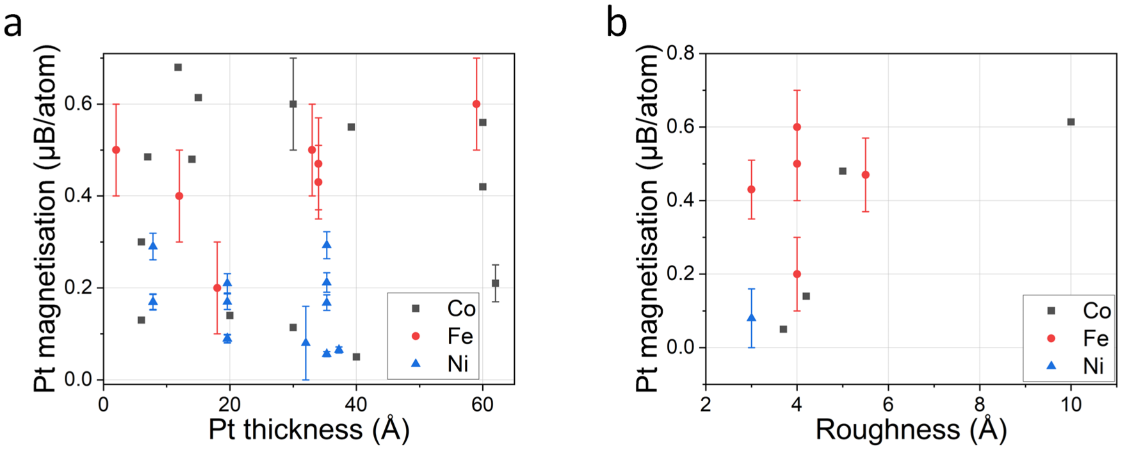

Figure 5.7: a) shows a generalised plot of Pt magnetisation values found in literature vs. the Pt thickness. The values are taken from Figures 5.2b, 5.4b and 5.6b. b) shows a generalised plot of interfacial roughness against Pt magnetisation. Values were taken from references: [156; 161; 162; 168; 171; 190]. In some cases an average of reported values was used.

Interfacial Asymmetry and Pt Polarisation Length

Various findings throughout this chapter have addressed a key question: is the induced moment equal at the top and bottom Pt/Co/Pt interface? Values extracted from the literature are summarised in Figure 5.8a which showed a clear trend, backed up by other literature studied, between the Pt magnetisation at a Pt/Co interface and a Co/Pt interface. The top Pt interface always showed a higher moment than the bottom interface, and the difference in values varies slightly, with an average ratio of around 2:1. Another question addressed by various studies was: how deep into the Pt layer is the Pt polarised? Figure 5.8b shows a summary of results, which supported a consistent decay length of around 10 Å, i.e. the length over which the Pt moments exponentially decrease from a maximum at the interface to zero, within the Pt layer. The length remained consistent for various Co and Pt thicknesses.

Other Correlations

Other investigated results of the proximity effect include: a decrease in the spin Hall conductivity with increased induced spin moments and an enhancement of the AHE in Pt/Py.[200; 201] Yang et al. found no direct correlation between the DMI and the proximity effect in Co/Pt bilayers. They presented from first principle calculations that the DMI doesn't extend far from the Co interface into the Co layer, and it is very weak in the proximity induced Pt spins. Any intermixing may, however, reduce the strength of the DMI.[35] Ryu et al. on the other hand, showed an intimate link between proximity effects in Pt and DMI. Claiming a strong correlation between the induced

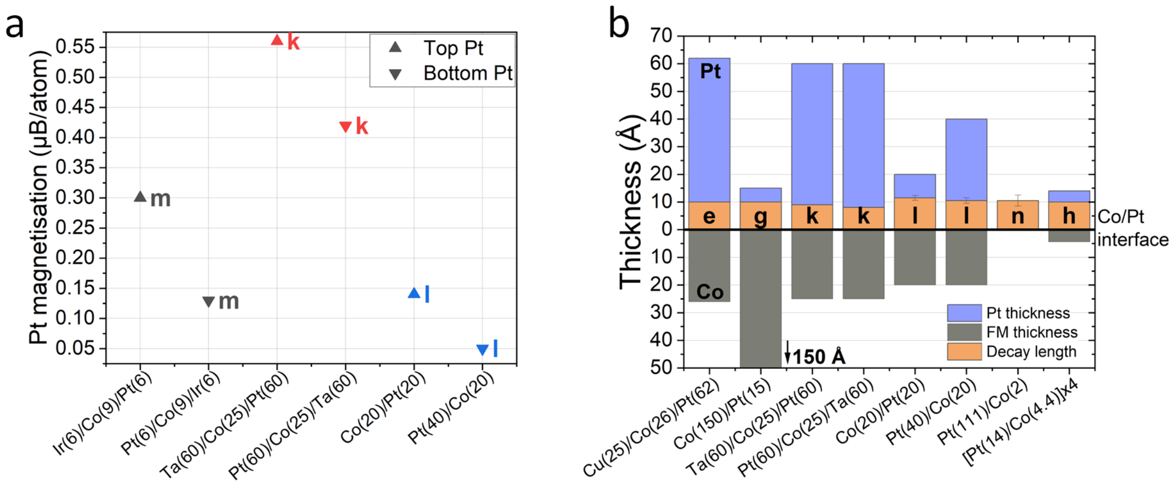

Figure 5.8: a) shows the difference in reported induced Pt moments from three separate sources: k-[32], l-[161], m-[97]. The up arrow represents the top Co/Pt interface, and the down arrow represents the bottom Pt/Co interface. Values from references k and l were found using XRMR and values from reference m was found using XMCD. b) plots as bars, the thickness of the Co, extending down from the Co/Pt interface. Above the Co/Pt interface, it shows the Pt thickness, and the reported thickness of polarised Pt within the layer (decay length). References in this figure are as follows: e-[188], g-[162], h-[190], k-[32], l-[161], n-[199]. For reference n, no Pt or Co thicknesses were given. All samples were grown via sputtering except for reference n, which used evaporation. All results were measured via XRMR, except g (XMCD), h (SQUID) and n (STM). The x-axes shows the sample structure.

moments and the strength of the chiral spin torque.[202] These conclusions were further investigated by Rowan-Robinson et al. in sputtered multilayers, to find that both DMI and proximity induced moments (measured by XRMR) were affected in different ways by small changes in thickness to a spacer layer between Co and Pt in the instance of thin spacer thicknesses. Any proximity effects became negligible at thicker spacer thicknesses, however, the DMI continued to change. They stated that spin-orbit interaction dictated the DMI, suggesting it is more dependent on itinerant electrons, whereas the density of states is the key factor in determining the proximity effects and is contingent on the bound d electrons.[33] Knepper et al. studied the link between Pt polarisation and the RKKY interaction, they suggested that the ferromagnetic interlayer coupling in Co/Pt multilayers is due to the polarisation of the Pt atoms, as the coupling becomes stronger when the temperature is lower, and therefore the polarisation extends deeper into the Pt layer.[203]
To summarise the interfacial proximity effect at a Co/Pt interface:

- No overall trend was observed between the Pt magnetisation and Co or Pt thickness (some small trends were observed on specific experiments).
- Moments were induced in the Pt, even with only 1 monolayer of Co.
- The Co and Pt moments followed the same applied field dependence.
- There was a weak dependence between interfacial roughness and Pt magnetisation.
- The polarisation of the Pt exponentially decayed over 10 Å from the interface within the Pt layer.
- A Co/Pt interface exhibited more induced moment than a Pt/Co interface. This was linked to a dependence of the Pt magnetisation on the interfacial roughness/intermixing and the lattice phase of the Co and Pt.

5.5 Ir Proximity Effects

Where literature very clearly reports Pt to have an induced moment in vicinity to a FM (except Ni via the VSM method), the effects in Ir are more ambiguous. From some research groups there are reports of induced moments, whereas others report a dead layer. Most studies were performed on alloys of Ir with Co, Ni or Fe by Krishnamurthy et al., however, there are also some studies with PMA stacks. In theory, Ir is another heavy metal near the Stoner criterion and next to Pt in the periodic table, it should possess similar proximity induced features to Pt, however, there are always multiple factors at play.

5.5.1 Alloys

Initially studied by Krishnamurthy et al., it was shown using XMCD that in alloys with Fe, Co and Ni, the Ir gained an induced magnetic moment which was proportional to the FM host material moment due to 3d-5d hybridisation. It was Krishnamurthy et al. that found a violation of Hund's rules in a Co/Ir alloy due to the orbital moments of the Ir aligning antiparallel to the spin moments, and therefore the moment of the FM. They also claimed a reduced moment on the neighbouring Co atoms. They showed that in Ir/Fe alloys, the Ir induced moment was around a fifth of the Fe moment. [204–206]

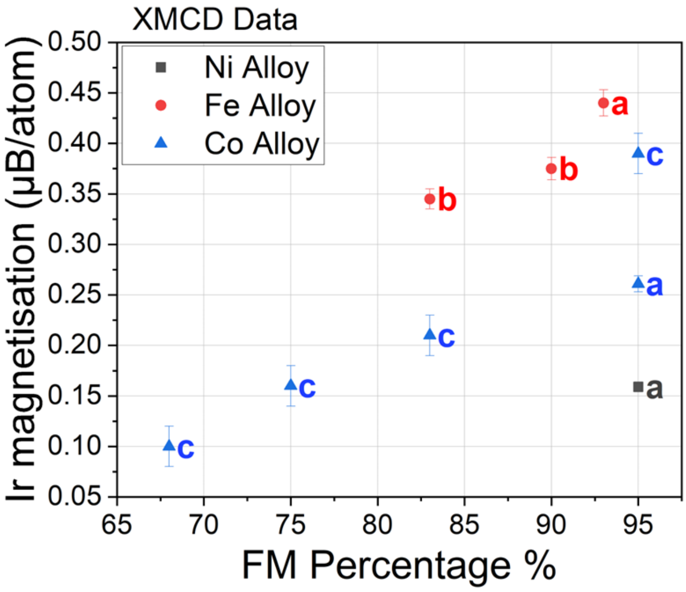

Figure 5.9: a) shows a collection of literature values for the magnetisation of Ir in alloys with Ni, Fe and Co, against the percentage of FM in the alloy. The letter represents the reference: a-[204] b-[205], c-[206]. All data was collected via XMCD.

The data in Figure 5.9 shows that, with an increasing percentage of FM material, the Ir magnetisation increased. It also revealed that for the Ir moment in alloys of a similar FM percentage, Fe was the highest moment and Ni the lowest. For Co alloys, the Ir had a larger range of values between those in Fe and Ni alloys - this reflects the trend found in Pt.

5.5.2 Thin Films

Induced Moments

Multilayer systems with a FM and Ir have also been studied via XMCD. Wilhelm et al. found that contrary to within alloys, the Ir orbital moment was parallel to the spin moment, as expected.

This was in Fe/Ir multilayers, grown by e-beam evaporation.[207] Jaouen et al. showed that the Ir orbital moment in an MBE grown Fe/Ir multilayer decreased considerably when changing the thickness of the Fe from 10 Å to 30 Å. With this thickness difference, the Fe also underwent a lattice structure change from BCT(001) to BCC(001), a change that was maintained also by the Ir. They claimed that in the BCC structure, there are more interfacial magnetic sites.[208]

Poulopoulos et al. showed that both Pt and Ir were coupled parallel to the FM in the system with a positive orbital moment contribution.[180] Whereas Schütz et al. showed that Ir had a positive spin contribution, but a negative orbital contribution.[185] Wilhelm, on the other hand, showed that orbital and spin components were parallel for Pt and Ir.[186] Figures 5.10a and b show a collection of the values found for the Ir magnetisation, measured by XMCD, at an Fe/Ir interface. There was a potential trend with the Ir magnetisation decreasing with increasing Fe thickness, however, there were not enough data points to conclude this. A more constant trend in Ir magnetisation was shown with increasing Ir thickness. The values have a small range around an average of (0.18±0.04) μ_B/atom, although these graphs cover only a small range of Ir and Fe thicknesses.

Dead Layers

There are also many literature articles suggesting that a dead layer forms at the interface between Ir and a FM. Chen et al. reported a dead layer in Fe/Ir(111), because in the first three monolayers of Fe, no magnetic signal was detected (contrary to Jaouen et al. who showed Ir moments at around 3 ML (~ 6 Å) of Fe [208]). They related this to the FCC structure in that thickness range, as they showed a BCC Fe phase forming for more than 3 ML.[209] Belmeguenai et al. reported dead layers forming at interfaces in a Ir/Co_2FeAl/Ti, however, they indicated that a dead layer in their case meant an area with intermixing and therefore a lower magnetisation. This is because they reported both a dead layer from the VSM method, and induced moments from XRMR measurements.[143; 211] Although, in the VSM measurements which sum all the proximity effects, they do not consider any effects from the Ti interface, which has been shown to produce dead layers.[212] It was a similar report by Belmeguenai et al., for CoFeB/Ir samples, the interface with the substrate Si/SiOx was not considered as they reported a dead layer at the Ir interface from VSM measurements, plus possible proximity induced Ir moments.[210] From VSM measurements, it was shown by Benguettat-El Mokhtari et al. that there was a magnetic dead layer in sputter grown Ir/Co/Pt and Pt/Co/Ir measurements. This was not attributed to the Pt/Co interface, as a similar sample Pt/Co/Pt did not show any magnetic dead layer. Therefore, it was concluded that the Ir caused a magnetic dead layer at the interface with Co, which was larger at the top Ir/Co interface. However, this difference could be due to there being more induced moments at the top Pt/Co interface.[213] White et al. claimed that there were no proximity effects at the Py/Ir interface.[214] Figures 5.10c and d, display the dead layer results taken from literature. Figure

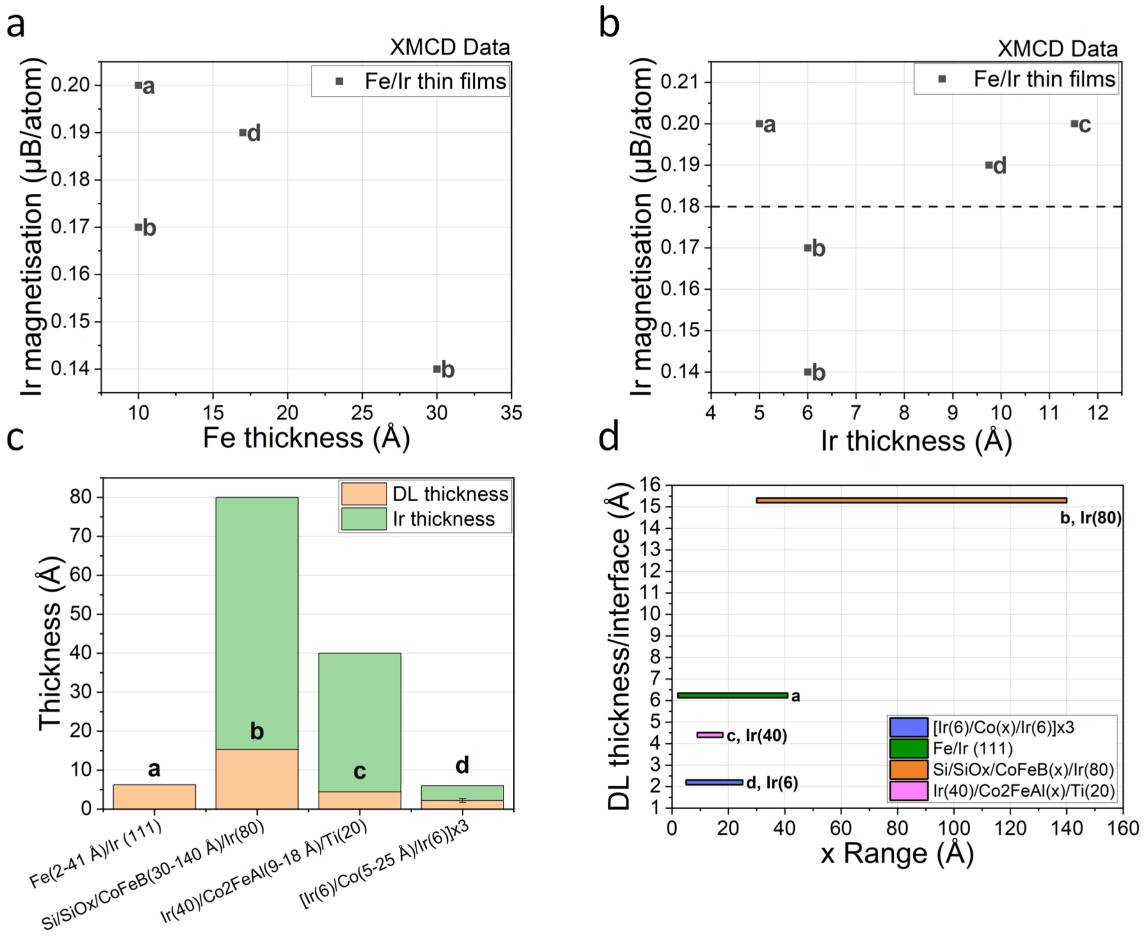

Figure 5.10: a) and b) show literature values of the moments induced in Ir at the interface with Fe, against Fe thickness (a) and Ir thickness (b). The numbers correspond to references: a-[207] b-[208], c-[180], d-[186]. The average value of 0.18 is marked by a dashed line on b). Samples were grown via e-beam evaporation and MBE. c) shows a graph with a bar illustrating the thickness of the Ir, and how far into the Ir the reported dead layer reached. The sample structures are labelled along the x-axis, and the references are: [97; 143; 209; 210], from left to right. The Ir thickness was not reported in the sample of a and samples were grown via sputtering and measured via the VSM method. d) represents the dead layer thickness in the magnetic layer, against the range of magnetic layer thicknesses studied to achieve the dead layer thickness - for the same samples as c). References are the same as c), and the Ir thickness of each sample is quoted next to it.

5.10c shows for four different samples, the proportion of the Ir thickness that was proposed to be magnetically dead with the Ir thickness. There was potentially a trend between the Ir thickness and the reported dead layer thickness, however, the values of the dead layers themselves were perhaps not accurate due to the reasons mentioned above. Figure 5.10d shows the FM thickness ranges over which the samples were studied. The largest dead layer thickness did not cover very thin FM layers, which may have impacted the result, compared to the smaller dead layer thicknesses, which only consider thin FM layers.

To summarise the results on proximity effects at the Ir/FM interface:

- Both induced moments and dead layers were reported in Ir.
- Fully dead layers were only reported from the VSM method and are likely to be less accurate, giving a sum of all interfacial effects.
- Induced moments were reported from XMCD measurements, plus a decrease in FM interfacial moments for some FMs.
- In alloys, the Ir magnetisation increased as the alloys FM percentage increased, with the highest magnetisation seen in Fe, followed by Co, then Ni, suggesting a link between the FM moment and the Ir moment.
- Induced Ir moments were on average (0.18±0.04) μ_B/atom.
- A dependence on lattice structure was demonstrated.

5.6 Ta Proximity Effects

Literature measurements on Ta/FM interfaces tended to report the same thing: a magnetic dead layer, and the VSM method was used for working out the dead layer thickness. Shringi et al. showed a 5 Å dead layer in sputter grown Ta/Fe multilayers, assuming it was equal on the top and bottom interface. They also stated that when the Ta is above 24 Å, there was no change to the magnetisation with Ta thickness, however below, the magnetisation increased as the Ta thickness decreased, showing a bulk value for Fe when the Ta was 7 Å. This was taken to mean that the amount of alloying between Ta and Fe decreased as the Ta thickness decreased.[215]

When using ion beam deposition to make samples, it was found that the Ta/NiFe interfacial dead layer thickness increased with an increasing ion beam voltage. This was ascribed to the atomic mixing of atoms on the surface, with atoms reaching the surface. The dead layer thicknesses were found to be between 4 and 6 Å with an ion beam voltage of 1000 V. The dead layer thickness increased with the thickness of top Ta in a Ta/NiFe/Ta stack, then plateaued at 6 Å when the Ta = 50 Å.[217] NiFe was again investigated by Kowalewski et al., as they found a magnetic dead layer

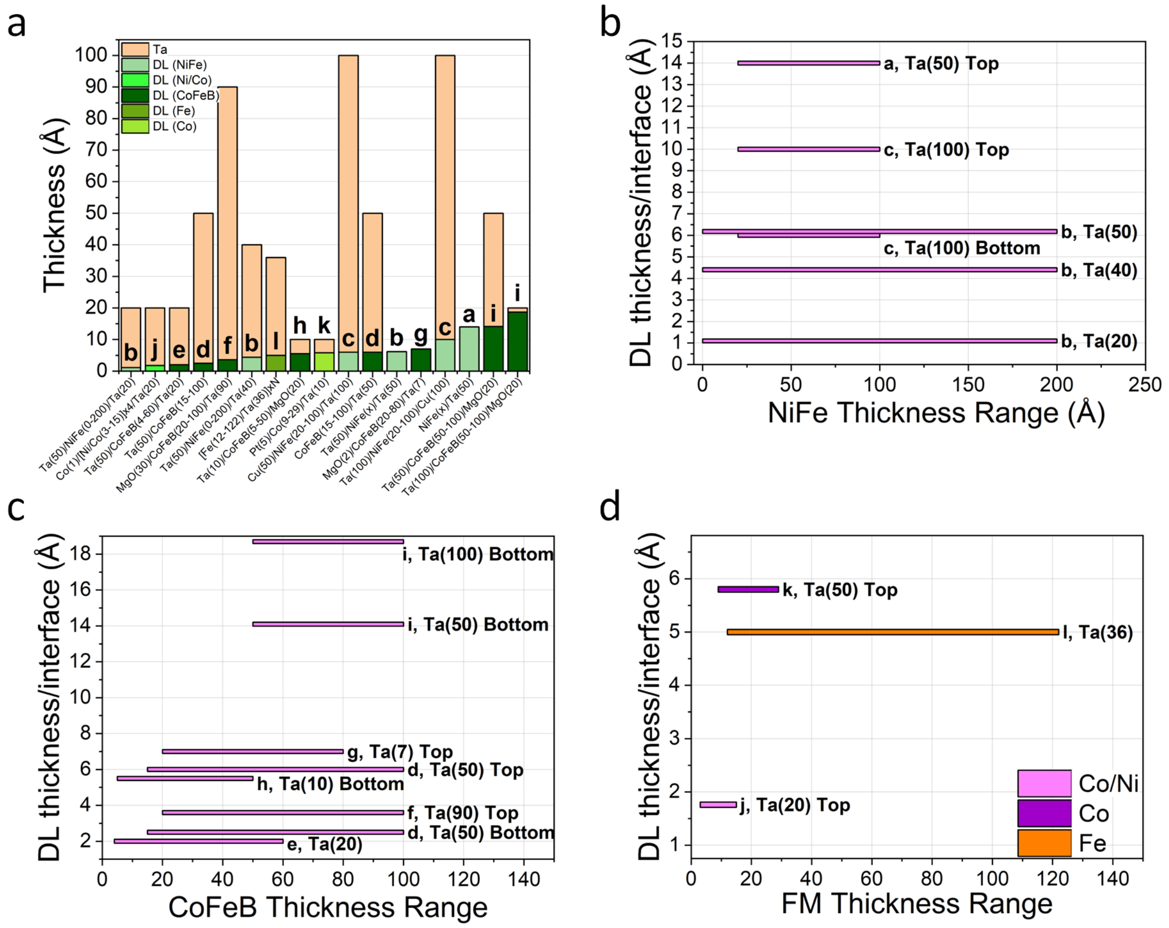

Figure 5.11: a) is comprised of bars showing the thickness of Ta and the dead layer within the magnetic material at a Ta/FM interface. This is shown for multiple different samples, the different FM materials are separated by colour. All samples were grown via sputtering and the dead layer thickness found using the VSM method. If no thickness was reported, the sample is shown without a Ta thickness. b), c) and d) show the dead layer thickness per interface against the FM thickness range used to work out the DL thickness for NiFe, CoFeB, and other FMs, respectively. Labelled for each sample is the thickness of the Ta and whether it's on the top or bottom interface. The letters represent the reference: a-[216], b-[217], c-[218], d-[219], e-[220], f-[221], g-[222], h-[223], i-[224], j-[178], k-[194], l-[215]. For the compositions of CoFeB in c), references e, f and i are $Co_{40}Fe_{40}B_{20}$, d is $Co_{60}Fe_{20}B_{20}$, h is $Co_{20}Fe_{60}B_{20}$, and g is $Co_{31.5}Fe_{58.5}B_{10}$.

of 6 Å at the Ta/NiFe interface, and 10 Å at the NiFe/Ta interface. This was accounted for by considering that the surface free energy of Ta is higher that Ni, so the top Ta atoms were more likely to intermix into the NiFe than the Ni atoms into the Ta. They also concluded that post annealing, this difference in dead layer thickness is removed.[218] Wang et al. showed Ta dead layers at the interfaces of Ta/CoFeB/Ta samples: 6.0 Å for the top interface and 2.5 Å for the bottom, this was assuming that the dead layers in a Ru/CoFeB/Ru sample measured were equal at both interfaces, which may not be true according to Jang et al..[221] A transmission electron microscope image was also shown of the two samples and the Ru sample had much sharper interfaces than the Ta sample, plus, the Ta top layer shows a TaO_x layer almost the same thickness as the Ta layer itself.[219] Other similar studies into Ta/FM dead layer thickness include References: [216; 220; 222].

Jang et al. explained a difference in the top and bottom layer dead layer thickness of Ru/CoFeB/Ru samples by considering the effective atomic weights of the materials - Ru is heavier so the top interface showed more intermixing. This does, however, consider that all layers have a thickness of 50 Å. As Ta is even heavier than Ru, this emerged as an even thicker dead layer at the top interface.[221] It was shown by Kim et al. via XMCD that in CoFeB/MgO bilayers with various underlayers, including Ta, the Fe perpendicular orbital moment was suppressed by the interfacial intermixing, and the perpendicular and IP orbital moments of Co were suppressed.[212] Via XMCD in CoCrPtTa alloys, it was shown that Ta orbital moments were antiparallel to the spin moments, which obeys Hund's rules as expected for a transition metal with a d shell less than half full.[179] As for trends between the magnetic dead layer and Ta thickness, Akyol et al. performed a study with a Ta/CoFeB/MgO sample and showed that the dead layer remained constant within error until 5 Å, above which it increased with Ta thickness.[224]

From Figure 5.11a, we can infer that there is no obvious trend between the Ta thickness and the dead layer thickness, nor between different FM materials. The dead layers range between 1.1 Å and 18.7 Å. From Figures 5.11b, c, and d, it became apparent that the studies which presented a DL of more than 8 Å, did not include FM thicknesses less than 20 Å, which may be less accurate. Alternatively, it may suggest that over thicker ranges of FM thickness, the DL was thicker. Studies also showed that the dead layer at a top interface was thicker than at a bottom interface. Two studies which gave the values for the different interfaces were by Kowalewski et al. and Wang et al.. [218; 219] The average ratio of DL thickness at the top to bottom ratio was 2:1, however, more samples should be compared.

To summarise the proximity effects at Ta/FM interfaces:

- There was a large range of dead layers reported (1.1 Å and 18.7 Å), which didn't show an obvious, large scale dependence on FM material or Ta thickness.
- Individual studies reported trends: the DL thickness decreased with Ta thickness below 50 Å and plateaued again below 7 Å, Fe moments began to increase with decreasing Ta thickness

below 24 Å.

- The largest dead layer thickness came from studies which did not use FM thicknesses below 20 Å.
- The Ta was found to suppress the interfacial orbital moments in Co and Fe in a CoFeB sample.
- An asymmetry was observed in DL thickness of the top and bottom Ta/FM interfaces which was on average 2:1.

5.7 CoB Proximity Effects

Another, less studied, FM material used throughout this thesis is CoB. CoB is an amorphous material, which differs to polycrystalline Co with a reduced amount of grain boundaries.[225] Tanaka et al. performed calculations to determine the electronic states of CoB in a spin polarised state and in a paramagnetic state. They claimed that the boron s and p states split into bonding and antibonding states and hybridised with the Co d states. The exchange splitting of the Co d states decreased as the content of boron increased due to the enhancement of hybridisation, i.e. they became less ferromagnetic. The density of states for different percentages of boron can be seen in Figure 5.12b. The density of states at the Fermi level increased as the percentage of boron increased, as the tallest peak of cobalt in the minority d band moves towards the Fermi level, decreasing the exchange splitting.[226]

Konč et al. studied the saturation magnetisation of CoB alloys with different compositions. They described the decrease in moments as the boron content increased as due to electron transfer from boron atoms to the holes of the cobalt atom.[227] Asahi et al. and Agui et al. investigated CoB/Pd multilayers, sputtered at 260°C with added N_2 gas during the growth, to change the grain size. It was shown by Asahi et al. that adding B to Co can reduce cluster sizes. Agui et al. showed a trend in the CoB magnetisation that was constant between 16 and 8 Å, then started to decrease as the thickness decreased down to 2 Å.[228] Agui et al. reported that the crystal grain size in the CoB was 15 - 17 nm.[228]

Lavrijsen et al. studied the dependence of domain wall pinning for different compositions of Co and B. They used PMA stacks, which sandwiched the CoB with Pt, and found that the increase in boron reduces the domain wall pinning site density and/or strength.[225] Ngo et al. also investigated domain wall speeds in CoB/Ni based nanowires. They confirmed a reduction in pinning due to reducing the number of pinning sites and henceforth enhancing domain wall velocity. They commented that due to boron's small atomic radius occupying vacancies in the Co, diffusion between layers was reduced, allowing it to maintain magnetic properties despite exposure to air or heating from currents.[229]

Additionally, CoB based samples have been used in experiments regarding tilt free domain wall motion [230], measuring the stiffness and damping of spin waves [231] and skyrmion hosting stacks investigating the dependence of skyrmion diameter on the skyrmion Hall angle.[232]

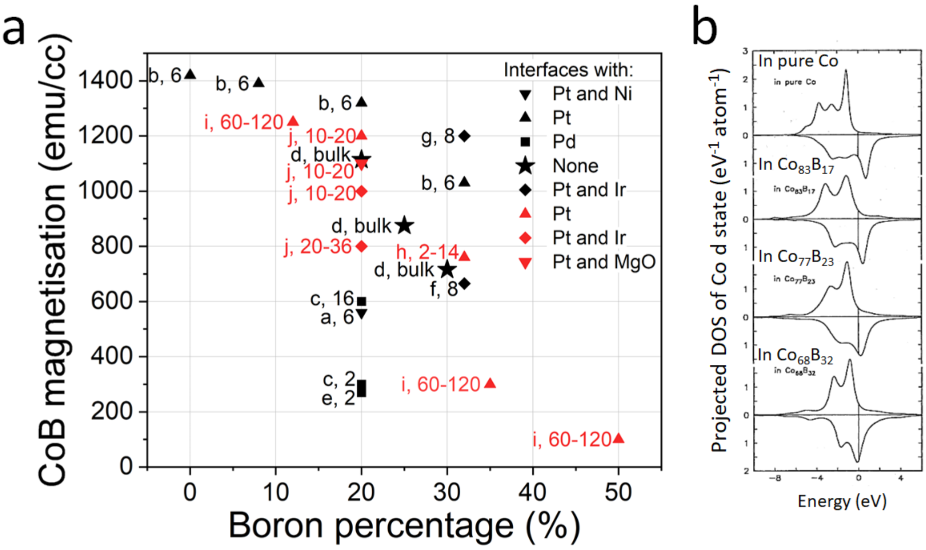

Figure 5.12: The graph shows the boron percentage in a CoB sample compared to its reported magnetisation. The red symbols are worked out using a thickness series (VSM method) and the black symbols just used one CoB thickness. The type of symbol represents the interfacial materials with the CoB in the samples. The number labels show the CoB thickness in Å. The letters represent the references: a-[229], b-[225], c-[228], d-[227], e-[233], f-[230], g-[232], h-[234], i-[231], j-[235]. All samples except for reference d were grown via sputtering, and measurements were performed via VSM, SQUID or MOKE for all samples except from reference c, which used XMCD on the Co edge. b) is taken from Reference [226], it shows the predicted density of states of the d band of Co in CoB alloys, where zero energy is the Fermi level.

From Figure 5.12a, a trend can be seen between the CoB magnetisation and the percentage of boron to Co, the lowest magnetisation is shown for $Co_{50}B_{50}$, and the highest for $Co_{92}B_8$. This trend can be assigned a linear fit: CoB magnetisation = (-28.2 × Boron percentage) + 1506.4. Of course, there are variations for individual samples due to different CoB thicknesses, for example, when the CoB thickness is 2 Å, the magnetisation is much lower than other samples for the sample CoB composition. Also, for those samples in which the magnetisation was calculated without factoring in any proximity effects (black symbols which used SQUID VSM or MOKE), and differences in growth conditions may also cause variation. Furthermore, the CoB thicknesses used in a thickness series to measure the magnetisation have ranges which are either only considering small thicknesses (<36 Å), or not considering small thicknesses (>60 Å), which may lead to some inaccuracies.

In 2021, Satchell et al. used CoB samples with Pt interfaces to make Josephson junctions with

PMA. Upon analysis of the CoB magnetisation via the VSM method, they found that below 6 Å, the moment/area diverted from its linear trend against CoB thickness and exhibited a down turn. This was explained by an inhomogeneous CoB layer below 6 Å, though the Pt appeared to have stabilised the magnetisation allowing a magnetic response for CoB thicknesses as low as 2 Å. They showed a magnetic response from the Pt of (46 ± 9) μemu/cm^2, taken from the y-axis intercept of the linear fit. The down turn was modelled using this equation,

$$\text{moment/area} = \begin{cases} (\text{Mx}+\text{y}_{int})(d/d_{crit}) & \text{for } 0 < \text{d} < \text{d}_{crit} \\ \text{Mx}+\text{y}_{int} & \text{for d} \geq d_{crit} \end{cases} \tag{5.3}$$

where M is the gradient of the linear fit (the magnetisation), y_{int} is the y-axis intercept, d_{crit} is the last thickness at which the CoB layer coverage is 100% before becoming inhomogeneous. Figure 5.13b displays the down turn and fit.[234]

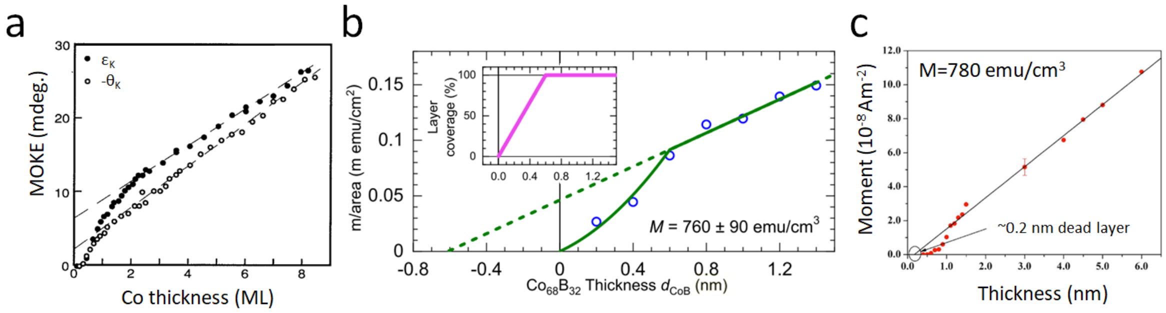

Figure 5.13: a) shows a plot of Co thickness in monolayers against MOKE signal, showing a down turn below around 2 ML (i.e. around 7 Å).[189] b) shows the results of Satchell et al. for sputtered Pt/CoB/Pt samples, plotting moment/area against CoB thickness. The inset shows their partial layer coverage model and the magnetisation taken from the gradient of the linear fit was 760 emu/cm^3.[234] c) shows a plot of CoFeB/MgO samples from Oguz et al., plotting CoFeB thickness against moment. This plot shows a 0.2 nm dead layer and a magnetisation of 780 emu/cm^3. There is also a down turn visible below 10 Å.[220]

Oguz et al. showed a similar down turn in their results for sputtered CoFeB samples interfaced with MgO. They also proposed that the shape of the curve suggested that the ultra thin films became granular and behaved paramagnetically. They calculated the size of the paramagnetic particles by fitting the data to a Langevin function with Equation 5.4,

$$M/M_S \sim (\coth x - 1/x) \tag{5.4}$$

where x = mB/k$_B$T, m is the moment of the magnetic grain (Am^2), k$_B$ is the Boltzmann constant.[220]

Finally, Tan et al. researched CoB based multilayers with Pt, Ir and MgO interfaces. They performed magnetisation measurements using an alternating gradient magnetometer and showed that for Pt(50 Å)/CoB(x)/Ir(10 Å) samples, there was a dead layer of 4 Å, as the linear fit to the moment/area vs. CoB thickness data crossed the x-axis at 4 Å. Contrary to this, they showed that for Ir(10 Å)/CoB(x)/Pt(50 Å) the linear fit crossed the x-axis at -3 Å and for Pt(50 Å)/CoB(x)/Pt(50 Å) samples at -6 Å. This would signify that there was a dead layer in the first case, and induced moments in the second two cases, further suggesting asymmetry between the upper and lower interfaces, as seen with Co. It is true that Pt tends to contribute more moments at the top interface, however, the range of CoB thicknesses used in this study was small and were different for the different samples. This could have caused some inaccuracy in these values or the magnetisation values.

To summarise the literature reports on the magnetisation and proximity effects of CoB:

- As the boron content in CoB increased, its magnetisation decreased.
- Many studies of the CoB magnetisation did not account for proximity effects or the CoB thickness range used was limiting.
- A down turn in the moment/area vs. CoB (and other FMs) thickness was present below around 8 Å due to inhomogeneous layers.

5.8 Co and CoB Results

We performed a simple study in which we grew stacks consisting of either Co or $Co_{68}B_{32}$ at varying thicknesses, sandwiched between 30 Å of either Ta, Pt or Ir. DC magnetron sputtering was used to deposit the stacks at a base pressure of $\sim 10^{-9}$ mTorr and an argon pressure of 4.6×10^{-3} mbar. The growth powers were 80 W, 30 W, 30 W, 50 W, and 50 W and the growth rates were 0.9 Å/s, 0.72 Å/s, 0.4 Å/s, 0.55 Å/s, and 0.24 Å/s for Ta, Pt, Ir, Co, and CoB respectively. The stacks were grown at room temperature on thermally oxidised silicon. An initial layer of Ta was used as a buffer for all samples, though in the Ta samples this layer also contributed to the interfacial effects.

We did methodical measurements of the saturation magnetisation of Co and CoB and how the interfaces with Pt, Ir and Ta affect it. Stacks were grown of Ta(30 Å)/CoB(x)/Ta(30 Å), Ta(30 Å)/Pt(30 Å)/CoB(x)/Pt(30 Å) and Ta(30 Å)/Ir(30 Å)/CoB(x)/Ir(30 Å), where the thickness of the CoB/Co was varied between 2 Å and 200 Å. The CoB was grown from a $Co_{68}B_{32}$ target and each sample was measured IP using SQUID magnetometry to find the moment of the sample. The area of a sample was found by photographing it next to a scale, then, after working out the number of pixels per area, making a trace of the samples edge to find the area (Figure 5.14b), it had a measurement error of 5%. The thickness of each layer for the samples was found by making a fit of a XRR scan with GenX (Figure 5.14c).[136]

To find the M_S, based on the equation: M_S = magnetic moment/(area × thickness), we plotted the moment/area against the Co/CoB thickness and fitted a straight line to the points (as shown in

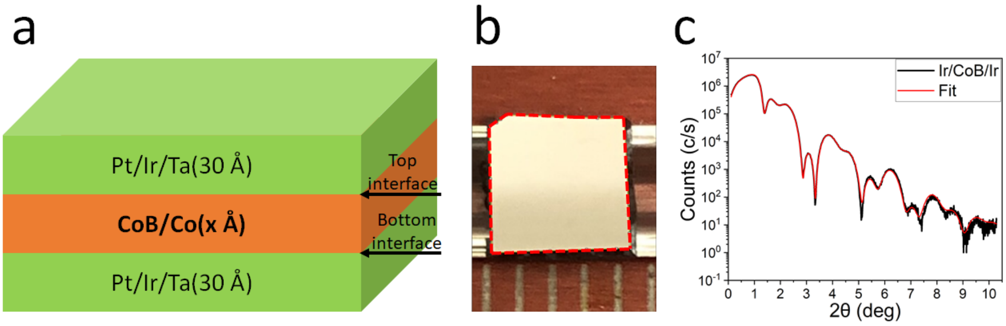

Figure 5.14: a) shows a schematic of the stack: either Co or CoB sandwiched by either two layers of Ta, Pt or Ir, with a nominal thickness of 30 Å. In the case of Pt and Ir, there was also a base layer of Ta. b) shows an example of a sample photographed with a scale to calculate the area. c) shows an example of a low angle x-ray scan (black line) with a fit (red line) performed using GenX [136] to get the thicknesses of the material components. Both b) and c) show the sample of Ta(29 Å)/Ir(33 Å)/CoB(10.2 Å)/Ir(30 Å).

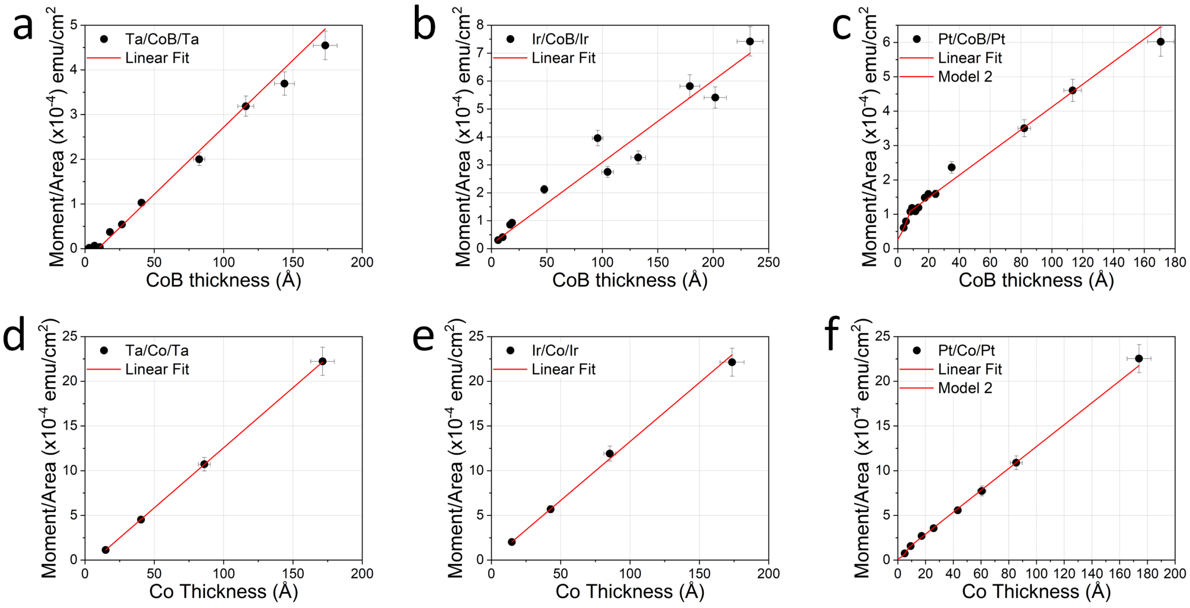

Figure 5.15: a) to f) all show plots of the NM(30 Å)/Co or CoB(x)/NM(30 Å) sample series, in which the Co/CoB thickness was varied. Plotted, is the Co/CoB thickness against each samples moment/area. a) to c) show CoB thin films and d) to f) show Co, a) and d) show Ta as the NM, b) and e) show Ir, and c) and f) show Pt. All graphs show a linear fit and c) and f) also show the fit of Equation 5.6 for below 8 Å.

Figure 5.15a). We took the gradient of the line to be equal to the M_S independent any interfacial effects (VSM method). The values of M_S worked out using this method, for each sample series, can be found in Table 5.1. When considering the linear fit, with 0 Å of CoB, the magnetic moment should be 0, and therefore the fit should cross the y-intercept at 0, however, this wasn't always the case. If it crossed the y-intercept after 0 it signified a dead layer. If it crossed the y-intercept before 0, it signified there were induced moments in the NM material. Then, from the x-axis, either the thickness of the dead layer was obtained, or an 'effective increase' in the Co/CoB thickness from the induced moments in the NM layer. These parameters are also listed in Table 5.1. We saw that in the case of Ta, the y-intercept was negative (and the x-intercept was positive) showing a dead layer. For both the Ir and Pt, the y-intercept was positive (and x-intercept negative) indicating induced moments. These results are also shown in Figure 5.16a, b and c.

It can be seen for Figure 5.16a, that the y-intercepts for the CoB samples were higher than Co for Pt and Ir with the induced moments, and for the Ta samples with a dead layer, the y-intercept was lower for the CoB linear fit than Co. The reverse trend is echoed in the x-intercept data, Figure 5.16b. As the x-intercept represents an 'effective increase' in the Co/CoB thickness from the induced moments in the NM layer, it is clear that due to CoB samples having a lower M_S than Co (Figure 5.16c), there is a larger 'effective thickness' of CoB needed to account for the induced moments within the Pt/Ir. Another difference between Co and CoB is that Co has a polycrystalline structure, whereas CoB is amorphous, and it has been shown that the type of lattice structure can affect the induced moments therefore this could be a reason for the difference.[161; 208] It was also evident that the linear fit to the samples with Pt had a higher y-intercept than the Ir series, which again, is echoed in the x-intercept data. This could be due to Pt being closer to the Stoner criterion than Ir. For both the Ir magnetisation and the Pt magnetisation, the CoB samples to Co samples had a ratio of around 1.85:1. The Pt magnetisation to Ir magnetisation in both CoB and Co had a ratio of around 5.6:1. The M_S was on average (1.55 ± 0.06) μ_B/atom for Co ((1300 ± 50) emu/cc) and (0.50 ± 0.03) μ_B/atom for CoB ((310 ± 20) emu/cc). The bulk value for Co at 0 K is 1.72 μ_B/atom [16] which is higher than our value, however, not unreasonable considering the measurements were performed at room temperatures and the FM thickness does not exceed 200 Å and therefore doesn't extend far into the bulk-like range. The percentage of boron in the CoB was presumed to be 32% based off the target material. To confirm the boron percentage, x-ray photoelectron spectroscopy (XPS) measurements were performed and found the percentage to be (51 ± 4)%. If a linear fit is made on Figure 5.12a, a magnetisation of 310 emu/cc corresponds to at the 48% boron content, suggesting the magnetisation is accurate for the boron percentage.

Figure 5.16d, shows the magnetisation of the Ir and Pt atoms for Co and CoB. These values were found from the y-intercept value of the linear fits for the NM/FM/NM sample series. The y-intercept represents the additional moment per area, which comes from the induced moments. The depth of the induced moments was estimated to be 10 Å, based on Figure 5.8b, therefore the

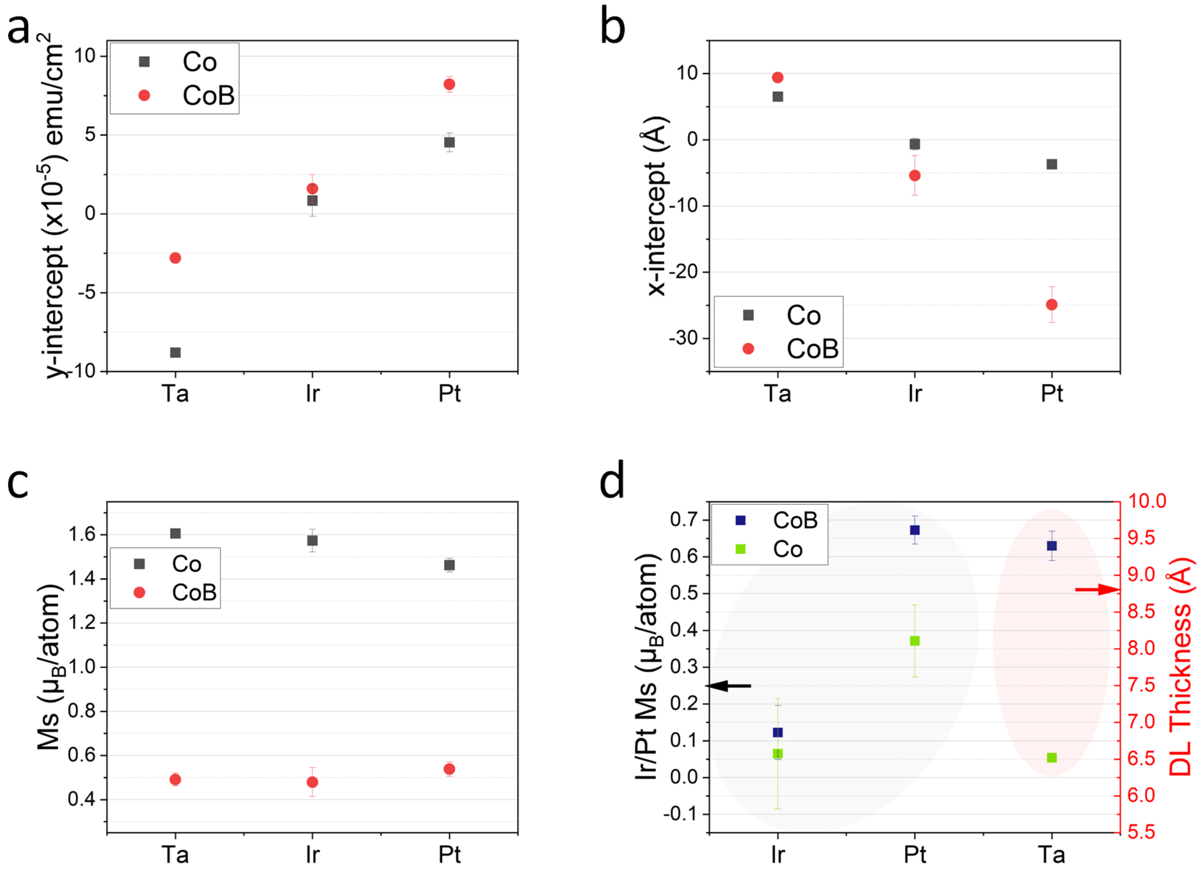

Figure 5.16: These figures show the parameters for Co/CoB samples sandwiched between Ta, Ir or Pt. a) the value of the y-intercept i.e. the induced moments/area for Pt and Ir, and the effective decrease in moments/area for Ta, from Figure 5.15 which is in units of the FM moment/area. b) the x-intercept, i.e. the dead layer thickness for Ta and the effective increase in Co/CoB thickness for Pt and Ir, which is in units of the FM thickness. c) the saturation magnetisation (M_S) of Co/CoB, which was taken from the gradient of the linear fits in Figure 5.15. d) shows the magnetic moment per atom induced in the Pt and Ir, plus, the DL thickness at a FM/Ta interface for Co and CoB. These values were found under the assumptions that the two interfaces have a symmetric moment, and the Pt/Ir magnetisation depth is 10 Å.

Stack	y-intercept x10^{-5} (emu/cm^2)	x-intercept (Å)	Slope (emu/cc)
Ta(30)/CoB(x)/Ta(30)	-2.8±0.2	9.4±0.2	300±20
Ir(30)/CoB(x)/Ir(30)	1.6±0.9	-5.4±3	290±40
Pt(30)/CoB(x)/Pt(30)	8.2±0.5	-25±3	330±20
Ta(30)/Co(x)/Ta(30)	-8.8±0.1	6.52±0.06	1345±5
Ir(30)/Co(x)/Ir(30)	1±1	-1±1	1320±40
Pt(30)/Co(x)/Pt(30)	4.5±0.6	-3.7±0.6	1220±30

Table 5.1: The y-intercept signifies the additional or reduced moment/area from both FM/NM interfaces which is positive in the presence of induced magnetism and negative with the presence of a dead layer. The x-intercept signifies 'effective increase' in Co/CoB thickness from both interfaces in the case of Pt and Ir interfaces and the dead layer thickness from both interfaces in the case of the Ta. The gradient of the slope represents the M_S of the FM material, irrespective of the proximity effects.

magnetisation could be approximated. These approximations may under estimate the interfacial moments as it is expected that in the 10 Å of polarised moments within the NM, that the moment decays over this length. The magnetisation per interface is shown, however, under the assumption that the top and bottom interfaces hold an equal moment.

For the Co and CoB samples, the values of the magnetisation of Ir was (0.1 ± 0.1) μ_B/atom (under the assumption of symmetric interfaces), which has a large error, to the point that the magnetisation could tend to zero. It is therefore lower than the magnetisation values found in the literature, though dead layers were mainly found when using the VSM method.

For Pt/Co interfaces (under the assumption of symmetric interfaces) was (0.4 ± 0.1) μ_B/atom, which is within the wide range of values found within the literature. Based off the literature, it is likely that there is in fact, asymmetry in the moments at each interface (Figure 5.8a). If this asymmetry for the top to the bottom interface is around 2:1, as found by Lau et al. [97], it put the top and bottom magnetisation of Pt for Co at (0.5 ± 0.1) μ_B/atom and (0.25 ± 0.07) μ_B/atom, respectively, which agrees with literature values. It puts the magnetisation for the top and bottom Pt interface with CoB at (0.90 ± 0.05) μ_B/atom and (0.45 ± 0.03) μ_B/atom, respectively, although there were no comparable literature values found, the top interface value was higher than expected. Even if like Moskaltsova et al. [32], the ratio is lower (around 1.3:1), the top Pt interface is still (0.76 ± 0.04) μ_B/atom for CoB, which is higher than any literature values found for the magnetisation of Pt interfaced with Co.

The Ta DL thickness for the Co samples was (6.53 ± 0.06) Å (under the assumption of symmetric interfaces), which sits within the range of values found within the literature, comparable to those of References [194] and [217]. The DL thickness for the CoB samples was higher at (9.4 ± 0.2) Å (under the assumption of symmetric interfaces), though still within the range of DL thicknesses found in the literature.[218]

Despite this, it is likely that there is asymmetry, as the roughness of the bottom interface (NM/FM) does not match the roughness of the top interface (FM/NM), as shown in Figure 5.17. The bottom interfaces show a more flat-like trend in roughness compared to FM thickness, being particularly high in the Ta/CoB samples (potentially due to an unpredictable difference in growth conditions), and in the samples with low FM thicknesses. The CoB samples tended to show higher roughness than the Co samples, which was also true for the top interface (FM/NM). However, at the top interfaces, there was an increase in roughness as the FM thickness increased.

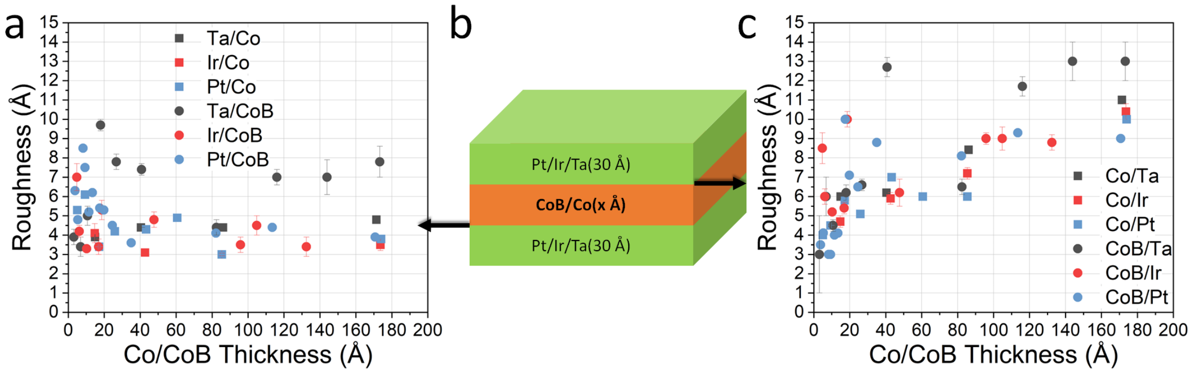

Figure 5.17: a) shows a plot of the FM (Co or CoB) thickness against the roughness at the bottom interface - as indicated in the diagram of b). c) shows the FM (Co or CoB) thickness against the roughness at the top interface - as indicated in the diagram of b). The squares represent Co samples, and the circles represent CoB. The black, red and blue symbols, represent Ta, Ir and Pt, respectively.

When fitted using GenX, the samples of Ta/CoB/Ta consistently showed a high level of oxidation, leaving the top Ta layer thinner, ∼25 Å, and a large oxide layer, ∼20 Å. Platinum and iridium showed little oxidation. The Pt/Ir top layer thicknesses showed an expected thicknesses of ∼30 Å, followed by a layer of, on average, (4 ± 1) Å of an oxide material.

Using the values in Table 5.1, as we know the induced moment/area from the Pt/Ir for the two interfaces, this can be subtracted from the total moment/area of each sample and the magnetisation recalculated. In the case of Ta, the total thickness of the dead layers in a Ta/FM/Ta sample can be subtracted from the FM thickness, and the magnetisation recalculated. The difference in the magnetisation can be seen in Figure 5.18, when proximity effects are not considered in magnetisation calculations, this has a large effect on the magnetisation for thin films (<100 Å). In the case of Pt and Ir (particularly Pt) the magnetisation was over estimated, and in the case of Ta,

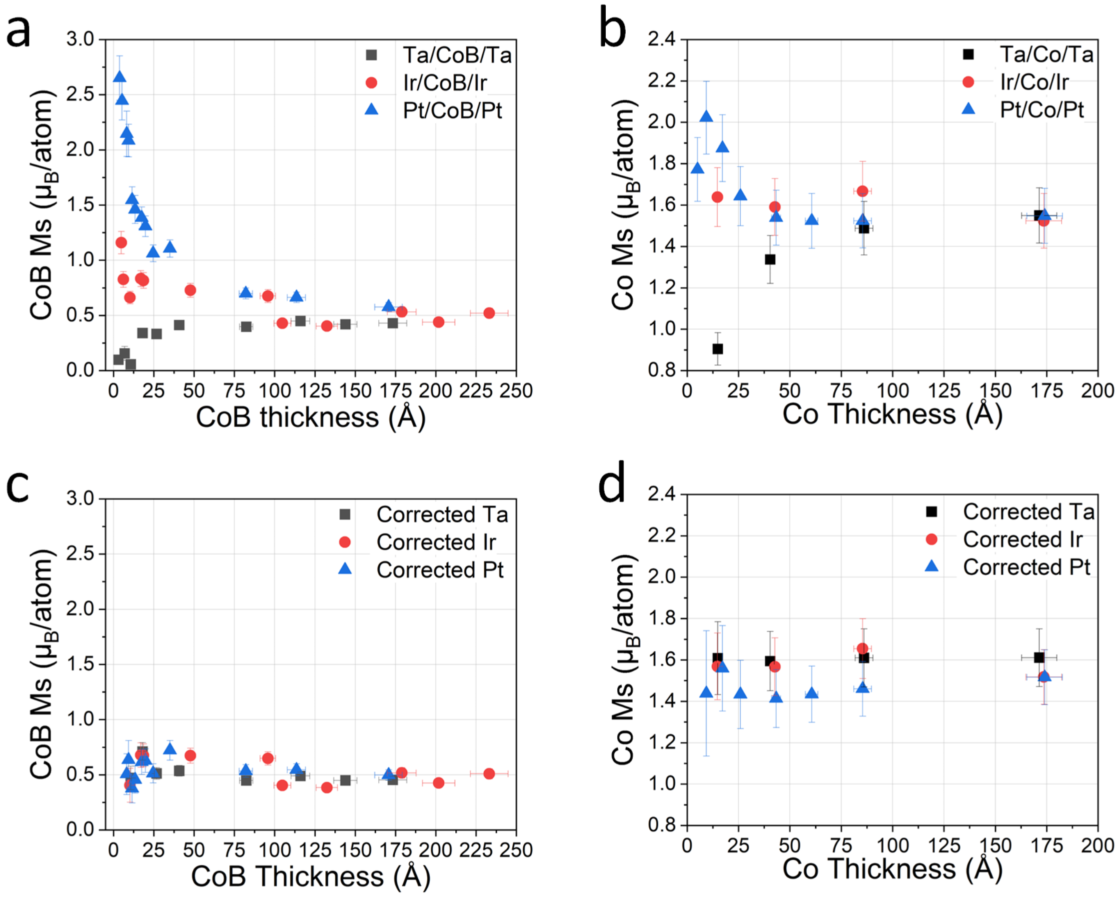

Figure 5.18: a) and b) represent the magnetisation against FM thickness worked out for CoB and Co, sandwiched between Ta, Pt and Ir, when only the thickness of the FM is considered in the calculation, discarding proximity effects. c) and d) show the magnetisation of Co and CoB, sandwiched between Ta, Pt and Ir, when the proximity effects are considered and for Pt and Ir samples, the induced moments are subtracted, and for the Ta samples, the dead layer thickness is subtracted.

the magnetisation was underestimated. With the corrections applied, the magnetisation followed a more steady value down to low FM thicknesses. Although showing a steady trend in M_S, the values for the Pt/Co/Pt samples were consistently lower than for the Ir and Ta, as was the magnetisation found from the gradient of the linear fit of the moment/area vs. Co thickness plot. The reason for this was not clear. The average value of the corrected M_S from Figures 5.18c and d, was (0.53 ± 0.09) μ_B/atom for CoB and for Co, (1.5 ± 0.2) μ_B/atom.

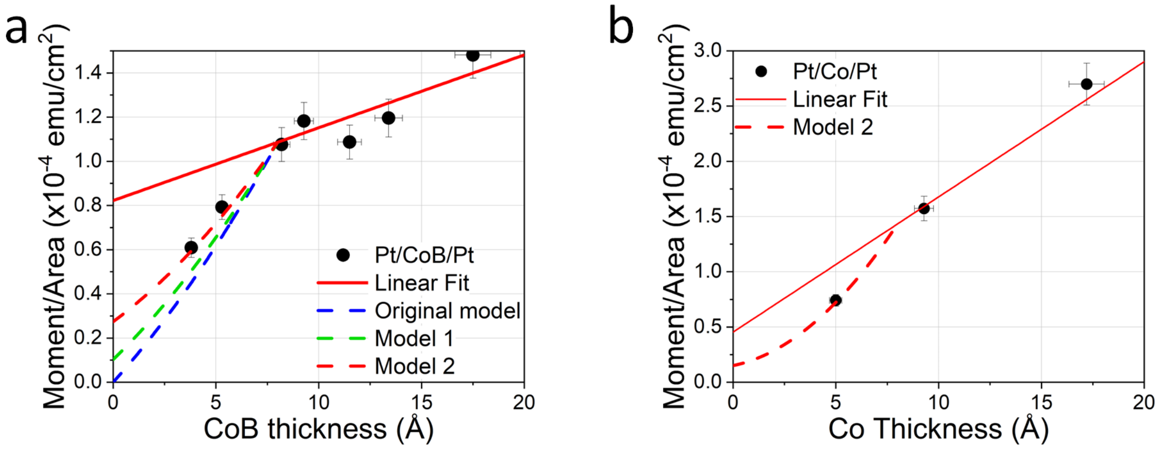

Figure 5.19: a) shows a zoomed in part of Figure 5.15c, the Pt/CoB/Pt sample series, including the linear fit. Additionally are fits from the original model - Equation 5.3, model 1 - Equation 5.5 and model 2 - Equation 5.6. b) shows a zoomed in part of Figure 5.15f, for the Pt/Co/Pt samples, showing the linear fit and the fit from model 2 - Equation 5.6.

In these corrections, values below 8 Å were not included as it was shown that they show a different relationship between the moment/area and FM thickness, exhibiting a down turn. This was due to the FM material no longer forming a continuous layer. In the case of the sample series with induced moments, a magnetic signal was still observed, however, in the Ta samples below a critical thickness of around 8 Å, the samples no longer exhibited a measurable magnetic moment.[220; 234] The model used by Satchell et al. is shown in Equation 5.3, this model was tested against our Pt series data and referred to as 'original model' in Figure 5.19. The model, however, reduces the moment/area at a rate of 1/d_{crit} and does not consider that even when there is a discontinuous FM layer below a critical thickness (d_{crit}), there would still be induced moments. Model 1, then considers that there are induced moments that decrease at the same rate as the moment/area decreases, see Equation 5.5,

$$\text{moment/area} = \begin{cases} (\mathrm{Mx}+\mathrm{y}_{int})(d/\mathrm{d}_{crit}) \text{ - } (\mathrm{y}_{int}/\mathrm{d}_{crit})(\mathrm{x}/\mathrm{x}\text{-}1) & \text{for } 0 < \mathrm{d} < \mathrm{d}_{crit} \\ \mathrm{Mx}+\mathrm{y}_{int} & \text{for d} \geq d_{crit} \end{cases} \tag{5.5}$$

where M is the gradient of the linear line (the magnetisation), y_{int} is the y-axis intercept, d_{crit} is the thickness at which the CoB layer coverage is 100%. This, however, does not consider that with the Pt filling the gaps between the CoB islands, may come the opportunity for a higher percentage of induced moments in the Pt. Therefore, the rate in which the induced moment decreased was instead fitted to the data, and showed a reduction rate of 1/3. This is model 2, Equation 5.6:

$$\text{moment/area} = \begin{cases} (\mathrm{Mx}+\mathrm{y}_{int})(d/d_{crit}) \text{ - } (\mathrm{y}_{int}/3)(\mathrm{x}/\mathrm{x}\text{-}1) & \text{for } 0 < \mathrm{d} < \mathrm{d}_{crit} \\ \mathrm{Mx}+\mathrm{y}_{int} & \text{for d} \geq d_{crit} \end{cases} \tag{5.6}$$

This model also fits with the Pt/Co/Pt samples in Figure 5.19, however, there was only one sample below the 8 Å critical thickness, therefore a definite trend could not be confirmed.

5.9 Conclusions

To conclude, a review of the literature studies into dead layers and induced moments at FM/NM interfaces was done for Ir, Ta and Pt, and the main results were summarised in bullet points throughout the chapter. Three main methods were used to investigate this, via SQUID/VSM, XMCD, and XRMR. To find outright values of the induced magnetisation within materials, XRMR with its ability to consider the depth dependence appeared to be the best way to investigate, however, the VSM method could be used more easily to investigated a specific stack to work out the total interfacial effects. For calculating dead layer thicknesses, the VSM method was the main method used, though again, it gives a sum of the effects which will include both interfaces, and the dead layers may not be symmetrical at the top and bottom of the FM. The VSM method could be used most effectively, if one interface is with a material that does not cause a dead layer or exhibit spin polarisation, however, even Au and Cu have been shown to possess some induced moments.[236–238] We confirmed that the samples with Pt and Co agreed with literature values of magnetisation of the Pt, though for Ir, the magnetisation found was lower. In the case of CoB interfaced with Pt, the magnetic moment calculated was higher than any value found for Pt with Co alone, which was unexpected considering that CoB has a much lower magnetisation than Co. The Ir magnetisation with CoB was in the range of moments found for Co/Ir interfaces, although, larger than our value of Ir interfaced with Co. The dead layer thicknesses in both Co and CoB samples with Ta interfaces, were confirmed to be within the range of those found in literature for FM/Ta interfaces. A general difference in the roughness at the top and bottom interface was found, the top interface being rougher, which would most likely cause asymmetry between the top and bottom interfacial induced moments, however, the VSM method cannot determine this difference. Finally, it was shown that for the samples with Pt, at thicknesses less than 8 Å, a down turn is visible signifying a discontinuous growth layer. This was fitted using a model which accounted for the fact that there would still be some induced moments within the sample.

Therefore, in order to accurately calculate the M_S of a thin magnetic film, it is clear that the proximity effects should be accounted for. The induced moments and dead layer thickness can be tuned based on firstly, the growth conditions/method which will determine the degree of roughness. Mainly, the materials and their thicknesses, which can change the amount of intermixing and lattice structures, and therefore the amount of hybridisation. Each interface must be fully accounted for which must be considered when studying bilayers vs. multilayers. Finally, more controllable, the composition of the FM, and measurement temperature can also have an effect. For a sample in which it is important to know the the magnetisation value accurately, it should be advised to grow a sample series of the sample, varying the FM thickness, and use the VSM method to determine the magnetisation.

Chapter 6

Determination of the Interfacial DMI

6.1 Introduction

The DMI in materials is an important property which can nucleate Néel domain walls and therefore skyrmions. This is significant as skyrmions have a lot of potential storage or logic device applications and the DMI is a prominent factor in controlling skyrmion characteristics, for example, stability, diameter and density if considering a skyrmion lattice. It is, therefore, essential to accurately calculate the DMI strength, which is obtained by considering the saturation magnetisation, the effective anisotropy, the exchange stiffness, and the DMI field within a sample (Equation 2.40). In thin PMA films, such as Pt/Co/Pt or Pt/Co/Ir multilayers, the DMI is an interfacial effect which acts like an effective IP field causing variations in the characteristics of the domain walls within the sample. Néel walls are favoured energetically over Bloch walls when strong DMI is present.[4; 239; 240] The DMI strength can control the stability of the skyrmions and other magnetic chiral patterns in a sample. The sign and magnitude of it can be adjusted by the heavy metal material combination on the top and bottom FM interface. For example, a symmetric Pt/Co/Pt sample may have a lower DMI due to the two interfaces cancelling out the effect, whereas an asymmetric interface, such as Pt/Co/Ir or Ta, can cause an addition of the interfacial DMI due to Ir and Ta having oppositely signed DMI values to Pt.[35; 59; 240] Although, note that this is a debated topic due to studies also reporting that Pt and Ir have the same sign DMI.[142–145]

This chapter was done in collaboration with Reference [4]. The values of the DMI strength were investigated thoroughly for PMA Co thin films supporting Pt, Ir and Ta interfaces, both symmetric and asymmetric. This was performed via the bubble expansion method, and compared to measurements taken on the same sample at other institutes using both the bubble expansion method and the Brillouin light scattering method (BLS). Measuring the DMI strength via bubble expansions, a domain wall velocity based measurement, is more accessible for most laboratories and doesn't require the elaborate set up used for BLS measurements. The comparison was made between 5 laboratories: The University of Leeds (our measurements), The National Institute of Metrology Research (INRIM), The National Institute of Standards and Technology (NIST), Korea Research Institute of Standards and Science (KRISS) and The Official Institute of Materials in Perugia (UPerugia). The samples were prepared at the University of Leeds on two 10x10 mm substrates, the samples were divided into 4 parts (post growth) and sent to the different laboratories. The values reported in this thesis may differ slightly from Reference [4] due to a different method being used to calculate the proximity effects, however, this does not affect any overall trends or results.

6.1.1 Brillouin Light Scattering

BLS is a technique in which photons are inelastically scattered by vibrations of low frequencies due to phonons (thermal vibrations) or magnons (changes in magnetic order). In this case, magnons within a magnetic sample interact with a laser (photon) incident upon it. In a perfect system, a magnon propagating towards the incident laser would be annihilated and the photon would be backscattered with higher energy (anti-Stokes scattering). However, the magnon propagating away from the incident laser causes the opposite effect and the backscattered photon would have lower energy. Based on this concept, from the energy of the backscattered photon, the frequency of propagating spin waves can be determined. Due to a non-reciprocal propagation caused by DMI within a sample, the sign and magnitude of the DMI strength can be determined from the frequency shift.[146; 241; 242]

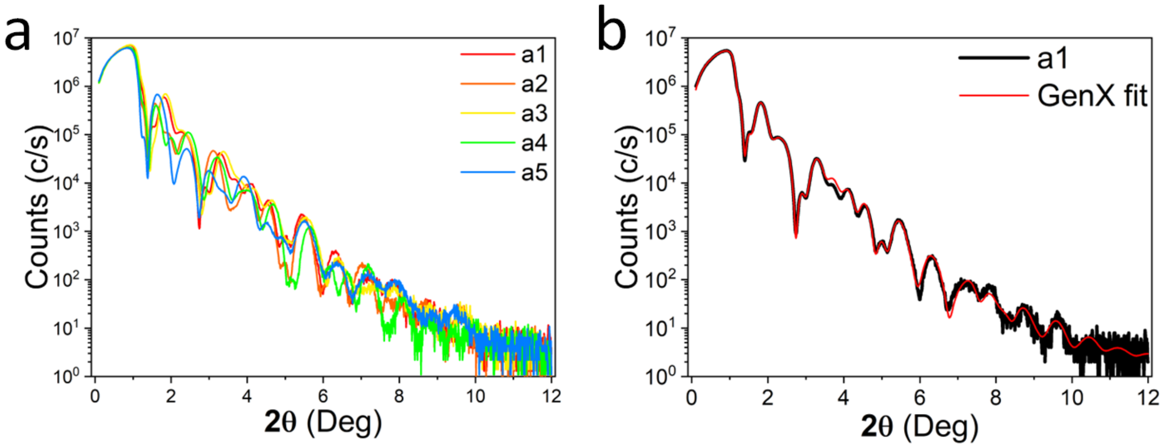

Figure 6.1: a) shows the low angle x-ray scans of all 5 samples overlaid. b) shows a1 with a fit performed by GenX in order to evaluate the thicknesses, roughness and densities in the sample layers.[136]

6.1.2 Sample Characterisation

In this chapter, samples were grown via sputtering onto Si substrates. The samples consisted of Ta/Pt/Co/x/Ta, where x was a layer of either: Pt(37 Å), Pt(19 Å), Ir(35 Å), Ir(16 Å) or no layer (a1 to a5 in Table 6.1). The intended thickness of the lower Pt layer was 40 Å, and 10 Å for the Co for all samples, however, these differed slightly as found by performing low angle x-ray scans, as shown in Figure 6.1a, and using GenX fitting (an example is shown in Figure 6.1b).[136] The thicknesses are listed in Table 6.1. The PMA stacks with Ta, Pt, Co and Ir were grown with powers, 19 W, 9 W, 17 W, and 19 W respectively, and rates of 1.2 Å/s, 1.6 Å/s, 0.9 Å/s and 0.8 Å/s respectively. The pressure in the sputter chamber was originally to the order of 10^{-8} and became around 3x10^{-3} mbar after the Ar was introduced into the chamber at a 28 sccm flow rate. From the GenX fits, the densities of cobalt, platinum, iridium and tantalum were 97%, 98%, 101%, and 95% respectively, of their literature values.[9; 16] There was also indication of a tantalum oxide layer on top of the stack of around 20 Å, most likely intermixed with the Ta layer below it, and between the Ta base and the substrate, a thin tantalum oxide layer of around 3 Å. The roughness was estimated at the top Co interface to be on average (4.8 ± 0.5) Å, and (2.5 ± 0.3) Å at the bottom Co interface with Pt. From this sample set, we could investigate symmetric and asymmetric interface combinations with different materials, and the effect of different thicknesses of the material upon the Co.

Label	Sample structure
a1	Ta(65)/Pt(40)/Co(10.6)/Pt(37)/Ta(36)
a2	Ta(66)/Pt(38)/Co(10.7)/Pt(19)/Ta(35)
a3	Ta(61)/Pt(40)/Co(10.7)/Ir(35)/Ta(35)
a4	Ta(64)/Pt(37)/Co(10.1)/Ir(16)/Ta(37)
a5	Ta(66)/Pt(39)/Co(10.6)/Ta(37)

Table 6.1: This table shows the five samples measured throughout this chapter, next to their label. All thicknesses are in Å.

Figure 6.2 shows, the normalised hysteresis loops both IP and OP for the five samples. The OP loops in 6.2a, exhibited a square shape, confirming the PMA of the samples. The coercivity was similar for all samples at around 20 mT, except a4 which showed a slightly lower coercive field, and comparable to other values of similar samples in literature.[142] Figure 6.2b, shows IP linear hysteresis, there was more diversity between the loop shapes of different samples, including different saturation fields (summarised in Figure 6.4).

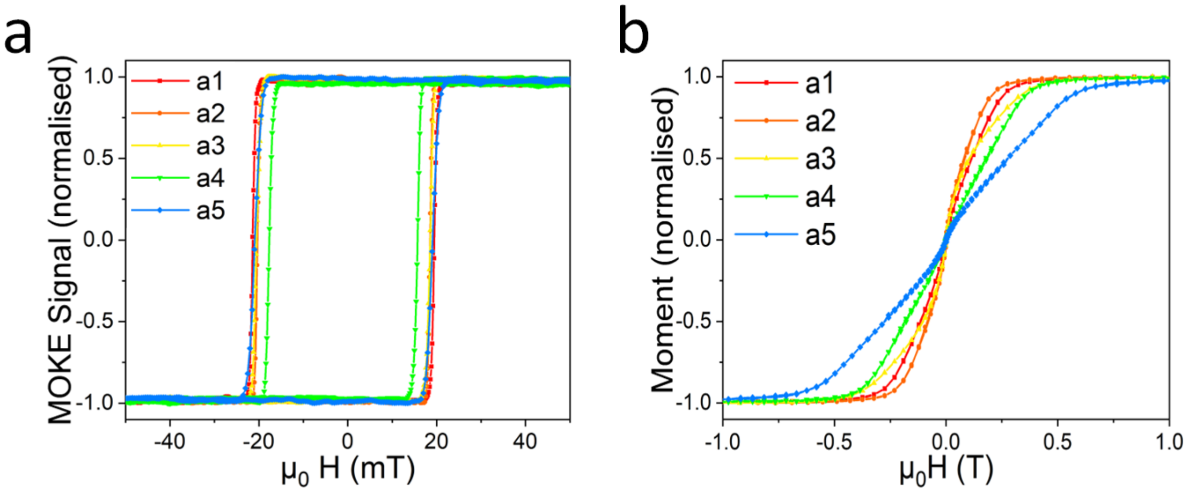

Figure 6.2: a) shows the OP hysteresis loops for samples a1 to a5, which were measured via MOKE, and normalised. b) shows the normalised moment measured IP by SQUID magnetometry of samples a1 to a5.

6.2 Saturation Magnetisation

The saturation magnetisation was originally calculated by measuring the magnetic moment of the sample via SQUID magnetometry, applying a correction factor, and using the equation M_S = moment/(thickness×area). The measurement error was 5%. The areas were determined as described in Chapter 5, by taking an image of the sample with a scale, calculating the pixel/mm ratio and measuring the circumference of the sample. The thickness of the ferromagnetic Co layer was used, which had a 5% measurement error from the XRR scans. These original magnetisation values (shown in Figure 6.4a) were similar to other values not corrected for proximity effects in literature.[142; 243]

As in Chapter 5, a thickness series (labelled a1-a5 series) was made for each of the samples in which each stack was grown multiple times with different Co thicknesses between 8 and 200 Å. The thicknesses of these samples were calculated via the growth rates, calibrated prior to the growth. The moment/area vs. Co thickness was plotted for each sample series, and a linear fit was performed, this is shown in Figure 6.3a for a1. The slope of the linear fit represented the magnetisation without any proximity effects. When positive, the y-axis intercept represented an induced moment/area at the FM interfaces, when negative, it represented a reduction in moment/area of the FM due to dead layers. When positive, the x-axis intercept represented the thickness of an interfacial dead layer, when negative, it described a representative additional Co thickness that would account for the additional moments.

The slopes for the five sample types are shown in Figure 6.3b, the average magnetisation was represented by the dotted line at (1260 ± 30) emu/cc (or (1.56 ± 0.03) μ_B/atom), this value is within the error of the value found in Chapter 5 for Co. The y-intercept values for each sample series are plotted in Figure 6.3c, and again, were comparable with the values in Chapter 5; in the a1 series, a value of (6 ± 2) emu/cm^2 was found, compared to (4.5 ± 0.6) emu/cm^2 for the Pt/Co/Pt samples in Chapter 5. The a3 series gave a value of (2 ± 2) emu/cm^2, compared to (1 ± 1) emu/cm^2 for the Ir/Co/Ir samples in Chapter 5, however here, Pt/Co/Ir was used which could explain why the value is slightly higher, as more moment tends to be induced at a Pt interface. In both cases, the values were close to zero with high error. Sample series a1 to a4 showed an induced moment, as expected from the results of Chapter 5. In a comparison of the a5 series to the Ta/Co/Ta samples in Chapter 5, a dead layer was shown for both, however, it was much less in the a5 series. This suggested that the dead layer at the Co/Ta interface caused a larger loss in moment than the moments induced at the Pt/Co interface, causing an overall reduction in measured magnetisation. However, it was less reduction than if there was Ta at both interfaces. It was also evident that the two samples of structure Pt/Co/Pt and Pt/Co/Ir, showed little dependence on the thickness of the top Pt(Ir) layer, as the linear fit parameters were similar for both 37(35) Å and 19(16) Å, supporting the argument that the proximity effects are negligible after 10 Å.

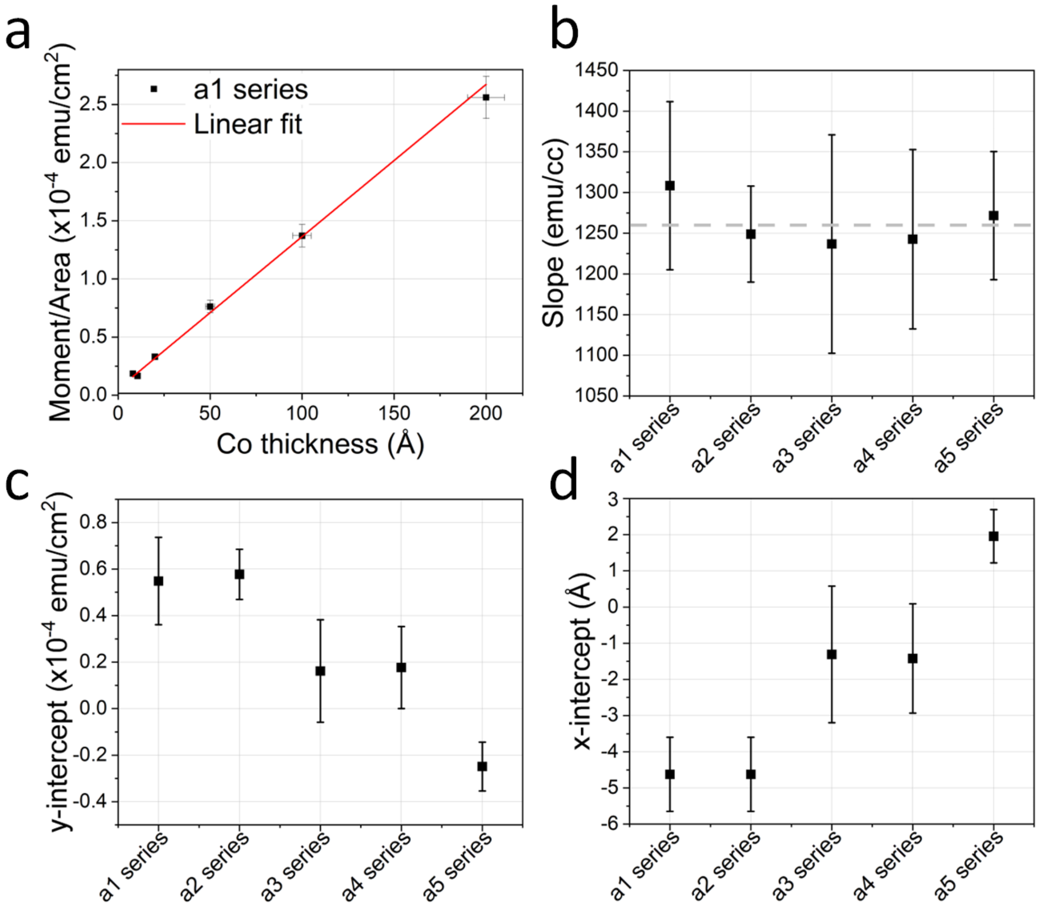

Figure 6.3: a) shows a plot of the moment/area against Co thickness for the a1 series, it is shown with a linear fit. b) shows the gradient of the slope (i.e. the magnetisation without any proximity effects) of the linear fit of each sample series in emu/cc. A dashed line denotes the average slope gradient and therefore the average magnetisation of Co - (1260 ± 30) emu/cc (or (1.56 ± 0.03) μ_B/atom). c) shows the value of the y-intercept from the linear fit for each series, which is in units of the FM moment/area. d) shows the x-intercept of the linear fits, for each series. It is in units of the FM thickness. Errors were extracted from the linear fits.

Following this, the saturation magnetisation for samples a1 to a5 was corrected to account for the proximity effects, from here forth values calculated using this corrected magnetisation will be referred to as 'corrected'. In the case of a1 to a4, which showed an overall increase in the expected moment, the extra moment/area was subtracted from the measured moment/area and the magnetisation was then recalculated, exhibiting a decrease. The change in M_S is depicted in Figure 6.4a and was more substantial for a1 and a2, than a3 and a4. On the other hand, for a5, there was an overall decrease in the expected moments hence the thickness of Co associated with this loss was subtracted from the total Co thickness and the magnetisation recalculated, exhibiting an increase. It was clear from the figure, that the M_S values, once corrected, were more agreeable compared to the original values which varied by ±0.46 μ_B/atom The corrected average was M_S=(1.3 ± 0.2) μ_B/atom. This is less than the literature value for Co, of 1.72 μ_B/atom[6], although, these measurements were taken at room temperature and the FM thickness was not bulk-like. The result was comparable to those presented in References [194; 244].

Figure 6.4b, shows the saturation field (H_{sat}) for each sample, based off the loops in Figure 6.2b, the values found were comparable to those in literature.[142] It was calculated by fitting a straight line along the saturated moment and the saturation field was established at the point below which the change in magnetic moment was more than 0.5 times the error in the saturated moment. The sample with Ta had a much higher saturation field than the other samples, and the samples with a thicker layer above the ferromagnet (a1 and a3) had a slightly higher saturation field than the samples with the thinner layer (a2 and a4).

6.3 Anisotropy

The next parameter calculated was the anisotropy, and as it was assumed from the hysteresis loops the samples exhibit PMA, we used two methods to calculate the effective anisotropy. When the OP, easy axis, hysteresis loop is square (therefore with larger domains) and the IP hard axis loop is linear, the effective anisotropy can be calculated using Equation 2.32, with the saturation field and the magnetisation (H_{sat} method). Despite the OP measurement showing a square hysteresis loop, the IP hysteresis loops do not possess solely linear behaviour (particularly at the point just before/after saturation), therefore a more accurate method to work out K_{eff} could be the standard integration method between the hard axis and easy axis hysteresis loops (area method).[22] In Figure 6.4c, we compare the difference in K_{eff} when using the H_{sat} method and the area method. The area method showed less error, due to high error in the saturation field, and showed considerably lower values, with some values decreasing by more than half. We deemed the area method more accurate in this case, and therefore used the values found via the area method in further equations.

We also compared the difference in values of K_{eff} when using the original hysteresis loops and

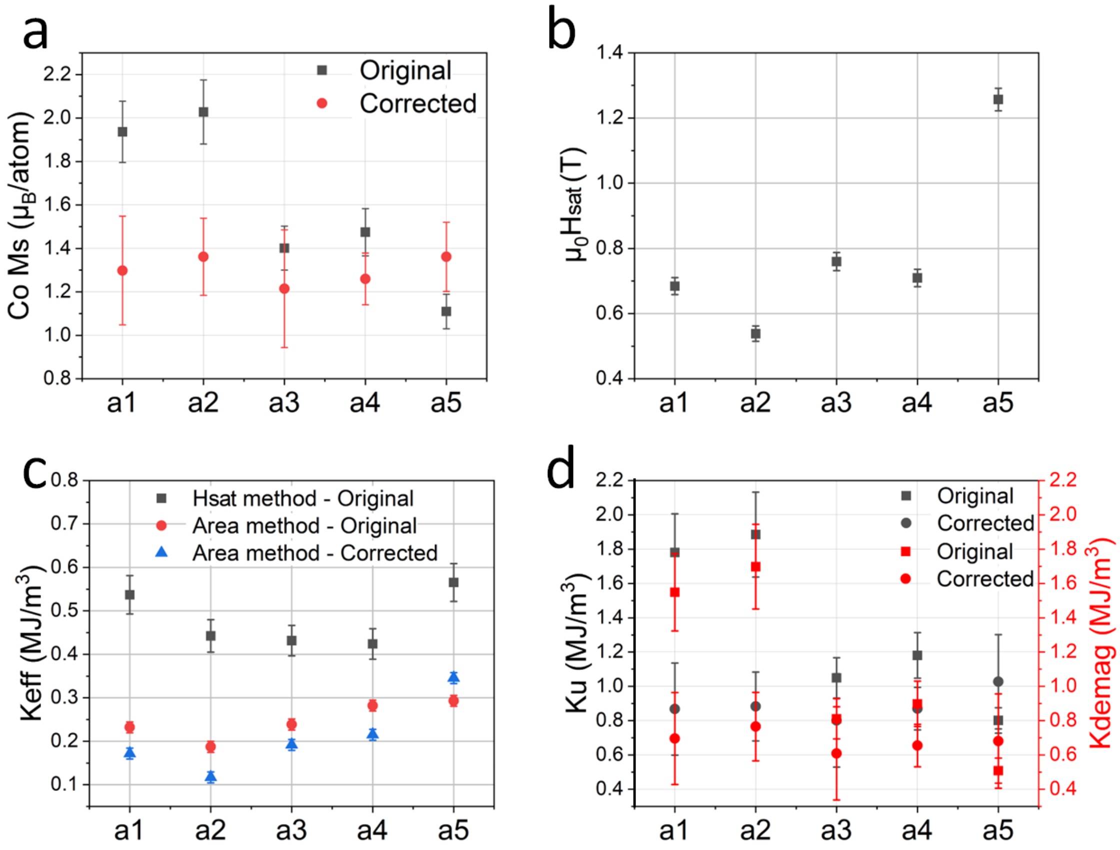

Figure 6.4: a) shows the values of M_S for samples a1 to a5 worked out using the measured moment and Co thickness, labelled as original. It also shows the magnetisation for samples a1 to a5 when corrected for proximity effects at the interfaces, labelled as corrected. b) shows the saturation field for a1 to a5. c) shows the effective anisotropy for samples a1 to a5 worked out via the H_{sat} method and the area method using the original values and the area method using the corrected values. d) shows the values of K_{demag}, worked out using Equation 2.30 with the original and corrected M_S. It also shows K_u, worked out using Equation 2.33 with original and corrected values. These used the values of K_{eff} found using the area method.

the corrected hysteresis loops. The difference was logical but less significant, in samples a1 to a4 there was a decrease of on average 27%, and in a5 an increase of 15%. The K_{eff} values matched values found in literature.[145] K_{demag} was also calculated using both the original values and the corrected values of M_S with Equation 2.30, solely to compare the difference in calculated values when proximity effects are not accounted for. Then, for the same purpose, K_u was calculated from Equation 2.33, using both the original and corrected values of K_{demag} and K_{eff} - these results are plotted in Figure 6.4d. For both K_{demag} and K_u, the original values were higher than the corrected values for a1 to a4, and vice versa for a5. All errors were propagated in the standard procedure.

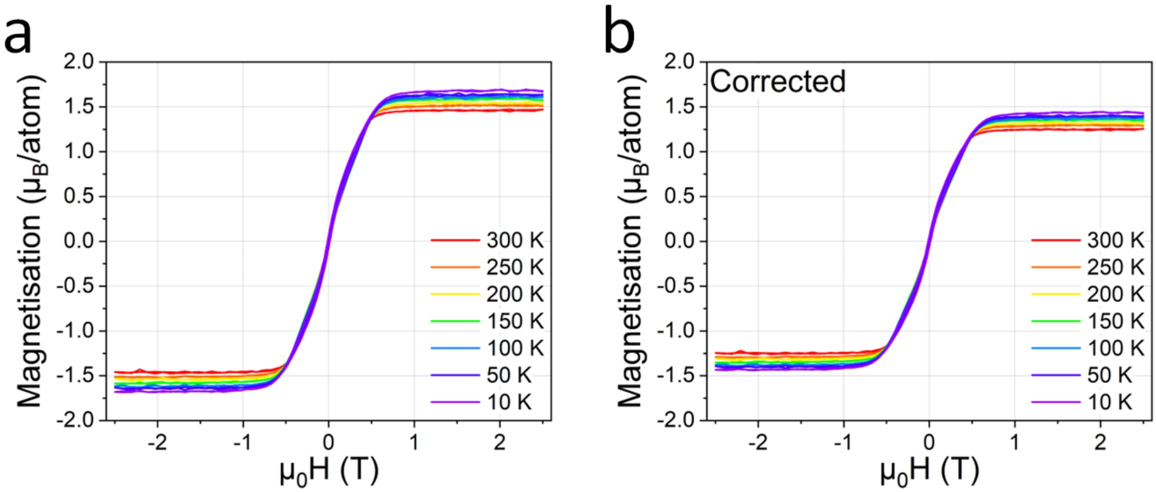

Figure 6.5: a) shows the magnetisation vs. magnetic field data from a SQUID measurement performed IP on sample a4, it shows the hysteresis loop over a range of temperatures between 10 K and 300 K. b) shows the same measurement, however, the magnetisation values have been corrected for proximity effects.

6.4 Exchange Stiffness

In order to determine the exchange stiffness, SQUID magnetometry measurements were performed as a function of temperature between 10 K and 300 K. An example of these measurements is shown in Figure 6.5a. Figure 6.5b also shows the hysteresis loops as a function of temperature, however, corrected. A python code was used to fit Bloch's law (Equation 2.19) to a plot of M_S vs. temperature, this is however, a fit designed for bulk materials. As we were using thin films, we also fitted a thin film approximation (Equation 2.25), as described in the 'magnons' section, to the data.[245] The g-factor was taken from literature to be 2.1 for FCC cobalt[17], where N=4, and the lattice constant was 3.54 Å. To perform the fits, the magnetisation at 0 K, $M_S(0)$, was required. The magnetisation was plotted against $T^{\frac{3}{2}}$, which allowed a straight line to be fitted to the data and therefore an estimated value of M_S when T=0 K, i.e. the y-intercept of the linear fit. This $M_S(0)$ value, specific to each sample, was used along with the Co thickness and the saturation fields for each sample to create the bulk and thin film Bloch's law fits for the original and corrected data - this can be seen in Figure 6.6.

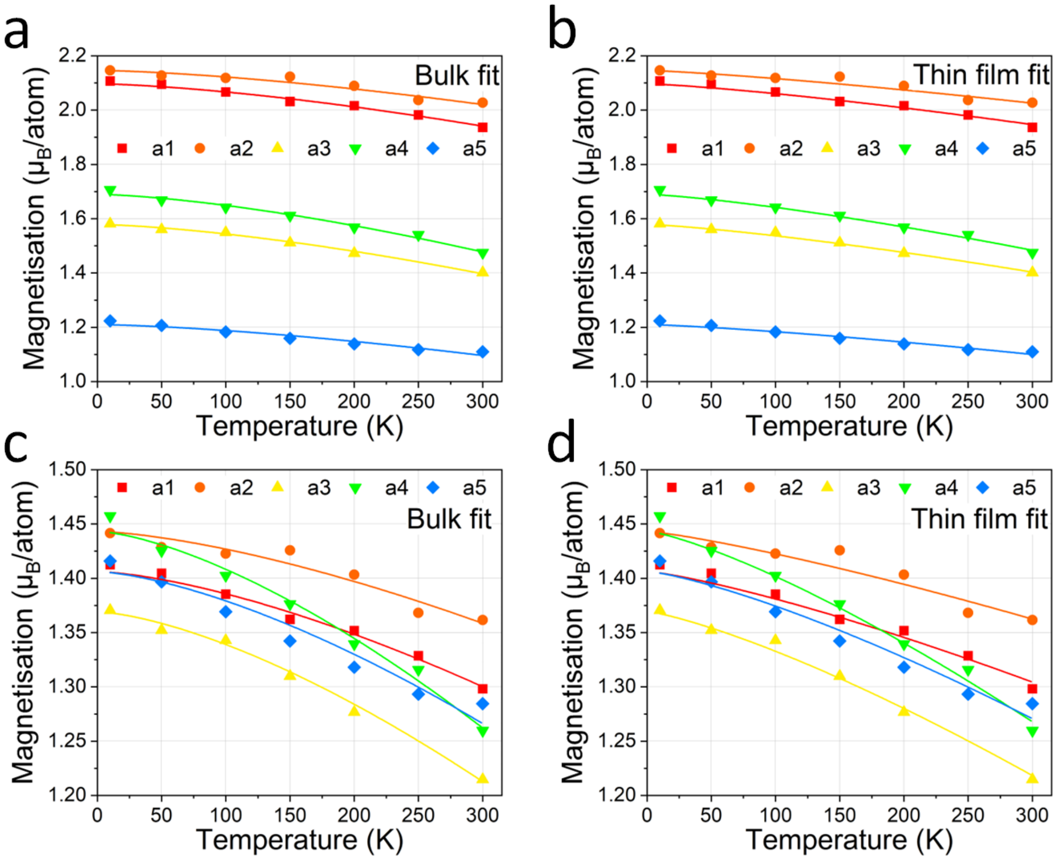

Figure 6.6: a) and c) show the magnetisation measured by SQUID magnetometry of samples a1 to a5 as a function of temperature, fitted using Equation 2.19, Bloch's law for bulk samples. b) and d) show the magnetisation measured by SQUID magnetometry of samples a1 to a5 as a function of temperature, fitted using Equation 2.25, Bloch's law for thin films. a) and b) show the fits for the original data, and c) and d) show the fits for the corrected data.

Based off these fits, two parameters were outputted, D_{sw}, the spinwave stiffness and A, the exchange stiffness (Equation 2.26). These values are plotted in Figure 6.7 for both the original and the corrected data, fitted via both the bulk and the thin film Bloch equations, errors were taken from the fits. Despite there being little difference in the appearance of the Bloch's law fits between the bulk and thin film, the spinwave stiffness and the exchange stiffness always supported a higher value using the thin film equation and also with the corrected data. There was little difference between the original and corrected values for a3 to a5, and only a small difference in samples a1 and a2.

Samples a1 and a2 sustained the largest difference between using the bulk and thin film method, however, on all samples the difference was not negligible. The thin film fit considers that the number of k-points in the thickness are not enough to perform an integration in the z-direction, and instead uses a sum, implying the thin film fit will be more correct for the thin film samples in this chapter. The thin film fit however, is not widely used in literature, most likely due to its complexity in comparison to the bulk law fit.[19; 20; 245] The thin film values of exchange stiffness shown in Figure 6.7b were not dissimilar to other literature values.[246; 247]

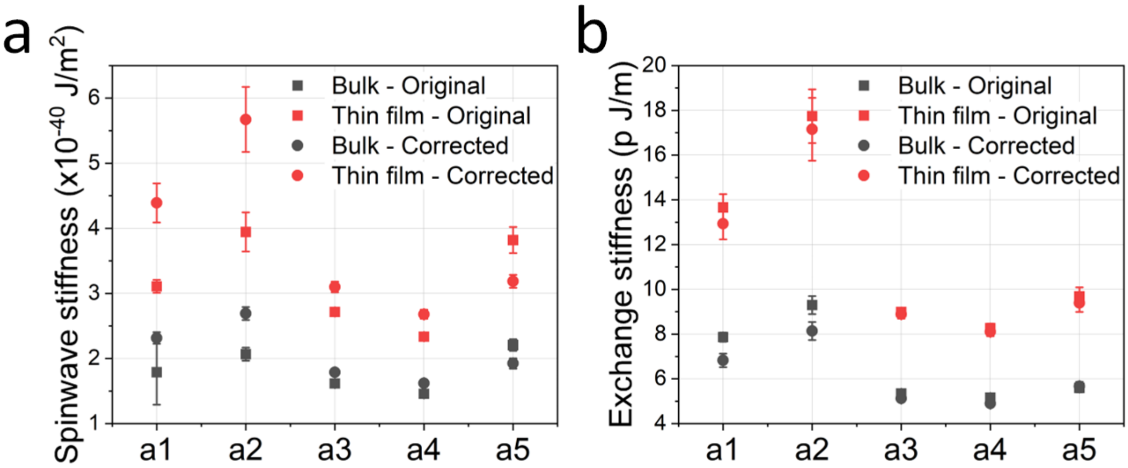

Figure 6.7: a) shows the spinwave stiffness for samples a1 to a5, calculated by fitting Bloch's bulk and thin film equation to the original and corrected data. b) shows the exchange stiffness for samples a1 to a5, calculated by fitting Bloch's bulk and thin film equation to the original and corrected data.

Two other parameters which are involved in the Bloch's law equations are n$_m$(T), related to the magnon density at temperature T, and η, the dimensionless prefactor for Bloch's law, proportional to the magnon density and dependent on the lattice type.[19; 20; 245] The difference between n$_m$(T) for the original values of a1 to a5 is shown in Figure 6.8c. All samples showed n$_m$(T)=0 at 0 K, followed by an almost linear increase by various degrees to 300 K. The trend for the corrected data is similar (for example in Figure 6.8a for the thin film equation), reaching only slightly higher values of n$_m$(T) in all but a5, where the corrected values end at a slightly lower value at 300 K than the original values. Figure 6.8b, shows the difference in the original n$_m$(T) when the bulk equation vs. the thin film equation of Bloch's law is used. The difference was more prominent, and showed a much steeper gradient to a higher n$_m$(T) value when fitted using the bulk equation. Figures 6.8d to f show the same plots, however, for η. In general, for the thin film approach, η decreased sharply as the temperature increased and then decreased more steadily after around 100

K. The values for the original and corrected data (6.8d) showed a similar trend as a function of temperature, however, the corrected data was shifted higher in the y-axis. The bulk version of η is a constant, as shown in Figure 6.8e, and much lower than the thin film equation fit values. Finally, 6.8f shows the difference between η for samples a1 to a5, all samples followed the same trend with temperature where η increased as the temperature decreased, however, this was to varying degrees for each sample.

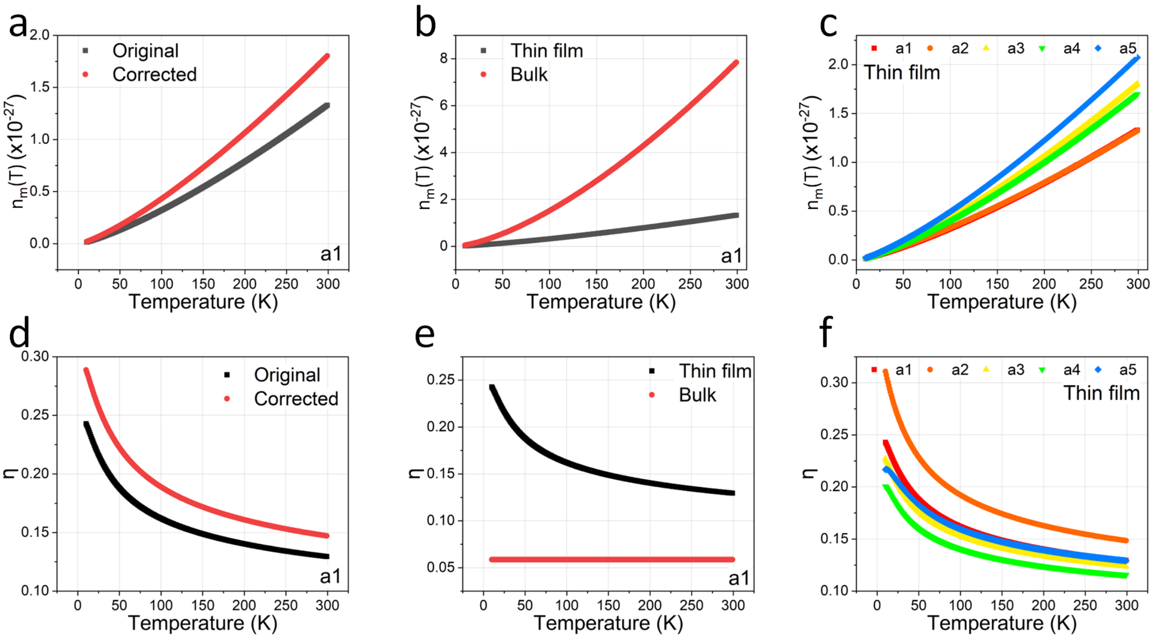

Figure 6.8: a) to c) show $n_m(T)$, the magnon density, as a function of temperature. d) to f) show η, the prefactor for Bloch's law. a) and d) compare the trends between the original and corrected values, b) and e) compare the trends between using the bulk Bloch equation and the thin film Bloch equation, c) and f) compare the five samples via the thin film equation, using the original values. a), b), d) and e) all show the data taken from a1.

6.5 DMI Field

To calculate the DMI field, the bubble expansion method was used, as explained in Chapter 4. It was confirmed that the samples followed the creep regime at the chosen OP fields, as the log of the velocity increased linearly with the OP field $H^{-\frac{1}{4}}$ (based off Equation 2.38). This can be seen in Figure 6.9a, which shows the results for the right and left hand side of a bubble in a1, fitted with a linear fit - this trend was true for all the samples and for a range of different OP fields.

Therefore, bubble expansion measurements were performed on all samples. Plots can be seen in Figures 6.9b to f for samples a1 to a5, respectively, of the calculated bubble velocity when an OP

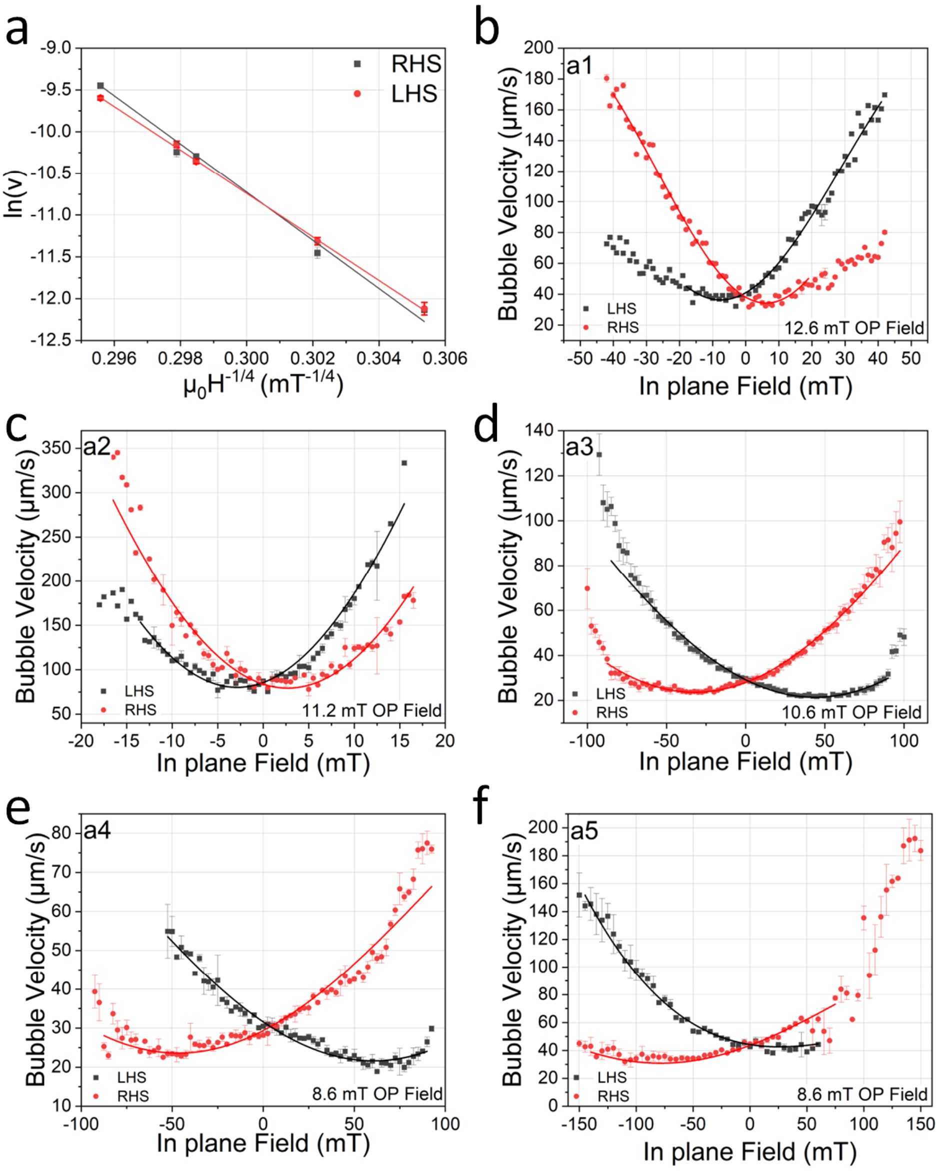

Figure 6.9: a) shows the log velocity of a bubble when using different applied OP fields, plotted against $H^{-\frac{1}{4}}$, and fitted with a linear fit for both the left and right hand side of the bubble. Its linearity indicated the measurements were taken within the creep regime. b) to f) show the bubble velocity vs. IP field for samples a1 to a5, measured via the bubble expansion method. The right hand side (RHS) and left hand side (LHS) of the bubble were analysed and plotted for a specific OP field (used to nucleate the bubble) and a Gaussian curve was fitted to find the minima.

field was pulsed at the annotated value, with various set IP fields. A Gaussian fit was used to obtain the minima. The first thing considered, was that a1 and a2 had a velocity minimum at a negative IP field for the LHS curve and a velocity minimum at a positive IP field for the RHS curve. This meant that LHS DMI field was positive and the RHS DMI field negative, indicating left handed chirality of the domain walls - this was considered as a negative DMI field. For samples a3 to a5, the opposite was true, indicating that they had right handed chirality and a positive DMI field. The DMI field values are plotted in Figure 6.12c, with the errors calculated from the standard deviation of multiple measurements, they are an average of the LHS and RHS values found by performing multiple bubble expansions and analysis, using different OP field pulses. The shapes of the curves were also different, a1 showed a less curved trend with a sharper minimum than a2, and a3 to a5 showed very broad peaks. For a5, the LHS velocities were limited by interference from other bubbles at such high IP fields and in general was flatter than would be expected (quadratic behaviour of the IP field). Furthermore, when observing the actual bubbles (Figure 6.10), there were obvious differences. Samples a1 and a2 hosted a bubble with a rougher domain wall, samples a3 and a4 showed smoother domain walls, and a5 showed the smoothest domain walls. This could be a reason behind the differences in curve shapes. There is evidence from Alessandro et al. to suggest a link between the domain wall roughness and the interfacial roughness.[4]

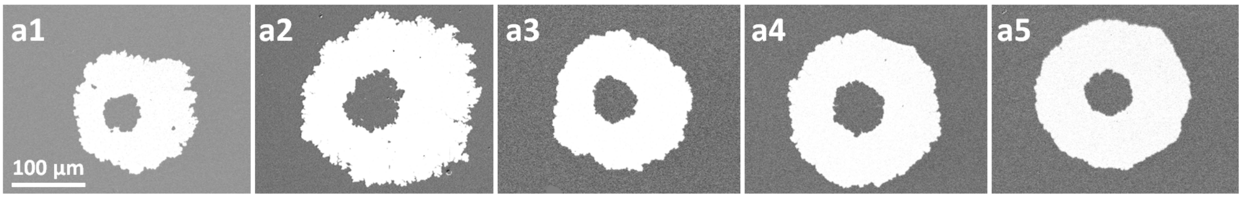

Figure 6.10: Examples of bubbles are shown for the five labelled samples, with a 100 μm scale bar. These measurements were taken with a bubble in the centre, nucleated with an OP field pulse, without an IP field, subtracted from a bubble nucleated with the same OP field pulse, but in an IP field of around 150 mT. In these images, the IP field was always in the same direction, however, different magnitude OP fields were used.

It should be noted that the DMI field is not necessarily found at the minimum velocity, however, a basic creep model would be needed to assess this and the difference for our measurements was not significant, as shown in Figure 6.11a taken from Reference [4]. In this figure, the DMI field values were compared to the values found by bubble expansion measurements by INRIM, these values on the other hand, showed a notable difference between using the creep model or not.[4] In the article, they commented that the velocity curves were not easily fit using the standard creep model, and the H_{DMI} values from different laboratories did not coincide well. They suggested possible sources for the variation to be: inhomogeneities within a sample, error due to different methods of evaluating the minimum of the curve, or fitting difficulties due to noise or field ranges which do not extend high enough to gather a full picture of the curve. The most likely cause being the latter, as can be seen from the velocity curves, there were limitations in IP field range before nearby bubbles began to interfere with the measured bubble in certain samples. Multiple measurements were also performed on different bubbles in the same sample, this resulted in some small differences between the resulting DMI fields, which could also be a reason behind the discrepancies and supports the theory of inhomogeneities. For this reason, multiple measurements were performed and an average taken.[4]

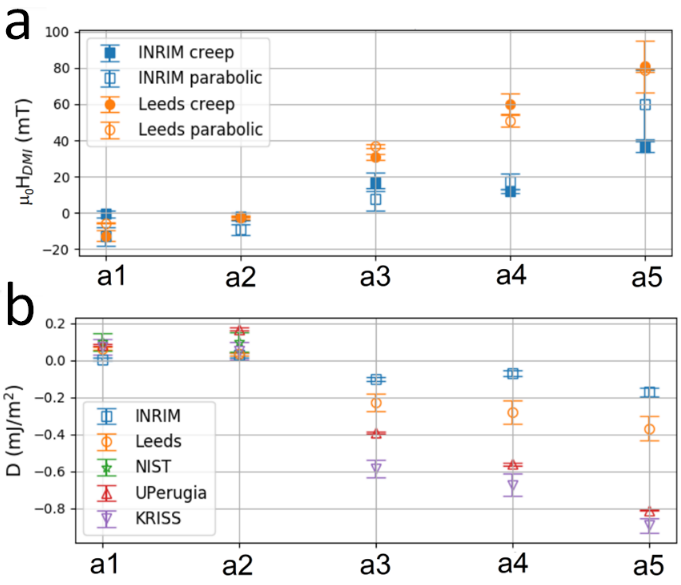

Figure 6.11: These graphs were taken from Reference [4]. a) shows a comparison between the DMI field found from bubble expansion measurements by the University of Leeds and INRIM, the data was analysed both via a parabolic fit and using a standard creep model. b) shows the DMI strength as measured by different laboratories. Leeds and INRIM used the bubble expansion method, NIST, UPerugia and KRISS used BLS.

6.6 Domain Wall Width

The final parameter needed to calculate the DMI strength was the domain wall width, which was calculated using Equation 2.36. It involved the exchange stiffness and the effective anisotropy - from which the errors were propagated. In Figure 6.12a, the domain wall width is shown for samples a1 to a5 for both the original and the corrected data. The corrected data gave a higher domain wall width than the original data in a1 to a4, and the opposite in a5, comparable to literature.[247; 248] The difference was only around 10% in all samples except a2, which exhibited a larger increase of 20% in its corrected value. For the corrected values, the difference between using the exchange stiffness calculated via the bulk and thin film equation was also shown, Figure 6.12b. The thin film equation caused a decrease in values by around 30% compared to when using the bulk equation, except again for a2, for which the width decreased by 45%.

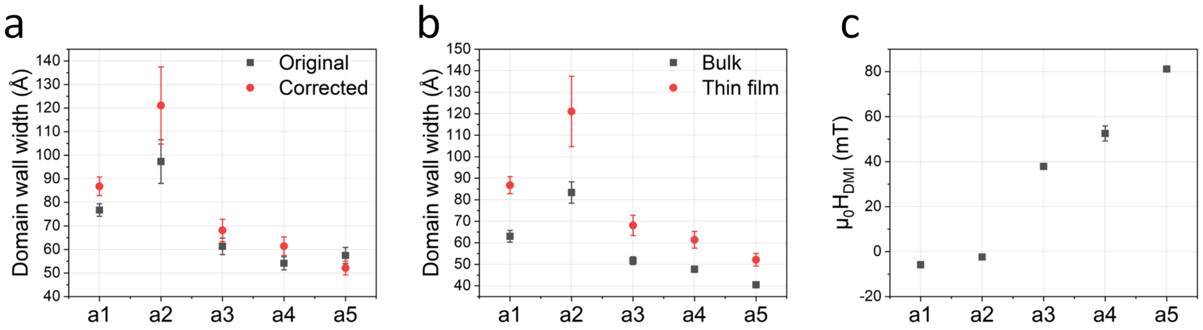

Figure 6.12: a) and b) show the domain wall width, calculated via Equation 2.36 for, a) the original measured data, and data corrected for the proximity effects. b) the corrected data when the exchange stiffness was calculated using the bulk and the thin film Bloch's law equations. c) shows the average DMI field, measured for samples a1 to a5.

6.7 DMI Strength

Finally, all these parameters came together to calculate the DMI strength for each sample stack using Equation 2.40, standard error propagation was used to calculate the error. The DMI strength is shown for samples a1 to a5 for both the original and the corrected data in Figure 6.13a. In the end, the DMI strength was influenced more by its dependence on the DMI field than the proximity effects. As a percentage, they created a 32% and 20% decrease when using the corrected values compared to original values in a1 and a2, respectively. For a3 and a4, the decrease was only by 4% and 3%, respectively, and for a5, an increase of 5% was found in the corrected DMI strength compared to the original. For the Pt/Co/Pt samples, this could be significant and it should therefore be accounted for in order to accurately measure the DMI strength. The difference between using the thin film Bloch's law equation and that for bulk samples was also considered. There was a decrease in DMI strength of on average 25% when using the thin film equation, again, this could be considered significant.

A comparison taken from Reference [4], of the DMI strength measured at the different laboratories is shown in Figure 6.11b. Leeds and INRIM performed bubble expansion measurements and NIST, KRISS, and UPerugia performed BLS measurements. The BLS measurements tended to yield higher magnitude DMI values than those calculated from bubble expansion measurements. This comparison was performed due to disagreements in literature about the two methods.[249; 250] For example, the creep models may not apply in certain conditions, or differences could arise

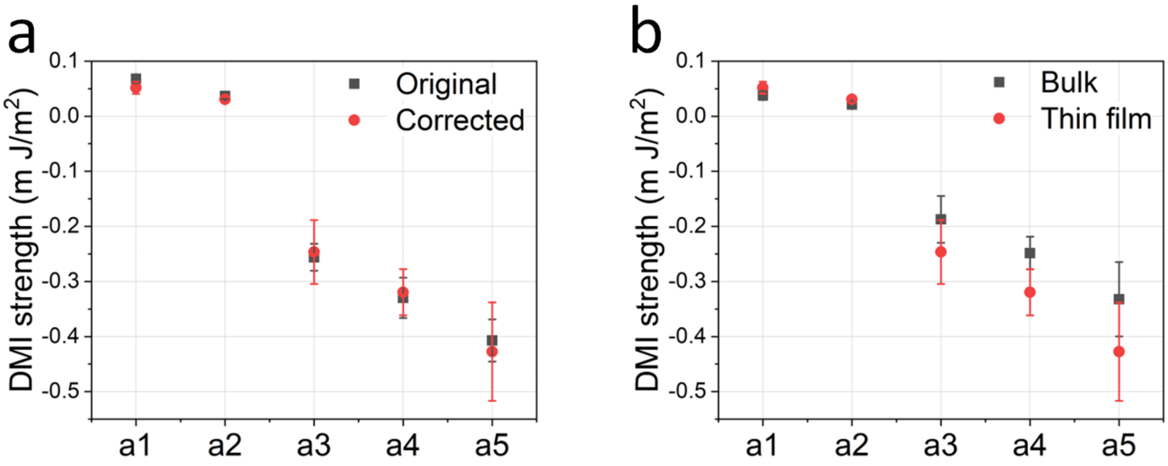

Figure 6.13: a) and b) show the DMI strength, calculated via Equation 2.40. a) shows the original measured data, and data corrected for the proximity effects. b) shows the corrected data when the exchange stiffness was calculated using the bulk and the thin film Bloch's law equations.

from a FM thickness dependence on the asymmetry.[251; 252] This study shows that even when measurements are performed on the same sample, the DMI strength is not always agreed upon. These differences in DMI strength values may occur for the two measurement types due to them being sensitive to defects of different length scales.[4; 252; 253] Comparable values of the DMI strength in similar samples were found in the literature[142], and some values which were slightly higher[59; 243].

6.8 Conclusions

To conclude, the grown samples exhibited the expected PMA, and maintained standard values of both the coercivity and the saturation field. The saturation magnetisation values calculated for samples a1 to a5 displayed a considerable disagreement considering the samples had similar Co thicknesses, an inconsistency also echoed in other literature values (see Chapter 5). A correction was performed on these values to account for different proximity effects at the Co interfaces, following this, the M_S values became more consistent. The change in values was -49%, -48%, -15%, -17%, and 18% for a1 to a5, respectively. The corrections also agreed well with the parameters found in Chapter 5. The corrections were propagated through all other values considered in the calculation of the DMI strength. K_{eff} showed a change from original to corrected values of -35%, -60%, -24%, -31%, and 15% for a1 to a5, respectively. The exchange stiffness was worked out in two different ways: a standard method for bulk values and an approximation for thin films. The average increase in values from using the bulk to the thin film equation fit was 44%, and the corrected values were

on average only 3% less than the original values. The domain wall width was affected on average by a 10% increase for the corrected values from the original, and a 30% increase when using the values found via thin film approximation compared to the bulk law. The DMI field was measured and compared to measurements performed on the same sample at different laboratories, as was the DMI strength. The DMI strength decreased by on average by 25% when using the bulk exchange stiffness fit compared to the thin film fit, and the corrected values varied by 30%, 20%, 4%, 3%, and -5% for a1 to a5, respectively, from the original values.
To summarise the conclusions:

- Correcting the parameters for the proximity effects had the largest effect on the M_S and the effective anisotropy. The exchange stiffness, domain wall thickness, and DMI strength were less affected.
- The correction was more significant in the samples with Pt at the top interface than the others.
- The difference in values of exchange stiffness calculated via the standard bulk method and the thin film approximation were substantial. The thin film approximation was more accurate for samples a1 to a5 and showed higher values, more comparable to those in literature. This can have a significant affect on the values of DMI strength.
- For the measurements performed in different laboratories, the bubble expansion method gave reliable results, though they did not compare as well with the values found via BLS measurements, particularly for larger DMI values.
- These discrepancies were considered to be due to the different sensitivities of the two techniques (nm-scale for bubble expansions and μm-scale for BLS). This therefore requires further investigations.

CHAPTER 7

Antiferromagnetic Interlayer Exchange Coupling of CoB Multilayers

7.1 Introduction

In this chapter, we present multilayer stacks with delicate balance of CoB, Ir and Pt which combines the RKKY interaction, DMI and PMA to make a SAF with skyrmion hosting benefits. The CoB, unlike Co or annealed CoFeB, reduces possibilities of pinning due to its amorphous property.[2] Including both Ir and Pt in the multilayers yields not only an additive DMI but also provides numerous degrees of freedom to manipulate.

We report a study performed to understand the AFM-IEC within these materials by inducing AFM coupling between each magnetic layer (known as stack 1). Then, we present a stack which consists of two ferromagnetically coupled multilayers of CoB/Ir/Pt with five repetitions, coupled together antiferromagnetically with an iridium layer (known as stack 2).[254–257] Designing the stack in this way allows the magnetic textures to be observed more easily with various imaging techniques, such as Kerr microscopy and MFM, and when it is not completely compensated, it could give a larger read out signal. Finally, we investigated a variation of this stack, with its stacking order reversed (known as stack 3).

The chapter combines both CoB/Ir/Pt multilayers and SAF configurations for a potential skyrmion hosting device or multilevel memory device. The multilayer dependence on thickness of each material and number of repeats[95] were investigated, exploiting the RKKY coupling as a new degree of freedom. Changes in the materials behaviour as a function of temperature were also studied to determine whether a phase transition would occur, due to interest in spintronic devices for information coding based on AFM to FM transitions.[258; 259] Electrical measurements were also performed to gain a better understanding of the characteristics of the AFM-IEC within the multilayer.

7.2 Sample Characterisation

Initially, two types of SAF stack were considered in this work, as shown in Figure 7.1. Figure 7.1a shows a sample designed with N repeats of $Co_{68}B_{32}$ with a spacer of Ir and Pt. The Ir thickness was chosen to create a negative (i.e. antiparallel) IEC between each CoB layer and the Pt thickness was chosen to create PMA. This stack was studied to understand the behavior of the IEC coupling in these materials and will be referred to as stack 1. Figure 7.1b shows two multilayers of CoB, Ir and Pt, X_1 and X_2, which both consist of 5 FM layers with positive IEC. X_1 and X_2 are separated by a 4.2 Å layer of Ir, causing a negative IEC between the two FM multilayers. This stack will be referred to as stack 2. Throughout the text, stack 1 and stack 2 may have small variations in thicknesses, however, if relevant to the study, the thicknesses will be stated.

The stacks were deposited on thermally oxidized silicon at room temperature via DC magnetron sputtering in the EPSRC funded sputter deposition system at the University of Leeds. The base

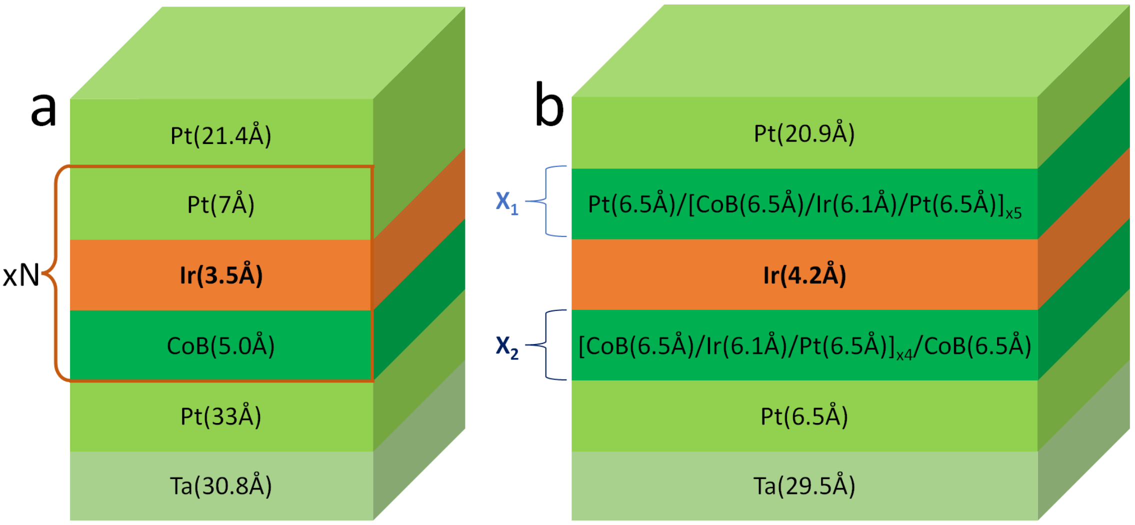

Figure 7.1: a) shows a multilayer of CoB/Ir/Pt, repeated N times with 3.5 Å Ir that caused each the CoB layer to couple antiferromagnetically with its subsequent layer. This is referred to as stack 1. b) shows two FM multilayers separated by 4.2 Å Ir causing the two FM multilayers (X_1 and X_2) to couple together antiferromagnetically. This is referred to as stack 2.

pressure was 10^{-9} mbar and the argon pressure was 4.6×10^{-3} mbar at a 10 sccm Ar flow rate. For Ta, Pt, Ir, and CoB sequentially, the growth powers were 80 W, 30 W, 30 W, and 50 W and the growth rates were 0.9 Å/s, 0.7 Å/s, 0.36 Å/s, and 0.24 Å/s. Below both stacks was a 30 Å seed layer of Ta, and in stack 1, an additional layer of 30 Å of Pt, above the stacks, there was a cap of Pt 20 Å to prevent oxidation. Throughout the growth, the samples were rotating at 60° per second to ensure an even distribution of atoms.

Small differences in the thickness could change the coupling within the stacks significantly, therefore low angle x-ray scans were used to verify the thicknesses of the layers by fitting the scattering using GenX.[136] Figure 7.2 shows examples of GenX fits performed on stack 1 (a) and stack 2 (b).

The parameters obtained from a low angle x-ray scan performed on stack 1 with N=3 (Figure 7.2a) and fitted using GenX are shown in Table 7.1. The base was 30.8 Å of Ta and 33 Å of Pt with both having around 5 Å roughness and lower densities compared to literature. The cap was 21.4 Å of Pt, with a small amount of roughness and an expected density, within the error. The Pt in the multilayer however, was 7 Å, and the roughness was estimated to be 4.5 Å of the layer, though, the density was lower than expected. For the CoB layers within the multilayer, the roughness was also shown to be the majority of the layer, however, the Ir roughness was lower. The density of CoB and Ir were slightly higher than the literature. The Ir thickness was 3.5 Å, which was within the range that caused the AFM-IEC (Figure 7.3c).

A low angle x-ray scan was also performed on stack 2 and fitted using GenX, as was shown in

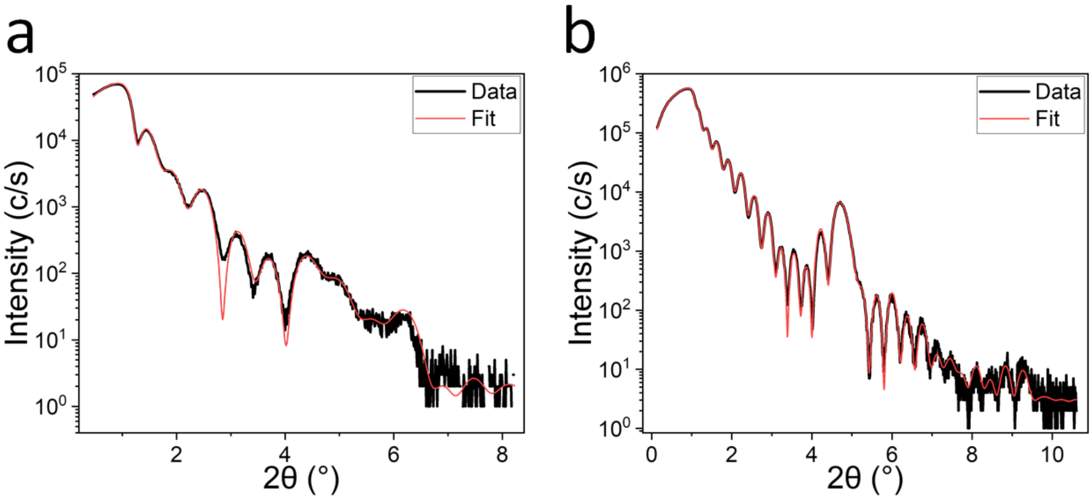

Figure 7.2: This shows the low angle x-ray scans of a) stack 1 with N=3, and b) stack 2. The intensity was measured in counts per second and plotted against 2θ. The black line represents the data taken during the measurement, and the red line shows the GenX fit.[136]

Layer	Thickness (Å)	Roughness (Å)	Density difference (%)
Cap Pt	21.4±1	2.2±0.7	102±2
Pt	7.0±0.3	4.5±0.8	97.7±0.1
Ir	3.5±0.5	2.0±0.6	104.2±0.4
CoB	5.0±0.2	4.4±0.9	105.2±0.7
Pt base	33±1	5.0±0.3	95.9±0.4
Ta base	30.8±0.7	5±2	93.4±0.3

Table 7.1: The parameters from the GenX[136] fit of stack 1, N=3. For each layer, it shows the thickness, roughness, and the difference in density compared to standard values found in literature, as a percentage.

Figure 7.2b. The results of this fit are shown in Table 7.2. The base was 29.5 Å of Ta with little roughness, though, a lower Ta density compared to literature. The cap was 20.9 Å of Pt, with a small amount of roughness and an expected density. The Pt in the multilayer was 6.46 Å, and the roughness was estimated to be throughout almost all of the layer, plus, the density was higher than expected. These parameters were almost the same for the CoB layers within the multilayer (similar to the parameters from stack 1 with N=3), suggesting that there was roughness and intermixing between the CoB/Pt and CoB/Ir interfaces. However, the Ir roughness was lower, suggesting there was less roughness/intermixing between the Ir and Pt. The density of Ir was also slightly less than the literature, potentially due to how thin the layers were. The middle Ir thickness was 4.2 Å, which was within the range that caused the AFM-IEC (Figure 7.3c).

Layer	Thickness (Å)	Roughness (Å)	Density difference (%)
Cap Pt	20.9±0.2	2.88±0.06	99±5
Middle Ir	4.2±0.2	1.3±0.2	96.3±0.6
Ir	6.11±0.09	1±1	96.3±0.9
CoB	6.50±0.02	5.0±0.1	105±10
Pt	6.48±0.09	5.1±0.3	102±6
Ta base	29.5±0.3	3.2±0.3	93±6

Table 7.2: The parameters from the GenX[136] fit of stack 2. For each layer, it shows the thickness, roughness, and the difference in density compared to standard values found in literature, as a percentage.

The values of saturation magnetisation for stack 1 where N=1 to N=8 were calculated using the only the volume of the $Co_{68}B_{32}$, this achieved an average value of (0.71 ± 0.02) MA/m. An estimation can also be made of the magnetisation including platinum's strong proximity effects by including some volume of the Pt in the M_S calculation. An assumption was made that as the polarisation depth from the FM/Pt interface tended to be up to 10 Å (Figure 5.8), the Pt in the multilayer was fully polarised, and there was an additional 10 Å of polarised Pt material from the base. Including this extra volume, the M_S became (0.32 ± 0.01) MA/m, as an average M_S of all samples N=1 to N=8, which is comparable to the value found in Chapter 5. It does not, however, consider that the moments from Co and Pt are different, nor the magnetic moment full depth profile within the Pt, a thickness series would be required to calculate the Pt contribution more accurately.[162]

7.3 Stack 1

7.3.1 Building Stack 1

In stack 1, the Pt and the Ir cause PMA, they cause the inversion symmetry to be broken along the stacking axis, and therefore an interfacial DMI, plus, they play the role of providing coupling between the $Co_{68}B_{32}$ layers in the stack. The antiferromagnetic coupling is still present with a Pt layer between the Ir and CoB, however, its strength is reduced.[95; 111] First, a study was performed to confirm the thicknesses of the stack components at which the AFM-IEC arises. Films of stack 1 were grown, whilst varying the thickness of either the CoB, Ir or Pt in a multilayer with N=3. When the AFM-IEC occurs, the hysteresis should show a separate switch for each FM layer, as shown in Figure 7.3a. The hysteresis loops were measured via laser MOKE.

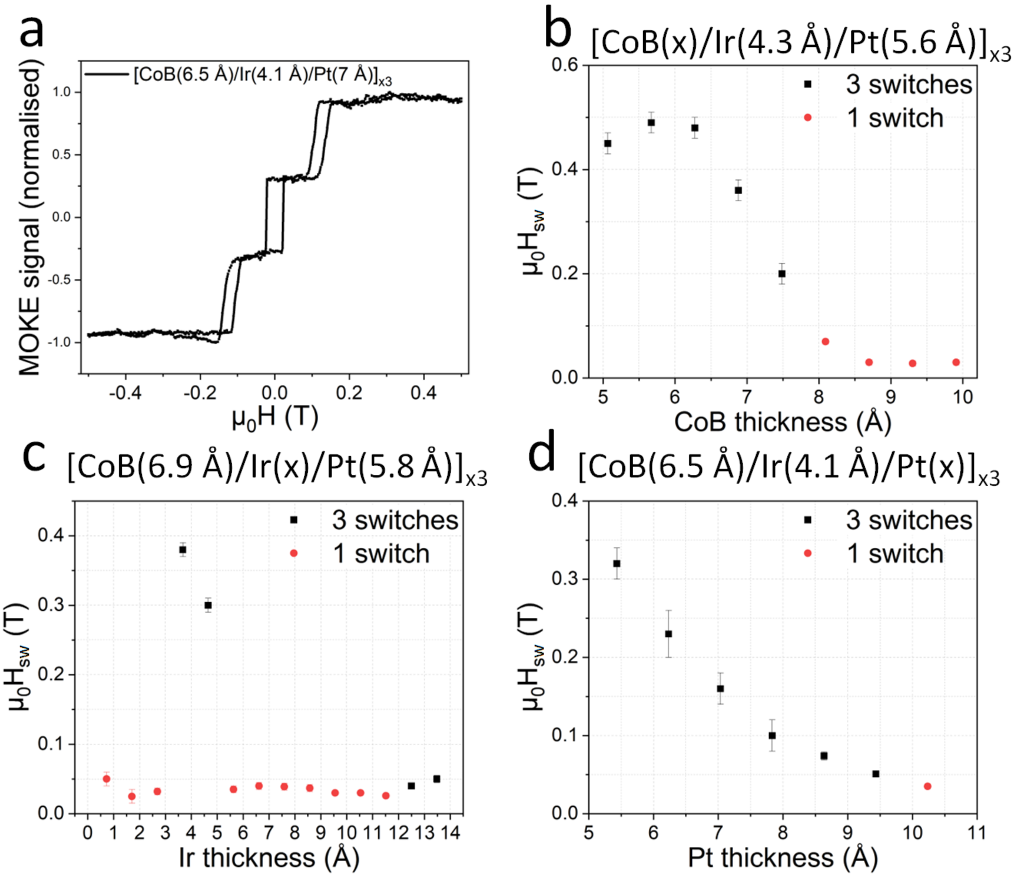

Figure 7.3: This figure shows how the switching field (H_{sw}) for a three repeat multilayer sample changes with the thickness of each material in the multilayer. The black squares indicate when AFM-IEC caused three individual switches and the red circles indicate when there is ferromagnetic IEC.

In Figure 7.3b to d, the switching field (i.e. the field at which the hysteresis loop measured out of the plane saturates) was plotted against the thickness of the considered material. In the case of CoB (7.3b), the sample exhibited PMA at 5 Å, which remained until at least 14 Å of CoB (although not all shown on the graph). Samples showed the characteristic three switches until 8 Å of CoB after which only one switch occurs. The switching field peaked at around 6 Å of CoB, then decreased until it plateaued at 9 Å. For the platinum (7.3d), H_{sw} decreased as the Pt thickness increased, and the AF-IEC was present until the Pt reached a thickness of 10 Å when the platinum fully dampened the IEC. Most importantly, when Ir was varied as a function of thickness (7.3c), it showed a trend comparable to Figure 2.4, there was a peak in H_{sw} at 3.5-5 Å, in which the AFM-IEC occurred, then only one switch (FM coupling) was present until 12.5-14 Å where there was a smaller (dampened) peak in H_{sw} in which the AFM-IEC occurred. These results agreed with the results of Parkin et al. which state an AFM peak occurs at 4 Å, and reoccurs, dampened, at 13 Å with an error of Δ3 Å.[13] The thickness of Ir in the CoB and Pt studies was chosen to be 4 Å to allow for strong AFM-IEC to occur when the other materials allowed. Variations in the switching fields may occur due to small variations in the thicknesses of the layers. In a SAF, the anisotropy field (H_{eff}) and the switching (RKKY coupling) field (H_{sw}) both contribute to the saturation field (H_{sat}), as shown in Equation 7.1 for a sample with two magnetic layers.[111]

$$\pm \mu_0 H_{sat} = \mu_0 H_{eff} + 2\mu_0 H_{sw} \tag{7.1}$$

When the sample is placed in an OP field, the number of CoB layers that have spin orientation against the direction of the applied field is decreased one by one as the field is swept from a positive saturation state to a negative state. For example, with five CoB layers, the spin orientation of each layer would change from saturation in the ↑ direction after each switch as follows: ↑↑↑↑↑, ↑↑↓↑↑, ↑↓↑↓↑, ↓↑↓↑↓, ↓↓↑↓↓, ↓↓↓↓↓.

Measured by SQUID magnetometry, Figure 7.4a shows the hysteresis loop of stack 1 grown with five repetitions and Figure 7.4b shows a similar stack, however, with an increased thickness of Ir of 6.1 Å between each layer. When the Ir thickness was at 3.5 Å and within the AFM coupling regime, the hysteresis shows 5 separate switches signifying AFM-IEC between each layer. When the Ir thickness was increased, the hysteresis no longer exhibited AFM-IEC between all the layers, but displayed only one wasp-like switch indicating that the coupling between the layers was ferromagnetic. This further confirmed the AFM coupling role of the Ir layer for an increased number of repetitions. The inset of Figure 7.4a shows the sample measured in the plane to confirm its PMA.

7.3.2 Stack 1: Function of Repetitions

How the AFM-IEC changed with the number of repeats of the $[\mathrm{CoB/Ir/Pt}]_{\times N}$ stack was investigated, the hysteresis loop results are shown in Figure 7.5 and 7.6. Firstly, the study showed that

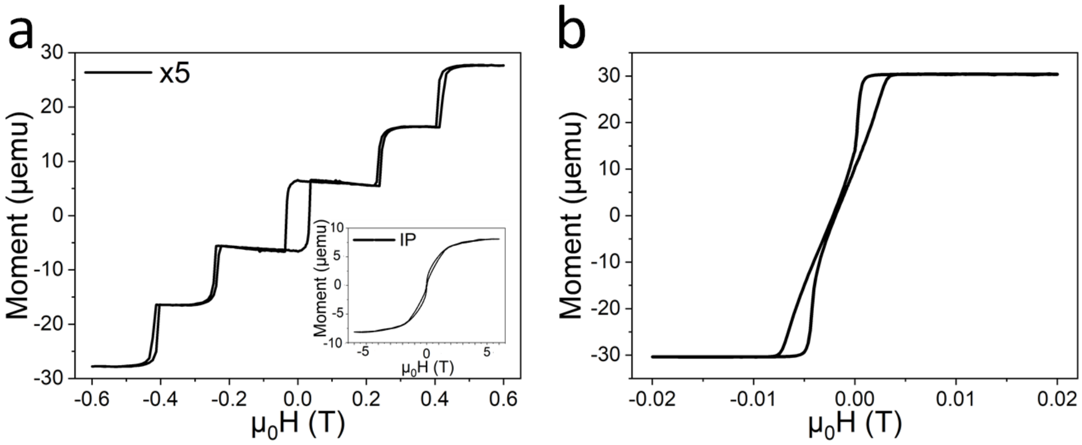

Figure 7.4: a) shows the hysteresis loop measured OP by SQUID magnetometry of stack 1 where N=5, the inset shows the IP hysteresis loop. b) shows the OP hysteresis loop for a stack similar to stack 1 where N=5, however, with the Ir thickness of each layer 6.1 Å.

the AFM-IEC was predominant up until 7 repeats of the stack, as the number of clear individual switches was the same as the number of repeats. Beyond 7 repeats, some switches began to merge together, this was evident due to the amplitude of one switch doubling. This could have been due to the orange-peel effect, which causes rough surfaces to couple via dipolar fields.[6; 260] Furthermore, when N was >8 there tended to always be one switch at around ±0.4 T. For N=2, 3, 5 and 6, the switching fields were of equal distance apart, and symmetric around 0. The innermost switches tended to have larger coercivities, and for odd numbers of N, there was always a switch around zero. It was also noted that due to the sharp switches, the DMI was likely to be dominated by the AFM-IEC not allowing skyrmions to form naturally.

The hysteresis loops in Figure 7.5 were measured by SQUID magnetometry and showed a switch of equal amplitude for all layers. The hysteresis loops in Figure 7.6 were measured via laser MOKE, which could cause some switch amplitudes to appear less due to laser depth limitations. For this reason, loop crossing may be seen at zero field, where it was not present in SQUID measurements. For N=9 to N=12, the switching fields were all below ±0.1 T, except for the very outer switches between ±0.3-0.4 T. For N=13, the switching fields begin to separate out, and for N=14, the switching fields are again very spread out.

$$J_{IEC} = \mu_0 M_S t_{CoB} H_{sw} \tag{7.2}$$

The interlayer exchange coupling strength can be calculated using Equation 7.2, where t_{CoB} is the CoB thickness, M_S is the saturation magnetisation and H_{sw} is the switching field in an OP hysteresis loop. For N=2, J_{IEC} = (-0.22 ± 0.09) mJ/m^2, for N=3 J_{IEC} = (-0.25 ± 0.03) mJ/m^2. Above N=3, the switches were not evenly spaced, therefore the assumptions of Equation 7.2 can no

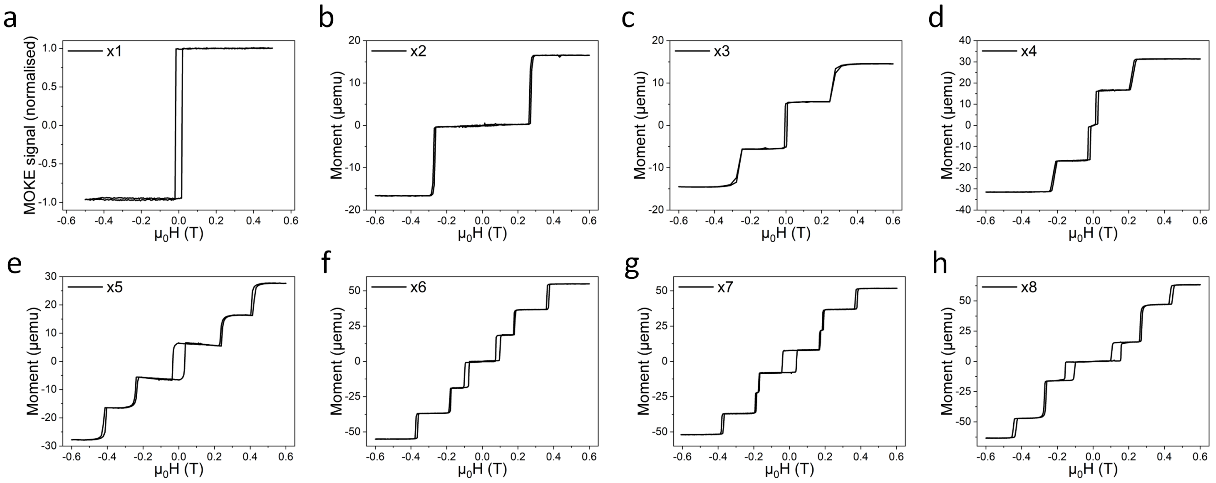

Figure 7.5: This figure shows the hysteresis loops measured by MOKE/SQUID magnetometry of $[\mathrm{CoB/Ir/Pt}]_{\times N}$, where N is the number of times the trilayer was repeated and is stated on each graph, from 1 to 8 repeats.

longer be valid, however, it is unlikely this was due to changes in the coupling strength and more likely due to changes in the effective field.[261] These values are relatively comparable to others within the literature.[244; 262]

The sample with N=10 was observed under a Kerr microscope. It showed at each switch, a domain wall sweeping across the area of the sample being observed, examples are shown in Figure 7.7. The figure shows a zoomed in version of the N=10 hysteresis loop, with images taken at different fields along the hysteresis loop as a layer switch was occurring. Domain walls of different smoothness were seen moving across the imaged area of the sample. The difference in the appearance of the domain walls at different fields, and therefore different layers, may be due to different roughness between the layers and due to some layers being coupled together. At around 0.045 T, it was seen that when sweeping the field from positive to negative, there was a switch, whereas when sweeping from negative to positive there was not confirming the observation from the laser MOKE.

Stack 1 with three repetitions was grown without either the middle layer of Ir or middle layer of Pt and compared to the full multilayer stack in order to understand the samples better, as shown in Figure 7.8a. The results showed that the sample without an Ir layer still had three switches for each CoB layer. Considering how the spins change orientation, one possibility for how the spin flips could occur with two layers coupled ferromagnetically and two layers coupling antiferromagnetically is as follows: ↑↑↑, ↓↑↑, ↓↓↑, ↓↓↓, in this case there would still be three individual switches observed. The outer two switches, represented the switching of the bottom CoB layer, which was coupled antiferromagnetically to the two upper layers of CoB which, without the Ir between them, coupled ferromagnetically. The increased amplitude of the middle switch indicated that the two CoB layers coupled together ferromagnetically possessed more moments, this may be due to the Pt having two

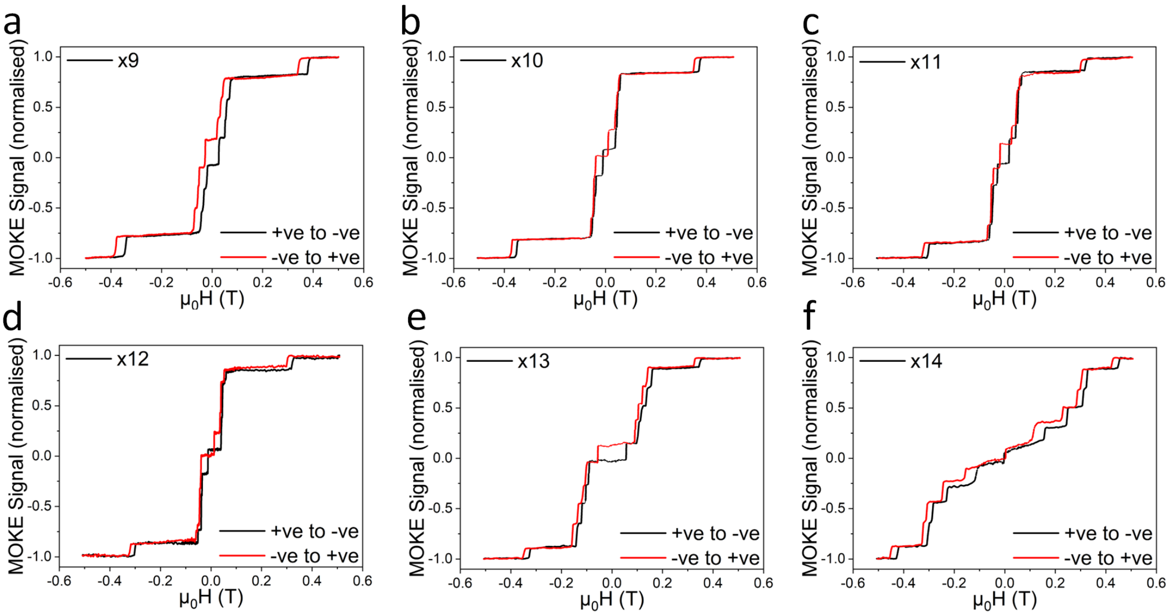

Figure 7.6: This figure shows the hysteresis loops measured by laser MOKE of $[\mathrm{CoB/Ir/Pt}]_{\times N}$, where N is the number of times the trilayer is repeated and is stated on each graph, from 9 to 14 repeats. The positive to negative, and vice versa, field sweeps are shown in different colours to make it easier to see where the loops cross. The MOKE signal is normalised in all graphs.

interfaces with CoB instead of one. The outer switches also had a slightly higher switching field. The sample without Pt showed similar outer switching fields, however, with a larger coercivity and amplitude. The middle switch was very different, with a very low amplitude and larger coercivity. This could be due to the considerable deduction in moment with a missing CoB/Pt interface.

Figure 7.8b, shows a study, growing stack 1 with N=3 as a function of rotation speed of the samples during the deposition. It showed that the middle switch did not change dependent on the rotation speed, however, the outer switches only became more square and sharp above 45°/s. For this reason, all samples were grown with 60°/s rotation. Following this, during a deposition of stack 1 with N=2, the CoB was co-sputtered with Co to increase the cobalt to boron ratio. In Figure 7.8c, the Co was sputtered at 10 W with the CoB and the growth time, therefore the thickness of the CoB with increased Co content, was varied. As expected, it showed that the switching field decreased with increasing CoB thickness, and with a change of 1 Å of CoB, the switching field reduced by around 0.1 T. For the thickest CoB, the centre of the hysteresis loop was no longer closed and flat, suggesting it was reaching a limit for the AFM-IEC being dominant. Additionally, the rate at which the Co was co-sputtered with the CoB was systematically altered to study how the increased Co content in CoB affects the switching fields. This was studied for stack 1 with N=3 and shown in Figure 7.8d. As the Co content is increased, the coercivity of the inner switch

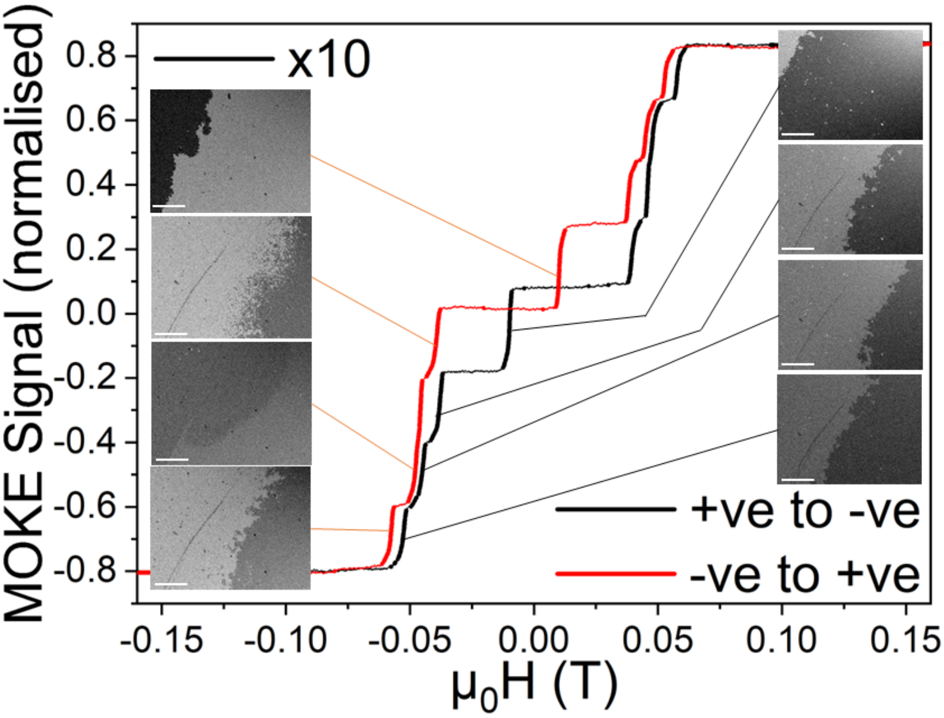

Figure 7.7: Here can be seen a zoomed in version of the normalised MOKE hysteresis loop of stack 1 with N=10. The field sweeps were performed whilst using a Kerr microscope and an image was taken, capturing a static representation of a domain wall during its sweep across the sample for some of the switches. The black line represents the field sweeping from positive to negative and the red line represents the opposite direction field sweep. The scale bars represent 200 μm.

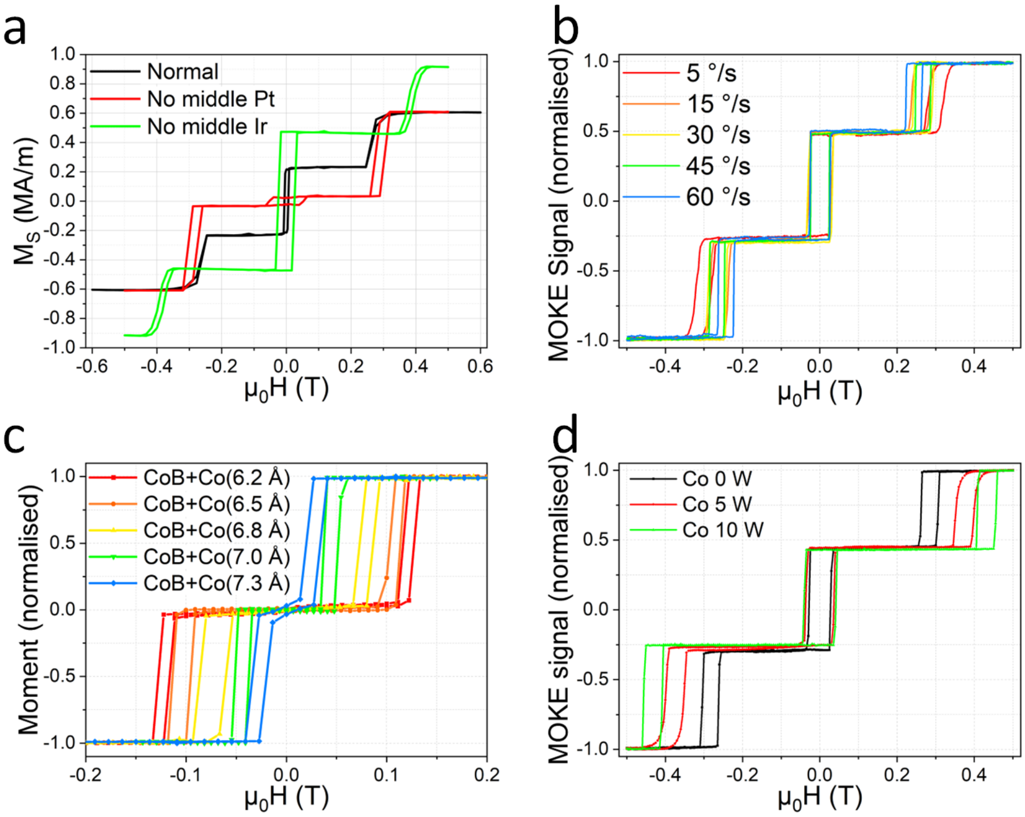

Figure 7.8: a) shows the SQUID hysteresis loops for stack 1 with N=3, compared with a sample grown without the middle platinum layer or without the middle iridium layer. b) shows the hysteresis loops measured by MOKE for stack 1 with N=3, grown with different rotation speeds. c) shows the normalised moment measured via SQUID for a version of stack 1 with N=2, when different thicknesses of CoB were deposited. The CoB was co-sputtered with Co at 10 W to increase the cobalt to boron ratio. d) shows the normalised MOKE hysteresis loops of a version of stack 1 with N=3, with Co co-sputtered with the CoB at different growth powers.

increased, and the switching field of the outer switches increased.

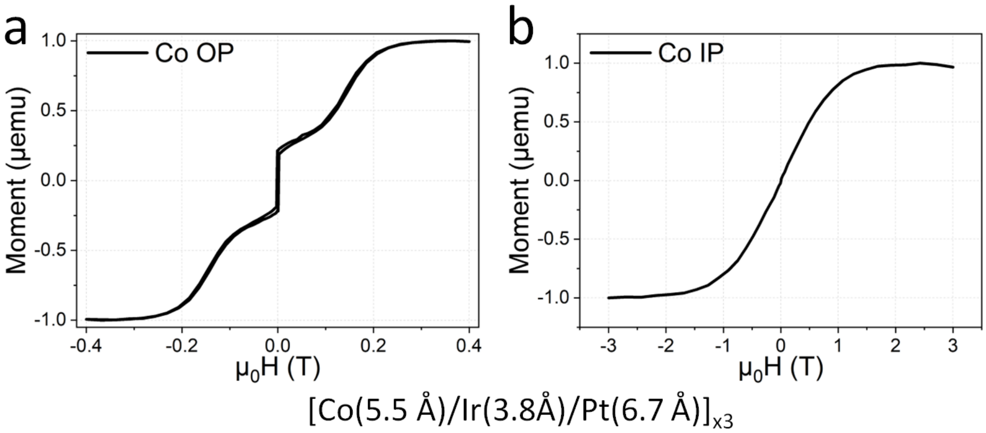

Figure 7.9: a) shows the normalised hysteresis loop measured OP by SQUID of a version of stack 1 with N=3, however, with Co replacing the CoB. b) shows the same sample measured in the plane.

Finally, stack 1 with N=3 was created using Co instead of CoB. The sample was measured OP via SQUID magnetometry and the outer switch was much less defined as a square switch compared to the CoB, as shown in Figure 7.9a. Figure 7.9b shows the IP hysteresis loops measured by SQUID magnetometry, confirming the sample had PMA. It's interesting to note that in Reference [96], the hysteresis loops of similar samples with Co were more square-like. It is likely that the stack could be tuned to create a more defined SAF.

7.3.3 Stack 1: Temperature Dependence

Stack 1 was also investigated as a function of temperature. As can be seen in Figure 7.10, the AFM-IEC remained with temperatures down to 5 K. The coercivity of the loops increased with decreasing temperature as expected due to less influence from thermal excitation. Figure 7.11 shows the loops from Figure 7.10 separated out to see the trends more clearly. In both the case for N=3 and N=8, the moment increased as the temperature decreased. As the temperature decreased, the coercivity of the inner switches began to increase quicker than the outer switches.

Figure 7.12a shows the hysteresis loops of stack 1 with N=2, measured OP via SQUID magnetometry as a function of temperature. Similarly to when N=3 and 8, the AFM-IEC remained between the two layers at 10 K, the magnetic moment increased as the temperature decreased, and the coercivity of the two switches increased as the temperature decreased. The inset shows an almost linear relationship between the temperature and the switching field, which was calculated as the centre of the switch. Figure 7.12b, shows the same sample measured in the plane, to confirm the PMA at all measured temperatures.

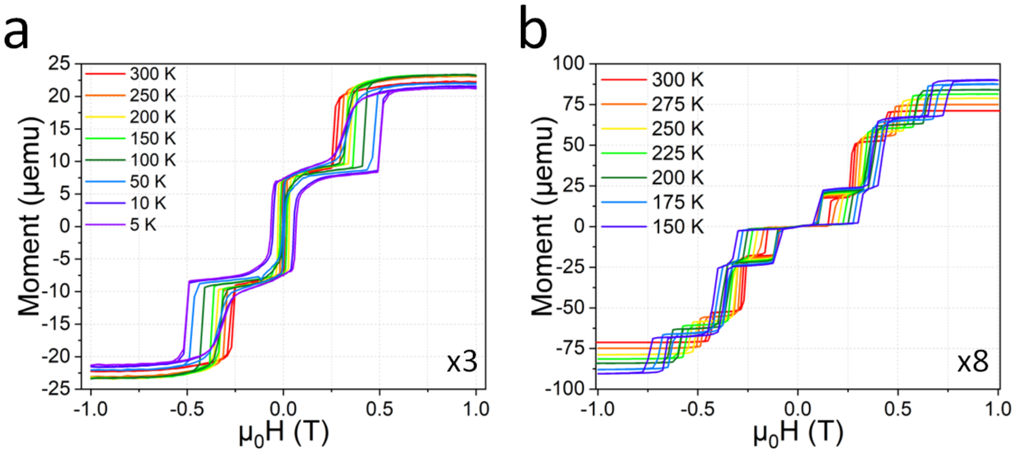

Figure 7.10: a) shows the hysteresis loops from 300 K to 5 K measured OP via SQUID for stack 1 with N=3. b) shows the hysteresis loops from 300 K to 150 K measured OP via SQUID for stack 1 with N=8.

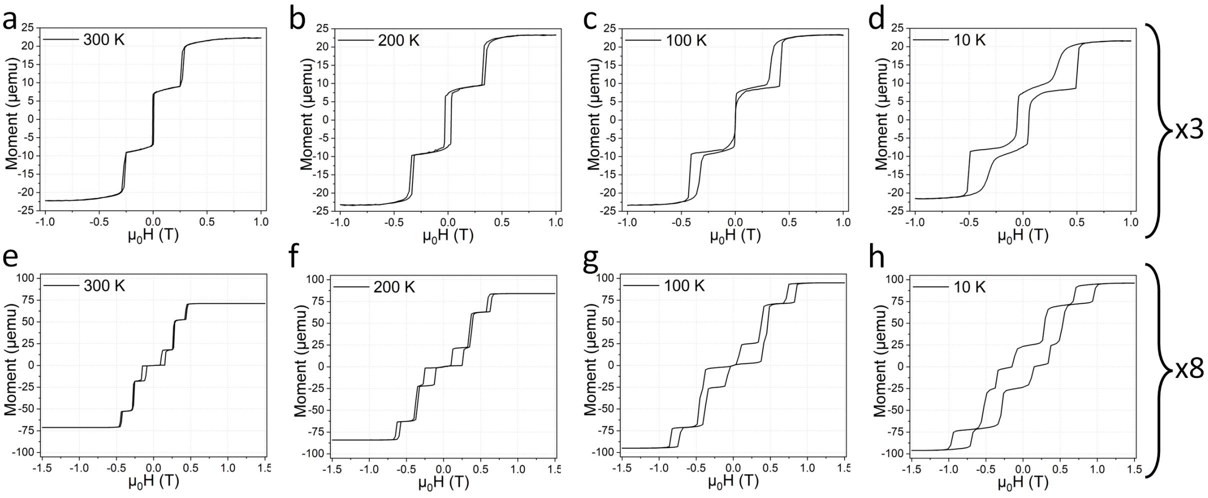

Figure 7.11: a) to d) show the hysteresis loops at 300 K, 200 K, 100 K and 10 K, measured OP via SQUID for stack 1 with N=3. e) to h) show the hysteresis loops at 300 K, 200 K, 100 K and 10 K, measured OP via SQUID for stack 1 with N=8.

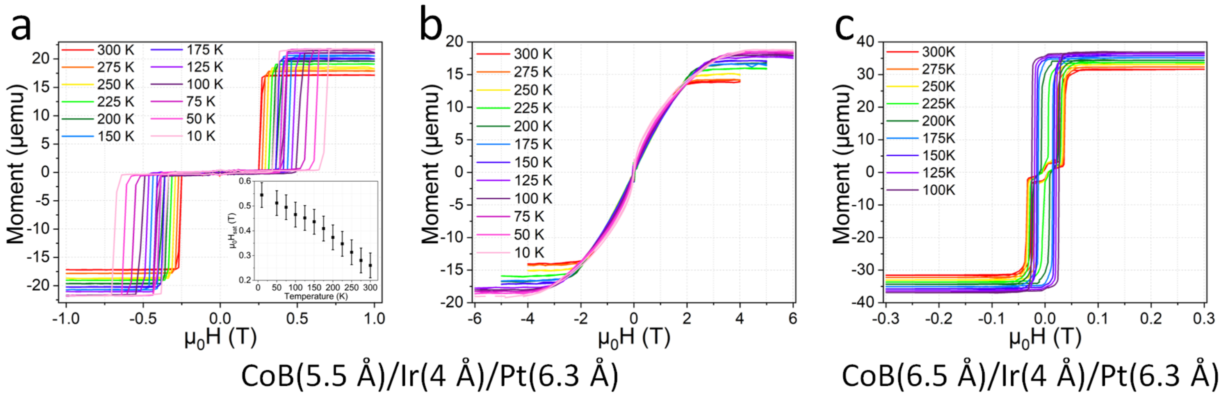

Figure 7.12: a) shows the hysteresis loops of stack 1 with N=2, measured OP via SQUID magnetometry as a function of temperature. The inset shows the switching field as a function of temperature. b) shows the hysteresis loops of a) measured IP via SQUID magnetometry as a function of temperature. c) shows the hysteresis loops of a version of stack 1 with N=2, in which the CoB was thicker and was co-sputtered with Co at 10 W. It was measured OP via SQUID magnetometry as a function of temperature.

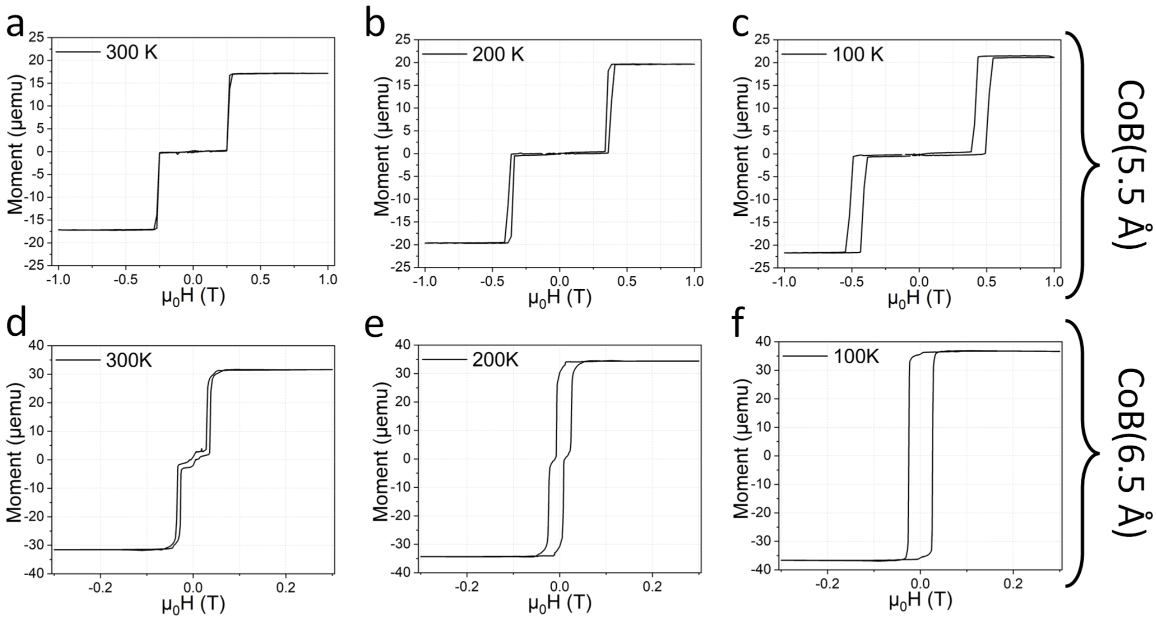

Figure 7.13: a) to c) the hysteresis loops of stack 1 with N=2, measured OP via SQUID magnetometry at 300, 200 and 100 K. d) to f) the hysteresis loops of a version of stack 1 with N=2, measured OP via SQUID magnetometry at 300, 200 and 100 K, the CoB was thicker and was co-sputtered with Co at 10 W.

Figure 7.12c, shows the hysteresis loops of a version of stack 1 with N=2, measured OP via SQUID magnetometry as a function of temperature, however, the CoB is thicker at was co-sputtered with Co at 10 W. Firstly, the centre of the sample has a slight bump which was most likely due to the edge of this sample having a different structure due to shadowing from the sample holder. Despite this, there was a clear difference when the CoB was thicker with more Co content. This difference is displayed in Figure 7.13. As it can be seen, initially at 300 K, the switching fields were much lower for the thicker CoB with a higher Co ratio. Then, as the temperature decreased, for both samples the coercivity increased the moment increased. Interestingly, the switching field increased as the temperature decreased in the thinner CoB sample, however, in the thicker CoB sample the switching field decreased as the temperature decreased. For the thicker CoB sample, by 100 K, the AFM-IEC was no longer present, with the hysteresis loop possessing features of FM-IEC displaying only one switch.

To summarise the discussions on stack 1:

- An iridium layer caused AFM-IEC when it is of thicknesses: 3.5 - 5 Å and 12.5 - 14 Å, specifically, when sandwiched along with Pt between CoB layers.
- CoB layers can be coupled together antiferromagnetically with a spacer of Pt between 5 - 10 Å and Ir of 3.5 - 5 Å, when the CoB layer is between 5 - 8 Å.
- The layers switched independently for repetitions of a CoB/Ir/Pt multilayer with AFM-IEC until seven repetitions, after which some layers began to switch together. The domain walls in each layer did not always show the same properties.
- The Pt was important within the stack to ensure strong PMA and contribute to the moments.
- When the thickness of the CoB in the stack was increased, the switching fields decreased.
- When the thickness of the Pt in the stack was increased, the switching fields decreased.
- When increasing the ratio of Co to B in CoB, the switching fields increased.
- Substituting the CoB for Co, resulted in the outer switches of a three repetition sample becoming much less sharp.
- For two, three and eight repetitions of stack 1, the individual switching of the layers remained from 300 K down to 10 K. The coercivity of the switches increased as the temperature decreased.
- For two repetitions of CoB/Ir/Pt coupled antiferromagnetically, with increased Co content in the CoB, and increased CoB thickness, the AFM-IEC became ferromagnetic below 100 K. The switching fields instead decreased as the temperature decreased, producing a temperature controlled SAF.

7.4 Stack 2

7.4.1 Building Stack 2

The second proposal was to harness the combination of CoB, Ir and Pt to create a SAF device that was easily measurable and able to host skyrmions. The device design, as described in the introduction, involved coupling two ferromagnetic multilayers together antiferromagnetically. Naturally, the first step involved creating a FM multilayer which could host skyrmions.

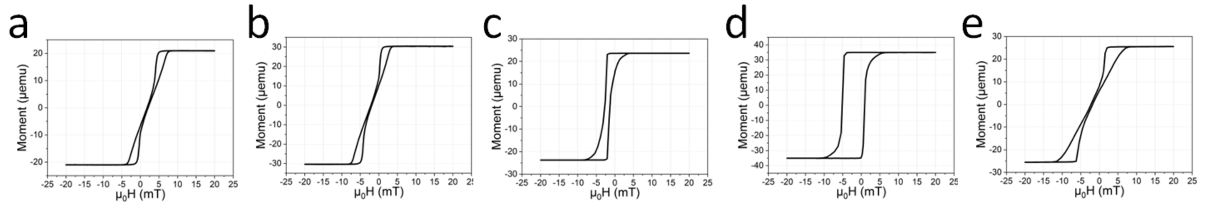

[CoB(6.3 Å)/Ir(6.2 Å)/Pt(6.5 Å)]$_{x4}$ /CoB(6.3 Å)/Ir(4 Å)/Pt(6.5 Å) [CoB(6.2 Å)/Ir(6.2 Å)/Pt(6.5 Å)]$_{x5}$ [CoB(6.3 Å)/Ir(9.2 Å)/Pt(6.3 Å)]$_{x5}$ [CoB(6.6 Å)/Ir(6.0 Å)/Pt(10.1 Å)]$_{x5}$ [Ir(9.2 Å)/ CoB(6.3 Å)/Pt(6.3 Å)]$_{x5}$

Figure 7.14: SQUID magnetometry OP measurements of five repetition multilayers on a base of Ta and Pt and capped with Pt. a) shows the bottom half of stack 2 (X_2) and b) shows the top half of stack 2 (X_1). c) shows a sample grown similar to b), however, with thicker Ir. d) shows a sample grown similar to b), however, with thicker Pt. e) shows a sample grown similar to c), however, with Ir below the CoB and Pt above it. The thicknesses of the repeated parts are labelled below the corresponding measurements.

Figure 7.14a and b shows OP SQUID hysteresis loops for the bottom half of stack 2 (X_2) and the top half of stack 2 (X_1), respectively, as shown in Figure 7.1b. These two loops show wasp-like hysteresis of almost identical shape, slightly off centre on the x-axis. Figure 7.15a and b show the Kerr microscope images of the same samples as in Figure 7.14a and b, showing domain patterns which echo the hysteresis loops. The samples were saturated in a positive magnetic field, then taken through hysteresis until they were saturated in a negative magnetic field. For both, at around 6 mT, small, light coloured skyrmions emerged of around 200 nm. Then, a maze-like domain pattern formed as the light coloured domains became more dominant, until around -6 mT, where only small, dark coloured skyrmions remained of around 200 nm. This confirmed the ability of the FM multilayers of these parameters to host skyrmions.

To confirm these thicknesses were optimal, samples were also grown with either thicker Ir or thicker Pt, as shown in Figure 7.14c and d, and Figure 7.15c and d. The hysteresis loops no longer possessed the strong wasp-like shape and exhibited more square hysteresis loops. Again, this was echoed in the domain images, which showed domains which were either thicker and less maze-like, or long, thin line domains - no skyrmions were observed.

Finally, a stack was grown with the materials in reverse order, i.e. with Ir/CoB/Pt instead of Pt/CoB/Ir. This stack was grown with the thick Ir, as in Figure 7.14c, and the hysteresis loop

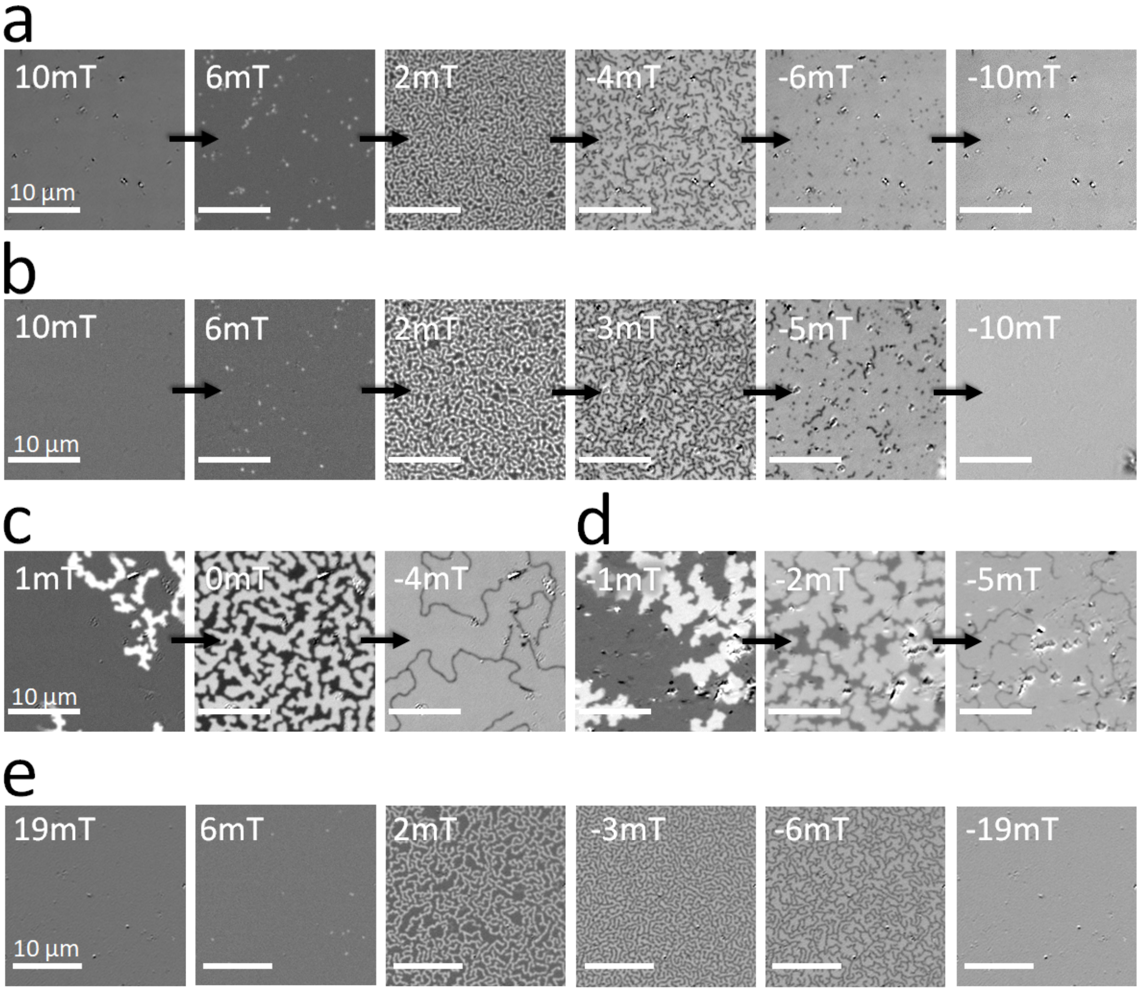

Figure 7.15: Polar Kerr microscopy measurements of five repetition FM multilayers on a base of Ta and Pt and capped with Pt. a) shows the bottom half of stack 2 (X_2) and b) shows the top half of stack 2 (X_1). c) shows a sample grown similar to b), however, with thicker Ir. d) shows a sample grown similar to b), however, with thicker Pt. e) shows a sample grown similar to c), however, with Ir below the CoB and Pt above it.

was similar to those of 7.14a and 7.14b. This meant that skyrmion and tight maze-like domains were observed when this sample was imaged undergoing hysteresis by the Kerr microscope, Figure 7.15e.

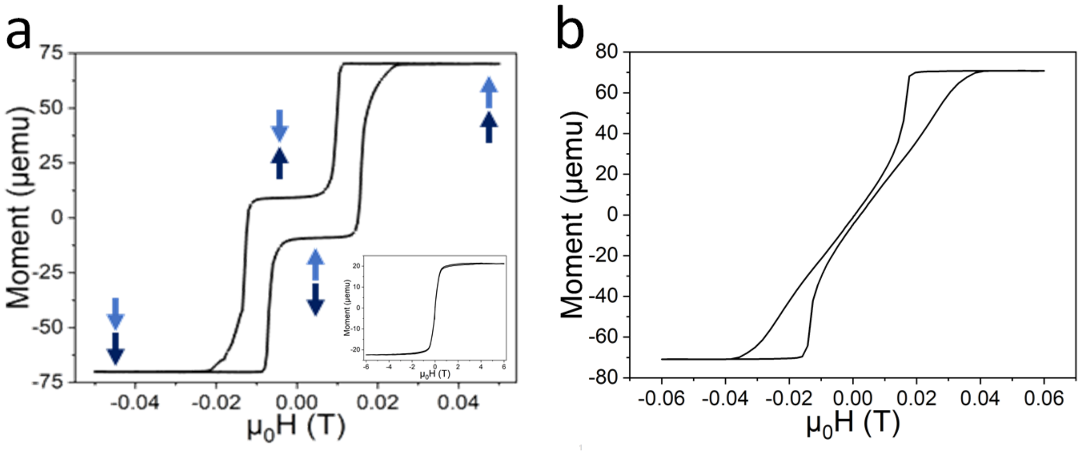

Figure 7.16: a) shows the OP SQUID measurement of stack 2, the dark and light blue arrows represent the bottom half of stack 2 (X_2) and the top half of stack 2 (X_1), as described in Figure 7.1b. The inset shows the sample measured in the plane. b) shows a stack similar to stack 2, however, the middle layer of Ir was not 4 Å and was the same thickness as the other Ir layers in the sample.

Based off the ferromagnetic stacks in Figure 7.14a and b, stack 2 was made by placing a layer of ∼4 Å of Ir between the two FM stacks, making it is essentially a FM magnetic multilayer with ten repetitions, however, the Ir layer in the centre of the stack had a lower thickness, which could introduce AFM-IEC. As expected, this caused the two ferromagnetic multilayers (X_1 and X_2) to couple together antiferromagnetically, as can be interpreted from the hysteresis loop shown in Figure 7.16a. The light blue arrows indicate X_1 and the dark blue arrows indicate X_2, it was observed that as the magnetic field was swept from positive to negative, one FM multilayer switched before zero, and the other FM multilayer switched separately, after zero. This is similar to stack 1 with N=2, however, the switches were less square and more wasp-like due to there being five repetitions, plus, the loop was open at zero field, suggesting the SAF was not completely balanced. The inset shows the IP SQUID measurement, to confirm the PMA of the sample. Figure 7.16b, shows the stack 2, however, the middle layer of Ir was not thinner but the same thickness as the other Ir layers in the sample. As expected, the sample no longer exhibited two separate switches, but only one maze-like switch, suggesting all ten $Co_{68}B_{32}$ layers were coupled together ferromagnetically. Again, confirming the AFM coupling role of the Ir.

7.4.2 Stack 2: Temperature Dependence

As with stack 1, stack 2 was measured as a function of temperature. Figure 7.17a shows the OP hysteresis loops of stack 2 between 300 and 100 K. Stack 2, in contrast to stack 1, maintained two switches only until 250 K, after which the hysteresis loop takes the shape of a stack coupled ferromagnetically. Although, small individual switches were observed at the start/end of the hysteresis. This suggests that at this point, the magnetostatic force from the FM layers overcomes the AFM-IEC. The features of one layer, perhaps the top layer with more Pt above it, behave slightly differently to the other layers. Stack 2 was also measured in the plane, shown in Figure 7.17b, proving the PMA at all temperatures.

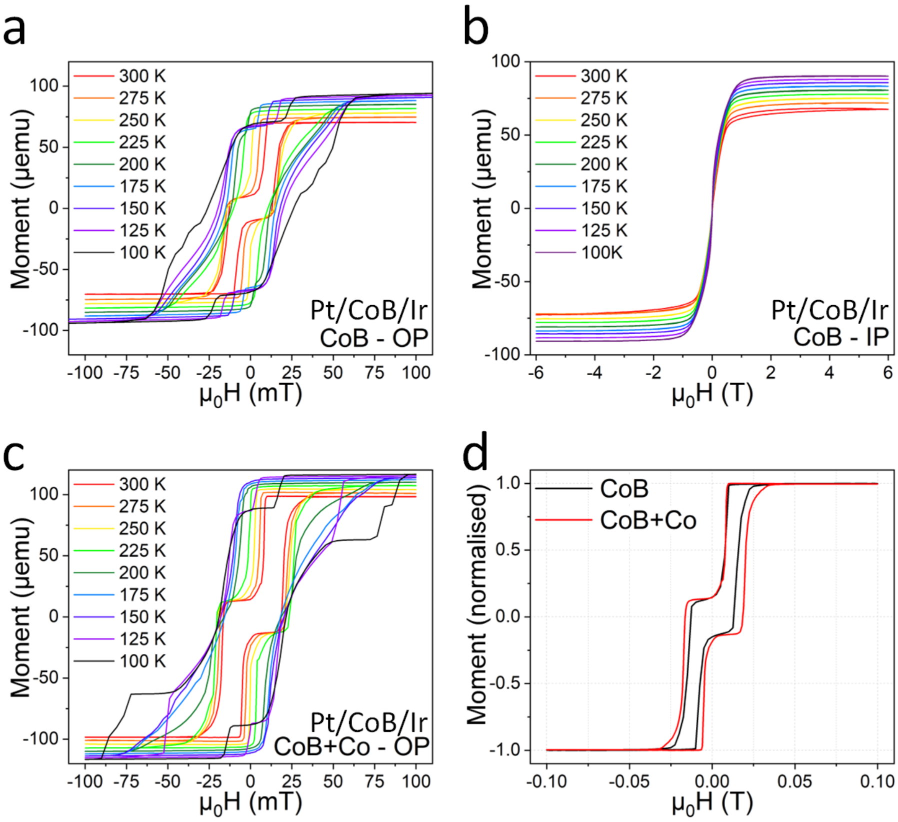

Figure 7.17: a) shows the hysteresis loops of stack 2 measured OP via SQUID magnetometry as a function of temperature. b) shows the hysteresis loops of a) measured IP via SQUID magnetometry as a function of temperature. c) shows the hysteresis loops of a version of stack 2 measured OP via SQUID magnetometry as a function of temperature, however, the CoB was co-sputtered with Co at 10 W. d) shows a normalised comparison between the 300 K hysteresis loops of stack 2, and stack 2 with more Co content (a and c).

Stack 2 was also grown with the CoB co-sputtered with Co to increase the cobalt to boron ratio and investigate the effect it had on the stack. The hysteresis loops measured OP by SQUID magnetometry are shown in Figure 7.17c. The loop maintained two switches only until 200 K, after which the hysteresis loop takes the shape of a stack coupled ferromagnetically until below 125 K, when small individual switches were observed at the start/end of the hysteresis.

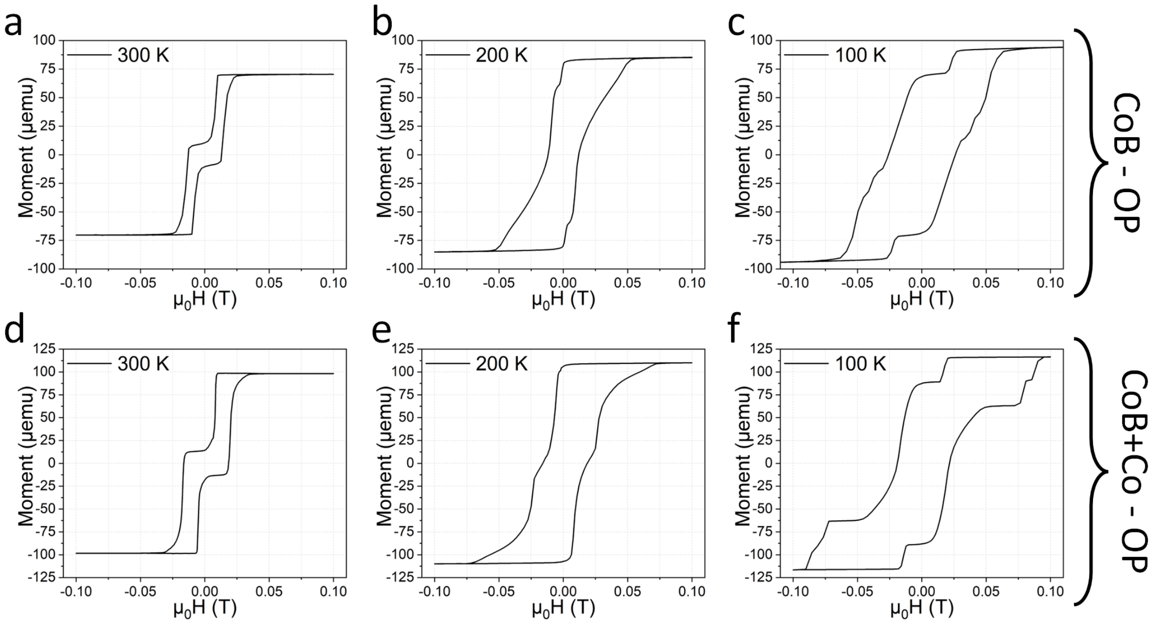

Figure 7.18: This shows a selection of the hysteresis loops from Figure 7.17 in separate plots. a) to c) show stack 2 at 300, 200 and 100 K. d) to f) show stack 2 with the CoB co-sputtered with Co at 300, 200 and 100 K.

The hysteresis loops at different temperatures are separated out in Figure 7.18 for a clear comparison. At 300 K the loops looked similar, a direct comparison of this can be seen in Figure 7.17d, which shows the only difference was the coercivity increased slightly with the added Co. At 200 K, the stack without the extra Co showed FM coupling with a small lip at the start of the hysteresis, by 100 K, other small kinks began to appear. For stack 2 with extra Co, at 200 K, there was only a small kink in the centre of the switch, and by 100 K a small lip at the start and end of the hysteresis was also observed.

7.4.3 Stack 2: Thickness Dependence

As stack 2 relies on the balance of many different effects within the sample, this meant small changes in the thicknesses of the components could eradicate the AFM-IEC. Thicknesses in which the AFM-IEC did occur, comparisons were made to understand how changes in thickness affected the stack. In Figure 7.19a, OP hysteresis loops measured via SQUID magnetometry are shown whilst the CoB thickness was varied. For 6.5 Å of CoB, the typical two switches were visible, for a much higher CoB thickness of 8.7 Å, the two switches were no longer observed suggesting the sample was in a state of FM coupling.

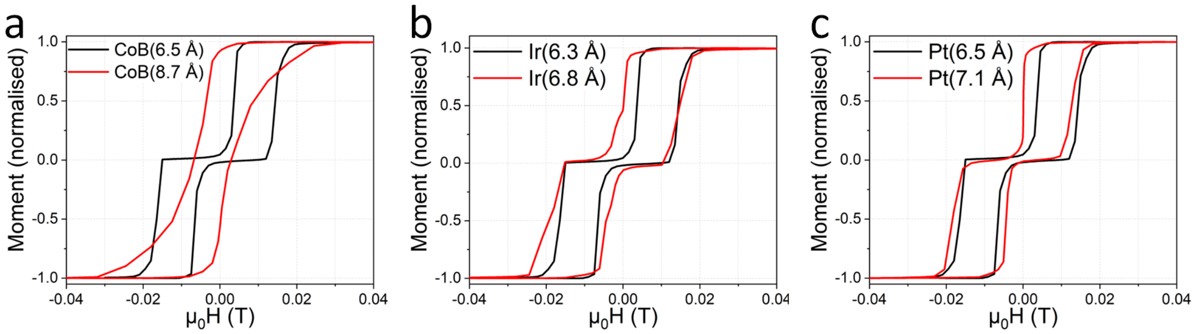

Figure 7.19: a) shows a variation of stack 2 with two different CoB thicknesses compared. b) shows two different Ir thicknesses. c) shows two different Pt thicknesses. All measurements were performed OP via SQUID magnetometry. These stacks were grown on base layers of Ta(30 Å)/Pt(30 Å) and capped with Pt(20 Å).

Figure 7.19b shows stack 2 with two different thicknesses of Ir, in this case, there was less of a difference between the two thicknesses of Ir and therefore there was not a significant difference between the two hysteresis loops. Although, for the thicker Ir it could be argued the switching field was slightly lower and the coercivity slightly higher. For the two Pt thicknesses in Figure 7.19c, again the difference is minimal, however, like with the Ir, it could be argued there was a decrease in switching field and a larger coercivity for the stack with thicker Pt. The samples used in this section had less of an opening at zero field, they also had a thicker base of Pt with 30 Å, compared to 6 Å in the original stack.

7.4.4 Stack 2: Imaging

Stack 1 was then imaged with the Kerr microscope at various points along the hysteresis. The images are shown in Figure 7.20, arranged around the normalised hysteresis loop measured by SQUID magnetometry. The sample was first saturated in a field of -200 mT, then, the field was returned to -30 mT and a background image was taken and subtracted in order to get a better contrast of the domains. Then, after starting in a saturated state at -30 mT, the field was gradually decreased and at -9 mT, lighter circular domains were observed of diameters between 250-500 nm. These lighter domains grew as the field was increased further, until they became maze-like and then more dominant. At the same time, the darker domains became thinner and reduced until only small circular domains of diameters between 250-500 nm remained at 0 mT. The field was then increased below zero and at 9 mT, lighter circular domains were again observed and grew into a maze-like pattern and reduced the darker domains until there were only small circular domains remaining. The state was saturated above 30 mT. The field was then decreased back down to -30 mT and the same process occurred: first switch at 10 mT and then at -9 mT, the darker domains appeared and became dominant after undergoing a maze-like switch. The maze-like domains were not as tight as in the five repetition FM sample, suggesting that in becoming part of the SAF, the properties of the domains change slightly. It was also found that small circular-like domains which appeared at -9 mT could be induced using a field-pulse protocol, i.e. from a 0 mT saturated state, pulsing the field for 1 second at -9 mT, then returning to zero field. The small domains, once formed, remained unchanged upon returning to zero field, and their size depended on the pulse length and magnitude. The sample was also measured by MFM at the University of Leeds, which was only possible at the higher fields and in air. In agreement with the Kerr microscope images, after saturating the sample in a negative field, on the return to zero field, small circular domains appeared from the saturated state at -8.5 mT, as shown in Figure 7.20, which most likely were not visible with Kerr microscopy. Underneath, shows a zoomed in image of a small circular domain, a 450 nm skyrmion was identified.

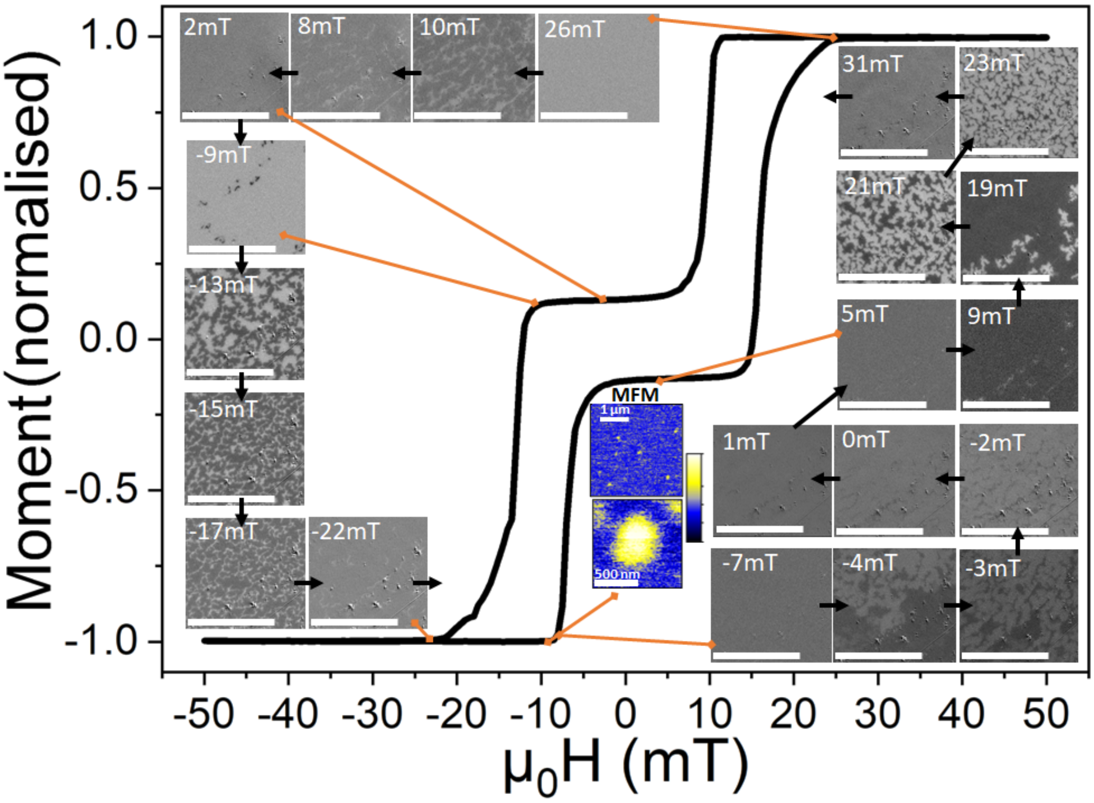

Figure 7.20: This figure shows the hysteresis loop of stack 2 and images taken by Kerr microscopy at the different fields along the hysteresis. All scale bars are 20 μm. It also shows two MFM images taken at -8.5 mT with the lower MFM image being a small scale measurement of a small circular domain in the upper MFM image.

In order to image stack 2 more thoroughly using MFM, a sample was grown of stack 2, however, with Pt (30 Å) included in the base instead of Pt (6 Å), its hysteresis loop is shown in Figure 7.21. The sample was sent to the Swiss Federal Laboratories for Materials Science and Technology (EMPA) to be measured by state of the art MFM, however, the results did not show any skyrmions present in the sample (Figure 7.21). Only small line-like domains were observed around the switches. It is therefore possible that the small domains observed by the Kerr microscope were of this nature, however, appeared as small circular domains due to the low resolution of the image compared to MFM. It was also noted that due to the strong signal from these particular domains, that they were not antiferromagnetic domains, as this would lead to a less well defined domain picture. It was concluded that the two layers begin in a saturated state with the spin orientation of both layers in the same direction, then, the first switch involves one layer breaking into a domain pattern before becoming fully saturated in the opposite direction and being in a SAF state at zero field. Then, when taking the applied field above zero, the other layer splits into domains meaning there were areas with the two layers coupled ferromagnetically and areas with the two layers coupled antiferromagnetically, before the whole sample became saturated in the opposite direction.

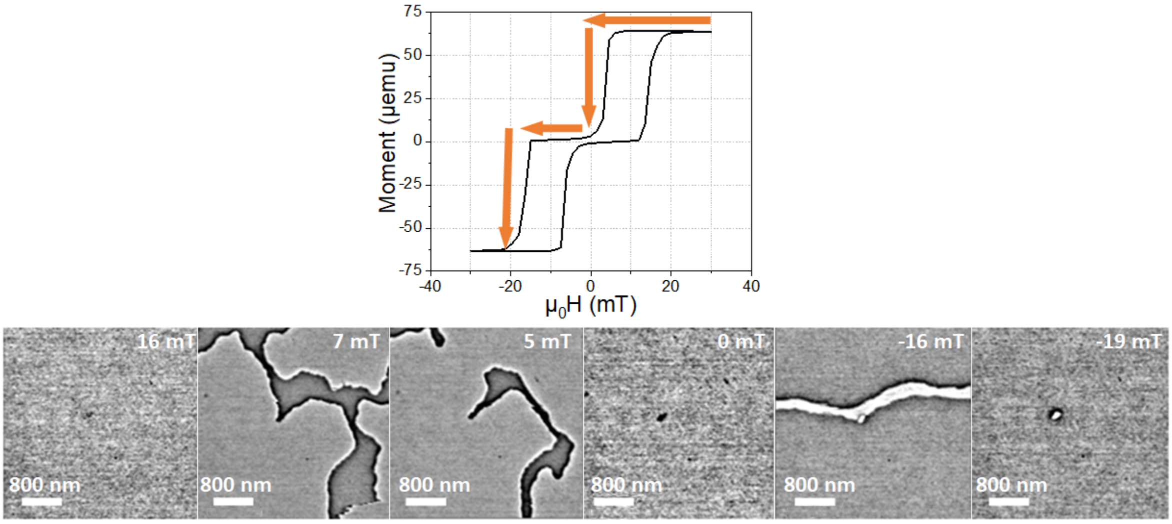

Figure 7.21: This figure shows the SQUID measured OP hysteresis loops for a version of stack 2, grown with Pt (30 Å) included in the base instead of Pt (6 Å). The arrows indicated the direction of the field sweep performed on the MFM images below. The MFM images were taken at EMPA in Switzerland and show images of the sample between 16 and -19 mT. The scale bars represent 800 nm.

To conclude the discussions on stack 2:

- A five repetition multilayer of CoB/Ir/Pt was successfully designed to host room temperature ferromagnetic skyrmions.
- This FM multilayer was turned into a SAF in which two of the FM multilayers, coupled

antiferromagnetically by Ir, switched separately.

- X-ray analysis showed that there was roughness/intermixing at the CoB interfaces but not at the Ir/Pt interfaces.
- The temperature dependent measurements found that stack 2 maintained the typical SAF like behaviour until 250 K, and stack 2 with increased Co ratio until 200 K.
- For stack 2, with increased CoB thickness, the switching fields decreased with temperature and the coercivity increased.
- Increasing the cobalt to boron ratio in stack 2 caused the switching fields to increase very slightly.
- After increasing the CoB thickness past a certain threshold the stack showed FM-IEC instead of AFM-IEC.
- When the thickness of the Pt or Ir in the FM multilayer was increased, the switching fields decreased and coercivity decreased slightly.
- Kerr microscope images showed two clear switches with maze-like domains, and MFM images showed 450 nm skyrmions present at -8.5 mT.
- Measurements performed at EMPA of stack 2 showed line-like domains only and no skyrmions.
- It was likely that the two FM multilayers were coupled antiferromagnetically at zero field, however, the domain patterns were not coupled together antiferromagnetically.

7.5 Stack 3

7.5.1 Building Stack 3

Following the drawbacks with stack 2, a third stack was proposed, which involved reversing the order of the stack as the FM multilayer in Figure 7.15e showed strong potential for skyrmion nucleation. Therefore, this stack was grown as a ten repetition stack, with the middle Ir layer of thickness within the AFM coupling thickness range. Figure 7.22a shows the thicknesses of the Ir, $Co_{68}B_{32}$ and Pt in the two FM multilayers of five repetitions, coupled together antiferromagnetically by the thinner Ir layer, above the hysteresis loop of the sample, measured OP by SQUID magnetometry. The hysteresis loop appeared to exist in four parts, with a small overlap in the centre. The different effects within the sample seemed to combine in an interesting way. This was reinforced by the image taken at -23 mT on the Kerr microscope, which shows three different coloured domains, inferring that some layers are coupled together and others are not. It shows dark line domains, shaded in with medium dark domains, on a background of light domains.

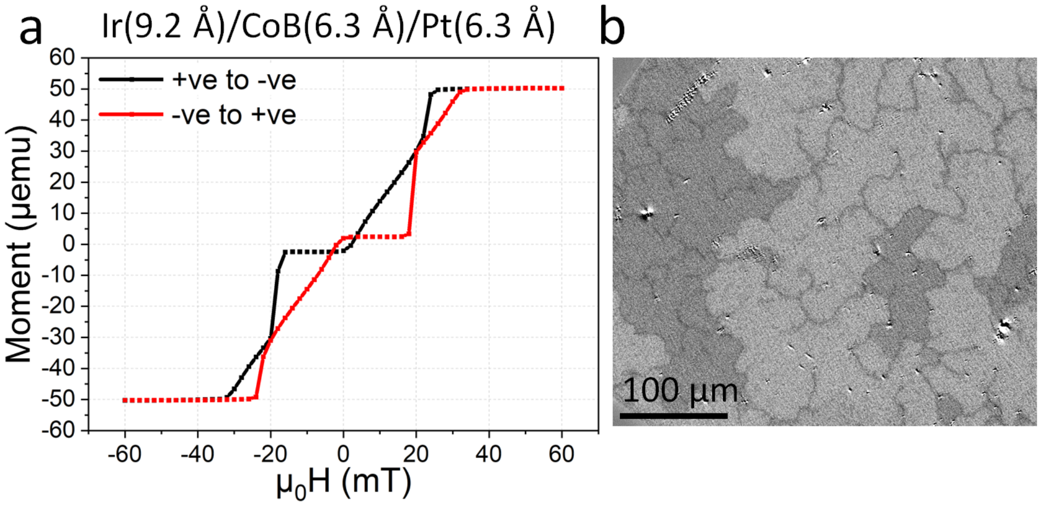

Figure 7.22: a) shows the OP SQUID hysteresis loop of a reversed version of stack 2 consisting of Ta(30 Å)/Pt(30 Å)/[Ir(9.2 Å)/CoB(6.3 Å)/Pt(6.3 Å)]$_{\times 5}$/Ir(4 Å)/CoB(6.3 Å)/Pt(6.3 Å)/[Ir(9.2 Å)/CoB(6.3 Å)/Pt(6.3 Å)]$_{\times 4}$/Pt(20 Å). b) shows a Kerr microscope image of the sample at -23 mT.

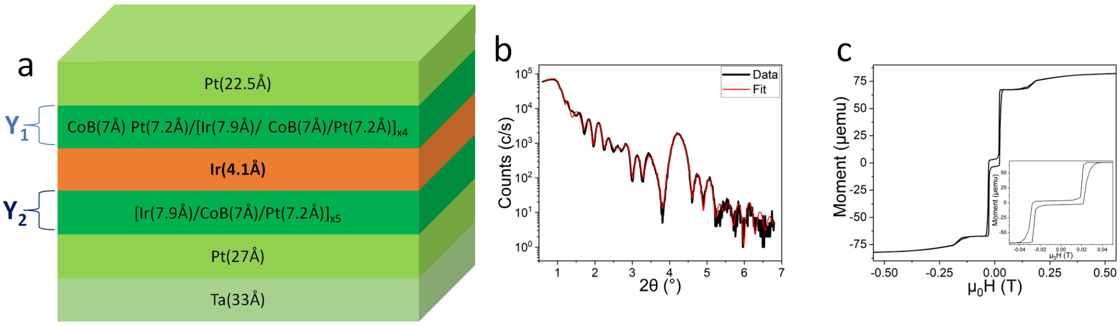

Figure 7.23: a) shows stack 3, consisting of two FM multilayers coupled antiferromagnetically by the 4.1 Å of Ir in the centre. The upper FM multilayer is labelled as Y_1, and the lower FM multilayer as Y_2. b) shows a low angle x-ray scan, fitted using GenX[136], of stack 3. c) shows the hysteresis loop of stack 3, measured OP by SQUID magnetometry. The inset shows a zoomed in version of the centre of the loop.

The thicknesses were tweaked until the hysteresis loop of the stack appeared more consistent with the behaviour of two FM multilayers coupled together antiferromagnetically. This will be referred to as stack 3 and the new thicknesses are shown in a schematic of the whole structure in Figure 7.23a. A low angle x-ray scan fitted using GenX[136] was used to estimate the thicknesses, as shown in Figure 7.23b. The changes in the FM multilayers from the sample in Figure 7.22, included a reduction in the Ir thickness, and an increase in the Pt and CoB thicknesses. The hysteresis loop of this stack measured OP via SQUID magnetometry is shown in Figure 7.23c. It showed two sharp switches either side of zero, shown more clearly in the inset, which were at around ±0.04 T, however, there was a small outer switch at both the start and end of the hysteresis loop, around ±0.16 T. There was also a open loop at zero field, indicating an imbalance within the stack. The switching fields tended to be higher than those of stack 2, similarly to the pattern found by Lau et al..[97]

7.5.2 Stack 3: Temperature Dependence

The temperature dependence was also considered for stack 3, as shown in Figure 7.24a. Two switches remained down to 10 K, with the switching fields reducing with temperature and the coercivity increasing with temperature. The small outer switches became less sharp below 100 K, as they appeared to move closer to the main two switches.

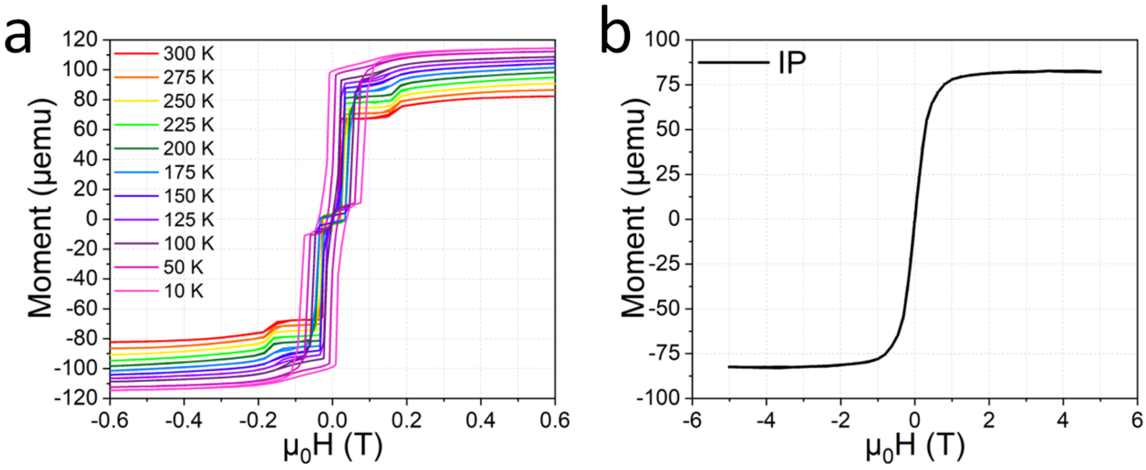

Figure 7.24: a) shows the OP hysteresis loops for stack 3 measured over a range of temperatures between 300 and 10 K with a SQUID. b) shows the same sample, instead, measured at 300 K in the plane.

The magnetic moment also increased as the temperature decreased. These trends can be seen more clearly in Figure 7.25. Figure 7.24b shows stack 3 measured IP to confirm the PMA of the stack.

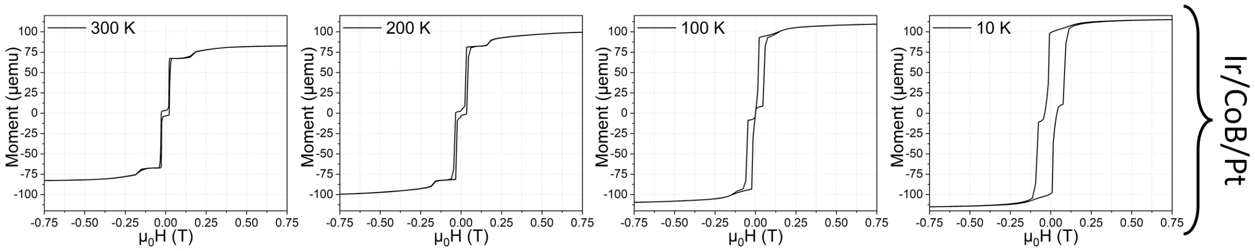

Figure 7.25: Four hysteresis loops of stack 3, measured at different temperatures: 300, 200, 100 and 10 K, taken from Figure 7.24a, via OP SQUID magnetometry.

7.5.3 Stack 3: Thickness Dependence

The thickness dependence of the components of stack 3 were also considered by changing the thickness of one material and comparing the hysteresis loops measured by the SQUID. Firstly, the thickness of CoB was varied in a version of stack 3, shown in Figure 7.26. Lower Ir and Pt thicknesses were used, compared to Figure 7.23, of 6.5 Å, however, the features of the hysteresis loops were similar. When the CoB thickness was increased from 6.75 Å to 7.25 Å, the loop became similar to that in Figure 7.22, indicating that if the thickness of one material in the multilayer goes over a certain threshold, the sample properties can become unusual.

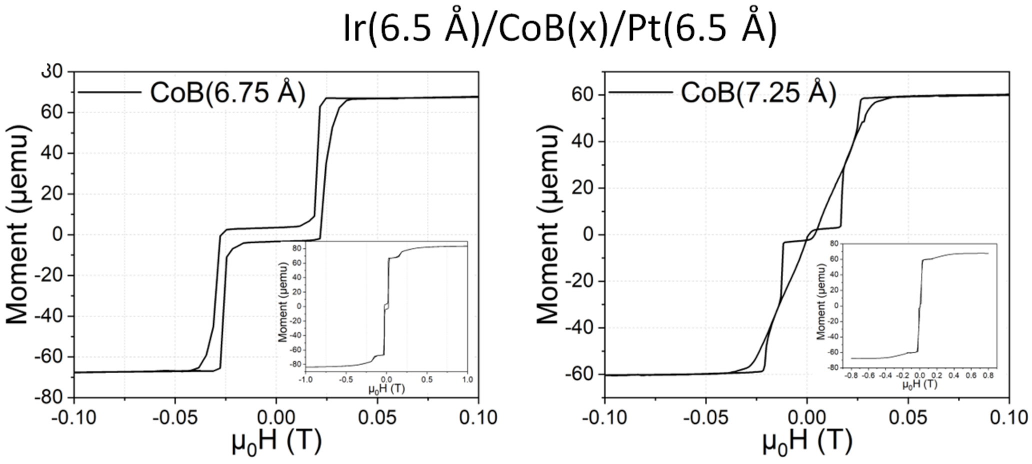

Figure 7.26: Hysteresis loops measured OP with SQUID magnetometry. It shows two versions of stack 3, where the material thicknesses of Y_1 and Y_2 are labelled above the graphs, with two different CoB thicknesses labelled on each graph. The graphs shows a zoomed in version of the hysteresis loop, with the whole loop shown in the inset.

Next, the thickness of Pt was varied in a version of stack 3, shown in Figure 7.27. Again the Ir and CoB thicknesses in the FM multilayer were slightly lower, compared to Figure 7.23, at

6.5 Å and 6.75 Å, respectively. When increasing the Pt thickness by 0.5 Å, two obvious changes were observed; the switching fields of both the main inner switches and the small outer switches increased. Although the gap in the centre of the loop does not change in amplitude.

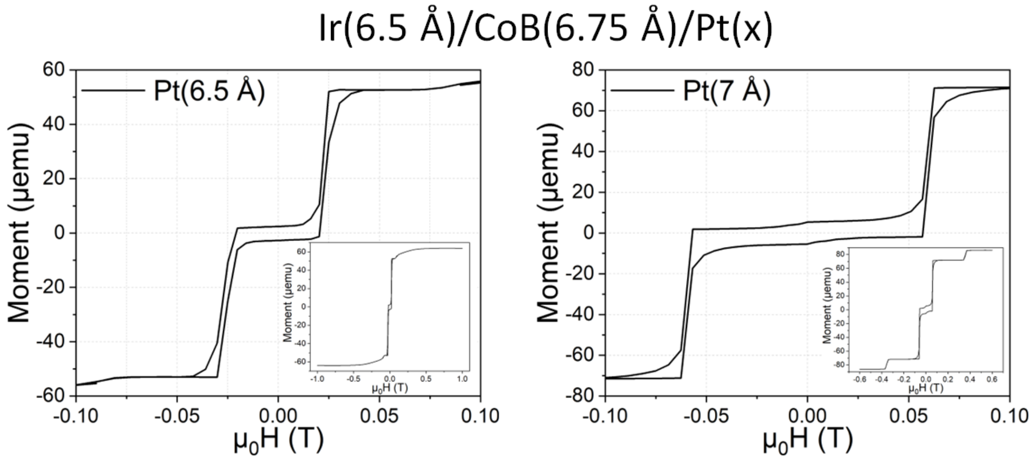

Figure 7.27: Hysteresis loops measured OP with SQUID magnetometry. It shows two versions of stack 3, where the material thicknesses of Y_1 and Y_2 are labelled above the graphs, with two different Pt thicknesses labelled on each graph. The graphs shows a zoomed in version on the hysteresis loop, with the whole loop shown in the inset.

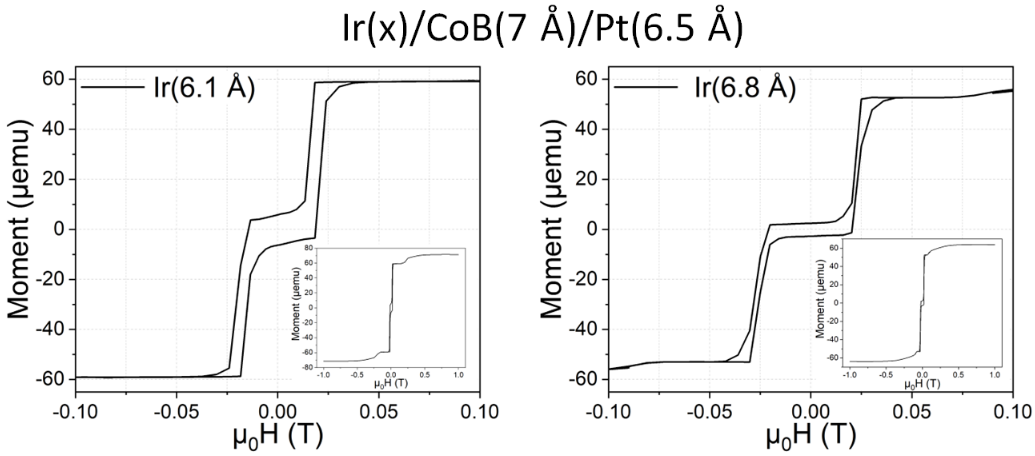

Figure 7.28: Hysteresis loops measured OP with SQUID magnetometry. It shows two versions of stack 3, where the material thicknesses of Y_1 and Y_2 are labelled above the graphs, with two different Ir thicknesses labelled on each graph. The graphs shows a zoomed in version on the hysteresis loop, with the whole loop shown in the inset.

Finally, the thickness of the Ir in the FM multilayers Y_1 and Y_2 was varied. This is shown in Figure 7.28, and the CoB and Pt thicknesses were 7 Å and 6.5 Å, respectively. Here, we saw a

different trend to when Pt was varied, the lower Ir thickness showed a lower switching field for the main switches. However, for the outer switches, the switching field decreased when the Ir thickness was increased.
To conclude the discussions on stack 3:

- When a ferromagnetic multilayer consisting of Ir/CoB/Pt multilayers was grown, it showed skyrmions present.
- When the FM multilayer was placed into the SAF design (stack 3), unusual domain patterns formed, supporting the claim that the properties of the FM multilayers were changed when two are coupled together antiferromagnetically.
- Altering the thicknesses of the materials in the stack lead to stack 3, showing a hysteresis loop with the two FM multilayers switching separately.
- This change in thicknesses, however, reduced the potential of the sample to host skyrmions easily.
- Compared to stack 2, this stack was much more reliable to grow and could exhibit higher switching fields.
- There were always two small switches at the start and end of the hysteresis loop suggesting part of the sample was consistently exhibiting different properties.
- Unlike stack 2, stack 3 maintained the SAF behaviour from 300 K to 10 K.
- The switching field of the main switches and the small outer switches both decreased as the temperature decreased, and the coercivity increased - as with stack 2.
- As the CoB thickness in stack 3 was increased, the hysteresis loop became abnormal.
- As the Pt thickness was increased, the switching fields increased, contrary to stacks 1 and 2.
- As the Ir thickness in the FM multilayer was increased, the main switching fields increased, contrary to stacks 1 and 2. However, the small outer switching fields decreased, suggesting there may not be a link between the thickness and the outer switching field.

7.6 Stack 1 and 2: Electrical Measurements

Electrical transport measurements were made on stacks 1 and 2. At the University of Leeds, measurements were made of the transverse resistance (R_{xy}) and of longitudinal resistance (R_{xx}). These measurements were performed using a Hall bar for all plots in Figure 7.29. Figure 7.30a and b used a 3x10 mm strip of material (therefore the longitudinal measurement taken with an OP field was not reliable due to the contacts not being perfectly in line, which resulted in an R_{xy} component). Figure 7.30c and d, were performed at Northwestern University, Illinois, in longitudinal mode, with both an in and OP field. Figure 7.30c shows the measurement with an OP field compared to the magnetic moment measurement taken using SQUID magnetometry. The measurements are described in detail in Chapter 4.

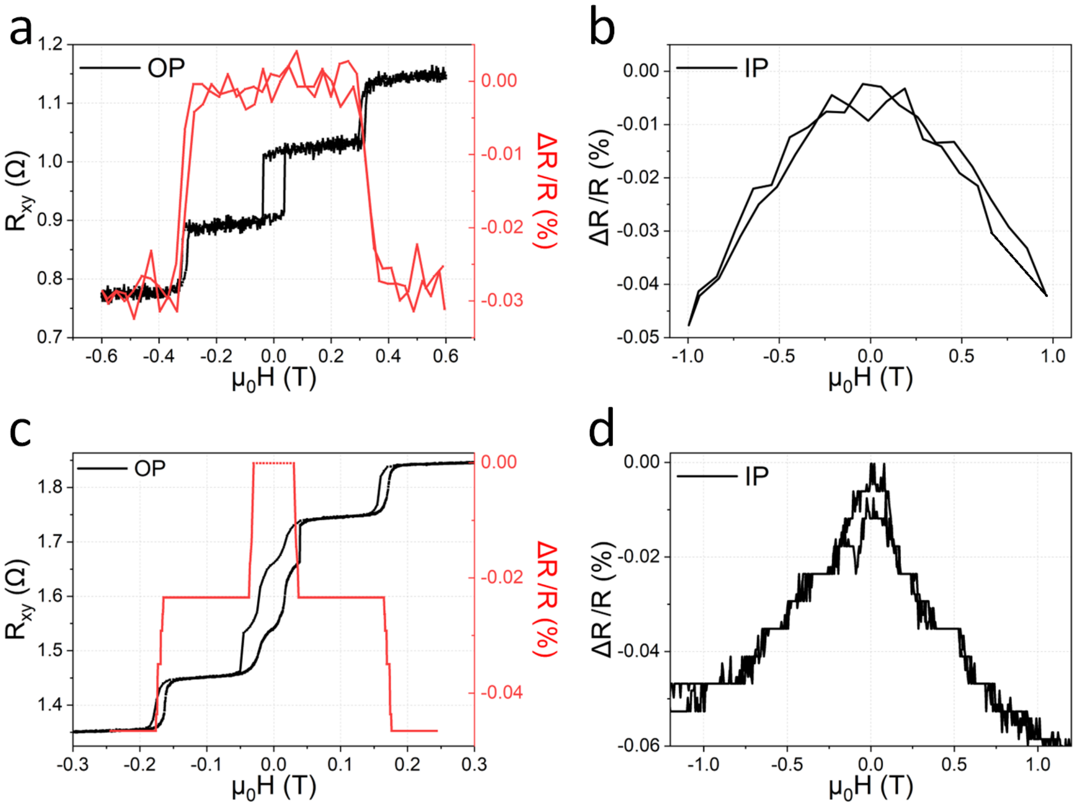

Figure 7.29: a) and c) show both the transverse resistance (R_{xy}) and the longitudinal resistance (magnetoresistance as a percentage) as an applied field was swept OP for stack 1 with N=3 (a) and N=5 (c). b) and d) show the longitudinal resistance (magnetoresistance as a percentage) as an applied field was swept IP for stack 1 with N=3 (b) and N=5 (d). These electrical measurements were taken on Hall bars at the University of Leeds.

Electrical resistance measurements are a useful tool for understanding the intrinsic properties of the stacks. For stack 1 with N=3, Figure 7.29a, when measured OP, the transverse resistance reflected the hysteresis loop and the longitudinal resistance increased at the first switch, as the spins in one of the three layers switched directions (↑↓↑). This resistance remained across the second switch, as the number of layers coupled antiferromagnetically did not change (↓↑↓), then, the resistance decreased once all the spin of all the layers were orientated in the same direction again (↓↓↓). The IP field measurement, 7.29b, showed a typical parabolic shape for a PMA sample, these measurements compared well to those made by Lau et al. with Ir/Co/Pt samples.[97] Figure 7.29c and d show the same measurements for stack 1 with N=5, the magnetoresistance in 7.29c had been processed to remove the noise and the data <0 has been reflected around y=0, due to a connection problem during the measurement. The data suggested that as one FM layer switched, AFM-IEC was present between two sets of FM layers (↑↑↓↑↑), after the second switch the resistance increased by the same amount, suggesting that now all layers were coupled together antiferromagnetically (↑↓↑↓↑). Over the middle switch, the resistance did not change, showing all 5 layers were still coupled together antiferromagnetically (↓↑↓↑↓), then as the fourth switch occurred, the resistance dropped (↓↓↑↓↓) as only two layer couplings were antiferromagnetic, then a similar drop in resistance as the stack became fully saturated in the ↓ orientation. Again, the IP magnetoresistance measurement showed a gradual change in the orientation of all moments from ← to → as the resistance increased gradually to zero, then decreases gradually. Contrarily to the N=3 sample, the curve was of opposite inflection and slightly asymmetric.

Figure 7.30a, shows the transverse resistance of stack 2 measured with an OP field, the electrical measurement replicates the magnetic measurement of the sample very well. The longitudinal measurement with an IP field is shown in 7.30b, again, an expected gradual increase, then decrease around zero in the resistance was observed. In Figure 7.30c, the magnetic moment of a sample similar to stack 2, with some variations in thickness, to that in 7.30a is shown. The difference in the hysteresis loops being that the switching fields were higher in 7.30c and a small volume of the five repetitions ferromagnetically coupled together appeared to have a slightly higher switching field. The longitudinal resistance was measured with an OP field, and the resistance was shown to increase when X_1 switched, then remain with the higher resistance until X_2 switched. Modelling the two FM multilayers X_1 and X_2 as one spin (↑ / ↓), the lower resistance would exist with the configuration of ↑↑ and ↓↓, and the higher resistance would occur with the configurations ↑↓ and ↓↑. The forward and backwards field sweeps did not exactly coincide, indicating the hysteresis in the sample. The longitudinal measurement with an IP field, Figure 7.30d largely resembled the measurement in 7.30b.

7.7 Conclusions

It was concluded that a strong AFM-IEC coupling was found in repetitions of $Co_{68}B_{32}$/Ir/Pt, when the Ir has a thickness which supports the negative coupling, i.e. stack 1. This stack supported a typical behaviour in which an increase of the FM magnetic or Pt layer thickness caused a decrease in the switching fields due to the strength of the AFM-IEC being reduced, this trend was followed also by stack 2. Stack 3 also agreed in terms of the CoB, however, the switching field was increased when the thickness of Ir or Pt in the FM multilayer was increased, indicating that the coupling strength increased. For both stacks 1 and 2, an increase in the ratio of cobalt to boron atoms

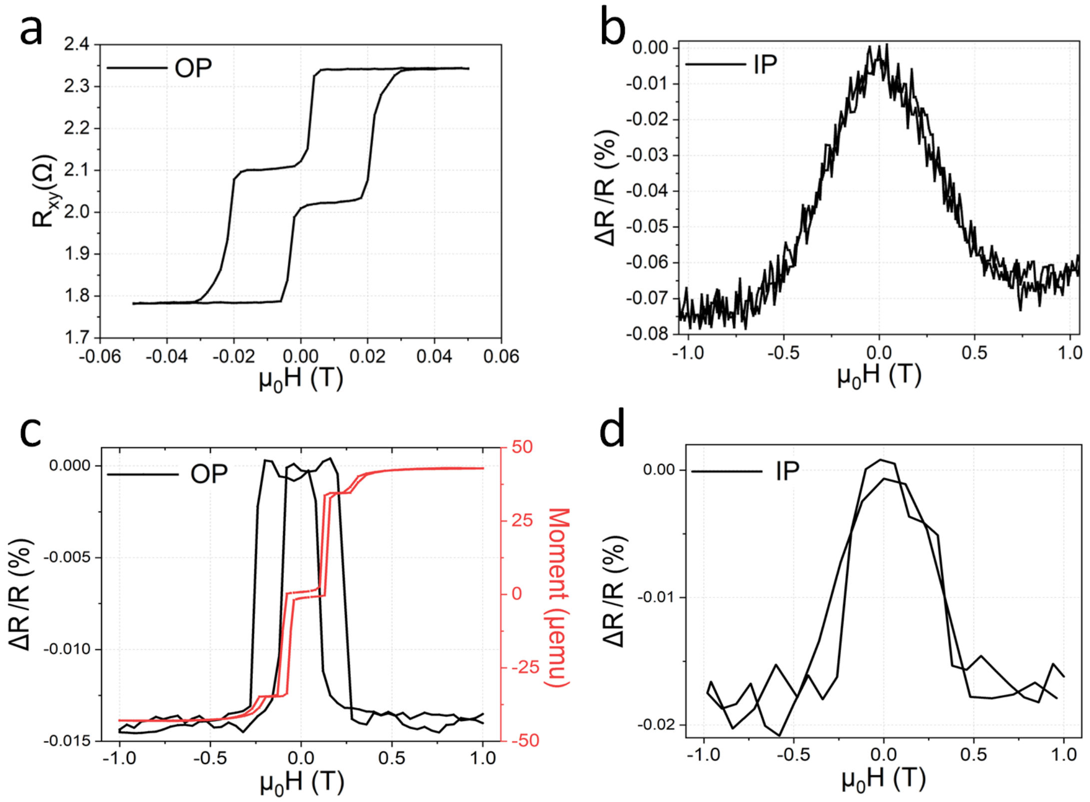

Figure 7.30: a) shows the transverse resistance (R_{xy}) measured with an OP field, and b) shows the longitudinal resistance (magnetoresistance as a percentage) measured with an IP field for stack 2. c) shows both the magnetic moment measured by SQUID magnetometry and the longitudinal resistance (magnetoresistance as a percentage), as an applied field was swept OP of stack 2. d) shows the longitudinal resistance (magnetoresistance as a percentage) as an applied field was swept IP for stack 2. a) and b) were measured on a 3x10 mm thin film at the University of Leeds, c) and d) were measured on a 8.5x60 μm bar at Northwestern University.

by co-sputtering Co with the CoB, lead to an increase in the switching fields, perhaps due to the structure becoming more defined. In terms of trends with temperature, in all samples, the coercivity of the switches increased as the temperature decreased. With stack 1, the switching fields increased as the temperature decreased, indicating the coupling strength becomes stronger at low temperatures, perhaps for the same reason it increases with more Co content. However, for the N=2 stack 1 with thicker CoB, and for stack 2 and 3, the switching field reduced as the temperature reduced. From this, it was concluded that when the Ir layer was negatively coupling together more magnetic material, it behaved in an opposite way to when two single layers were coupled together. Stack 3 also continued to display a small outer switch at the start and end of both halves of the hysteresis loop independent of layer thicknesses, the cause of which is unknown. We also confirmed a temperature dependent phase change was possible in both stack 1 (with increased Co content) and stack 2. The material could be optimised to shift the phase transition to higher temperatures and allow it to be induced by joule heating from currents[258].

From the electrical measurements, an understanding of how the individual layers were switching was achieved. In stack 1, a layer which resulted in the most antiferromagnetically coupled layers always switched first, irrelevant of its position in the stack. The resistance measurements of stack 2 also confirmed the two ferromagnetic multilayers switching separately. Systematic resistance measurements of all stack 1 for N=2 to N=8 would give gainful insight into the intrinsic competition within the sample and where the limitations of the AFM-IEC lie.

We concluded that the top and bottom part of stack 2 have the ability to host stable, room temperature skyrmions, though an increase in thickness of the Pt or Ir can overturn this. The nature of the domains can also become slightly altered when the AFM-IEC is also introduced into the system. Despite not being able to prove that SAF skyrmions exist in stack 2, these systems are promising in different areas of application. In a uniform out-of-plane state, the magnetisation could be excited via a spin-orbit torque from the spin Hall effect, and due to the SAF nature of the sample, it is expected that the frequencies would be in the tens of gigahertz range. Conversely, the same system could be used as a rectifier with frequencies in this range with an AC power supply. For a system with a non-uniform state, in which skyrmions are present, spin-orbit torque motion could be promoted with zero skyrmion Hall angle and a relatively high velocity.[263–266] These applications would all have the advantage that the magnetisation dynamics can be measured with a larger signal than a fully compensated, two FM layer SAF. Despite adaptations of the stacks still being needed to create a SAF which could easily host SAF skyrmions, this chapter takes a large step in understanding how these complex systems work. Tweaking parameters such as the thicknesses and number of repetitions of the layers in the systems is key to creating a reliable SAF samples with the ability to host SAF skyrmions.

CHAPTER 8

Terahertz Time Domain Spectroscopy with CoB Multilayers

8.1 Introduction

Performing THz-TDS, as described in Chapter 4, yielded a graph which plots the current read by the lock-in amplifier (measured from when the probe beam hits the detecting LT-GaAs square) against the time domain, the time difference for the probe beam to reach the LT-GaAs square as the delay stage is moved - labelled as ‘delay’, see Figure 8.2a. Information from this signal, such as the amplitude, full width half maximum (FWHM), and relative positions in the time domain of the peak, was used to characterise the THz-TDS system for each device. These measurements were also performed using different DC bias voltages (Figure 8.2c) and different laser optical powers (Figure 8.2d). A fast Fourier transform (FFT) was performed on the signal to analyse it in the frequency domain and to determine the bandwidth of the measurements (Figure 8.2b).

In this work, we consider seven different coplanar waveguides, with the differences displayed in Figure 8.1 and Table 8.1. CPW 1 (Figure 8.1a) was the original design, made entirely of Ti/Au (10 nm/150 nm), to use as a reference. CPW 2 (Figure 8.1b) was also made from Ti/Au (10 nm/150 nm) for a reference, however, it tapered down to a Hall bar in the centre of the waveguide; in this case the Hall bar was made from thinner Ti/Au (5 nm/15 nm). CPW 4, 5, 6 and 7 (Figure 8.1c) were the same as CPW 2, however, the Hall bar was made from a Co or $Co_{68}B_{32}$ magnetic multilayer, as detailed in Table 8.1. The grounding planes, central line and contacts (including the six from the Hall bar were all made from Ti/Au (10 nm/150 nm), the Ti was used to secure the gold onto the substrate. CPW 3 (Figure 8.1d) differed, as not only the Hall bar was made from the magnetic material, but the whole tapered central line.

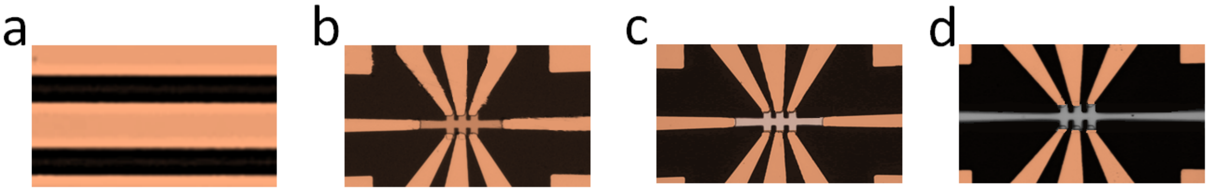

Figure 8.1: a) shows CPW 1, zoomed in on the centre, it shows the central line surrounded by two grounding planes made entirely of thicker Ti/Au. b) shows a Hall bar placed in the centre of a tapered central line made of a thinner gold layer than the contacts, fabricated in a separate lithography step (CPW 2). Coming from the Hall bar are six gold contacts and the edges of the grounding planes are shown in the corners. c) shows a Hall bar made from a magnetic multilayer material in the centre of a tapered central line (CPW 4, 5, 6 and 7). d) shows a Hall bar in the centre of a tapered central line, with both components made from the same magnetic multilayer (CPW 3).

These magnetic multilayers were chosen as they have the ability to host skyrmions, with the aim to measure any possible responses from magnetic skyrmions within the Hall bars. Addition-

Waveguide	Hall Bar material	Central line material
CPW 1	Ti/Au (10 nm/150 nm)	Ti/Au (10 nm/150 nm)
CPW 2	Ti/Au (10 nm/15 nm)	Ti/Au (10 nm/150 nm), T
CPW 3	[CoB(8 Å)/Ir(5 Å)/Pt(6 Å)]$_{\times10}$	[CoB(8 Å)/Ir(5 Å)/Pt(6 Å)]$_{\times10}$, T
CPW 4	[CoB(8 Å)/Ir(5 Å)/Pt(12 Å)]$_{\times10}$	Ti/Au (10 nm/150 nm), T
CPW 5	[Co(9 Å)/Ir(3 Å)/Pt(6 Å)]$_{\times10}$	Ti/Au (10 nm/150 nm), T
CPW 6	[x]$_{\times4}$/CoB(7 Å)/Ir(4 Å)/Pt(6.5 Å)/[x]$_{\times5}$	Ti/Au (10 nm/150 nm), T
CPW 7	[CoB(8 Å)/Ir(4 Å)/Pt(6 Å)]$_{\times3}$	Ti/Au (10 nm/150 nm), T

Table 8.1: This table explains the different coplanar waveguides measured in this study, labelling them 1 to 7. The 'Hall bar material' column signifies the material of which the Hall bar was made, where x = $Co_{68}B_{32}$ (7 Å)/Ir (6.5 Å)/Pt (6.5 Å). The 'central line material' column signifies the material of which the central line was made and it is commented whether the central line was tapered or not. All other contacts (to the LT-GaAs squares and Hall bar) and grounding planes were made from Ti/Au (10 nm/150 nm). The thicknesses were calculated determined by fits to x-ray reflectivity using GenX or estimated based off the growth rates. T = tapered.

ally, synthetic antiferromagnets were used which have been shown to have resonances in the THz frequency range, as detailed in Chapter 3.

8.2 Characterisation Measurements

Figure 8.2a maps out the THz pulse in the time domain of an input pulse, with 50 V DC bias, measured on CPW 1. From this signal, we can take the amplitude of the peak (∼0.56 nA), and the FWHM (∼0.96 ps). The position of the peak is arbitrary and only relevant when considering it in terms of position compared to another peak, e.g. input vs. transmission measurements, or measurements in opposite directions. In the FFT of the pulse, Figure 8.2b, the main parameter was the bandwidth which is defined at the point when the signal becomes more flat and noisy. In waveguides which are not solely made from Ti/Au, a dip or peak may be visible within the bandwidth, where the THz pulse interacts with the material in its path.

Figure 8.2c, shows an example of transmission measurements for different DC biases in coplanar mode on a tapered waveguide with a Hall bar. The obvious trend was how the amplitude decreased linearly as the DC bias decreased, as expected. The pulse width, on the other hand, remained more constant. Another feature that was present, more dominantly in the measurements on the tapered waveguides, was signals from reflections that appeared after the main peak. These reflections should be analysed in order to remove them, after verifying they are not part of the main response. Finally, to ensure ohmic behaviour of the switches, meaning it followed the linear regimes where heating of

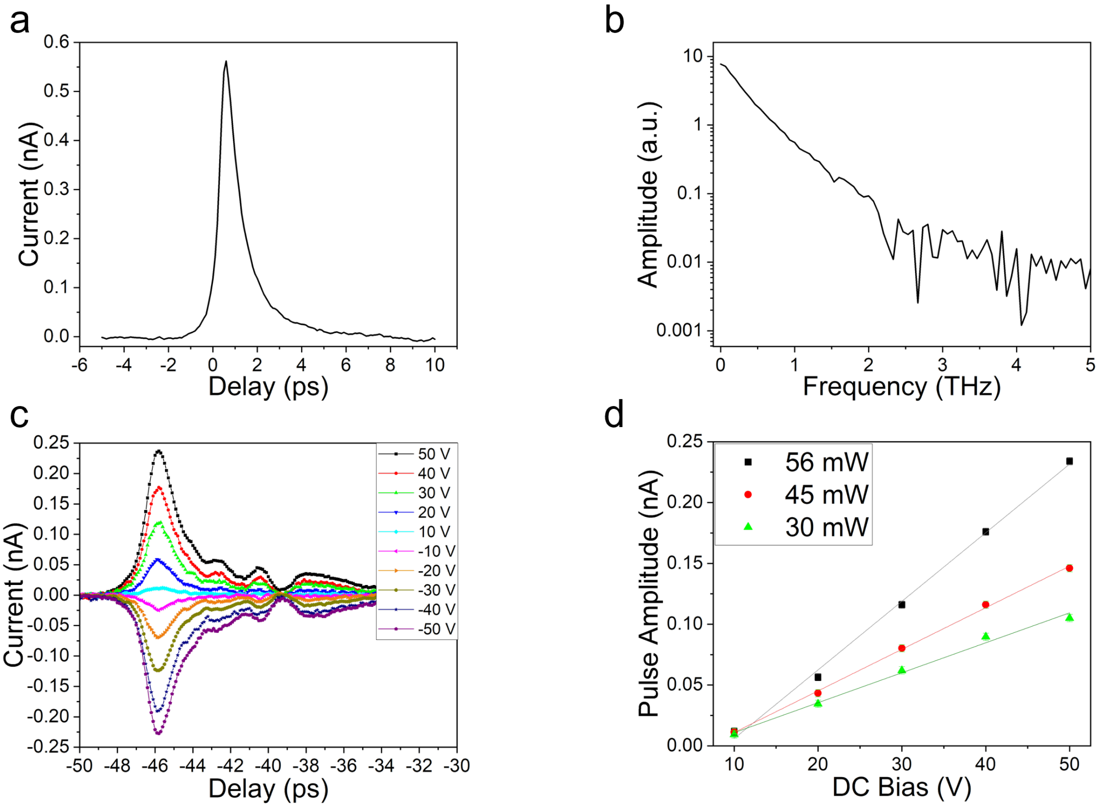

Figure 8.2: a) represents a typical current vs. delay measurement from THz-TDS. It shows an input measurement with 50 V DC bias, from CPW 1. b) shows the FFT from a), with a bandwidth of around 2 THz. c) shows the current-delay measurements performed whilst using different DC bias from 50 V to -50 V. These transmission measurements were performed in coplanar mode on a tapered Ti/Au waveguide (CPW 2). Note that the values of delay only depended on the software calibration of the delay stage. d) takes the amplitude of the peaks in c), from 0 to 50 V, and plots them as a function of DC bias. This was done with different powers of the pump beam.

the substrate was not influencing carrier lifetime, the amplitude of the peak at different DC bias should be plotted for different optical powers of the pump beam. The trend for each optical power should be linear, with eventual decreasing gradient owing to saturation effects.[267]

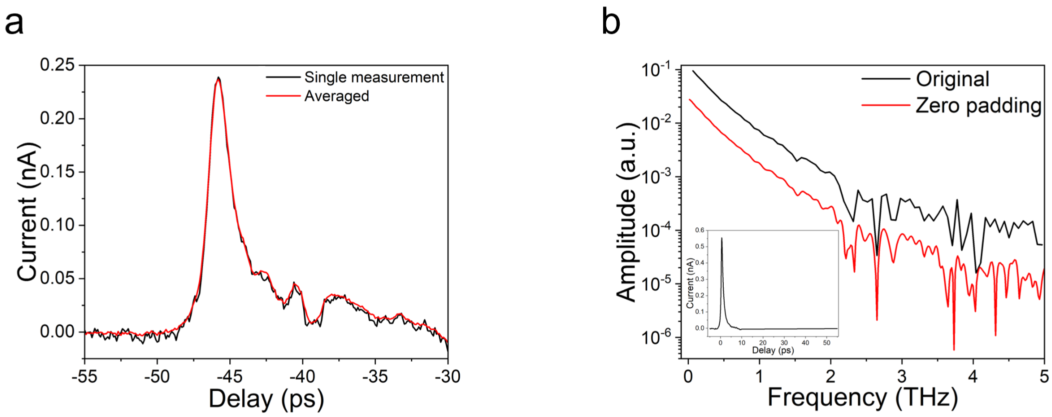

Figure 8.3: a) shows a single THz-TDS measurement in coplanar mode compared to 10 measurements which were averaged, performed on CPW 2 at 50 V DC bias. b) shows in the inset, the pulse from Figure 8.2a with zero-padding. This pulse, fast Fourier transformed, is shown both with and without zero-padding.

When analysing the signal, certain protocols were used in order to enhance the results. One of these, was to perform multiple sweeps of the delay stage, then, take an average of the signals. This leaves a smoother signal, as is shown in Figure 8.3a, and was particularly important for more noisy data, such as at lower DC bias values (10 V) or to distinguish reflections. Another method used was zero-padding; a technique to increase the detail of the FFT. Figure 8.3b shows the difference between the Fourier transform of the pulse without zero-padding (original), and the Fourier transform with zero-padding to 100 ps with 755 data points (as shown in the inset). Zero-padding is a technique in which zeros are added to the end of the measured signal, allowing the total number of data points to be increased. Therefore, after performing an FFT, the information in the signal does not change and therefore bandwidth remains the same, however, the signal is interpolated so it can appear smoother and allow features to become more clear. It should be noted that artifacts can sometimes arise, thus the data should be carefully compared to similar data obtained without zero-padding.

8.3 Reflection Analysis

To understand the origin of reflections, the entire geometry of the coplanar waveguide should be considered, as shown in Figure 4.18h. Distinguishing the origin of reflections allowed them to be separated from the main THz pulse and therefore improve the frequency resolution of the measurement. The possible sites for reflections were the contacts at either side of the central line, the LT-GaAs squares, and the Hall bar in the centre. To assign points of reflection, it was necessary to calculate the velocity of the THz pulse.

Figure 8.4 shows a schematic of the waveguide. Transmission measurements were taken where the switch at the top of the left-hand LT-GaAs was used as the THz generator, and the switch at the top of the right-hand LT-GaAs square was used as the detector (scan 1), or vice versa (scan 2) - for detail of the switches refer to Figure 4.15. During this measurement the THz wave travelled on average 1200 μm down the waveguide. This is based on the assumption that the THz wave was generated at the centre of the 100 μm^2 LT-GaAs squares, however, in reality this distance may have varied by ±100 μm if, for example, the THz wave was generated or detected at the far left or far right of the squares. This was taken into account in the uncertainty in the distance.

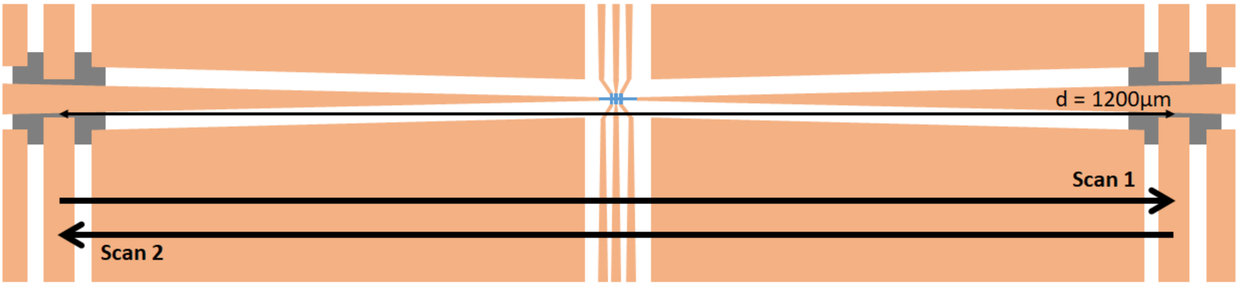

Figure 8.4: A schematic is shown of the central line of the fabricated CPW. The central line can be seen tapering down from the LT-GaAs squares to the Hall bar in the centre. The average distance, d, the THz wave travelled after it was injected to being detected. It also shows how a scan can be made with the THz generator at the left LT-GaAs square and the detector as the right LT-GaAs square (scan 1), and vice versa (scan 2). In both scans, the pump beam is on the left LT-GaAs square and the probe beam is on right LT-GaAs square.

To calculate the velocity of the pulse, measurements were required with the configuration of scan 1 and scan 2. In these scans, the pump beam (direct laser path) was placed on the left LT-GaAs square and the probe beam (time delayed laser path) was on right LT-GaAs square. For scan 1, the THz generator, i.e. the DC bias was placed on the left LT-GaAs square and the right LT-GaAs square was connected to the lock-in amplifier, acting as the detector. For scan 2, the THz generator is placed on the right LT-GaAs square and the detector on the left LT-GaAs square. This yielded a pulse in the same time domain, but in the opposite direction - as shown in Figure 8.5. The time difference between the main pulses (usually the first peak with the largest amplitude) in both of these scans corresponded to twice the time it took for the THz pulse to travel from the generator to the detector (Δt). This is because scan 1 shows the position of the transmitted pulse in the time domain as its position with respect to the position of an input pulse. Scan 2 has an input pulse in the same position as scan 1, however, the transmitted pulse travels in the opposite direction. This meant the time difference between the two transmitted pulses is two lengths of the propagation, Δt. Using this propagation time, and the distance between the generator and the detector (d), the velocity of the pulse was calculated, $v = 2d/\Delta t$. In this case, Δt = (6.8±0.2) ps and d = (1200±100) μm, which gave a pulse velocity of $(1.8\pm0.2)\times10^8$ ms^{-1}; this was similar for all measured waveguides in this thesis.

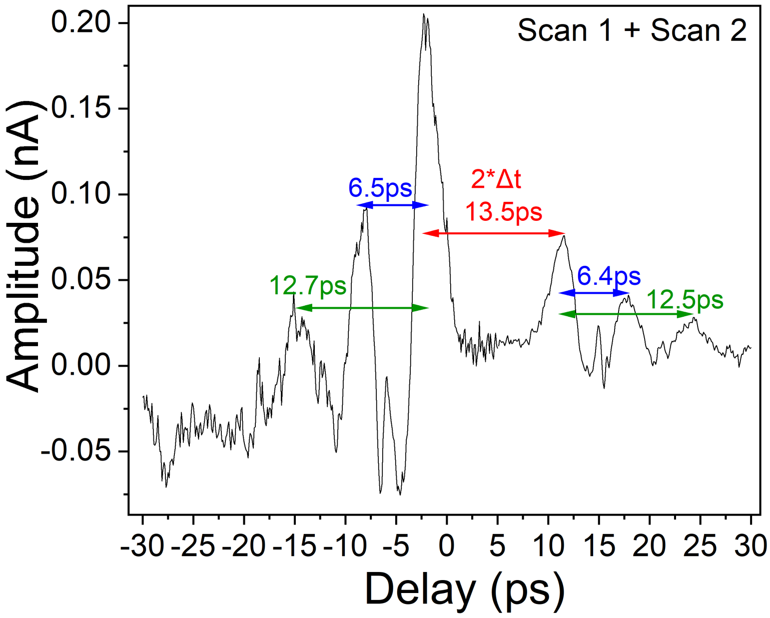

Figure 8.5: The graph shows scan 1 and scan 2 combined, using slotline mode of CPW 4, with a translation in the y-axis to align them, but not in the x-axis. The time difference between the main peaks of scan 1 and scan 2 was 13.5 ps - which is twice the time it takes for the wave to travel down the waveguide. 6.5 ps and 6.4 ps are the times from the main peaks to the second peaks of each scan, and 12.7 ps and 12.5 ps are the times from the main peaks to the third peaks of each scan.

Following this, estimations were made using the pulse velocity to determine where a reflection may be expected in the time domain due to various features of the CPW. For a reflection from the end of one of the contacts on the central line, the extra distance travelled would be approximately 5400 μm, which should correspond to a reflection at approximately 30 ps. This was not observed in Figure 8.5 as the measurement did not cover a large enough time range. For reflections from the Hall bar, there were two things to consider; firstly, there could be primary reflections, but also secondary reflections, as detailed in Figure 8.6c and d. Secondly, the reflections could occur over a range of distances due to the various components of the Hall bar (the bars, the step between contacts and Hall bar and the gaps in the grounding planes) as shown in Figure 8.6b; this range was taken into consideration with the uncertainty in the distance.

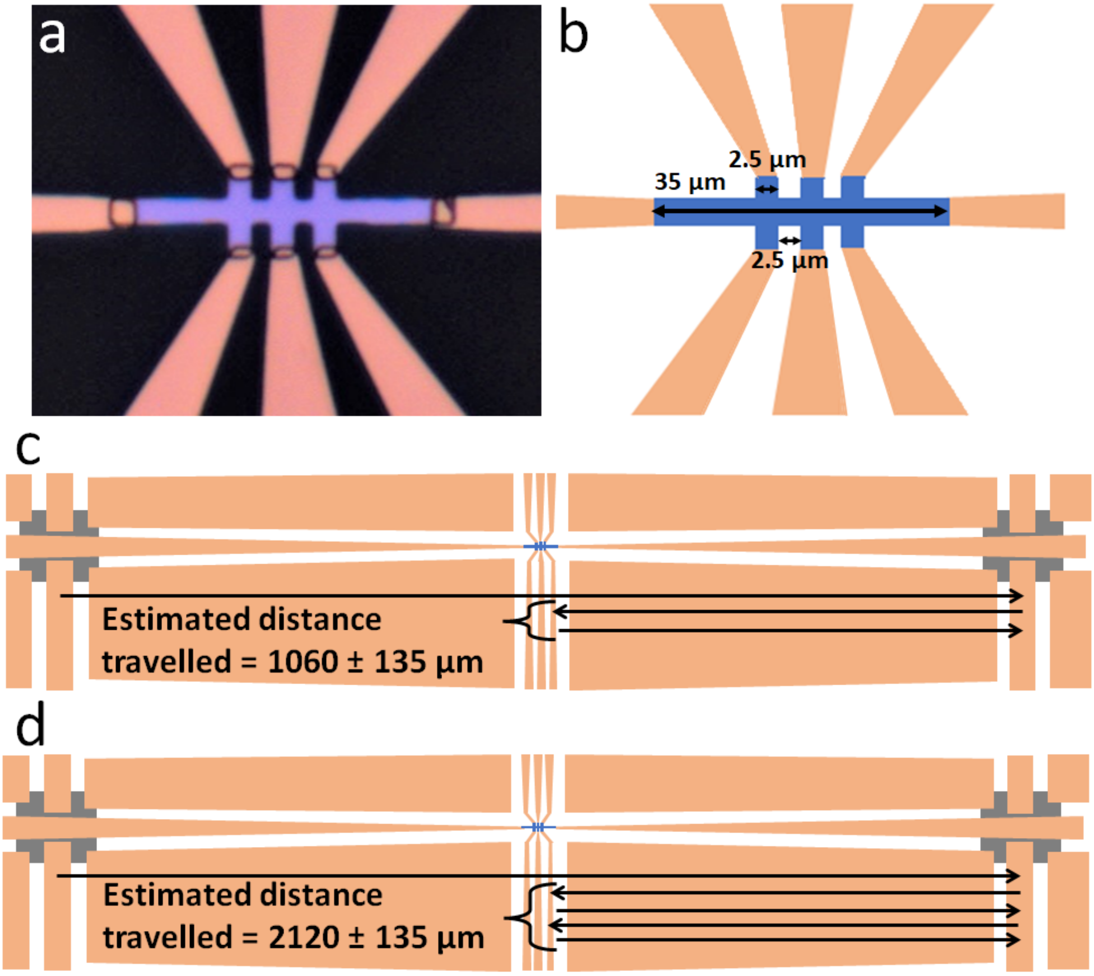

Figure 8.6: a) is the fabricated Hall bar in the centre of the CPW, with the electrical contacts attached to it. b) is a schematic of this showing the lengths of the Hall bar features. c) shows the schematic of the central line of the CPW showing a primary reflection from the Hall bar: the THz pulse reaches the detector, then is reflected to the Hall bar, then back to the detector. d) shows the schematic of the central line of the CPW showing a secondary reflection from the Hall bar: again, the THz pulse reaches the detector, then is reflected to the Hall bar, then back to the detector, however this occurs twice.

For a primary reflection from the Hall bar region, the extra distance travelled would have been approximately (1200±135) μm, which should correspond to a reflection approximately (7±1) ps after the original pulse; this was consistent with the second peaks shown in Figure 8.5, where a peak occurred at (6.4±0.2) ps and (6.5±0.2) ps after the initial peak for scan 1 and scan 2 respectively. It was therefore likely that this peak was a reflection due to the Hall bar, as illustrated in Figure 8.6. Another option for the same distance would be for the pulse to travel to the Hall bar, back to the generator, then to the detector. For a secondary reflection from the Hall bar region, as illustrated in Figure 8.6, the extra distance travelled would have been approximately (2400±270) μm, which should correspond to a reflection approximately (13±2) ps after the original pulse; this was in agreement with the third peaks shown in Figure 8.5, where a peak occurred at (12.5±0.2) ps and (12.7±0.2) ps after the initial peak for scan 1 and scan 2 respectively. Again, it is therefore likely that this peak was a secondary reflection due to the Hall bar. Another option for the same distance would be for the pulse to travel to the Hall bar and back to the generator twice, then to the detector, or simply back and forth from the generator to the detector twice.

Following the reflection calculations, it was reasonable to assume that the second and third large peaks after the initial peak were caused by reflections from the Hall bar, and were therefore excluded (by truncating the signal) during the Fourier transform analysis of the data. The smaller peak that followed the main peak was not accounted for by any reflections and was therefore included in the Fourier transform of the data. This truncation was used in all the analysis for this thesis.

8.4 Analysis of a Multilayer Waveguide

8.4.1 Comparison: Different Magnetic Multilayer vs. TiAu Waveguide

First, a comparison was made between a Ti/Au waveguide without tapering (CPW 1), a Ti/Au waveguide with tapering (CPW 2), and a tapered magnetic multilayer waveguide (CPW 7). As can be seen from Figure 8.7, there were differences in the reflections for the three types of waveguide. Figure 8.7, shows the signals measured in coplanar mode, at multiple DC biases. Without the tapering and Hall bar (a), no reflections were observed. With the tapered central line and the Hall bar made from thinner material, many more reflections were visible (b and c).

Transport measurements were performed on the Hall bar of CPW 7, via the Au contacts attached to it. The transverse and longitudinal measurement signals (the experimental details were described in Chapter 4) were measured to get the transverse (R_{xy}) and longitudinal (R_{xx}) resistance, as an OP field was swept. This proved the SAF material on the waveguide as three separate switches were observed, as expected in the R_{xy} signal, which reflects the hysteresis of the sample. The longitudinal signal showed two levels of resistance, a lower resistance when the waveguide was in a saturated state with each of the three magnetic layers having the same spin orientation. There was

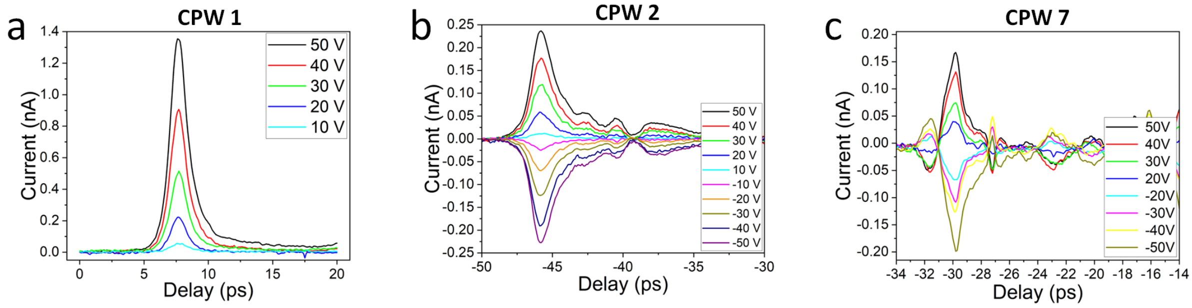

Figure 8.7: This shows the coplanar mode THz signal in the time domain at multiple DC biases, for CPW 1 (a), CPW 2 (b) and CPW 7 (c).

a higher resistance state in between the two outer switches as in this period, there was AFM-IEC between each layer (both ↓↑↓ and ↑↓↑).

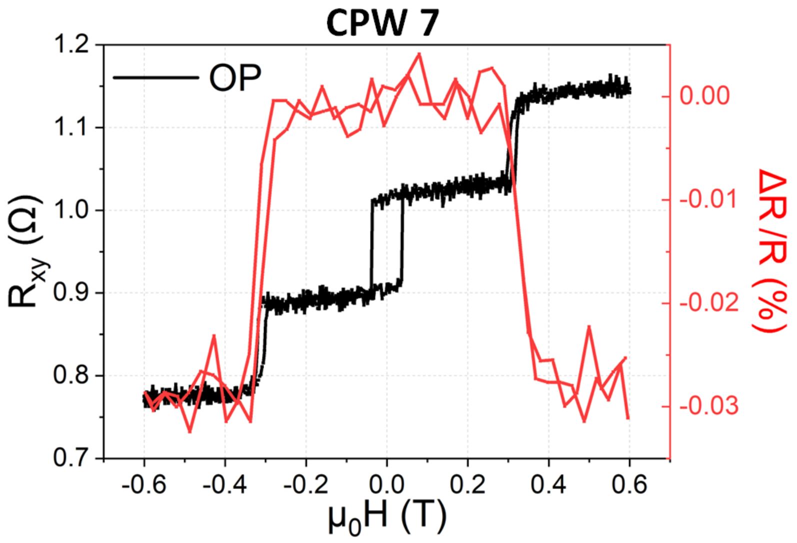

Figure 8.8: This shows the transverse (R_{xy}) and longitudinal (magnetoresistance) resistance measurements of CPW 7, as an OP field was swept. This was measured via the contacts on the Hall bar and the central line.

These coplanar measurements on the three waveguides were compared both against each other, and against their input and slotline mode measurements. Figure 8.9 presents a comparison between the input and coplanar THz-TDS measurements in the time and frequency domain for CPW 1, and input, coplanar and slotline measurements for CPW 2 and 7. The pulses were normalised to compare their shapes. CPW 1 shows an input pulse which was less symmetrical to the pulse from the coplanar measurement, though neither of them had reflections. The bandwidth of the input measurement was up to 2 THz, whereas the coplanar bandwidth was around 1 THz. For CPW 2, the input and coplanar pulses had a similar shape, though in slotline mode, the main peak signal dropped more abruptly. The slotline and coplanar signals had similarly placed reflections after the main peak (being more pronounced in slotline mode), whereas the input pulse showed only one reflection after around 7 ps. The bandwidth for the coplanar and slotline modes was just over 0.5 THz, however, for the input mode it was not clear. Finally, for CPW 7, we saw a similar pulse shape for the input and coplanar modes, however, the slotline mode differed, this time the pulse had a larger width. As with the other tapered waveguide, we saw aligned reflections in the coplanar and slotline modes, and only one reflection of the opposite inflection to CPW 2, at around 7 ps after the pulse. The bandwidth for CPW 7 measured in input mode was around 1 THz, for the coplanar mode, it was around 0.8 THz, however, it was under 0.5 THz for the pulse measured in slotline mode.

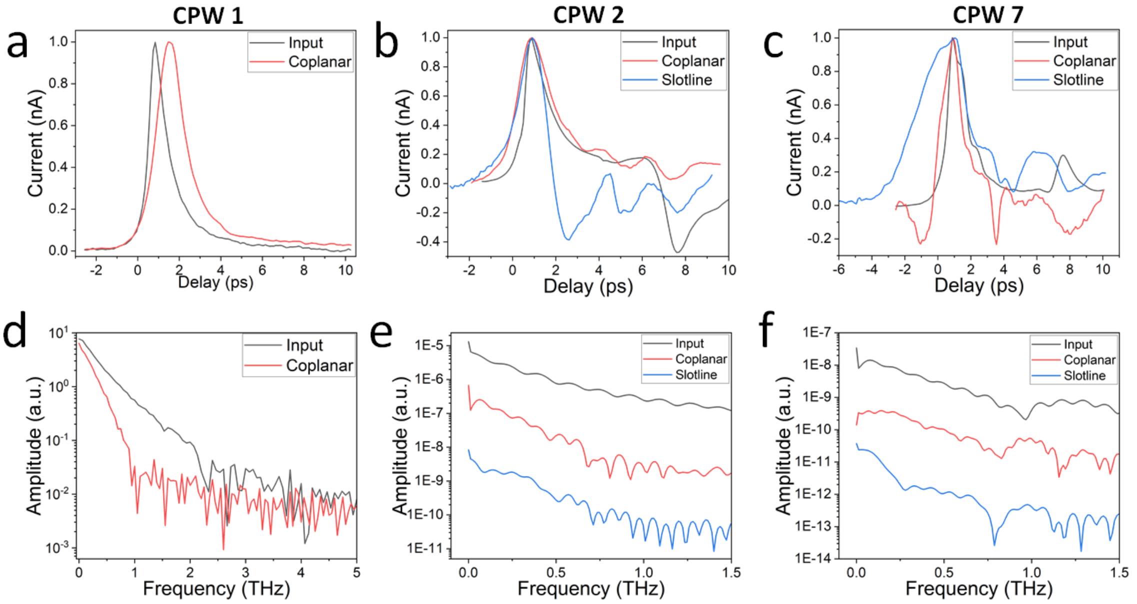

Figure 8.9: a) to c) show the pulses in the time domain for input, coplanar and slotline THz-TDS measurements, they are normalised and offset in the x-axis to overlay them. d) to f) shows the Fourier transform of these signals, these were offset in the y-axis to allow them to be viewed easily. All measurements were performed with 50 V DC bias. a) and d) show CPW 1, b) and e) show CPW 2 and c) and f) show CPW 7.

Figure 8.10 displays trends between these three waveguides, in terms of the pulse width and bandwidth. Figure 8.10a and d show the coplanar pulse width as a function of DC bias for different optical powers for CPW 2 and 7, respectively. There appeared to be little difference in the pulse width as a function of DC bias for CPW 2, except for 45 mW, where there was a slight increase with DC bias above 20 V. The values were however, within the range of the other values. At 10 V DC bias, there was much larger width, which was due to the signal being much weaker with the low DC bias. Overall, the values measured with 56 mW optical power, were larger than for 45 mW, which were larger on average than for 30 mW. CPW 7, showed similar trends in Figure 8.10d, however, the pulse widths from measurements taken with a 30 mW optical power were much higher. This was due to the deteriorating signal from a lower optical power. A comparison of the pulse widths with 56 mW optical power and 50 V DC bias in coplanar mode is shown in Figure 8.10b. CPW 2 had the largest average pulse width, followed by CPW 1 and CPW 7 had the smallest average pulse width.

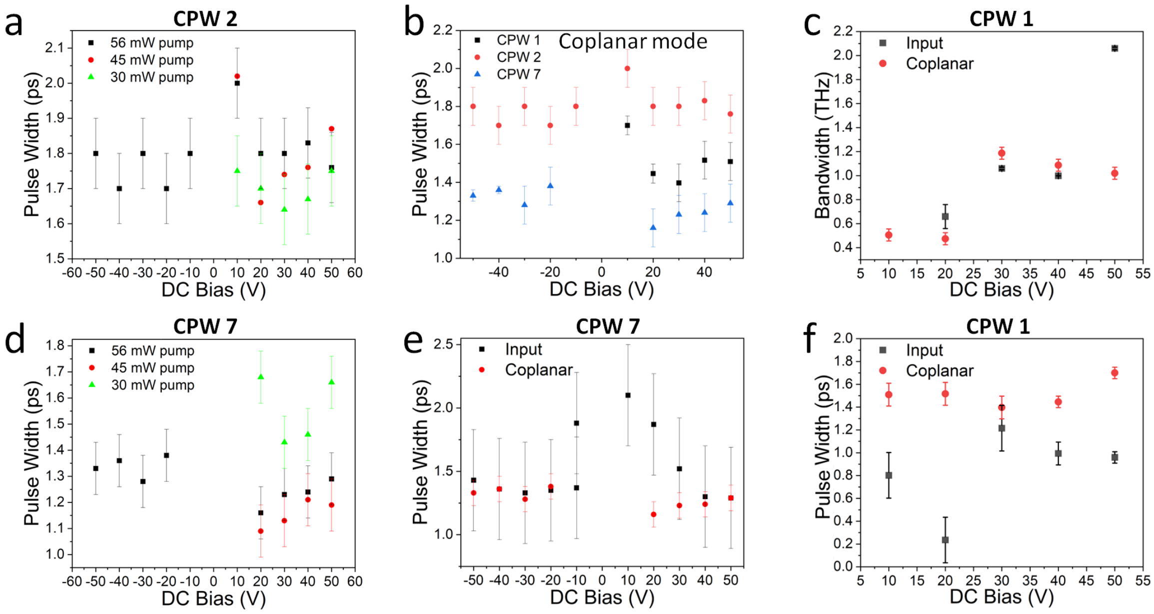

Figure 8.10: a) shows the pulse width of coplanar measurements of CPW 2 at different DC biases for different pump beam optical powers. b) shows the pulse width of coplanar measurements for CPW 1, 2 and 7 at different DC biases. c) shows the different bandwidths of CPW 1 in input and coplanar mode at different DC biases. d) shows the pulse width of coplanar measurements of CPW 7 at different DC biases for different optical powers. e) shows the different pulse widths of CPW 7 in input and coplanar mode at different DC biases. f) shows the different pulse widths of CPW 1 in input and coplanar mode at different DC biases.

Figure 8.10c shows how the bandwidth changed with DC bias for CPW 1 in both input and coplanar mode. There appeared to be an increase in bandwidth above 20 V DC bias, suggesting reliability in using 30 V DC bias or more. Above which, the coplanar mode showed a relatively constant bandwidth, similar to the input bandwidth, except for at 50 V DC bias where the input measurement showed a particularly high bandwidth of over 2 THz. The Figure 8.10e shows similar pulse widths for the input and coplanar measurements of CPW 7 as a function of DC bias. Again, the low DC bias measurements showed an increased pulse width. Figure 8.10f, shows the same for

CPW 1, however, it showed the coplanar measurements with a slightly larger width, as expected, as the pulse travels a further distance along the waveguide.

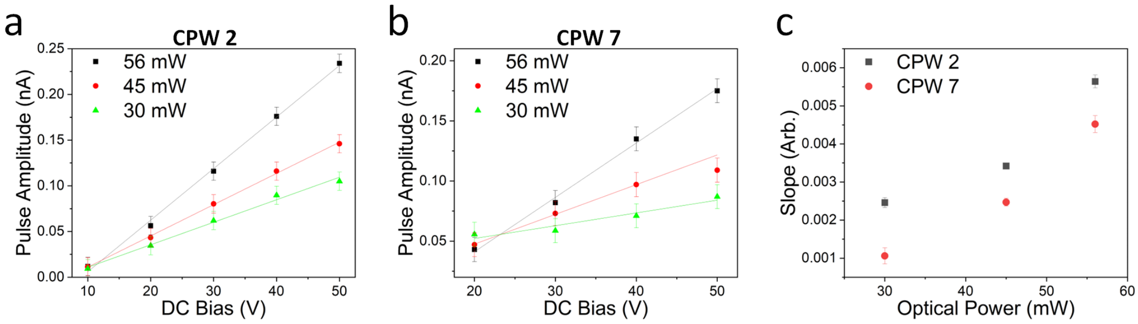

Figure 8.11: a) shows the amplitude of the pulses measured in coplanar mode of CPW 2 as a function of DC bias, with the pump beam set to different optical powers. b) shows the amplitude of the pulses measured in coplanar mode of CPW 7 as a function of DC bias, with the pump beam set to different optical powers. A linear fit is shown for each optical power. c) shows the gradient of the linear fits for each optical power for CPW 2 and 7.

The other parameter compared was the pulse amplitude. As shown in Figure 8.11a and b, the amplitude increased as a function of DC bias in CPW 2 and 7 using coplanar mode, confirming ohmic behaviour. The rate at which it increased was dependent on the optical power, as shown in Figure 8.11c, and was similar for both waveguides.

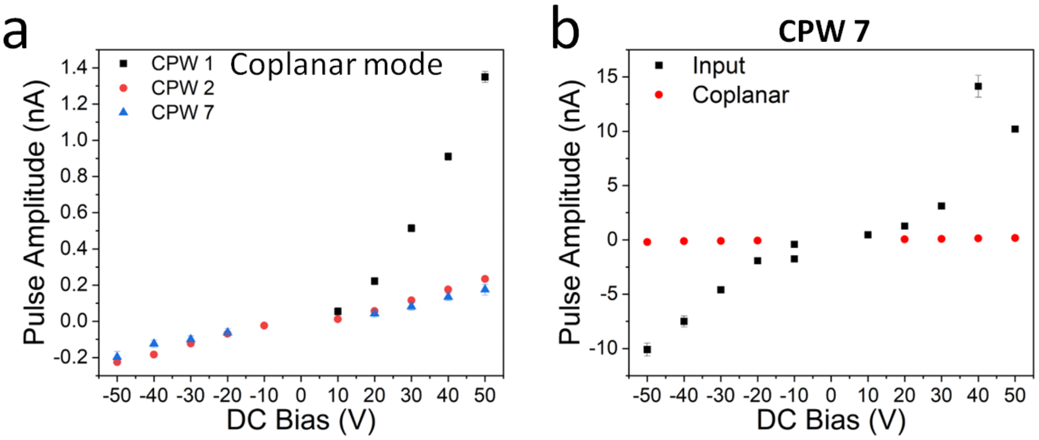

Figure 8.12: a) shows the coplanar measurement pulse amplitude for CPW 1, 2 and 7, as a function of DC bias. b) shows the pulse amplitude of input and coplanar mode measurements at different DC biases.

Finally, the pulse amplitudes for the three waveguides (CPW 1, 2 and 7) were compared at different DC bias in coplanar mode. All waveguides exhibited, Figure 8.12a the trend of increasing amplitude magnitude with increasing DC bias, including for negative bias. CPW 1 showed the largest pulse amplitudes, which were considerably higher than for the other two tapered waveguides. At generally much lower amplitudes, CPW 2 showed amplitudes slightly higher than CPW 7, with the thinner Hall bar magnetic material. Figure 8.12b, shows the difference between the pulse amplitude when performing a measurement in input and coplanar mode on CPW 7. The input amplitudes were much larger than any coplanar measurements due to the short path of the THz wave.

To summarise, tapering a multilayer CPW and including a magnetic material in the central line added more reflections to the pulse signal and reduced the output current amplitude. The reflections can however, be analysed and removed and the signal, when using 50 V DC bias, was substantial enough to perform analysis and a Fourier transform of the signal. This means successful measurements can be made using this device design.

8.4.2 Comparison: Different Magnetic Multilayer Waveguides

The second comparison we consider is between CPW 3, 4, 5 and 7, waveguides with different magnetic multilayers in the centre in a Hall bar configuration. Figure 8.13 shows the hysteresis loops for the different multilayers. CPW 3, 4 and 5, show ferromagnetic material with wasp-like hysteresis loops, indicating maze-like domains within the Hall bar material. CPW 7 shows three separate switches, representing a SAF of three magnetic layers, all coupled together antiferromagnetically. These hysteresis loops were measured by MOKE or SQUID magnetometry on samples grown on a silicon oxide substrate with the same recipe as that deposited on the Hall bar of the corresponding CPW. The waveguides themselves were not able to be measured using these techniques due to the small dimensions of the Hall bar.

Some of the Hall bars were, however, observed via Kerr microscopy. Figure 8.14 shows Kerr microscopy images of the Hall bar at the centre of the waveguides for CPW 4 (a) and CPW 5 (b), at different OP magnetic fields. The dark and lighter domains represent domains with opposite spin orientations. CPW 4, Figure 8.14a, showed two different magnetic textures within the Hall bar material at different applied fields. At around 0 mT, after increasing from a large negative applied field, some small, maze-like domains of a lighter colour were seen starting to develop, and at 4 mT, these domains dominated the darker domains. The sample saturated and the dark domains completely disappeared at around 15 mT. Figure 8.14b shows the Hall bar of CPW 5 in a saturated state at an OP applied magnetic field of -200 mT. Then, when the field was increased to 1 mT, dark, maze-like domains began to appear. These grew as the field was increased to 15 mT, reducing the lighter domains, until the material was fully saturated at around 50 mT. A similar process was observed in the reverse, after the Hall bar was saturated in a large positive field, small circular domains began to appear at around 1 mT, which grew into maze-like domains as the field was decreased further to -6 mT. These images proved that the material on these waveguides showed skyrmion hosting abilities, similar to that of the FM samples shown in Chapter 7.

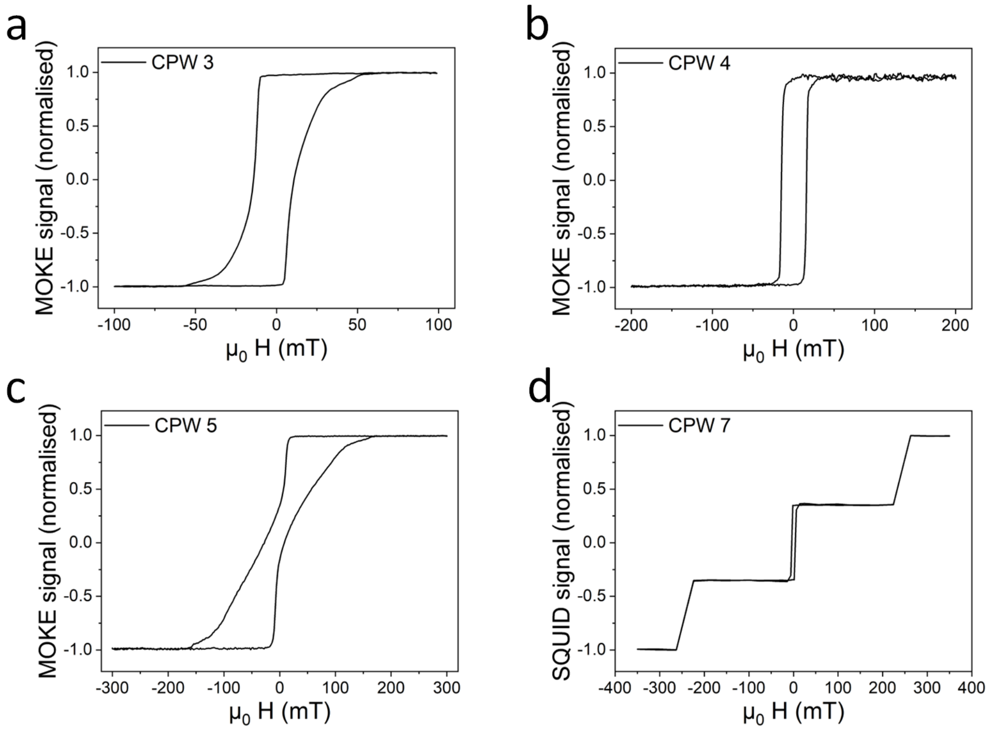

Figure 8.13: The graphs show the hysteresis loops, measured by SQUID or MOKE, on samples grown using the same recipe of the material on the Hall bar of the corresponding CPW, but grown on SiO substrates. The hysteresis loops for the Hall bar material of CPW 3, 4, 5 and 7, respectively, are shown. The signals have been normalised.

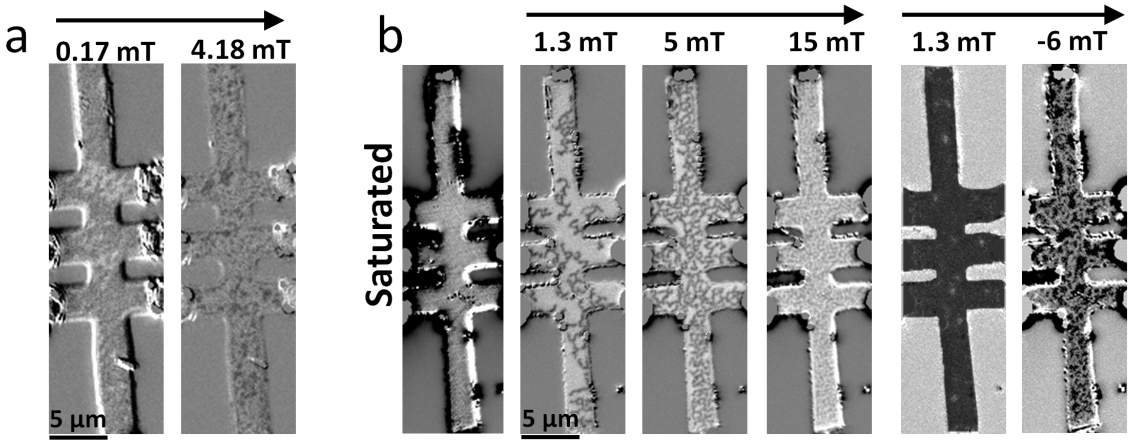

Figure 8.14: Shown are the Hall bars of CPW 4 (a) and CPW 5 (b), which show dark and light textures, representing the up and down spin magnetic domains. A scale bar of 5 μm is shown at the bottom of both figures and the applied fields are shown above the figure, with the arrow representing the direction of the field increase/decrease. The initial image in b) shows the Hall bar in a saturated state.

Displayed in Figure 8.15 is a comparison of the parameters taken from measurements on these four waveguide. Measurements of CPW 4, 5, and 7 were taken in coplanar mode, however, CPW 3 measurements had to be taken in slotline mode due to defects in the waveguide contacts. Figure 8.15a, compares the THz pulses in the time domain, the signals were normalised and translated in the x-axis to allow for the comparison. CPW 3, 4 and 5 all showed a similar width peak, CPW 4 being slightly thinner which was likely a result of the entire central line being made from the thinner multilayer material. CPW 7, however, showed a much thinner peak width, it is the waveguide with the SAF Hall bar with only 3 repetitions, making it much thinner material than other samples. Alternatively, the cause of the difference could lie with the quality of the LT-GaAs squares producing the THz pulse.

The second observation was that all samples appeared to have a peak around 3 ps after the main peak, which was not accounted for by any reflections, however, it is likely a feature of the tapered waveguide as it is observed for all samples. Following this, there was a second peak observed around 6 ps. CPW 3 had larger peaks and dips, most likely due to the measurements being made in slotline mode as opposed to coplanar. CPW 7, also showed a small bump in the downside of the peak.

Figure 8.15b shows the FFT results from the THz-TDS measurements in Figure 8.15a. All waveguides showed a bandwidth of around 0.5 THz, with no particular features present. Figure 8.15c, gives the amplitudes of the peaks when measured using different DC bias, which increased as the bias increased, both at positive and negative voltages. All samples showed a similar trend, with the largest amplitudes seen for CPW 7 and the lowest for CPW 3. Again, this was likely a feature of the quality of the LT-GaAs or waveguide contacts. Figure 8.15d, shows the peak width as a function of DC bias, which remained more constant across different DC biases. CPW 7 showed the smallest width, as noted in 8.15a, followed by CPW 4. CPW 3 and CPW 5 show a similarly large width, and also similarly scattered.

8.5 Synthetic Antiferromagnetic Waveguide

Another type of synthetic antiferromagnetic material with two ferromagnetic multilayers coupled together antiferromagnetically, stack 2 in Chapter 7, was deposited on the Hall bar in CPW 6 and measured. Figure 8.16a shows the hysteresis loop of the sister samples, grown at the same time as the material was grown on the waveguide, however, on a silicon substrate. It showed two separate switches of the two FM multilayers. 8.16b shows Kerr microscopy images of a sister waveguide, also grown at the same time as CPW 6. It depicts the Hall bar in a saturated state, with an applied field of 200 mT, the applied field was then taken to 10 mT and decreased gradually. At 7 mT, domains were visible within the Hall bar, which shrank as the field was decreased to 2 mT and it saturated fully below 2 mT. A similar process was observed as the field was decreased further to negative fields, and also in the reverse of the loop. In Figure 8.16c, the THz-TDS signal for this

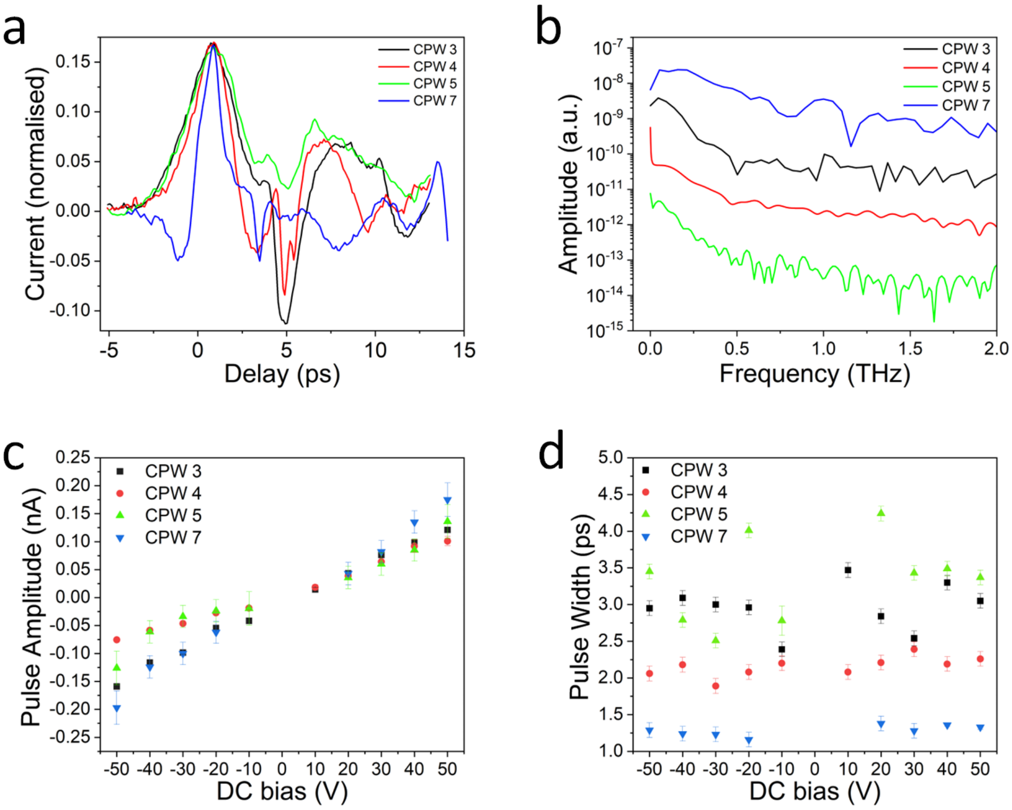

Figure 8.15: a) shows normalised peaks from THz-TDS measurements in coplanar mode (or slotline for CPW 3), at 50 V DC bias for CPW 3, 4, 5, and 7. b) shows the Fourier transform of these measurements. c) shows the peak amplitudes as a function of DC bias and d) shows the peak widths (FWHM) as a function of DC bias. All measurements were performed at zero field.

sample is shown. It was measured in coplanar mode with 50 V DC bias, and as with the other waveguides, a bump is observed 3 ps after the main peak, and again at 6 ps. These bumps were less pronounced than in the other waveguides and the peak amplitude was larger, suggesting a better quality waveguide. The pulse width was around 2.59 ps, similar to that of CPW 4 and 5, however, it exhibited a bump in the downside of the main peak, as did the other SAF sample, CPW 7. The Fourier transform of this peak is shown in Figure 8.16d, which had a bandwidth of just under 0.5 THz, however, no features were observed within the bandwidth. This measurement was also performed for different applied magnetic fields, and no differences were observed in the signals.

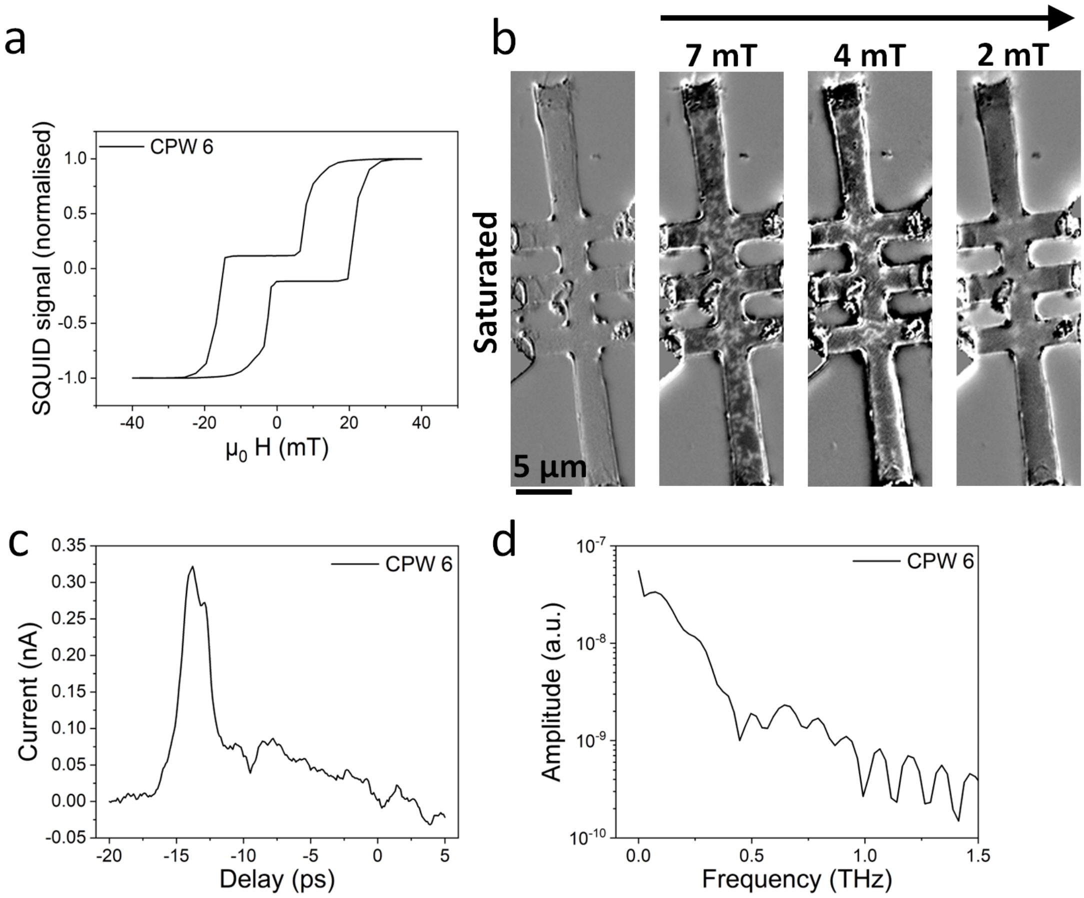

Figure 8.16: a) shows the hysteresis loop of a sister samples to CPW 6, deposited at the same time on SiO, measured by SQUID magnetometry. b) shows Kerr microscopy images of a sister Hall bar grown at the same time as CPW 6, it is shown in a saturated state, then at three different applied fields. The arrow represents the direction of the field decrease and there is a 5 μm scale bar. c) shows the pulse in the time domain of CPW 6, measured with 50 V DC bias in coplanar mode. d) shows the Fourier transform of the pulse in c).

8.6 Field Dependent Measurements

Field dependent measurements were performed on CPW 7. This included both measuring the THz pulse in the time domain and performing the Fourier transform at different OP fields, and measuring the current as the applied field was swept. Figure 8.17a shows the THz pulse measured in slotline mode (due to difficulty stabilising the photocurrent with the field in coplanar mode) on CPW 7, in various OP magnetic fields between -187 mT and 184 mT; all measurements were performed with 50 V DC bias. Each measurement was then Fourier transformed, as shown in Figure 8.17b. There were negligible differences between the signal at different fields and no particular features observed within the 0.25 THz bandwidth. This is reflected in Figures 8.17c and d, which show the pulse amplitude and width as a function of field, respectively, compared with in input, slotline mode, and with the tapered Ti/Au waveguide (CPW 2). The results showed that CPW 7 in coplanar mode had the lowest pulse amplitude, and the slotline mode had the largest amplitude, larger than the Ti/Au waveguide (CPW 2) in coplanar mode (though it did not exceed the amplitude of the coplanar measurements of CPW 1). As for the pulse width, the largest width was also found for the slotline mode of CPW 7. The input mode had thinner pulses, comparable to the coplanar mode widths and those from CPW 2 in coplanar mode. The smallest width was observed in the input measurements of CPW 2. No significant trend with field was observed in the waveguide with the magnetic material (CPW 7) compared to the Ti/Au Hall bar (CPW 2), in the pulse amplitude, nor the pulse width.

To perform field sweeps whilst measuring the current, the following protocol was used: a normal THz-TDS measurement, with the laser beams aligned at zero field, was performed to find the position of the pulse, see Figure 8.18a, in this case the peak was at -45.8 ps of the delay stage values. The delay stage was then set to this value, the rest of the configuration remained the same, and the magnetic field was swept from positive to negative, or negative to positive whilst measuring the current at the detecting LT-GaAs square. The result of this is shown in Figure 8.18d, where the two field sweeps are plotted on the left axis, it was clarified that the position of the delay stage is on the peak, as the initial current value was close to that of the corresponding pulse amplitude. This measurement was repeated 100 times and an was average taken (see Figure 8.19). On the right y-axis of Figure 8.18d, is the hysteresis loop from the transport measurement in Figure 8.8a for comparison. The changes in current do correspond to similar fields to the changes in resistance in the transport measurements and therefore changes in the magnetic behaviour within the sample, considering there may be some systematic error in the magnetic field calibration for the field sweep measurements.

A single field sweep was noisy and unclear, as can be seen from Figure 8.19a which shows 30 single field sweeps, however, when the sweeps were averaged the trend became more obvious. This meant that there were large errors in the averaged current plot (Figure 8.19b) which were not

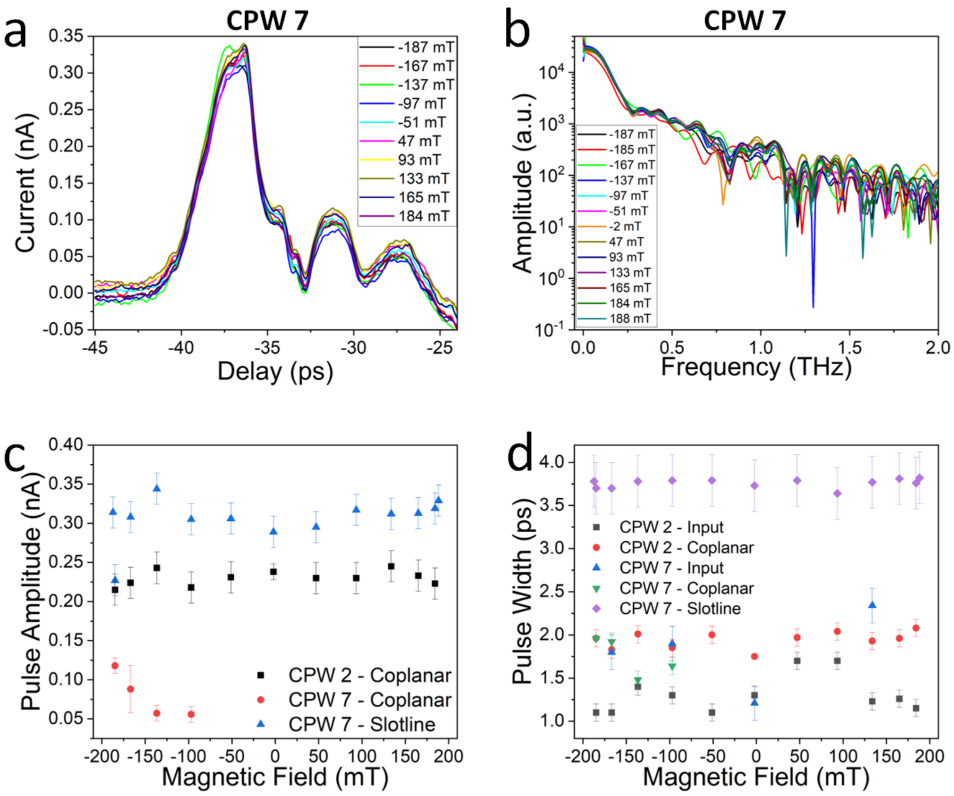

Figure 8.17: a) shows the THz-TDS signal for CPW 7 in slotline mode at different OP field values - 50 V DC bias. b) shows the Fourier transform results of a). c) shows the pulse amplitude as a function of field of CPW 7 in slotline and coplanar mode, compared with CPW 2 in coplanar mode. d) shows the pulse width as a function of field of CPW 7 in input, slotline and coplanar mode, compared with CPW 2 in input and coplanar mode. All measurements used a DC bias of 50 V.

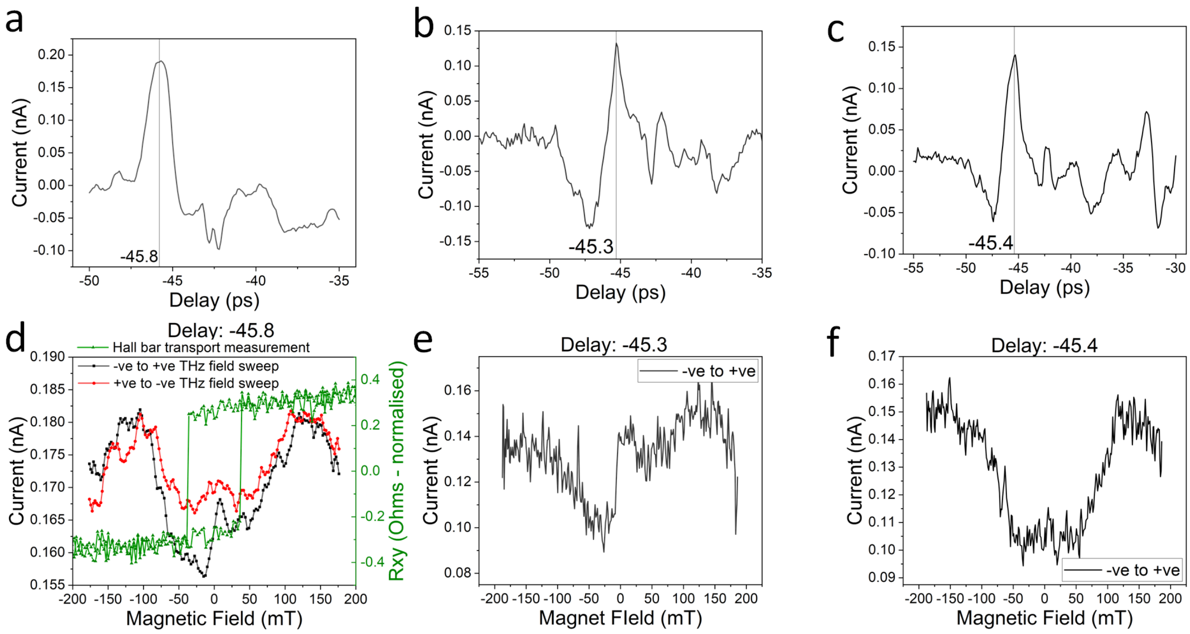

Figure 8.18: a) to c) show THz-TDS measurements performed in coplanar mode, set up in zero field for CPW 7. All measurements were taken with DC bias of 50 V. d) to f) show field sweeps against the measured current, with the delay stage set to the corresponding pulse peak (a and d, b and e, c and f). d) also shows the transport measurement of CPW 7 from Figure 8.8a.

plotted on all figures to allow the averaged data to remain clear, although, even within the error the trend still existed.

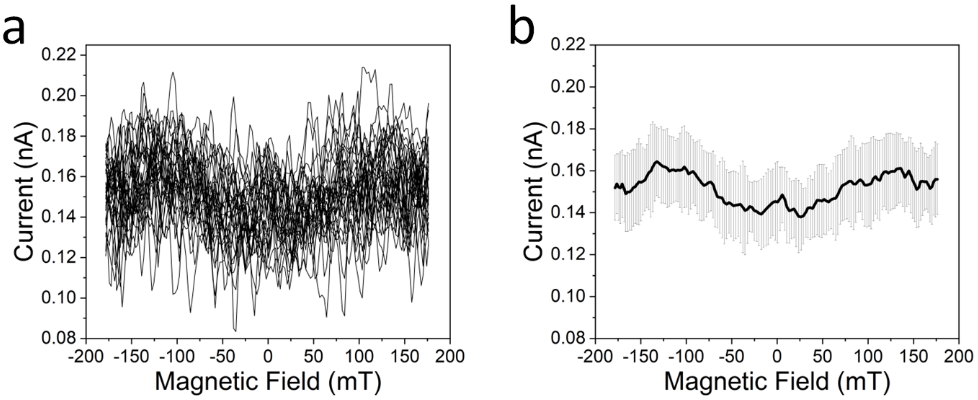

Figure 8.19: a) shows a sample of the field sweeps before they were averaged. b) shows the average of the current values in a) with error bars.

Figures 8.18b and c are repeat measurements of a, with the corresponding field sweeps, averaged over 50 measurements, below (e and f, respectively). It showed that the peak position varied only slightly during the measurements. The sharper look to the peaks of Figure 8.18b and c, was due to only one measurement being taken with no averaging across multiple sweeps, as was done in 8.18a. From Figure 8.18d, we saw that as the field was swept, the current decreased at around -100 mT, then flattened out and began to increase again, at 50 mT until it was around the original values at 100 mT (and vice versa). Figure 8.18e, showed a similar trend, however, with a less defined dip in and a sharp increase in current at 0 mT, this sharp increase was also seen in the negative to positive sweep in Figure 8.18d. Figure 8.18f, again showed a similar trend to d, with a lower current plateau that lined up perfectly with the central switch in the hysteresis loop of the Hall bar material.

It was then investigated whether setting the position of the delay stage to a region of time after the main pulse would have an effect on the current during the magnetic field sweep. Figure 8.20a shows three different delay stage positions corresponding to three different parts of the THz pulse and its reflections: -45.7, -43.7 and -41.7 ps. Based on the 50 repetition average magnetic field sweeps in Figure 8.20b, c and d, no significant difference was observed in the current compared to when the delay stage position was at the peak. The drop in current was observed to begin at -150 mT, instead of 100 mT, and increase until 150 mT, and vice versa.

To confirm the origin of this current trend, measurements were performed with the delay stage set to a region of time before the pulse, to the peak of an input mode measurement pulse, and the peak of a coplanar measurement on a Ti/Au waveguide (CPW 2). Figures 8.21a and d, show

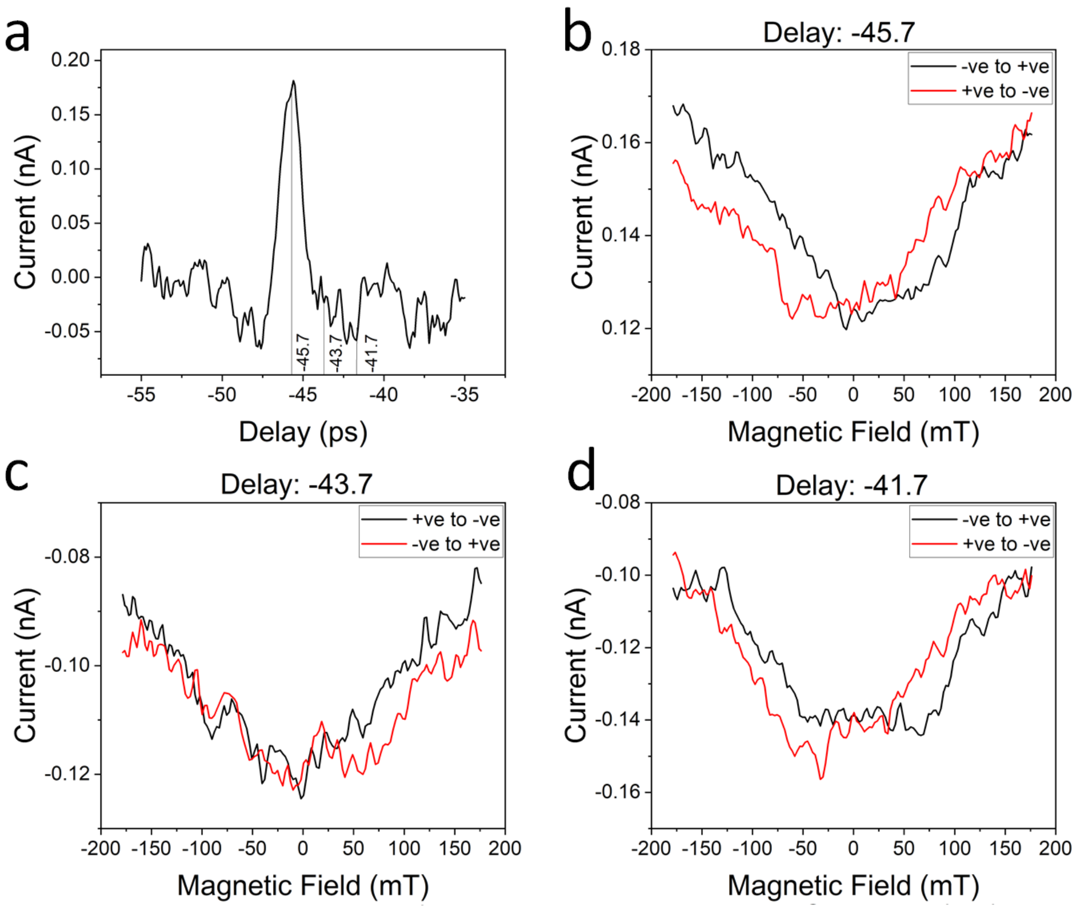

Figure 8.20: a) shows a THz-TDS measurement performed in coplanar mode, set up in zero field for CPW 7 and taken with DC bias of 50 V. b) to d) show field sweeps against the measured current, with the delay stage set to the corresponding delay stage position, as shown in a). They show an average of 50 repetitions.

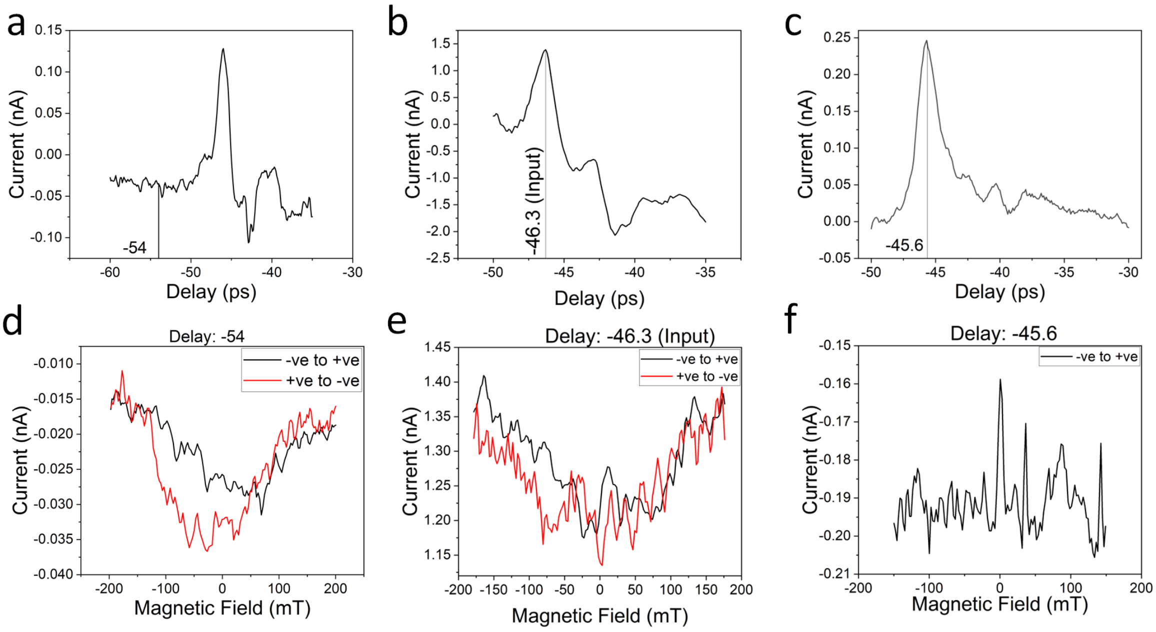

Figure 8.21: a) to c) show THz-TDS measurements performed in coplanar mode (a and c) or input mode (b), set up in zero field for CPW 7 (a and b) and CPW 2 (c). All measurements were taken with a DC bias of 50 V. d) to f) show measured current against field as a 50 repetition average, with the delay stage set to the corresponding delay stage position (a and d, b and e, c and f).

the result for the CPW 7 coplanar measurement when the delay stage was placed at a position before the THz pulse (-54 ps), the same current trend was observed. Figures 8.21b and e show the result for a CPW 7 input measurement, with the delay stage position on the peak of the input pulse. In this case, the field sweep was performed with the setup configured in input mode, and we should therefore not see a response from the magnetic material on the Hall bar, however, we saw a similar trend in current. These results suggested that the change in current was not a feature caused by the SAF material on the Hall bar in the centre of CPW 7. Figure 8.21c and f, show the measurement performed on CPW 2, the Ti/Au tapered waveguide. The THz-TDS pulse was measured with 50 V DC bias and the delay stage was set to the centre of the peak before the field sweep measurement was performed. This measurement did not show any dependence of current on the magnetic field, therefore suggesting that the dip in current observed was specific to CPW 7, in which the only difference to CPW 2 was the Hall bar material. This suggested it could be a feature due to the magnetic material, even though the dip appeared not only at the signal peak. These measurements leave contrasting results.

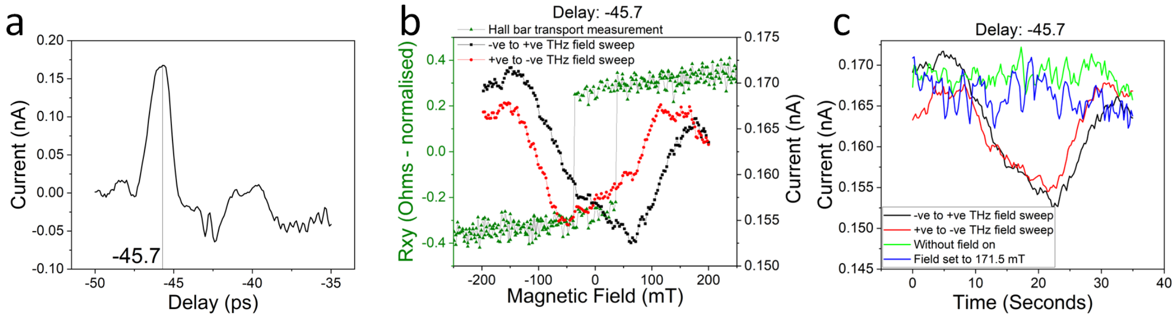

Figure 8.22: a) shows a THz-TDS measurement performed in coplanar mode, set up in zero field for CPW 7, taken with DC bias of 50 V. b) shows the field sweeps averaged over 200 measurements, against the measured current, with the delay stage set to the corresponding pulse peak, plus, the transport measurement of CPW 7 from Figure 8.8a. c) shows the same measurements as a function of time, plus the current readings over the same time period at a set field of 171.5 mT and without a field.

It was consequently investigated whether the change in current with field was a feature of drift or movement caused by the magnetic field, although it was not expected to be due to it not being observed in the CPW 2 field measurements. The original measurement process was repeated, setting the delay stage to the peak position whilst in coplanar mode (Figure 8.22a). The field was swept 200 times from positive to negative and vice versa, and an average taken of each. This is plotted in Figure 8.22b, again, alongside the transport measurement in Figure 8.8a, and the trend in current was very similar to Figure 8.18d. This current measurement was then plotted as a function of time (the time over which the measurements were taken) in 8.22c. As well as the current values measured whilst the field was swept, the current values over the measurement time are shown with a constant field at both 0 mT and 171.5 mT. The trend in current was only present in the measurements performed whilst the field was changing and the current remained almost constant when there was no change in field. This ruled out that the cause of the current dip was due to drift, meaning it was caused by changing the applied magnetic field. If moving magnetic field caused the whole waveguide to move slightly, which would have caused the lasers to move from their optimal positions on the optical switches, it would more likely show a trend in which the current reduces as the field moves away from 0 mT (where the optimal positions were set up) to 200 mT and -200 mT, the inverse trend.

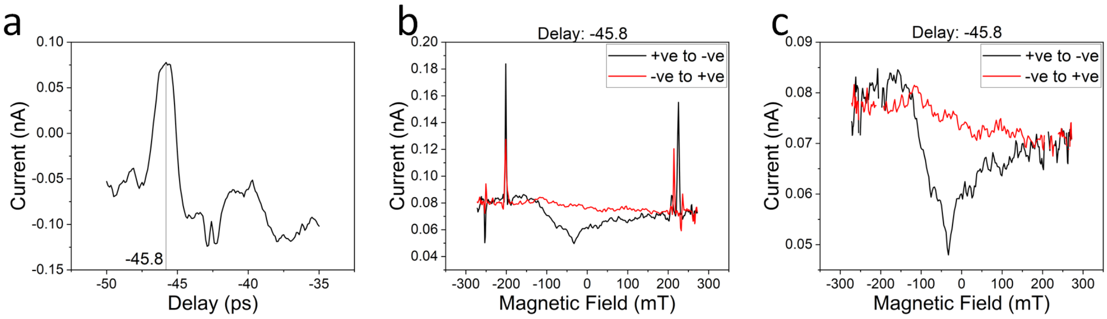

Figure 8.23: a) shows a THz-TDS measurement performed in coplanar mode, set up in zero field for CPW 7, taken with DC bias of 50 V. b) shows the field sweeps averaged over 50 measurements, against the measured current, with the delay stage set to the corresponding pulse peak. c) shows a version of b), without the spike data points.

Finally, the field range in which these measurements were performed was limited by the magnetic field set up used, to ±300 mT, however, above 200 mT sharp spikes in current were detected, the cause of which was unknown and occurred for all measured samples in all measurement modes. This meant that the data above 200 mT was unreliable. An example of these current spikes is shown in Figure 8.23, in which the time domain THz signal is shown in 8.23a, in coplanar mode, and the field sweep to high fields is shown in 8.23b with the spikes at around ±200 mT and above. Figure 8.23c shows a version of 8.23b, with the spike data points removed. Still present, is the decrease in current at around -100 mT, which appears more sharp than in previous measurements. However, interestingly, there is no decrease in current observed in the negative to positive sweep.

8.7 Conclusions

To summarise all the THz-TDS results, it has been proven that it is possible to create a tapered coplanar waveguide with a Hall bar in the centre and successfully measure the THz signal from a transmission measurement in both coplanar and slotline mode. Reflections were observed, however, accounted for. Furthermore, these measurements were also successful in the case that the Hall bar was fabricated from magnetic multilayers with different magnetic properties and thicknesses. Hall measurements and Kerr microscopy images on the same waveguide were also achieved to understand the exact properties of the small magnetic area. A measurement set up was created to allow for the collection of field dependent data. Further measurements must be performed to understand whether the effects measured as a function of field were a feature of the magnetic material. To do this, the magnetic field range must be expanded, or a waveguide fabricated with lower switching fields.

CHAPTER 9

Conclusion

9.1 Conclusions

As the demand for electronics and data storage is ever-growing and not sustainable in the long run, the need for a lower power alternative to current electronics is becoming more urgent. Spintronics is seen as a feasible candidate to help intercept this problem, as research focuses on skyrmions and their applications for data storage. The intention of this thesis was to both establish conformity in the methods used to carry out research into this topic, and to add to the knowledge, understanding and progress to the field of skyrmions. In particularly, involving synthetic antiferromagnets, with the hope that it can promote further research and accelerate the battle against climate change.

Chapter 5 summarised literature from multiple decades into the research of proximity effects at a FM/NM interface. Trends and discrepancies were analysed, discussed and summarised to allow informed decisions to be made about the accuracy of reported proximity effects in literature, and to guide accuracy of future measurements, where relevant. Furthermore, a sample series was grown to compare the proximity effects at the Co/NM (with the NM as Pt, Ir or Ta) interface, which agreed well with other literature. Then, the less studied proximity effects at the CoB/NM (with the NM as Pt, Ir or Ta) interface were investigated, and showed both agreeable and differing qualities compared to Co.

Chapter 6 was part of a multi-partner research investigation into discrepancies when calculating the DMI in Co multilayers. It considered various approaches to work out different parameters that contributed to the DMI constant. Proximity effects mainly affected the anisotropy and the saturation magnetisation, whereas the bulk vs. thin film method of calculating the exchange stiffness had a significant difference on the DMI strength, however, the main factor was the DMI field. The DMI field was calculated for the same sample in different laboratories via the bubble expansion method, and the DMI strength was measured on the same sample at multiple laboratories via both the bubble expansion method and BLS. The conclusions highlighted the way in which the DMI strength can be cited differently, even for the same sample. The work from this chapter was published in Reference [4].

Chapter 7 investigated the antiferromagnetic interlayer exchange coupling of CoB/Ir/Pt as a function of temperature, number of repeats and thickness of the different components. It also proposed a method in which to host skyrmions in synthetic antiferromagnets. This resulted in a SAF stack which allowed for the presence skyrmions, however, the skyrmions were not coupled antiferromagnetically throughout the SAF. The skyrmion hosting SAF was also studied as a function of temperature and thickness of the layers.

Chapter 8 created coplanar waveguides, adapted from Reference [5], to perform on-chip THz-TDS measurements. The waveguides included a Hall bar in which it was possible to deposit the FM multilayers and SAFs used throughout the thesis. Successful THz-TDS measurements were performed on these CPW with the magnetic material, and compared to waveguides made solely of TiAu. The magnetic materials were probed by the THz wave as a function of magnetic field, however, it would require further fabrication and measurements to determine the true nature of the signals observed.

9.2 Future Work

Firstly, it would be instrumental to take the research of Chapter 6 further and look further into discrepancies when different laboratories calculate the saturation magnetisation as it is a vital component for the both the DMI, and many other parameters. This may offer an insight into the differences of DMI values measured in different laboratories. If it is possible to calculate the DMI with high accuracy and have a universal method of characterisation of DMI, this would allow for uncomplicated fine-tuning of material properties for multilayer-based applications. Secondly, further tweaking of the parameters of stack 2 in Chapter 7 is required to enable the skyrmions within the SAF to couple together antiferromagnetically. This could include: changing the number of repetitions in the top and bottom parts of the stack, increasing the thickness of the CoB closer to the point just before the magnetisation becomes in-plane, and therefore adjusting the thicknesses of the other layers. Otherwise, different materials could be tested to find a more appropriate balance of effects. To arrive at material with the ability to host functional SAF skyrmions would be a great step for skyrmion device application, opening a new platform for exploring skyrmion dynamics. Finally, in regard to Chapter 8, more CPWs should be fabricated with SAF materials that have switching fields within the magnetic field range of the magnet in the on-chip THz-TDS measurement set up. Following this, a different number of repetitions of stack 1 and 2 could be investigated, with an aim to uncover frequency responses from these materials. If these materials are shown to have high frequency responses, this could lead to possible material routes for faster technologies.

REFERENCES

[1] A. Fert, N. Reyren, and V. Cros, “Magnetic skyrmions: advances in physics and potential applications,” *Nature Reviews Materials*, vol. 2, no. 7, p. 17031, 2017.

[2] S. Finizio, K. Zeissler, S. Wintz, S. Mayr, T. Weßels, A. J. Huxtable, G. Burnell, C. H. Marrows, and J. Raabe, “Deterministic field-free skyrmion nucleation at a nanoengineered injector device,” *Nano letters*, vol. 19, no. 10, pp. 7246–7255, 2019.

[3] K. Zeissler, S. Finizio, K. Shahbazi, J. Massey, F. A. Ma’Mari, D. M. Bracher, A. Kleibert, M. C. Rosamond, E. H. Linfield, T. A. Moore, *et al.*, “Discrete hall resistivity contribution from néel skyrmions in multilayer nanodiscs,” *Nature Nanotechnology*, vol. 13, no. 12, pp. 1161–1166, 2018.

[4] A. Magni, G. Carlotti, A. Casiraghi, E. Darwin, G. Durin, L. H. Diez, B. J. Hickey, A. Huxtable, C. Y. Hwang, G. Jakob, C. Kim, M. Kläui, J. Langer, C. H. Marrows, H. T. Nembach, D. Ravelosona, G. A. Riley, J. M. Shaw, V. Sokalski, S. Tacchi, and M. Kuepferling, “Key points in the determination of the interfacial dzyaloshinskii-moriya interaction from asymmetric bubble domain expansion,” *IEEE Transactions on Magnetics*, vol. 58, no. 12, pp. 1–16, 2022.

[5] N. Peters, *THz On-Chip Waveguides for Ultrafast Magnetic Measurements.* PhD thesis, University of Leeds, 2018.

[6] J. Coey, *Magnetism and magnetic materials.* Cambridge university press, 2010.

[7] C. Hurd, “Varieties of magnetic order in solids,” *Contemporary Physics*, vol. 23, no. 5, pp. 469–493, 1982.

[8] S. Blundell, “Magnetism in condensed matter,” 2003.

[9] J. Coey, “Materials for spin electronics,” in *Spin electronics*, pp. 277–297, Springer, 2001.

[10] M. Ruderman and C. Kittel, “Indirect exchange coupling of nuclear magnetic moments by conduction electrons,” *Physical Review*, vol. 96, no. 1, p. 99, 1954.

[11] T. Kasuya, “A theory of metallic ferro-and antiferromagnetism on zener’s model,” *Progress of theoretical physics*, vol. 16, no. 1, pp. 45–57, 1956.

[12] K. Yosida, “Magnetic properties of cu-mn alloys,” *Physical Review*, vol. 106, no. 5, p. 893, 1957.

[13] S. Parkin, “Systematic variation of the strength and oscillation period of indirect magnetic exchange coupling through the 3d, 4d, and 5d transition metals,” *Physical Review Letters*, vol. 67, no. 25, p. 3598, 1991.

[14] R. Duine, K. Lee, S. Parkin, and M. Stiles, “Synthetic antiferromagnetic spintronics,” *Nature physics*, vol. 14, no. 3, pp. 217–219, 2018.

[15] D. Jiles, *Introduction to magnetism and magnetic materials.* CRC press, 2015.

[16] C. Kittel and P. McEuen, *Introduction to solid state physics*, vol. 8. Wiley New York, 1996.

[17] J. Pelzl, R. Meckenstock, D. Spoddig, F. Schreiber, J. Pflaum, and Z. Frait, “Spin–orbit-coupling effects on g-value and damping factor of the ferromagnetic resonance in co and fe films,” *Journal of Physics: Condensed Matter*, vol. 15, no. 5, p. S451, 2003.

[18] C. Kittel and C.-Y. Fong, *Quantum theory of solids.* Wiley, 1987.

[19] H. T. Nembach, J. M. Shaw, M. Weiler, E. Jué, and T. J. Silva, “Linear relation between heisenberg exchange and interfacial dzyaloshinskii–moriya interaction in metal films,” *Nature Physics*, vol. 11, no. 10, pp. 825–829, 2015.

[20] J. B. Mohammadi, B. Kardasz, G. Wolf, Y. Chen, M. Pinarbasi, and A. D. Kent, “Reduced exchange interactions in magnetic tunnel junction free layers with insertion layers,” *ACS Applied Electronic Materials*, vol. 1, no. 10, pp. 2025–2029, 2019.

[21] N. Spaldin, *Magnetic materials: fundamentals and applications.* Cambridge university press, 2010.

[22] M. Johnson, P. Bloemen, F. Den Broeder, and J. De Vries, “Magnetic anisotropy in metallic multilayers,” *Reports on Progress in Physics*, vol. 59, no. 11, p. 1409, 1996.

[23] S. Hashimoto, Y. Ochiai, and K. Aso, “Perpendicular magnetic anisotropy and magnetostriction of sputtered co/pd and co/pt multilayered films,” *Journal of applied physics*, vol. 66, no. 10, pp. 4909–4916, 1989.

[24] P. Carcia, A. Meinhaldt, and A. Suna, “Perpendicular magnetic anisotropy in pd/co thin film layered structures,” *Applied Physics Letters*, vol. 47, no. 2, pp. 178–180, 1985.

[25] P. Carcia, “Perpendicular magnetic anisotropy in pd/co and pt/co thin-film layered structures,” *Journal of applied physics*, vol. 63, no. 10, pp. 5066–5073, 1988.

[26] U. Gradmann and J. Müller, “Flat ferromagnetic, epitaxial 48ni/52fe (111) films of few atomic layers,” *physica status solidi (b)*, vol. 27, no. 1, pp. 313–324, 1968.

[27] N. Nakajima, T. Koide, T. Shidara, H. Miyauchi, H. Fukutani, A. Fujimori, K. Iio, T. Katayama, M. Nỳvlt, and Y. Suzuki, “Perpendicular magnetic anisotropy caused by interfacial hybridization via enhanced orbital moment in co/pt multilayers: Magnetic circular x-ray dichroism study,” *Physical Review Letters*, vol. 81, no. 23, p. 5229, 1998.

[28] B. Engel, M. Wiedmann, R. Van Leeuwen, and C. Falco, “Anomalous magnetic anisotropy in ultrathin transition metals,” *Physical Review B*, vol. 48, no. 13, p. 9894, 1993.

[29] P. Beauvillain, A. Bounouh, C. Chappert, R. Mégy, S. Ould-Mahfoud, J. Renard, P. Veillet, D. Weller, and J. Corno, “Effect of submonolayer coverage on magnetic anisotropy of ultrathin cobalt films m/co/au (111) with m= au, cu, pd,” *Journal of Applied Physics*, vol. 76, no. 10, pp. 6078–6080, 1994.

[30] R. White and D. Friedman, “Theory of the magnetic proximity effect,” *Journal of magnetism and magnetic materials*, vol. 49, no. 1-2, pp. 117–123, 1985.

[31] O. Inyang, L. Bouchenoire, B. Nicholson, M. Tokaç, R. Rowan-Robinson, C. Kinane, and A. Hindmarch, “Threshold interface magnetization required to induce magnetic proximity effect,” *Physical Review B*, vol. 100, no. 17, p. 174418, 2019.

[32] A. Moskaltsova, J. Krieft, D. Graulich, T. Matalla-Wagner, and T. Kuschel, “Impact of the magnetic proximity effect in pt on the total magnetic moment of pt/co/ta trilayers studied by x-ray resonant magnetic reflectivity,” *AIP Advances*, vol. 10, no. 1, p. 015154, 2020.

[33] R. Rowan-Robinson, A. Stashkevich, Y. Roussigné, M. Belmeguenai, S.-M. Chérif, A. Thiaville, T. Hase, A. Hindmarch, and D. Atkinson, “The interfacial nature of proximity-induced magnetism and the dzyaloshinskii-moriya interaction at the pt/co interface,” *Scientific Reports*, vol. 7, no. 1, pp. 1–11, 2017.

[34] M. Angelakeris, E. Papaioannou, P. Poulopoulos, A. Vlachos, G. Natsiopoulos, F. Wilhelm, A. Rogalev, and N. Flevaris, “Pt–co multilayers: Interface effects at the monolayer limit,” *physica status solidi (a)*, vol. 205, no. 10, pp. 2302–2306, 2008.

[35] H. Yang, A. Thiaville, S. Rohart, A. Fert, and M. Chshiev, “Anatomy of dzyaloshinskii-moriya interaction at co/pt interfaces,” *Physical review letters*, vol. 115, no. 26, p. 267210, 2015.

[36] A. Hrabec, N. Porter, A. Wells, M. Benitez, G. Burnell, S. McVitie, D. McGrouther, T. Moore, and C. Marrows, "Measuring and tailoring the dzyaloshinskii-moriya interaction in perpendicularly magnetized thin films," *Physical Review B*, vol. 90, no. 2, p. 020402, 2014.

[37] S. Rohart and A. Thiaville, "Skyrmion confinement in ultrathin film nanostructures in the presence of dzyaloshinskii-moriya interaction," *Physical Review B*, vol. 88, no. 18, p. 184422, 2013.

[38] S. Lemerle, J. Ferré, C. Chappert, V. Mathet, T. Giamarchi, and P. Le Doussal, "Domain wall creep in an ising ultrathin magnetic film," *Physical review letters*, vol. 80, no. 4, p. 849, 1998.

[39] P. Shepley, *Effect of piezoelectric strain on the magnetic properties of Pt/Co thin films.* PhD thesis, University of Leeds, 2015.

[40] P. Metaxas, J. Jamet, A. Mougin, M. Cormier, J. Ferré, V. Baltz, B. Rodmacq, B. Dieny, and R. Stamps, "Creep and flow regimes of magnetic domain-wall motion in ultrathin pt/co/pt films with perpendicular anisotropy," *Physical review letters*, vol. 99, no. 21, p. 217208, 2007.

[41] P. Chauve, T. Giamarchi, and P. Le Doussal, "Creep and depinning in disordered media," *Physical Review B*, vol. 62, no. 10, p. 6241, 2000.

[42] J. Gorchon, S. Bustingorry, J. Ferré, V. Jeudy, A. Kolton, and T. Giamarchi, "Pinning-dependent field-driven domain wall dynamics and thermal scaling in an ultrathin pt/co/pt magnetic film," *Physical review letters*, vol. 113, no. 2, p. 027205, 2014.

[43] O. Boulle, J. Vogel, H. Yang, S. Pizzini, D. de Souza Chaves, A. Locatelli, T. Menteş, A. Sala, L. Buda-Prejbeanu, O. Klein, *et al.*, "Room-temperature chiral magnetic skyrmions in ultrathin magnetic nanostructures," *Nature nanotechnology*, vol. 11, no. 5, p. 449, 2016.

[44] T. Skyrme, "A unified field theory of mesons and baryons," *Nuclear Physics*, vol. 31, pp. 556–569, 1962.

[45] A. Bogdanov and U. Rößler, "Chiral symmetry breaking in magnetic thin films and multilayers," *Physical review letters*, vol. 87, no. 3, p. 037203, 2001.

[46] U. K. Rößler, A. Bogdanov, and C. Pfleiderer, "Spontaneous skyrmion ground states in magnetic metals," *Nature*, vol. 442, no. 7104, pp. 797–801, 2006.

[47] X. Zhang, Y. Zhou, K. Song, T.-E. Park, J. Xia, M. Ezawa, X. Liu, W. Zhao, G. Zhao, and S. Woo, "Skyrmion-electronics: writing, deleting, reading and processing magnetic skyrmions toward spintronic applications," *Journal of Physics: Condensed Matter*, vol. 32, no. 14, p. 143001, 2020.

[48] E. H. Hall *et al.*, "On a new action of the magnet on electric currents," *American Journal of Mathematics*, vol. 2, no. 3, pp. 287–292, 1879.

[49] W. Thomson, "Xix. on the electro-dynamic qualities of metals: Effects of magnetization on the electric conductivity of nickel and of iron," *Proceedings of the Royal Society of London*, no. 8, pp. 546–550, 1857.

[50] J. Smit, "Magnetoresistance of ferromagnetic metals and alloys at low temperatures," *Physica*, vol. 17, no. 6, pp. 612–627, 1951.

[51] Z. Jin, A. Tkach, F. Casper, V. Spetter, H. Grimm, A. Thomas, T. Kampfrath, M. Bonn, M. Kläui, and D. Turchinovich, "Accessing the fundamentals of magnetotransport in metals with terahertz probes," *Nature Physics*, vol. 11, no. 9, pp. 761–766, 2015.

[52] F. Büttner, I. Lemesh, and G. S. Beach, "Theory of isolated magnetic skyrmions: From fundamentals to room temperature applications," *Scientific reports*, vol. 8, no. 1, pp. 1–12, 2018.

[53] S. Mühlbauer, B. Binz, F. Jonietz, C. Pfleiderer, A. Rosch, A. Neubauer, R. Georgii, and P. Böni, "Skyrmion lattice in a chiral magnet," *Science*, vol. 323, no. 5916, pp. 915–919, 2009.

[54] I. Kézsmárki, S. Bordács, P. Milde, E. Neuber, L. Eng, J. White, H. Rønnow, C. Dewhurst, M. Mochizuki, K. Yanai, *et al.*, "Néel-type skyrmion lattice with confined orientation in the polar magnetic semiconductor gav4s8," *Nature materials*, vol. 14, no. 11, p. 1116, 2015.

[55] S. Heinze, K. Von Bergmann, M. Menzel, J. Brede, A. Kubetzka, R. Wiesendanger, G. Bihlmayer, and S. Blügel, "Spontaneous atomic-scale magnetic skyrmion lattice in two dimensions," *nature physics*, vol. 7, no. 9, pp. 713–718, 2011.

[56] K. Zeissler, M. Mruczkiewicz, S. Finizio, J. Raabe, P. Shepley, A. Sadovnikov, S. Nikitov, K. Fallon, S. McFadzean, S. McVitie, *et al.*, "Pinning and hysteresis in the field dependent diameter evolution of skyrmions in pt/co/ir superlattice stacks," *Scientific reports*, vol. 7, no. 1, p. 15125, 2017.

[57] W. Jiang, P. Upadhyaya, W. Zhang, G. Yu, B. Jungfleisch, F. Fradin, J. Pearson, Y. Tserkovnyak, K. Wang, O. Heinonen, *et al.*, "Blowing magnetic skyrmion bubbles," *Science*, vol. 349, no. 6245, pp. 283–286, 2015.

[58] S. Woo, K. Litzius, B. Krüger, M. Im, L. Caretta, K. Richter, M. Mann, A. Krone, R. Reeve, M. Weigand, *et al.*, "Observation of room-temperature magnetic skyrmions and their current-driven dynamics in ultrathin metallic ferromagnets," *Nature materials*, vol. 15, no. 5, p. 501, 2016.

[59] C. Moreau-Luchaire, C. Moutafis, N. Reyren, J. Sampaio, C. Vaz, N. Van Horne, K. Bouzehouane, K. Garcia, C. Deranlot, P. Warnicke, *et al.*, "Additive interfacial chiral interaction in multilayers for stabilization of small individual skyrmions at room temperature," *Nature nanotechnology*, vol. 11, no. 5, pp. 444–448, 2016.

[60] A. Soumyanarayanan, M. Raju, A. Gonzalez Oyarce, A. Tan, M.-Y. Im, A. Petrović, P. Ho, K. Khoo, M. Tran, C. Gan, *et al.*, "Tunable room-temperature magnetic skyrmions in ir/fe/co/pt multilayers," *Nature materials*, vol. 16, no. 9, pp. 898–904, 2017.

[61] S. McVitie, S. Hughes, K. Fallon, S. McFadzean, D. McGrouther, M. Krajnak, W. Legrand, D. Maccariello, S. Collin, K. Garcia, *et al.*, "A transmission electron microscope study of néel skyrmion magnetic textures in multilayer thin film systems with large interfacial chiral interaction," *Scientific reports*, vol. 8, no. 1, p. 5703, 2018.

[62] I. Dzyaloshinsky, "A thermodynamic theory of "weak" ferromagnetism of antiferromagnetics," *Journal of physics and chemistry of solids*, vol. 4, no. 4, pp. 241–255, 1958.

[63] T. Moriya, "Anisotropic superexchange interaction and weak ferromagnetism," *Physical review*, vol. 120, no. 1, p. 91, 1960.

[64] A. Fert, V. Cros, and J. Sampaio, "Skyrmions on the track," *Nature nanotechnology*, vol. 8, no. 3, pp. 152–156, 2013.

[65] J. Sampaio, V. Cros, S. Rohart, A. Thiaville, and A. Fert, "Nucleation, stability and current-induced motion of isolated magnetic skyrmions in nanostructures," *Nature nanotechnology*, vol. 8, no. 11, pp. 839–844, 2013.

[66] X. Zhang, M. Ezawa, and Y. Zhou, "Magnetic skyrmion logic gates: conversion, duplication and merging of skyrmions," *Scientific reports*, vol. 5, no. 1, pp. 1–8, 2015.

[67] J. Zázvorka, F. Jakobs, D. Heinze, N. Keil, S. Kromin, S. Jaiswal, K. Litzius, G. Jakob, P. Virnau, D. Pinna, *et al.*, "Thermal skyrmion diffusion used in a reshuffler device," *Nature nanotechnology*, vol. 14, no. 7, pp. 658–661, 2019.

[68] R. Tomasello, E. Martinez, R. Zivieri, L. Torres, M. Carpentieri, and G. Finocchio, "A strategy for the design of skyrmion racetrack memories," *Scientific reports*, vol. 4, no. 1, pp. 1–7, 2014.

[69] S. Meyer, M. Perini, S. von Malottki, A. Kubetzka, R. Wiesendanger, K. von Bergmann, and S. Heinze, "Isolated zero field sub-10 nm skyrmions in ultrathin co films," *Nature communications*, vol. 10, no. 1, pp. 1–8, 2019.

[70] N. Nagaosa and Y. Tokura, “Topological properties and dynamics of magnetic skyrmions,” *Nature nanotechnology*, vol. 8, no. 12, pp. 899–911, 2013.

[71] W. Legrand, D. Maccariello, N. Reyren, K. Garcia, C. Moutafis, C. Moreau-Luchaire, S. Collin, K. Bouzehouane, V. Cros, and A. Fert, “Room-temperature current-induced generation and motion of sub-100 nm skyrmions,” *Nano letters*, vol. 17, no. 4, pp. 2703–2712, 2017.

[72] L. Peng, K. Karube, Y. Taguchi, N. Nagaosa, Y. Tokura, and X. Yu, “Dynamic transition of current-driven single-skyrmion motion in a room-temperature chiral-lattice magnet,” *Nature communications*, vol. 12, no. 1, pp. 1–7, 2021.

[73] D. Maccariello, W. Legrand, N. Reyren, K. Garcia, K. Bouzehouane, S. Collin, V. Cros, and A. Fert, “Electrical detection of single magnetic skyrmions in metallic multilayers at room temperature,” *Nature nanotechnology*, vol. 13, no. 3, pp. 233–237, 2018.

[74] R. Tomasello, M. Ricci, P. Burrascano, V. Puliafito, M. Carpentieri, and G. Finocchio, “Electrical detection of single magnetic skyrmion at room temperature,” *AIP Advances*, vol. 7, no. 5, p. 056022, 2017.

[75] F. Büttner, I. Lemesh, M. Schneider, B. Pfau, C. M. Günther, P. Hessing, J. Geilhufe, L. Caretta, D. Engel, B. Krüger, *et al.*, “Field-free deterministic ultrafast creation of magnetic skyrmions by spin–orbit torques,” *Nature Nanotechnology*, vol. 12, no. 11, pp. 1040–1044, 2017.

[76] S. Woo, K. M. Song, X. Zhang, M. Ezawa, Y. Zhou, X. Liu, M. Weigand, S. Finizio, J. Raabe, M.-C. Park, *et al.*, “Deterministic creation and deletion of a single magnetic skyrmion observed by direct time-resolved x-ray microscopy,” *Nature Electronics*, vol. 1, no. 5, pp. 288–296, 2018.

[77] N. Romming, C. Hanneken, M. Menzel, J. Bickel, B. Wolter, K. von Bergmann, A. Kubetzka, and R. Wiesendanger, “Writing and deleting single magnetic skyrmions,” *Science*, vol. 341, no. 6146, pp. 636–639, 2013.

[78] S. Zhang, J. Zhang, Q. Zhang, C. Barton, V. Neu, Y. Zhao, Z. Hou, Y. Wen, C. Gong, O. Kazakova, *et al.*, “Direct writing of room temperature and zero field skyrmion lattices by a scanning local magnetic field,” *Applied Physics Letters*, vol. 112, no. 13, p. 132405, 2018.

[79] K. Zeissler, K. Shahbazi, J. Massey, S. Finizio, J. Raabe, F. Al Ma’Mari, M. Rosamond, E. Linfield, T. Moore, G. Burnell, *et al.*, “Direct imaging and electrical detection at room temperature of a single skyrmion,” *interfaces*, vol. 20, no. 23, p. 24, 2017.

[80] O. Petrova and O. Tchernyshyov, “Spin waves in a skyrmion crystal,” *Physical Review B*, vol. 84, no. 21, p. 214433, 2011.

[81] M. Mochizuki, “Spin-wave modes and their intense excitation effects in skyrmion crystals,” *Physical review letters*, vol. 108, no. 1, p. 017601, 2012.

[82] Y. Onose, Y. Okamura, S. Seki, S. Ishiwata, and Y. Tokura, “Observation of magnetic excitations of skyrmion crystal in a helimagnetic insulator cu 2 oseo 3,” *Physical review letters*, vol. 109, no. 3, p. 037603, 2012.

[83] B. Satywali, V. P. Kravchuk, L. Pan, M. Raju, S. He, F. Ma, A. Petrović, M. Garst, and C. Panagopoulos, “Microwave resonances of magnetic skyrmions in thin film multilayers,” *Nature communications*, vol. 12, no. 1, pp. 1–8, 2021.

[84] J.-V. Kim, F. Garcia-Sanchez, J. Sampaio, C. Moreau-Luchaire, V. Cros, and A. Fert, “Breathing modes of confined skyrmions in ultrathin magnetic dots,” *Physical Review B*, vol. 90, no. 6, p. 064410, 2014.

[85] M. Lonsky and A. Hoffmann, “Dynamic excitations of chiral magnetic textures,” *APL Materials*, vol. 8, no. 10, p. 100903, 2020.

[86] M. Lonsky and A. Hoffmann, “Skyrmion breathing modes in synthetic ferri-and antiferromagnets,” *Bulletin of the American Physical Society*, vol. 65, 2020.

[87] C. E. Barker, E. Haltz, T. A. Moore, and C. H. Marrows, “Breathing modes of skyrmion strings in a synthetic antiferromagnet,” *arXiv preprint arXiv:2112.05481*, 2021.

[88] L. Shen, J. Xia, G. Zhao, X. Zhang, M. Ezawa, O. A. Tretiakov, X. Liu, and Y. Zhou, “Spin torque nano-oscillators based on antiferromagnetic skyrmions,” *Applied Physics Letters*, vol. 114, no. 4, p. 042402, 2019.

[89] B. Jiang, W. Zhang, H. Zhong, Y. Zhang, S. Yu, G. Han, S. Xiao, G. Liu, S. Yan, J. Li, *et al.*, “Towards terahertz spin hall nano-oscillator with synthesized anti-ferromagnets,” *Journal of Magnetism and Magnetic Materials*, vol. 490, p. 165470, 2019.

[90] H. Zhong, S. Qiao, S. Yan, L. Liang, Y. Zhao, and S. Kang, “Terahertz spin-transfer torque oscillator based on a synthetic antiferromagnet,” *Journal of Magnetism and Magnetic Materials*, vol. 497, p. 166070, 2020.

[91] N. Ogawa, S. Seki, and Y. Tokura, “Ultrafast optical excitation of magnetic skyrmions,” *Scientific reports*, vol. 5, p. 9552, 2015.

[92] Y. Okamura, F. Kagawa, M. Mochizuki, M. Kubota, S. Seki, S. Ishiwata, M. Kawasaki, Y. Onose, and Y. Tokura, “Microwave magnetoelectric effect via skyrmion resonance modes in a helimagnetic multiferroic,” *Nature communications*, vol. 4, p. 2391, 2013.

[93] K. Guslienko and Z. Gareeva, “Magnetic skyrmion low frequency dynamics in thin circular dots,” *Journal of Magnetism and Magnetic Materials*, vol. 442, pp. 176–182, 2017.

[94] J. Kim, F. Garcia-Sanchez, J. Sampaio, C. Moreau-Luchaire, V. Cros, and A. Fert, “Breathing modes of confined skyrmions in ultrathin magnetic dots,” *Physical Review B*, vol. 90, no. 6, p. 064410, 2014.

[95] S. Karayev, P. Murray, D. Khadka, T. Thapaliya, K. Liu, and S. Huang, “Interlayer exchange coupling in pt/co/ru and pt/co/ir superlattices,” *Physical Review Materials*, vol. 3, no. 4, p. 041401, 2019.

[96] Y. Ishikuro, M. Kawaguchi, T. Taniguchi, and M. Hayashi, “Highly efficient spin-orbit torque in pt/co/ir multilayers with antiferromagnetic interlayer exchange coupling,” *Physical Review B*, vol. 101, no. 1, p. 014404, 2020.

[97] Y.-C. Lau, Z. Chi, T. Taniguchi, M. Kawaguchi, G. Shibata, N. Kawamura, M. Suzuki, S. Fukami, A. Fujimori, H. Ohno, *et al.*, “Giant perpendicular magnetic anisotropy in ir/co/pt multilayers,” *Physical Review Materials*, vol. 3, no. 10, p. 104419, 2019.

[98] A. Hrabec, J. Sampaio, M. Belmeguenai, I. Gross, R. Weil, S. M. Chérif, A. Stashkevich, V. Jacques, A. Thiaville, and S. Rohart, “Current-induced skyrmion generation and dynamics in symmetric bilayers,” *Nature communications*, vol. 8, no. 1, pp. 1–6, 2017.

[99] W. Jiang, X. Zhang, G. Yu, W. Zhang, X. Wang, M. Benjamin Jungfleisch, J. E. Pearson, X. Cheng, O. Heinonen, K. L. Wang, *et al.*, “Direct observation of the skyrmion hall effect,” *Nature Physics*, vol. 13, no. 2, pp. 162–169, 2017.

[100] K. Litzius, I. Lemesh, B. Krüger, P. Bassirian, L. Caretta, K. Richter, F. Büttner, K. Sato, O. A. Tretiakov, J. Förster, *et al.*, “Skyrmion hall effect revealed by direct time-resolved x-ray microscopy,” *Nature Physics*, vol. 13, no. 2, pp. 170–175, 2017.

[101] J. Barker and O. A. Tretiakov, “Static and dynamical properties of antiferromagnetic skyrmions in the presence of applied current and temperature,” *Physical review letters*, vol. 116, no. 14, p. 147203, 2016.

[102] R. Jaeschke-Ubiergo and A. S. Nunez, “Stability of atomic-sized skyrmions in antiferromagnetic bilayers,” *Annals of Physics*, vol. 405, pp. 29–37, 2019.

[103] S. Gao, H. Rosales, F. A. Gómez Albarracín, V. Tsurkan, G. Kaur, T. Fennell, P. Steffens, M. Boehm, P. Čermák, A. Schneidewind, *et al.*, “Fractional antiferromagnetic skyrmion lattice induced by anisotropic couplings,” *Nature*, vol. 586, no. 7827, pp. 37–41, 2020.

[104] S. Zhou, C. Wang, C. Zheng, and Y. Liu, "Manipulating skyrmions in synthetic antiferromagnetic nanowires by magnetic field gradients," *Journal of Magnetism and Magnetic Materials*, vol. 493, p. 165740, 2020.

[105] L. Caretta, M. Mann, F. Büttner, K. Ueda, B. Pfau, C. M. Günther, P. Hessing, A. Churikova, C. Klose, M. Schneider, *et al.*, "Fast current-driven domain walls and small skyrmions in a compensated ferrimagnet," *Nature nanotechnology*, vol. 13, no. 12, pp. 1154–1160, 2018.

[106] A.-O. Mandru, O. Yıldırım, R. Tomasello, P. Heistracher, M. Penedo, A. Giordano, D. Suess, G. Finocchio, and H. J. Hug, "Coexistence of distinct skyrmion phases observed in hybrid ferromagnetic/ferrimagnetic multilayers," *Nature communications*, vol. 11, no. 1, pp. 1–7, 2020.

[107] X. Zhang, Y. Zhou, and M. Ezawa, "Magnetic bilayer-skyrmions without skyrmion hall effect," *Nature communications*, vol. 7, no. 1, pp. 1–7, 2016.

[108] X. Zhang, Y. Zhou, and M. Ezawa, "Antiferromagnetic skyrmion: stability, creation and manipulation," *Scientific reports*, vol. 6, no. 1, pp. 1–8, 2016.

[109] C. Jin, C. Song, J. Wang, and Q. Liu, "Dynamics of antiferromagnetic skyrmion driven by the spin hall effect," *Applied Physics Letters*, vol. 109, no. 18, p. 182404, 2016.

[110] R. Tomasello, V. Puliafito, E. Martinez, A. Manchon, M. Ricci, M. Carpentieri, and G. Finocchio, "Performance of synthetic antiferromagnetic racetrack memory: domain wall versus skyrmion," *Journal of Physics D: Applied Physics*, vol. 50, no. 32, p. 325302, 2017.

[111] W. Legrand, D. Maccariello, F. Ajejas, S. Collin, A. Vecchiola, K. Bouzehouane, N. Reyren, V. Cros, and A. Fert, "Room-temperature stabilization of antiferromagnetic skyrmions in synthetic antiferromagnets," *Nature materials*, vol. 19, no. 1, pp. 34–42, 2020.

[112] T. Dohi, S. DuttaGupta, S. Fukami, and H. Ohno, "Formation and current-induced motion of synthetic antiferromagnetic skyrmion bubbles," *Nature communications*, vol. 10, no. 1, pp. 1–6, 2019.

[113] R. Juge, N. Sisodia, J. U. Larrañaga, Q. Zhang, V. T. Pham, K. G. Rana, B. Sarpi, N. Mille, S. Stanescu, R. Belkhou, *et al.*, "Skyrmions in synthetic antiferromagnets and their nucleation via electrical current and ultra-fast laser illumination," *Nature Communications*, vol. 13, no. 1, pp. 1–9, 2022.

[114] P. Garbacz, "Terahertz imaging–principles, techniques, benefits, and limitations," *Problemy Eksploatacji*, 2016.

[115] R. Lewis, "Materials for terahertz engineering," in *Springer Handbook of Electronic and Photonic Materials*, pp. 1–1, Springer, 2017.

[116] M. Kimmitt, "Restrahlen to t-rays–100 years of terahertz radiation," *Journal of biological physics*, vol. 29, no. 2-3, pp. 77–85, 2003.

[117] P. Jepsen, D. Cooke, and M. Koch, "Terahertz spectroscopy and imaging–modern techniques and applications," *Laser & Photonics Reviews*, vol. 5, no. 1, pp. 124–166, 2011.

[118] A. Rogalski, *Infrared and Terahertz Detectors*. CRC Press, 2018.

[119] Y. Lee, *Principles of terahertz science and technology*, vol. 170. Springer Science & Business Media, 2009.

[120] P. Siegel, "Terahertz technology," *IEEE Transactions on microwave theory and techniques*, vol. 50, no. 3, pp. 910–928, 2002.

[121] T. Kampfrath, A. Sell, G. Klatt, A. Pashkin, S. Mährlein, T. Dekorsy, M. Wolf, M. Fiebig, A. Leitenstorfer, and R. Huber, "Coherent terahertz control of antiferromagnetic spin waves," *Nature Photonics*, vol. 5, no. 1, pp. 31–34, 2011.

[122] E. Beaurepaire, J.-C. Merle, A. Daunois, and J.-Y. Bigot, "Ultrafast spin dynamics in ferromagnetic nickel," *Physical review letters*, vol. 76, no. 22, p. 4250, 1996.

[123] E. Beaurepaire, G. Turner, S. Harrel, M. Beard, J.-Y. Bigot, and C. Schmuttenmaer, "Coherent terahertz emission from ferromagnetic films excited by femtosecond laser pulses," *Applied Physics Letters*, vol. 84, no. 18, pp. 3465–3467, 2004.

[124] J. Schleicher, S. Harrel, C. Schmuttenmaer, E. Beaurepaire, and J.-Y. Bigot, "Characterization of magnetization dynamics using terahertz emission spectroscopy," in *International Conference on Ultrafast Phenomena*, p. TuH8, Optical Society of America, 2006.

[125] J.-Y. Bigot, M. Vomir, and E. Beaurepaire, "Coherent ultrafast magnetism induced by femtosecond laser pulses," *Nature Physics*, vol. 5, no. 7, pp. 515–520, 2009.

[126] M. Battiato, K. Carva, and P. Oppeneer, "Superdiffusive spin transport as a mechanism of ultrafast demagnetization," *Physical review letters*, vol. 105, no. 2, p. 027203, 2010.

[127] B. Koopmans, G. Malinowski, F. Dalla Longa, D. Steiauf, M. Fähnle, T. Roth, M. Cinchetti, and M. Aeschlimann, "Explaining the paradoxical diversity of ultrafast laser-induced demagnetization," *Nature materials*, vol. 9, no. 3, pp. 259–265, 2010.

[128] C. Vicario, C. Ruchert, F. Ardana-Lamas, P. Derlet, B. Tudu, J. Luning, and C. Hauri, "Off-resonant magnetization dynamics phase-locked to an intense phase-stable terahertz transient," *Nature Photonics*, vol. 7, no. 9, p. 720, 2013.

[129] S. Bonetti, M. Hoffmann, M.-J. Sher, Z. Chen, S.-H. Yang, M. Samant, S. Parkin, and H. Dürr, "Thz-driven ultrafast spin-lattice scattering in amorphous metallic ferromagnets," *Physical review letters*, vol. 117, no. 8, p. 087205, 2016.

[130] T. Kampfrath, M. Battiato, P. Maldonado, G. Eilers, J. Nötzold, S. Mährlein, V. Zbarsky, F. Freimuth, Y. Mokrousov, S. Blügel, *et al.*, "Terahertz spin current pulses controlled by magnetic heterostructures," *Nature nanotechnology*, vol. 8, no. 4, p. 256, 2013.

[131] B. Choi, J. Rudge, K. Jordan, and T. Genet, "Terahertz excitation of spin dynamics in ferromagnetic thin films incorporated in metallic spintronic-thz-emitter," *Applied Physics Letters*, vol. 116, no. 13, p. 132406, 2020.

[132] Q. Zhang, Y. Yang, Z. Luo, Y. Xu, R. Nie, X. Zhang, and Y. Wu, "Terahertz emission from an exchange-coupled synthetic antiferromagnet," *Physical Review Applied*, vol. 13, no. 5, p. 054016, 2020.

[133] S.-H. Oh, S. K. Kim, D.-K. Lee, G. Go, K.-J. Kim, T. Ono, Y. Tserkovnyak, and K.-J. Lee, "Coherent terahertz spin-wave emission associated with ferrimagnetic domain wall dynamics," *Physical Review B*, vol. 96, no. 10, p. 100407, 2017.

[134] S. Kovalev, Z. Wang, J. Deinert, N. Awari, M. Chen, B. Green, S. Germanskiy, T. De Oliveira, J. Lee, A. Deac, *et al.*, "Selective thz control of magnetic order: new opportunities from superradiant undulator sources," *Journal of Physics D: Applied Physics*, vol. 51, no. 11, p. 114007, 2018.

[135] W. Bragg and W. Bragg, "The reflection of x-rays by crystals," *Proceedings of the Royal Society of London. Series A, Containing Papers of a Mathematical and Physical Character*, vol. 88, no. 605, pp. 428–438, 1913.

[136] A. Glavic and M. Björck, "Genx 3: the latest generation of an established tool," *Journal of applied crystallography*, vol. 55, no. 4, 2022.

[137] J. Clarke and A. Braginski, *The SQUID Handbook: Fundamentals and Technology of SQUIDs and SQUID Systems.* John Wiley & Sons, 2006.

[138] Q. Design, "Magnetic property measurement system: Squid vsm user's manual," *San Diego: Quantum Design*, 2009.

[139] Q. Design, "Accuracy of the reported moment: sample shape effects," *SQUID VSM Application Note*, 2010.

[140] M. Ali, *Growth and study of magnetostrictive FeSiBC thin films for device applications.* PhD thesis, University of Sheffield, 1999.

[141] R. Schäfer, “Investigation of domains and dynamics of domain walls by the magneto-optical k err-effect,” *Handbook of magnetism and advanced magnetic materials*, 2007.

[142] K. Shahbazi, J.-V. Kim, H. T. Nembach, J. M. Shaw, A. Bischof, M. D. Rossell, V. Jeudy, T. A. Moore, and C. H. Marrows, “Domain-wall motion and interfacial dzyaloshinskii-moriya interactions in pt/co/ir (t ir)/ta multilayers,” *Physical Review B*, vol. 99, no. 9, p. 094409, 2019.

[143] M. Belmeguenai, M. Gabor, Y. Roussigné, T. Petrisor Jr, R. Mos, A. Stashkevich, S. Chérif, and C. Tiusan, “Interfacial dzyaloshinskii-moriya interaction sign in ir/co 2 feal systems investigated by brillouin light scattering,” *Physical Review B*, vol. 97, no. 5, p. 054425, 2018.

[144] N.-H. Kim, J. Jung, J. Cho, D.-S. Han, Y. Yin, J.-S. Kim, H. J. Swagten, and C.-Y. You, “Interfacial dzyaloshinskii-moriya interaction, surface anisotropy energy, and spin pumping at spin orbit coupled ir/co interface,” *Applied Physics Letters*, vol. 108, no. 14, p. 142406, 2016.

[145] J. Cho, N.-H. Kim, S. K. Kang, H.-K. Hwang, J. Jung, H. J. Swagten, J.-S. Kim, and C.-Y. You, “The sign of the interfacial dzyaloshinskii–moriya interaction in ultrathin amorphous and polycrystalline magnetic films,” *Journal of Physics D: Applied Physics*, vol. 50, no. 42, p. 425004, 2017.

[146] K. Shahbazi, J.-V. Kim, H. Nembach, J. Shaw, A. Bischof, M. Rossell, V. Jeudy, T. Moore, and C. Marrows, “Domain-wall motion and interfacial dzyaloshinskii-moriya interactions in pt/co/ir (t ir)/ta multilayers,” *Physical Review B*, vol. 99, no. 9, p. 094409, 2019.

[147] P. Shepley, H. Tunnicliffe, K. Shahbazi, G. Burnell, and T. Moore, “Magnetic properties, domain-wall creep motion, and the dzyaloshinskii-moriya interaction in pt/co/ir thin films,” *Physical Review B*, vol. 97, no. 13, p. 134417, 2018.

[148] S. Porthun, L. Abelmann, and C. Lodder, “Magnetic force microscopy of thin film media for high density magnetic recording,” *Journal of magnetism and magnetic materials*, vol. 182, no. 1-2, pp. 238–273, 1998.

[149] J. Saenz, N. Garcia, P. Grütter, E. Meyer, H. Heinzelmann, R. Wiesendanger, L. Rosenthaler, H. Hidber, and H.-J. Güntherodt, “Observation of magnetic forces by the atomic force microscope,” *Journal of applied physics*, vol. 62, no. 10, pp. 4293–4295, 1987.

[150] Y. Martin and H. Wickramasinghe, “Magnetic imaging by “force microscopy”with 1000 å resolution,” *Applied Physics Letters*, vol. 50, no. 20, pp. 1455–1457, 1987.

[151] H. Mamin, D. Rugar, J. Stern, R. Fontana Jr, and P. Kasiraj, “Magnetic force microscopy of thin permalloy films,” *Applied physics letters*, vol. 55, no. 3, pp. 318–320, 1989.

[152] J. Saenz, N. Garcia, and J. Slonczewski, “Theory of magnetic imaging by force microscopy,” *Applied physics letters*, vol. 53, no. 15, pp. 1449–1451, 1988.

[153] Attocube, *Magnetic Force and Scanning Hall Probe Microscopes attoMFM/SHPM*. attocube systems AG, Brochure version: 2012 - 01, 2012.

[154] Y. Jiang, G. Li, H. Ge, F. Wang, L. Li, X. Chen, M. Lv, and Y. Zhang, “Machine learning and application in terahertz technology: A review on achievements and future challenges,” *IEEE Access*, 2022.

[155] R. Lavrijsen, D. Hartmann, A. van den Brink, Y. Yin, B. Barcones, R. Duine, M. Verheijen, H. Swagten, and B. Koopmans, “Asymmetric magnetic bubble expansion under in-plane field in pt/co/pt: Effect of interface engineering,” *Physical review B*, vol. 91, no. 10, p. 104414, 2015.

[156] D. Graulich, J. Krieft, A. Moskaltsova, J. Demir, T. Peters, T. Pohlmann, F. Bertram, J. Wollschläger, J. R. L. Mardegan, S. Francoual, *et al.*, “Quantitative comparison of the magnetic proximity effect in pt detected by xrmr and xmcd,” *Applied Physics Letters*, vol. 118, no. 1, p. 012407, 2021.

[157] M. González Rivas, “X-ray magnetic circular dichroism (xmcd),” 2021.

[158] B. Thole, P. Carra, F. Sette, and G. van der Laan, “X-ray circular dichroism as a probe of orbital magnetization,” *Physical review letters*, vol. 68, no. 12, p. 1943, 1992.

[159] P. Carra, B. Thole, M. Altarelli, and X. Wang, “X-ray circular dichroism and local magnetic fields,” *Physical Review Letters*, vol. 70, no. 5, p. 694, 1993.

[160] S. Ferrer, J. Alvarez, E. Lundgren, X. Torrelles, P. Fajardo, and F. Boscherini, “Surface x-ray diffraction from c o/p t (111) ultrathin films and alloys: Structure and magnetism,” *Physical Review B*, vol. 56, no. 15, p. 9848, 1997.

[161] A. Mukhopadhyay, S. K. Vayalil, D. Graulich, I. Ahamed, S. Francoual, A. Kashyap, T. Kuschel, and P. A. Kumar, “Asymmetric modification of the magnetic proximity effect in pt/co/pt trilayers by the insertion of a ta buffer layer,” *Physical Review B*, vol. 102, no. 14, p. 144435, 2020.

[162] M. Suzuki, H. Muraoka, Y. Inaba, H. Miyagawa, N. Kawamura, T. Shimatsu, H. Maruyama, N. Ishimatsu, Y. Isohama, and Y. Sonobe, “Depth profile of spin and orbital magnetic moments in a subnanometer pt film on co,” *Physical Review B*, vol. 72, no. 5, p. 054430, 2005.

[163] S. Rüegg, G. Schütz, P. Fischer, R. Wienke, W. Zeper, and H. Ebert, “Spin-dependent x-ray absorption in co/pt multilayers,” *Journal of applied physics*, vol. 69, no. 8, pp. 5655–5657, 1991.

[164] P. Poulopoulos, F. Wilhelm, H. Wende, G. Ceballos, K. Baberschke, D. Benea, H. Ebert, M. Angelakeris, N. Flevaris, A. Rogalev, *et al.*, "X-ray magnetic circular dichroic magnetometry on ni/pt multilayers," *Journal of Applied Physics*, vol. 89, no. 7, pp. 3874–3879, 2001.

[165] C. Ederer, M. Komelj, M. Fähnle, and G. Schütz, "Theory of induced magnetic moments and x-ray magnetic circular dichroism in co-pt multilayers," *Physical Review B*, vol. 66, no. 9, p. 094413, 2002.

[166] H. Ebert, "Magneto-optical effects in transition metal systems," *Reports on Progress in Physics*, vol. 59, no. 12, p. 1665, 1996.

[167] S. Macke and E. Goering, "Magnetic reflectometry of heterostructures," *Journal of Physics: Condensed Matter*, vol. 26, no. 36, p. 363201, 2014.

[168] T. Kuschel, C. Klewe, J.-M. Schmalhorst, F. Bertram, O. Kuschel, T. Schemme, J. Wollschläger, S. Francoual, J. Strempfer, A. Gupta, *et al.*, "Static magnetic proximity effect in pt/nife 2 o 4 and pt/fe bilayers investigated by x-ray resonant magnetic reflectivity," *Physical review letters*, vol. 115, no. 9, p. 097401, 2015.

[169] J.-M. Tonnerre, L. Seve, A. Barbara-Dechelette, F. Bartolomé, D. Raoux, V. Chakarian, C. Kao, H. Fischer, S. Andrieu, and O. Fruchart, "Soft x-ray resonant magnetic reflectivity study of thin films and multilayers," *Journal of applied physics*, vol. 83, no. 11, pp. 6293–6295, 1998.

[170] T. Kuschel, C. Klewe, P. Bougiatioti, O. Kuschel, J. Wollschläger, L. Bouchenoire, S. D. Brown, J.-M. Schmalhorst, D. Meier, and G. Reiss, "Static magnetic proximity effect in pt layers on sputter-deposited nife 2 o 4 and on fe of various thicknesses investigated by xrmr," *IEEE Transactions on Magnetics*, vol. 52, no. 7, pp. 1–4, 2016.

[171] C. Klewe, T. Kuschel, J.-M. Schmalhorst, F. Bertram, O. Kuschel, J. Wollschläger, J. Strempfer, M. Meinert, and G. Reiss, "Static magnetic proximity effect in pt/ni 1- x fe x bilayers investigated by x-ray resonant magnetic reflectivity," *Physical Review B*, vol. 93, no. 21, p. 214440, 2016.

[172] Y. Lee, J. Rhee, C. Whang, and Y. Lee, "Electronic structure of co-pt alloys: X-ray spectroscopy and density-functional calculations," *Physical Review B*, vol. 68, no. 23, p. 235111, 2003.

[173] S.-C. Shin, G. Srinivas, Y.-S. Kim, and M.-G. Kim, "Observation of perpendicular magnetic anisotropy in ni/pt multilayers at room temperature," *Applied physics letters*, vol. 73, no. 3, pp. 393–395, 1998.

[174] F. Wilhelm, P. Poulopoulos, G. Ceballos, H. Wende, K. Baberschke, P. Srivastava, D. Benea, H. Ebert, M. Angelakeris, N. Flevaris, *et al.*, "Layer-resolved magnetic moments in ni/pt multilayers," *Physical review letters*, vol. 85, no. 2, p. 413, 2000.

[175] Y.-S. Kim, J.-R. Jeong, M.-G. Kim, and S.-C. Shin, "Observation of magnetic dead layer in ni/pt multilayers," *IEEE transactions on magnetics*, vol. 35, no. 5, pp. 3073–3075, 1999.

[176] S.-K. Kim, J.-R. Jeong, J. Kortright, and S.-C. Shin, "Experimental observation of magnetically dead layers in ni/pt multilayer films," *Physical Review B*, vol. 64, no. 5, p. 052406, 2001.

[177] X. Zhou and H. Wadley, "Atomistic simulations of the vapor deposition of ni/cu/ni multilayers: The effects of adatom incident energy," *Journal of applied physics*, vol. 84, no. 4, pp. 2301–2315, 1998.

[178] J. Yu, X. Qiu, Y. Wu, J. Yoon, P. Deorani, J. M. Besbas, A. Manchon, and H. Yang, "Spin orbit torques and dzyaloshinskii-moriya interaction in dual-interfaced co-ni multilayers," *Scientific reports*, vol. 6, no. 1, pp. 1–9, 2016.

[179] P. Poulopoulos, F. Wilhelm, V. Kapaklis, N. Jaouen, M. Angelakeris, A. Rogalev, and C. Politis, "Cocr-based alloys: Pt and ta induced magnetic moments probed by x-ray magnetic circular dichroism," *physica status solidi (a)*, vol. 201, no. 15, pp. 3243–3246, 2004.

[180] P. Poulopoulos, A. Scherz, F. Wilhelm, H. Wende, and K. Baberschke, "Direct probe of induced magnetic moments at interfaces via x-ray magnetic circular dichroism," *physica status solidi (a)*, vol. 189, no. 2, pp. 293–300, 2002.

[181] P. Poulopoulos, F. Wilhelm, Z. Li, A. Scherz, H. Wende, K. Baberschke, M. Angelakeris, N. Flevaris, A. Rogalev, and N. Brookes, "Element-specific hysteresis loops and the anisotropy of the orbital moment of pt in ni/pt multilayers," *Journal of magnetism and magnetic materials*, vol. 272, pp. 317–318, 2004.

[182] R. Wu, C. Li, and A. Freeman, "Structural, electronic and magnetic properties of co/pd (111) and co/pt (111)," *Journal of Magnetism and Magnetic Materials*, vol. 99, no. 1-3, pp. 71–80, 1991.

[183] W. Antel Jr, M. Schwickert, T. Lin, W. O'Brien, and G. Harp, "Induced ferromagnetism and anisotropy of pt layers in fe/pt (001) multilayers," *Physical Review B*, vol. 60, no. 18, p. 12933, 1999.

[184] G. Schütz and P. Fischer, "Circularly polarized x-rays probing nuclear magnetic moments and magnetism of solids," *Zeitschrift für Physik A Hadrons and Nuclei*, vol. 341, no. 2, pp. 227–234, 1992.

[185] G. Schütz, S. Stähler, M. Knülle, P. Fischer, S. Parkin, and H. Ebert, “Distribution of magnetic moments in co/pt and co/pt/ir/pt multilayers detected by magnetic x-ray absorption,” *Journal of applied physics*, vol. 73, no. 10, pp. 6430–6432, 1993.

[186] F. Wilhelm, P. Poulopoulos, A. Scherz, H. Wende, K. Baberschke, M. Angelakeris, N. Flevaris, J. Goulon, and A. Rogalev, “Interface magnetism in 3d/5d multilayers probed by x-ray magnetic circular dichroism,” *physica status solidi (a)*, vol. 196, no. 1, pp. 33–36, 2003.

[187] T. Koyama, Y. Guan, Y. Hibino, M. Suzuki, and D. Chiba, “Magnetization switching by spin-orbit torque in pt with proximity-induced magnetic moment,” *Journal of Applied Physics*, vol. 121, no. 12, p. 123903, 2017.

[188] J. Geissler, E. Goering, M. Justen, F. Weigand, G. Schütz, J. Langer, D. Schmitz, H. Maletta, and R. Mattheis, “Pt magnetization profile in a pt/co bilayer studied by resonant magnetic x-ray reflectometry,” *Physical Review B*, vol. 65, no. 2, p. 020405, 2001.

[189] N. McGee, M. Johnson, J. De Vries, and J. aan De Stegge, “Localized kerr study of the magnetic properties of an ultrathin epitaxial co wedge grown on pt (111),” *Journal of applied physics*, vol. 73, no. 7, pp. 3418–3425, 1993.

[190] Q. Lv, J. Cai, S. He, and L. Sun, “Perpendicular magnetic anisotropy and magnetic proximity effect in pt1- δfeδ/co multilayer films,” *Journal of Magnetism and Magnetic Materials*, vol. 323, no. 5, pp. 465–470, 2011.

[191] F. Ece Demirer, R. Lavrijsen, and B. Koopmans, “An investigation of the interface and bulk contributions to the magneto-optic activity in co/pt multi-layered thin films,” *Journal of Applied Physics*, vol. 129, no. 16, p. 163904, 2021.

[192] C.-J. Lin, G. Gorman, C. Lee, R. Farrow, E. Marinero, H. Do, H. Notarys, and C. Chien, “Magnetic and structural properties of co/pt multilayers,” *Journal of Magnetism and Magnetic Materials*, vol. 93, pp. 194–206, 1991.

[193] M. Bersweiler, K. Dumesnil, D. Lacour, and M. Hehn, “Impact of buffer layer and pt thickness on the interface structure and magnetic properties in (co/pt) multilayers,” *Journal of Physics: Condensed Matter*, vol. 28, no. 33, p. 336005, 2016.

[194] S. Bandiera, R. Sousa, B. Rodmacq, and B. Dieny, “Asymmetric interfacial perpendicular magnetic anisotropy in pt/co/pt trilayers,” *IEEE Magnetics Letters*, vol. 2, pp. 3000504–3000504, 2011.

[195] J. Hannon, G. Trammell, M. Blume, and D. Gibbs, “X-ray resonance exchange scattering,” *Physical review letters*, vol. 61, no. 10, p. 1245, 1988.

[196] J. Alvarez, E. Lundgren, X. Torrelles, H. Isern, K. Peters, P. Steadman, and S. Ferrer, “Magnetization of pt in the co/pt (110) system investigated with surface x-ray magnetic diffraction: Evidence for in-plane magnetic anisotropy,” *Physical Review B*, vol. 60, no. 14, p. 10193, 1999.

[197] A. Verna, P. Alippi, F. Offi, G. Barucca, G. Varvaro, E. Agostinelli, M. Albrecht, B. Rutkowski, A. Ruocco, D. Paoloni, *et al.*, “Disclosing the nature of asymmetric interface magnetism in co/pt multilayers,” *ACS applied materials & interfaces*, vol. 14, no. 10, pp. 12766–12776, 2022.

[198] K. T. Kim, D.-O. Kim, J. Y. Kee, I. Seo, Y. Choi, J. W. Choi, and D. R. Lee, “X-ray reflectivity data analysis using bayesian inference: The study of induced pt magnetization in pt/co/pt,” *Current Applied Physics*, vol. 30, pp. 46–52, 2021.

[199] F. Meier, S. Lounis, J. Wiebe, L. Zhou, S. Heers, P. Mavropoulos, P. H. Dederichs, S. Blügel, and R. Wiesendanger, “Spin polarization of platinum (111) induced by the proximity to cobalt nanostripes,” *Physical Review B*, vol. 83, no. 7, p. 075407, 2011.

[200] W. Zhang, M. B. Jungfleisch, W. Jiang, Y. Liu, J. E. Pearson, S. G. Te Velthuis, A. Hoffmann, F. Freimuth, and Y. Mokrousov, “Reduced spin-hall effects from magnetic proximity,” *Physical Review B*, vol. 91, no. 11, p. 115316, 2015.

[201] Y. Zhang, N. Sun, W. Che, R. Shan, and Z. Zhu, “Origin of enhanced anomalous hall effect in ultrathin pt/permalloy bilayers,” *AIP Advances*, vol. 6, no. 2, p. 025214, 2016.

[202] K.-S. Ryu, S.-H. Yang, L. Thomas, and S. S. Parkin, “Chiral spin torque arising from proximity-induced magnetization,” *Nature communications*, vol. 5, no. 1, pp. 1–8, 2014.

[203] J. Knepper and F. Yang, “Oscillatory interlayer coupling in co/ pt multilayers with perpendicular anisotropy,” *Physical review B*, vol. 71, no. 22, p. 224403, 2005.

[204] V. Krishnamurthy, M. Suzuki, N. Kawamura, T. Ishikawa, and Y. Kohori, “Local moment of ir in fe, co and ni hosts probed by ir l 2, 3 edge x-ray magnetic circular dichroism,” *Hyperfine interactions*, vol. 136, no. 3, pp. 361–365, 2001.

[205] V. Krishnamurthy, M. Suzuki, N. Kawamura, T. Ishikawa, and Y. Kohori, “Iridium l2, 3 edge magnetic circular dichroism study of 5d moment formation in ferromagnetic ir–fe alloys,” *Physica B: Condensed Matter*, vol. 312, pp. 647–649, 2002.

[206] V. Krishnamurthy, D. J. Singh, N. Kawamura, M. Suzuki, and T. Ishikawa, “Composition-dependent induced spin and orbital magnetic moments of ir in co-ir alloys from x-ray magnetic circular dichroism,” *Physical Review B*, vol. 74, no. 6, p. 064411, 2006.

[207] F. Wilhelm, P. Poulopoulos, H. Wende, A. Scherz, K. Baberschke, M. Angelakeris, N. Flevaris, and A. Rogalev, “Systematics of the induced magnetic moments in 5 d layers and the violation of the third hund’s rule,” *Physical review letters*, vol. 87, no. 20, p. 207202, 2001.

[208] N. Jaouen, F. Wilhelm, A. Rogalev, J. Goulon, J. Tonnerre, and S. Andrieu, “Itnfluence of the structure of fe on the interfacial spin and orbital induced magnetic moments of ir in fe/ir multilayers,” *Journal of Magnetism and Magnetic Materials*, vol. 272, pp. E1615–E1616, 2004.

[209] W.-H. Chen, P.-C. Jiang, C.-Y. Hsieh, and J.-S. Tsay, “Structure related magnetic dead layer for ultrathin fe/ir (111) films,” *IEEE transactions on magnetics*, vol. 50, no. 1, pp. 1–4, 2013.

[210] M. Belmeguenai, D. Apalkov, M. Gabor, F. Zighem, G. Feng, and G. Tang, “Magnetic anisotropy and damping constant in cofeb/ir and cofeb/ru systems,” *IEEE Transactions on Magnetics*, vol. 54, no. 11, pp. 1–5, 2018.

[211] M. Belmeguenai, Y. Roussigné, H. Bouloussa, S. Chérif, A. Stashkevich, M. Nasui, M. Gabor, A. Mora-Hernández, B. Nicholson, O.-O. Inyang, *et al.*, “Thickness dependence of the dzyaloshinskii-moriya interaction in co 2 feal ultrathin films: Effects of annealing temperature and heavy-metal material,” *Physical Review Applied*, vol. 9, no. 4, p. 044044, 2018.

[212] S. Kim, S.-h. C. Baek, M. Ishibashi, K. Yamada, T. Taniguchi, T. Okuno, Y. Kotani, T. Nakamura, K.-J. Kim, T. Moriyama, *et al.*, “Contributions of co and fe orbitals to perpendicular magnetic anisotropy of mgo/cofeb bilayers with ta, w, irmn, and ti underlayers,” *Applied Physics Express*, vol. 10, no. 7, p. 073006, 2017.

[213] I. Benguettat-El Mokhtari, D. Ourdani, Y. Roussigné, R. Mos, M. Nasui, F. Kail, L. Chahed, S. Chérif, A. Stashkevich, M. Gabor, *et al.*, “Perpendicular magnetic anisotropy and interfacial dzyaloshinskii–moriya interaction in as grown and annealed x/co/y ultrathin systems,” *Journal of Physics: Condensed Matter*, vol. 32, no. 49, p. 495802, 2020.

[214] T. White, T. Bailey, M. Pierce, and C. W. Miller, “Strong spin pumping in permalloy-iridium heterostructures,” *IEEE Magnetics Letters*, vol. 8, pp. 1–4, 2017.

[215] S. Shringi, S. Piramanayagam, S. Prasad, N. Venkatramani, M. Patni, R. Krishnan, and M. Tessier, “Magnetic and conversion electron mössbauer spectroscopy studies in fe/ta multilayers,” *Journal of applied physics*, vol. 73, no. 10, pp. 6438–6440, 1993.

[216] S. Kezilebieke, M. Ali, B. Shadeke, and R. Gunnella, “Magnetic properties of ultrathin ni81fe19 films with ta and ru capping layers,” *Journal of Physics: Condensed Matter*, vol. 25, no. 47, p. 476003, 2013.

[217] Q. Leng, H. Han, M. Mao, C. Hiner, and F. Ryan, "Magnetic dead layers in nife/ta and nife/si/diamond-like carbon films," *Journal of Applied Physics*, vol. 87, no. 9, pp. 6621–6623, 2000.

[218] M. Kowalewski, W. Butler, N. Moghadam, G. Stocks, T. Schulthess, K. Song, J. Thompson, A. Arrott, T. Zhu, J. Drewes, *et al.*, "The effect of ta on the magnetic thickness of permalloy (ni 81 fe 19) films," *Journal of Applied Physics*, vol. 87, no. 9, pp. 5732–5734, 2000.

[219] Y.-H. Wang, W.-C. Chen, S.-Y. Yang, K.-H. Shen, C. Park, M.-J. Kao, and M.-J. Tsai, "Interfacial and annealing effects on magnetic properties of cofeb thin films," *Journal of applied physics*, vol. 99, no. 8, p. 08M307, 2006.

[220] K. Oguz, P. Jivrajka, M. Venkatesan, G. Feng, and J. Coey, "Magnetic dead layers in sputtered co 40 fe 40 b 20 films," *Journal of Applied Physics*, vol. 103, no. 7, p. 07B526, 2008.

[221] S. Y. Jang, S. H. Lim, and S. R. Lee, "Magnetic dead layer in amorphous cofeb layers with various top and bottom structures," *Journal of Applied Physics*, vol. 107, no. 9, p. 09C707, 2010.

[222] A. Natarajarathinam, Z. Tadisina, T. Mewes, S. Watts, E. Chen, and S. Gupta, "Influence of capping layers on cofeb anisotropy and damping," *Journal of Applied Physics*, vol. 112, no. 5, p. 053909, 2012.

[223] J. Sinha, M. Hayashi, A. J. Kellock, S. Fukami, M. Yamanouchi, H. Sato, S. Ikeda, S. Mitani, S.-h. Yang, S. S. Parkin, *et al.*, "Enhanced interface perpendicular magnetic anisotropy in ta/cofeb/mgo using nitrogen doped ta underlayers," *Applied Physics Letters*, vol. 102, no. 24, p. 242405, 2013.

[224] M. Akyol, B. Kıvrak, K. U. Tümen, and A. Ekicibil, "Effect of ta insertion between pt and cofeb on interfacial magnetic anisotropy in pt/cofeb/mgo multilayer thin-film stack," *Journal of Materials Science: Materials in Electronics*, vol. 31, no. 24, pp. 23037–23043, 2020.

[225] R. Lavrijsen, G. Malinowski, J. Franken, J. Kohlhepp, H. Swagten, B. Koopmans, M. Czapkiewicz, and T. Stobiecki, "Reduced domain wall pinning in ultrathin pt/co 100- x b x/pt with perpendicular magnetic anisotropy," *Applied Physics Letters*, vol. 96, no. 2, p. 022501, 2010.

[226] H. Tanaka, S. Takayama, M. Hasegawa, T. Fukunaga, U. Mizutani, A. Fujita, and K. Fukamichi, "Electronic structure and magnetism of amorphous co 1- x b x alloys," *Physical Review B*, vol. 47, no. 5, p. 2671, 1993.

[227] M. Konc, P. Spisak, P. Kollár, P. Sovák, O. Dusa, and T. Reininger, “Temperature dependence of the magnetization and of the other physical properties of rapidly quenched amorphous cob alloys,” *IEEE transactions on magnetics*, vol. 30, no. 2, pp. 524–526, 1994.

[228] A. Agui, A. Asahi, J. Sayama, M. Mizumaki, M. Tanaka, and T. Osaka, “Magnetic circular dichroism of [co/pd] and [cob/pd] multilayered films,” *Journal of magnetism and magnetic materials*, vol. 320, no. 22, pp. 3015–3018, 2008.

[229] N. Watanabe, H. Awano, *et al.*, “Cob/ni-based multilayer nanowire with high-speed domain wall motion under low current control,” *Japanese Journal of Applied Physics*, vol. 51, no. 9R, p. 093002, 2012.

[230] S. Finizio, S. Wintz, K. Zeissler, A. V. Sadovnikov, S. Mayr, S. A. Nikitov, C. H. Marrows, and J. Raabe, “Dynamic imaging of the delay-and tilt-free motion of néel domain walls in perpendicularly magnetized superlattices,” *Nano Letters*, vol. 19, no. 1, pp. 375–380, 2018.

[231] Y.-G. Choi and G.-M. Choi, “Investigation of stiffness and damping constant of spin waves in a soft magnet co100- x b x alloy,” *Applied Physics Letters*, vol. 121, no. 1, p. 012404, 2022.

[232] K. Zeissler, S. Finizio, C. Barton, A. J. Huxtable, J. Massey, J. Raabe, A. V. Sadovnikov, S. A. Nikitov, R. Brearton, T. Hesjedal, *et al.*, “Diameter-independent skyrmion hall angle observed in chiral magnetic multilayers,” *Nature communications*, vol. 11, no. 1, pp. 1–11, 2020.

[233] T. Asahi, M. Tanaka, J. Sayama, J. Kawaji, S. Matsunuma, and T. Osaka, “Effect of n2 additive gas during sputtering on magnetic properties and microstructure of cob/pd multilayered media,” *Journal of magnetism and magnetic materials*, vol. 287, pp. 199–203, 2005.

[234] N. Satchell, T. Mitchell, P. Shepley, E. Darwin, B. Hickey, and G. Burnell, “Pt and cob trilayer josephson π junctions with perpendicular magnetic anisotropy,” *Scientific reports*, vol. 11, no. 1, pp. 1–9, 2021.

[235] H. Tan, R. J. Lim, H. Seng, J. Shanmugam, H. Ko, X. Cheng, V. Putra, Z. Xing, A. Soumyanarayanan, and P. Ho, “Intermixing induced anisotropy variations in cob-based chiral multilayer films,” *Journal of Physics D: Applied Physics*, vol. 54, no. 35, p. 354003, 2021.

[236] Y. Yamamoto, T. Miura, M. Suzuki, N. Kawamura, H. Miyagawa, T. Nakamura, K. Kobayashi, T. Teranishi, and H. Hori, “Direct observation of ferromagnetic spin polarization in gold nanoparticles,” *Physical review letters*, vol. 93, no. 11, p. 116801, 2004.

[237] S. Pizzini, A. Fontaine, C. Giorgetti, E. Dartyge, J.-F. Bobo, M. Piecuch, and F. Baudelet, “Evidence for the spin polarization of copper in co/cu and fe/cu multilayers,” *Physical review letters*, vol. 74, no. 8, p. 1470, 1995.

[238] L. García, F. Bartolomé, J. Bartolomé, F. Luis, F. Petroff, C. Deranlot, F. Wilhelm, A. Rogalev, P. Bencok, and N. Brookes, "Magnetic polarization of copper in cu-capped co clusters," *Journal of Magnetism and Magnetic Materials*, vol. 316, no. 2, pp. e23–e26, 2007.

[239] M. Bode, M. Heide, K. Von Bergmann, P. Ferriani, S. Heinze, G. Bihlmayer, A. Kubetzka, O. Pietzsch, S. Blügel, and R. Wiesendanger, "Chiral magnetic order at surfaces driven by inversion asymmetry," *Nature*, vol. 447, no. 7141, pp. 190–193, 2007.

[240] G. Chen, T. Ma, A. T. N'Diaye, H. Kwon, C. Won, Y. Wu, and A. K. Schmid, "Tailoring the chirality of magnetic domain walls by interface engineering," *Nature communications*, vol. 4, no. 1, pp. 1–6, 2013.

[241] H. T. Nembach, J. M. Shaw, M. Weiler, E. Jué, and T. J. Silva, "Linear relation between heisenberg exchange and interfacial dzyaloshinskii–moriya interaction in metal films," *Nature Physics*, vol. 11, no. 10, pp. 825–829, 2015.

[242] Z. Wang, B. Zhang, Y. Cao, and P. Yan, "Probing the dzyaloshinskii-moriya interaction via the propagation of spin waves in ferromagnetic thin films," *Physical Review Applied*, vol. 10, no. 5, p. 054018, 2018.

[243] M. Belmeguenai, J.-P. Adam, Y. Roussigné, S. Eimer, T. Devolder, J. Kim, S. M. Cherif, A. Stashkevich, and j. v. n. p. y. p. Thiaville, A, "Interfacial dzyaloshinskii-moriya interaction in perpendicularly magnetized pt/co/alo x ultrathin films measured by brillouin light spectroscopy,"

[244] M. Gabor, T. Petrisor, R. Mos, M. Nasui, and C. Tiusan, "Interlayer exchange coupling in perpendicularly magnetized pt/co/ir/co/pt structures," *Journal of Physics D: Applied Physics*, vol. 50, no. 46, p. 465004, 2017.

[245] J. Barker, "Bloch's law derivations," 2020. University of Leeds.

[246] C. Eyrich, A. Zamani, W. Huttema, M. Arora, D. Harrison, F. Rashidi, D. Broun, B. Heinrich, O. Mryasov, M. Ahlberg, *et al.*, "Effects of substitution on the exchange stiffness and magnetization of co films," *Physical Review B*, vol. 90, no. 23, p. 235408, 2014.

[247] T. Eimüller, T. Ulbrich, E. Amaladass, I. Guhr, T. Tyliszczak, and M. Albrecht, "Spin-reorientation transition in co/ pt multilayers on nanospheres," *Physical Review B*, vol. 77, no. 13, p. 134415, 2008.

[248] I. Lemesh, F. Büttner, and G. S. Beach, "Accurate model of the stripe domain phase of perpendicularly magnetized multilayers," *Physical Review B*, vol. 95, no. 17, p. 174423, 2017.

[249] D. Lau, J. P. Pellegren, H. Nembach, J. Shaw, and V. Sokalski, “Disentangling factors governing dzyaloshinskii domain-wall creep in co/ni thin films using pt x ir 1- x seed layers,” *Physical Review B*, vol. 98, no. 18, p. 184410, 2018.

[250] L. H. Diez, Y. Liu, D. A. Gilbert, M. Belmeguenai, J. Vogel, S. Pizzini, E. Martinez, A. Lamperti, J. Mohammedi, A. Laborieux, *et al.*, “Nonvolatile ionic modification of the dzyaloshinskii-moriya interaction,” *Physical Review Applied*, vol. 12, no. 3, p. 034005, 2019.

[251] D.-Y. Kim, N.-H. Kim, Y.-K. Park, M.-H. Park, J.-S. Kim, Y.-S. Nam, J. Jung, J. Cho, D.-H. Kim, J.-S. Kim, *et al.*, “Quantitative accordance of dzyaloshinskii-moriya interaction between domain-wall and spin-wave dynamics,” *Physical Review B*, vol. 100, no. 22, p. 224419, 2019.

[252] R. Soucaille, M. Belmeguenai, J. Torrejon, J.-V. Kim, T. Devolder, Y. Roussigné, S.-M. Chérif, A. Stashkevich, M. Hayashi, and J.-P. Adam, “Probing the dzyaloshinskii-moriya interaction in cofeb ultrathin films using domain wall creep and brillouin light spectroscopy,” *Physical Review B*, vol. 94, no. 10, p. 104431, 2016.

[253] S. Lemerle, J. Ferré, C. Chappert, V. Mathet, T. Giamarchi, and P. Le Doussal, “Domain wall creep in an ising ultrathin magnetic film,” *Physical review letters*, vol. 80, no. 4, p. 849, 1998.

[254] K. Yakushiji, A. Sugihara, A. Fukushima, H. Kubota, and S. Yuasa, “Very strong antiferromagnetic interlayer exchange coupling with iridium spacer layer for perpendicular magnetic tunnel junctions,” *Applied Physics Letters*, vol. 110, no. 9, p. 092406, 2017.

[255] A. Fukushima, T. Taniguchi, A. Sugihara, K. Yakushiji, H. Kubota, and S. Yuasa, “Giant magnetoresistance in perpendicularly magnetized synthetic antiferromagnetic coupling with ir spacer,” *AIP Advances*, vol. 8, no. 5, p. 055925, 2018.

[256] R. Morgunov, A. Yurov, V. Yurov, A. Talantsev, A. Bezverhnii, and O. Koplak, “Oscillatory dynamics of the magnetic moment of a pt/co/ir/co/pt synthetic antiferromagnet,” *Physical Review B*, vol. 100, no. 14, p. 144407, 2019.

[257] N. Pandey, M. Li, M. De Graef, and V. Sokalski, “Stabilization of coupled dzyaloshinskii domain walls in fully compensated synthetic anti-ferromagnets,” *AIP Advances*, vol. 10, no. 1, p. 015233, 2020.

[258] V. Iurchuk, O. Kozlov, S. Sorokin, S. Zhou, J. Lindner, S. Reshetniak, A. Kravets, D. Polishchuk, and V. Korenivski, “All-electrical operation of a curie-switch at room temperature,” *arXiv preprint arXiv:2304.03040*, 2023.

[259] H. Wu, H. Zhang, B. Wang, F. Groß, C.-Y. Yang, G. Li, C. Guo, H. He, K. Wong, D. Wu, *et al.*, "Current-induced néel order switching facilitated by magnetic phase transition," *Nature Communications*, vol. 13, no. 1, p. 1629, 2022.

[260] J. Kools, T. G. Rijks, A. De Veirman, and R. Coehoorn, "On the ferromagnetic interlayer coupling in exchange-biased spin-valve multilayers," *IEEE Transactions on Magnetics*, vol. 31, no. 6, pp. 3918–3920, 1995.

[261] P. Bloemen, H. Van Kesteren, H. Swagten, and W. De Jonge, "Oscillatory interlayer exchange coupling in co/ru multilayers and bilayers," *Physical Review B*, vol. 50, no. 18, p. 13505, 1994.

[262] A. Dinia, M. Stoeffel, K. Rahmouni, D. Stoeffler, and H. Van Den Berg, "Exchange coupling and magnetoresistance in co/ir multilayers prepared by ion beam sputtering," *EPL (Europhysics Letters)*, vol. 42, no. 3, p. 331, 1998.

[263] P. N. Skirdkov and K. A. Zvezdin, "Spin-torque diodes: From fundamental research to applications," *Annalen der Physik*, vol. 532, no. 6, p. 1900460, 2020.

[264] Z. Zeng, G. Finocchio, and H. Jiang, "Spin transfer nano-oscillators," *Nanoscale*, vol. 5, no. 6, pp. 2219–2231, 2013.

[265] G. Finocchio, R. Tomasello, B. Fang, A. Giordano, V. Puliafito, M. Carpentieri, and Z. Zeng, "Perspectives on spintronic diodes," *Applied Physics Letters*, vol. 118, no. 16, p. 160502, 2021.

[266] A. Hirohata, K. Yamada, Y. Nakatani, I.-L. Prejbeanu, B. Diény, P. Pirro, and B. Hillebrands, "Review on spintronics: Principles and device applications," *Journal of Magnetism and Magnetic Materials*, vol. 509, p. 166711, 2020.

[267] X. Zheng, Y. Xu, R. Sobolewski, R. Adam, M. Mikulics, M. Siegel, and P. Kordoš, "Femtosecond response of a free-standing lt-gaas photoconductive switch," *Applied optics*, vol. 42, no. 9, pp. 1726–1731, 2003.